Université Ferhat ABBAS Sétif 1

University Ferhat Abbas Setif-1

Faculty of Sciences and Technology

Doctorat Thesis

Option: Micro-electronic

By

Benlakhdar Faiza

Submitted for the Degree of Doctorat LMD

<u>THEME</u>

Contribution to the study of the doping effect on the characteristics of some semiconductor compounds, theoretical study

Defended on 08/02/2024 before the Jury:

Lahcene Ziét	Professor	Univ. Ferhat Abbas Sétif 1	President
Tayeb Chihi	Professor	Univ. Ferhat Abbas Sétif 1	Supervisor
Brahim Ghebouli	Professor	Univ. Ferhat Abbas Sétif 1	Co-Director
Abdelhak Ferhat Hamida	Professor	Univ. Ferhat Abbas Sétif 1	Examiner
Foudil Sahnoune	Professor	Univ. Mohamed Boudiaf M'sila	Examiner
Idris Bouchama	Professor	Univ. Mohamed Boudiaf M'sila	Guest
Amar Messous	Doctor	Univ. Ferhat Abbas Sétif 1	Guest

Université Ferhat ABBAS Sétif 1

UNIVERSITÉ FERHAT ABBAS - SETIF1

FACULTÉ DE TECHNOLOGIE

<u>**THÈSE**</u>

Présentée au Département d'Electronique

Pour l'obtention du diplôme de

DOCTORAT

Domaine : Sciences et Technologie

Filière : Electronique   **Option : Micro-électronique**

Par

Benlakhdar Faiza

<div style="border:1px solid">

Contribution à l'étude de l'effet du dopage sur les caractéristiques de quelques composés semi-conducteurs.

Etude théorique

</div>

Soutenue le ……. /……./…… devant le Jury:

Ziét Lahcene	Professeur	Univ. Ferhat Abbas Sétif 1	Président
Chihi Tayeb	Professeur	Univ. Ferhat Abbas Sétif 1	Directeur de thèse
Ghebouli Brahim	Professeur	Univ. Ferhat Abbas Sétif 1	Co-Directeur
Ferhat Hamida Abdelhak	Professeur	Univ. Ferhat Abbas Sétif 1	Examinateur
Sahnoune Foudil	Professeur	Univ. Mohamed Boudiaf M'sila	Examinateur
Bouchama Idris	Professeur	Univ. Mohamed Boudiaf M'sila	Invité
Messous Amar	Docteur	Univ. Ferhat Abbas Sétif 1	Invité

بسم الله الرحمن الرحيم

"قل إن صلاتي ونسكي ومحياي ومماتي

لله رب العالمين لا شريك له

وبذلك أمرت و أنا أول المسلمين"

صدق الله العظيم

Dedicate

Praise be to God, the Powerful.

I dedicate this humble work: To the one whose eyes I used to see optimism... To my sun... My moon... To the one with whom my world was illuminated... To the one who drank the cup empty to give me a drop of love... To the one whose fingertips gave me a moment of happiness...The owner of a kind heart and sincere intentions... To the soul of my soul... My dear father Omar, may God have mercy on him with his vast and expanded mercy. To heal my soul... and soothe my heart, my dear mother... may God protect her from all evil and prolong her life. to the apple of my eye; My son Badreddin. May God bless you and may God protect you for me. To my dear and dear sister Nour El-Houda and her husband for their support during these four years of work. I pray to God for you both to grant you good offspring and make you happy in your life. To my brother Abdul Aziz and the beauty of our sunshine, and my sincere appreciation to their wives and children. To my brother Noureddine Hassan and Al-Moataz, whom I greatly appreciate and am proud of, and their wives and children. To my sisters, Latifa and Ruqayya, in whom I found unwavering support during all my years of study. To all friends and those who love happiness for all.

Faiza Benlakhdar

Thanks

LIST OF FIGURES

LIST OF TABLES

LIST OF ABBREVIATIONS

Frequently used abbreviations:

BOA　　　　Born-Oppenheimer approximation

BZ　　　　Brillouin zone

CB　　　　Conduction band

CBM　　　　Conduction band minimum

CIAlS　　　　$CuIn_{1-x}Al_xS_2$

CIS　　　　$CuInS_2$

CGS　　　　$CuGaSe_2$

DFT　　　　Density functional theory

DOS　　　　Density-of-states

FP-LPW　　　　Full-potential linearized augmented plane wave

GGA　　　　Generalized gradient approximation

HF　　　　Hartree-Fock

LDA　　　　Local density approximation

PAW　　　　Projector augmented wave

PBE　　　　 A simplified GGA

PV　　　　Photovoltaic

ZnO　　　　Zinc Oxide

UV　　　　Ultraviolet

TDOS　　　　Total Density of States

BV　　　　Valence Band

BC　　　　Conduction Band

Te　　　　Tellurium

DOS　　　　Density of States

PDOS　　　　Partial Density of States

TDOS　　　　Total Density of States

Fermi level　　　Energy level used as a reference

TABLE OF CONTENTS

Chapter II: Structural properties of perovskite SrTiO3 compound

Chapter III Structural properties of chalcopyrite CuInS$_2$ compound

SECTION II: RESULTS AND DISCUSSIONS

Chapter IV Effects of Zinc Doping on $SrTiO_3$ perovskite compound

Chapter V: Effects of Aluminum doping on $CuInS_2$ chalcopyrite compound

Chapter VI: Effects of Tellurium doping on the Zinc Oxide material

Chapter XII: Investigation of the properties of ZnX (X = Te, S and O) material: Application to photovoltaic solar cells

GENERAL INTRODUCTION

General Introduction

Today, materials-intensive physics and materials science are essential to advancing technology; As a result, this is a broad and renewable field in which many theoretical and experimental researchers are active.to make sure the physical and chemical properties of a material and before selection it is necessary to determine whether its structural, electronic, mechanical and optical properties are suitable for use in technological applications. Since the physical and chemical properties of solids are closely related to their electronic structure. The determination of electronic structure of solids is one of the main goals of both solid physics and chemistry. Studying the electronic structures of materials is necessary to interpret experimental results, as well as to predict the physical and chemical properties of materials that have not yet been used experimentally. The Schrödinger equation can be solved according to quantum mechanical theory to make sure the electronic structure of material. Chemists and physicists theoretical have used a variety of techniques and models to solve the Schrödinger equation for atoms and molecules into one of two categories. The second type uses a more accurate method that does not require experimental data to calculate the electronic structure of the material, regardless of the chemical composition of its components.

The electronic structure of atoms, molecules, and materials can now be calculated using computational methods based on first principles, which also makes it possible to predict the structural, electronic, mechanical, light, and other properties of the materials. These methods eventually took over as the most popular ones for analyzing and comprehending the findings of empirical research. In fact, they have frequently supplanted experience, where it is difficult or impossible to make empirical measurements.

➤ **The goal of the search:**

The field of semiconductors, particularly perovskites, nanoring, and catalysts, has received considerable attention due to their broad properties and wide range of applications, including solar cells, light-emitting devices, and catalysts. With recent scientific developments, research has focused on examining the structural and physical properties of these materials. The primary objective of this study is to verify the following:

1. Analyze the structural and physical properties (mechanical, electronic, electrical and optical) of pure perovskite and doped with Zn atom at different concentrations and compare our findings with both theoretical and experimental results.

2. Examination of pure chalcogenide and aluminum-doped chalcogenide in varying concentrations to determine their structural and physical properties (mechanical, electronic, electrical and optical) and compare them with previous research.

3. Studying the structural, physical, mechanical, electronic, electrical and optical properties of pure tellurium-saturated zinc oxide and comparing them with other experimental and theoretical results.

4. Evaluation of the effect of impurities on structural and physical properties and their potential benefits in technological applications.

5. Investigated the effect of dopants on the bandgap of semiconductors, a critical parameter that determines their optoelectronic properties.

> **Previous studies**

In the field of material science, several studies have been conducted to explore the structural, electronic, optical, and thermal properties of different materials. In 2021, Adewale *et al.* [1] conducted a study on the structural, electronic, mechanical, and thermoelectric properties of $ATiO_3$ (A = Be, Mg, Ca, Sr, and Ba) using the first DFT-based method within the GGA-PBEsol Exchange Correction. Moreover, in 2020, SSA. Gillani *et al.* [2] presented detailed results of structural, electronic, optical, and thermal properties using Zn-doping in the cuboctahedra structure of $SrTiO_3$.

For instance, according to the study conducted by (P. S. Aktaş *et al.*, 2022) [3] different values of x in nano powder $SrTi_{1-x}Nb_xO_3$ (STNO) were synthesized using the sol-gel auto combustion technique with two fuel mixtures. In 2014, Samia Bensalem *et al.* [4] investigated the structural, elastic, and thermodynamic properties of $SrTiO_3$ within the functional theoretical framework of density (DFT) and the pseudopotential plane wave approach.

$CuInS_2$ is a solar cell material with intriguing electronic structure and optical properties, as studied by (Soni *et al.*, 2010) [5]. This compound is of interest for photovoltaic applications due to its unique characteristics, making it a promising candidate for solar energy conversion. $CuInS_2$ thin-film homojunction solar cells were investigated by (L.Kazmerski et al., 1977) [6]. This research explored the potential of $CuInS_2$ as a material for solar cell applications, focusing on its homojunction properties and performance. (Z. Pachuau's, 2023) [7] provides a first-principles investigation of the electronic, optical, and thermoelectric properties of $CuInS_2$ and $CuInSe_2$. This research delves into the fundamental

characteristics of these compounds, offering insights into their potential applications in various fields.

In the study by (ZHANG *et al.,* 2011) [8], first-principles simulations and experimental evidence were used to investigate the enhancement of transmission in ZnO films. This research explored methods to improve the transmission properties of ZnO films, which have potential applications in various optoelectronic devices. In the study by (Sönmezoğlu *et al.*, 2014) [9], tellurium (Te) doping was employed to enhance the physical properties of ZnO thin films. This research aimed to improve the characteristics of ZnO thin films, which can be crucial for various applications, including electronic and optoelectronic devices.

➢ **Research structure**

The aim of this research is to investigate the doping effect on the physical properties of $SrTiO_3$ perovskite compound, $CuInS_2$ chalcopyrite compound and ZnO compound using Density Functional Theory (DFT) method and CASTEP program. In addition of the general introduction and conclusion, this study is divided into two parts:

✚ The first section presents a theoretical background divided into three chapters:

❖ The first chapter introduces the principal approaches of DFT, introduces pseudo-probability and plane-wave methods, and provides a good presentation of CASTEP program and SCAPS-1D.

❖ Chapter II provides a general introduction and physical properties of $SrTiO_3$ perovskite material.

❖ Chapter III provides a general introduction and physical properties of $CuInS_2$ chalcopyrite material.

✚ The second section presents the calculated results obtained using the CASTEP program

and discusses them scientifically with comparison with theoretical and experimental studies available in scientific publications. This section contains four chapters:

❖ Chapter IV, V and VI present a detailed study, the results obtained of the structural, mechanical, electronic, and optical properties of pure $SrTiO_3$, $CuInS_2$ and ZnO and the effects of doping on the properties of these compounds.

❖ Chapter VII present an application of the physical properties of ZnX (X = Te, S, and O) in solar cell structure, using the SCAPS program.

Finally, the study concludes with a general summary of the most important results.

References

[1]   AA. Adewale *et al.*, First principles calculations of structural, electronic, mechanical and thermoelectric properties of cubic ATiO3 (A= Be, Mg, Ca, Sr and Ba) perovskite oxide, Computational Condensed Matter, 28 (2021) e00562 https://doi.org/10.1016/j.cocom.2021.e00562.

[2]   SSA. Gillani et al., First-principles investigation of structural, electronic, optical and thermal properties of Zinc doped SrTiO3, Optik, 201 (2020) 163481, https://doi.org/10.1016/j.ijleo.2019.163481.

[3]   P. S. Aktaş et al., Influence of Synthesis Procedures on the Preparation of Strontium Titanate Nanoparticles and Photocatalytic application for Methylene blue degradation. SpringerLink, 136 (2023) 1107–1123, https://doi.org/10.1007/s11144-023-02375-2.

[4]   S. Bensalem, Theoretical study of structural, elastic and thermodynamic properties of CZTX (X = S and Se) alloys, Journal of Alloys and Compounds, 589 (2014) 137-142, https://doi.org/10.1016/j.jallcom.2013.11.113.

[5]   A. Soni, V. Gupta, C. Arora, A. Dashora, and B. Ahuja, "Electronic structure and optical properties of CuGaS2 and CuInS2 solar cell materials," Solar energy, vol. 84, no. 8, pp. 1481-1489, 2010.

[6]   L. Kazmerski and G. Sanborn, "CuInS2 thin-film homojunction solar cells," Journal of Applied Physics, vol. 48, no. 7, pp. 3178-3180, 1977.

[7]   Z. Pachuau, "First Principal Study of Electronic, Optical and Thermoelectric Properties of CuInS 2 and CuInSe 2," Indian Journal of Pure & Applied Physics (IJPAP), vol. 61, no. 2, pp. 108-114, 2023.

[8]   ZHANG, D., WANG, P., MURAKAMI, R., & SONG, X. (2011). First-principles simulation and experimental evidence for improvement of transmittance in ZnO films. Progress in Natural Science: Materials International, 21(1), 40–45. doi:10.1016/s1002-0071(12)60023-9.

[9]   Sönmezoğlu, S., & Akman, E. (2014). Improvement of physical properties of ZnO thin films by tellurium doping. Applied Surface Science, 318, 319-323. doi: 10.1016/j.apsusc.2014.06.187.

SECTION I

THEORETICAL BACKGROUND

CHAPTRE I

Density Functional Theory (DFT)

Chapter I: Density Functional Theory (DFT)

I.1 Introduction

Density Functional Theory (DFT) was initially proposed by Hohenberg and Kohn, with further development by Kohn and Sham by (Parr, Robert G, 1983) [1]. Despite initial skepticism, DFT has become a widely used computational method for predicting and analyzing electronic properties of materials [1].

In addition to DFT, several other ab initio codes are available for simulating and predicting material properties, including Quantum Espresso, ABINI, CASTEP, and VASP [2-5]. These codes have been extensively employed in studying various material types, such as metals, semiconductors and insulators.

DFT has been the primary tool for quantum mechanical simulation of periodic systems (P. Edwards *et al.*, 2013) [6]. Computational tools like DFT and other ab initio codes have played a crucial role in advancing material science research, enabling the design of materials with desired properties Robert R *et al.*, 1986) [7].

In conclusion, the development and applications of DFT and other ab initio codes have significantly contributed to material science research, leading to new discoveries and advancements in this.

I.2 Schrödinger's equation

The Schrödinger equation is essential in the non-relativistic quantum description of crystalline or molecular systems. It serves as the foundation for this formalism and can be simplified through various approximations for ease of solution. To tackle the multi-body problem in quantum mechanics, the following Schrödinger equations [8,9] must be solved:

$$H\Psi = E\Psi \tag{I.1}$$

Where E is the total energy of the system and Ψ is the wave function of the system.

H: Hamiltonian

The total Hamiltonian, denoted as H, is the Hamiltonian of the quantum system under study. In the non-relativistic case, it is written in the form:

$$H = T_N + T_e + V_{e-e} + V_{N-N} + V_{e-N} \tag{I.2}$$

$$T_N = \frac{-\hbar^2}{2M}\sum_k \Delta_k \tag{I.3}$$

Where:

TN: Kinetic energy of the nuclei:

T_e: Kinetic energy of the electrons:

$$T_e = \frac{-\hbar^2}{2m}\sum_i \Delta_i \tag{I.4}$$

$V_{e\text{-}e}$: Electron-electron interaction potential:

$$V_{e-e} = \frac{1}{2}\sum_{i,j\neq i} U_{ij} = \frac{1}{2}\sum_{i,j\neq i} \frac{e^2}{4\pi\varepsilon_0|\vec{r}_i-\vec{r}_j|} \tag{I.5}$$

$V_{N\text{-}N}$: Nuclei-nuclei interaction potential:

$$V_{N-N} = \frac{1}{2}\sum_{k,l\neq k} U_{kl} = \frac{1}{2}\sum_{k,l\neq k} \frac{e^2 Z_k Z_l}{4\pi\varepsilon_0|\vec{R}_k-\vec{R}_l|} \tag{I.6}$$

$V_{e\text{-}N}$: Electron-nuclei interaction potential:

$$V_{e-N} = \sum_{i,k} U_{ik} = \sum_{i,k} \frac{Z_k e^2}{4\pi\varepsilon_0|\vec{R}_k-\vec{r}_i|} \tag{I.7}$$

In an effort to simplify the notation, the spin coordinate was excluded. Nevertheless, the electrons' spin degree of freedom impacts the wave function.

For stationary processes, the time-independent Schrödinger equation can be expressed as follows:

For electrons:

$$(-\hbar^2/2m)\nabla^2\Psi(r) + V(r)\Psi(r) = E\Psi(r) \tag{I.8}$$

For nuclei:

$$(-\hbar^2/2M)\nabla^2\Phi(R) + U(R)\Phi(R) = ER\Phi(R) \tag{I.9}$$

Where:

- $\hbar$ is the reduced Planck's constant;

- m is the mass of an electron;

- M is the mass of a nucleus;

- ∇^2 is the Laplacian operator.

Where V(r) represents the electron potential energy in terms of its spatial coordinates, U(R) represents the nuclear potential energy in terms of its spatial coordinates, E represents

the total energy of the electron system and ER represents the total energy of the nuclear system.

Note: The equations provided assume a non-relativistic framework and neglect the spin-spin interactions between electrons and nuclei.

Where H is the Hamiltonian operator, Ψ is the wave function, E is the energy of the system, and the subscript "t" is omitted since the equation describes stationary states.

The total Hamiltonian operator (T H) for a system with multiple interacting particles, consisting of N nuclei and M electrons, can be obtained by adding the t. Total kinetic energy operator (T T) and the operator describing all Coulomb interactions (T V) in the Schrödinger equation.

The Hamiltonian operator plays a critical role in quantum mechanics as it describes the total energy of the system and is utilized to predict its time evolution.

The wave function must account for electron spin coordinates, introducing additional complexity. However, exact solutions are impractical for large systems due to the increasing number of particles. Consequently, simplifications are employed, such as the Born-Oppenheimer approximation, Density Functional Theory, and Hartree-Fock method (D. A. McQuarrie, 2007) [10].

The electromagnetic interaction becomes challenging for systems with numerous atoms and electrons, like solids with billions of nuclei and valence electrons. Without further simplification, solving the problem would be infeasible. Three common levels of simplification are the Born-Oppenheimer approximation, Density Functional Theory or Hartree-Fock approximation [11, 12].

I.2.1 Born Oppenheimer approximation

The Born-Oppenheimer approximation is a widely used technique in quantum mechanics to simplify the solution of the Schrödinger equation. This method assumes that the motion of the atomic nuclei is much slower than the motion of electrons, so the kinetic energy of the nuclei is neglected, and the Coulomb energy remains constant. Thus, the nuclei are considered to be stationary while the electrons move in their field. This approximation allows the separation of the electronic and nuclear motions, and the electronic Hamiltonian He is defined to describe the electronic behavior in the field of the nuclei. Using this

Hamiltonian, the Schrödinger equation can be written to solve for the electronic wave function. The Born-Oppenheimer approximation is a fundamental concept in quantum chemistry and has many practical applications in molecular spectroscopy and electronic structure calculations [13,14].

Born-Oppenheimer approximation:

Schrödinger equation simplification:

$$\nabla^2 \Psi(r,R) + (2\mu/\hbar^2)(E - V(R))\Psi(r,R) = 0 \qquad (I.10)$$

Electron motion decoupling from nuclear motion:

$$\Psi(r,R) = \psi(r)R(R) \qquad (I.11)$$

Nuclear kinetic energy term is neglected:

- $T(R) \approx 0$
- Electron term:
- Electron wavefunction:
- $\psi(r)$
- Nuclear term:
- Nuclear wavefunction:
- $R(R)$

Electrostatic interaction between nuclei becomes constant:

$$V_{N-N} = constant \qquad (I.12)$$

Electron-nucleus interaction potential is approximated as an external potential independent of nuclear positions:

$$V_{e-N} = V_{ext} \qquad (I.13)$$

Electronic Hamiltonian:

$$H_e = T_e + V_{ext} \qquad (I.14)$$

Second level of approximation:

Hartree-Fock method (approximation on wavefunctions):

$$\nabla^2 \psi_i(r) - 2\mu/\hbar^2 \sum[V_{ext} + \sum(J(r) - K(r))]\psi_i(r) = \varepsilon_i \psi_i(r) \qquad (I.15)$$

Density Functional Theory (approximation on Hamiltonian):

$$H_e[\rho(r)] = T_e[\rho(r)] + V_{ext} + \int \rho(r')v(r,r')dr' + Exc[\rho(r)] \qquad (I.16)$$

The decoupling technique of separating electron and nucleus movements is an important approximation method in quantum mechanics for addressing N-body problems. This technique is discussed in academic works like "Introduction to Quantum Mechanics" by (D. J. Griffiths *et al.*, 2018) [15] and "Quantum Mechanics: Concepts and Applications" by (N. Zettili *et al.*, 2003) [16]. However, obtaining analytical solutions for the Schrödinger equation for electrons is challenging, except in simple cases like hydrogen. To overcome this challenge, various approximation techniques are utilized, as mentioned in the aforementioned sources.

I.2.2 Approximation of Hartree and Hartree.Fock

I.2.2.1 Hartree approximation

The Hartree-Fock approximation simplifies the behavior of multi-electron systems in quantum mechanics. It assumes that each electron moves independently in a mean field created by the other electrons and nuclei. By reducing the complex N-electron system to a single-electron system, the Hamiltonian can be expressed as the sum of the Hamiltonians for each electron. This approximation is widely studied and discussed in academic works such as "Introduction to Quantum Mechanics" by [15] and "Quantum Mechanics: Concepts and Applications" by [16]. The wave function of the entire electronic system is the product of the individual wave functions of each electron multiplied by their corresponding energies. The Hamiltonian for such a system is given by: [Hamiltonian equation].

$$H = \Sigma_{i=1}^{N} h(i) \qquad (I.17)$$

Where h is the single-electron Hamiltonian.

$$\Psi(x_1; x_2; \ldots ; x_N) = \varphi_i(x_1)\varphi_j(x_2)\ldots\ldots\ldots\varphi_k(x_N) \qquad (I.18)$$

represents the electronic wave function Ψ for a system of N electrons. The wave function is expressed as a product of single-electron wave functions φ_i, φ_j, ..., φ_k, where each wave function depends on the coordinates x_1, x_2, x_N of the corresponding electron. This equation describes the spatial distribution of the electrons in the system, with each φ representing the probability amplitude of finding an electron at a specific position.

I.2.2.2 Hartree-Fock approximation

According to the article "Quantum Mechanics of Many-Electron Systems" by (P. A. M. Dirac, 1929) [17], the Hartree field can be used to break down a multiple equation into an equational system for a single electron. However, as [17] explain, the Hartree field neglects the exchange of any two particles, which means that the total wave function must be antisymmetric if the electron is a fermion. To address this, Fock suggested using Pauli's exclusion principle to correct the electron wave function, as mentioned in the article by [17], which can be expressed as a Slater determinant.

$$\Psi(r_1, r_2, \ldots, r_n) = 1/\sqrt{N!} \begin{vmatrix} \phi_1(r_1) \ \phi_2(r_1) & \phi_n(r1) \\ \phi_1(r_2) \ \phi_2(r_2) & \phi_n(r_2) \\ & . & . \\ & . & \\ \phi_1(r_n) \ \phi_2(r_n) & \phi_n(r_n) \end{vmatrix} \qquad (I.19)$$

The results of this approximation are good, but they are only applicable to small molecules with few electrons.

I.3 Functional Density Theory (DFT)

The energy of an electronic system can be expressed in terms of the density of the ground state, denoted as $\rho(r)$, which forms the basis of the density function. The theoretical model developed by Thomas and Fermi in 1920, which replaces the calculation of the wave function dependent on 3N spatial coordinates with a simpler function, the electron density that depends only on 3 spatial coordinates, is the origin of the DFT (Functional Density Theory). Hohenberg and Kohn, as well as Kohn and Sham, made significant contributions to the field in the 1960s. The Thomas-Fermi model is a remarkable concept in the field of quantum mechanics, as it simplifies the complex calculation of the electron density. The details on this model are available in the works of Thomas and Fermi (1927), (Hohenberg and Kohn, 1964) [18], and (Kohn and Sham, 1965) [19].

Let's recall that the electron density, $\rho(r)$, in an electronic system represents the number of electrons per unit volume in a given state (or the probability of finding an electron in a unit volume). It can be defined as:

$$\rho(r) = |\Psi(x_1, x_2, \ldots, x_N)|^2 \qquad (I.20)$$

Here, Ψ represents the wavefunction of the system, and N represents the total number of electrons. The electron density $\rho(r)$ approaches zero as r tends to infinity, and when integrated over all space, it equals the total number of electrons N:

$$\int \rho(r)dr = N \tag{I.21}$$

In 1964, Hohenberg and Kohn introduced two theorems to establish a mathematical framework for earlier concepts. These two theorems form the basis of the current form of DFT (Density Functional Theory).

I.3.1 Thomas-Fermi model

The work of Hohenberg and Kohn (1964) [18] initiated the development of density functional theory in 1964 and 1965. Their publications introduced two theorems that are considered the cornerstone of DFT.

➢ **First theorem:**

The relationship between the total energy E of an electronic system's ground state and its density $\rho(r)$ under a specific external potential Ve(r) was established through a theorem [18]. According to this theorem, knowing the electron density enables the determination of all wave functions. Consequently, a ground-state electron density functional denoted by $E[\rho(r)]$ is utilized to represent the total energy E of an electronic system interacting in an external potential [18].

➢ **Second theory:**

Every multiparticle system has a total functional energy, the minimum corresponding to the ground state. Ground-state particle density confirms:

According to the work of Hohenberg and Kohn (1964) [18], the actual density of the ground state is the one that minimizes the energy E. In fact, all other properties of the system are also dependent on this density. Vibration analysis is a method that is commonly employed to calculate the ground state energy of an electronic system when it is subjected to an external potential.

I.3.2 Hohenberg.Kohn theorems

The fundamental formalism of Density Functional Theory (DFT) applies to systems with multiple interacting particles that evolve in an external potential, and is rooted in the Hohenberg-Kohn theorem (Hohenberg & Kohn, 1964) [18]. The Hohenberg-Kohn theorem

is based on two underlying theorems that provide a framework for DFT, making it a widely applicable tool for studying electronic structure and properties of materials (Kohn & Sham 1965) [19].

➢ **Theorem I**

According to this theorem, the electron density function (r) is sufficient to determine all electronic properties of a system. This means that the ground state electron density 0(r) and the external potential Vext(r) have a direct correspondence, and similarly, the wave function of the ground state background(r) and background(r) also correspond. The energy functional E [ρ, Vext] can be written as an integral consisting of two parts. The first part is the integral of the external potential Vext multiplied by the electron density ρ(r):

$$E[\rho, V_{ext}] = \int V_{ext}\rho(r)dr + FHK[\rho] \qquad (I.22)$$

In this equation, FHK[ρ] represents the universal HK functional that combines the universal terms of electron kinetic energy T(ρ) and the potential energy due to electron-electron interaction Ve-e. It can be written as:

$$FHK[\rho] = T[\rho] + V_e - e[\rho] \qquad (I.23)$$

The second theorem of Hohenberg and Kohn attempts to answer the question of how to determine whether any density is that of the ground state, given that it is known that the electronic density of the ground state is sufficient to obtain all the properties of this state.

➢ **Theorem II**

This theorem demonstrates that the energy functional E is minimal when any electron density corresponds to the electron density of the ground state background(r).

In this theorem, the energy functional E[ρ(r)] that provides access to the ground state energy is minimized when the electron density exactly matches that of the ground state.

$$E = minE[\rho(r)] \qquad (I.24)$$

In other words, according to the first theorem, a test wave function and a test Hamiltonian are both defined for a test electron density. From this, we can establish a correspondence between the wave function of the variational principle and the electronic density versions.

However, an important problem remains to be solved: how to rewrite an exact analytical formulation of the FHK functional for an interacting N-electron system?

I.4 Kohn and Sham equations

The description of kinetic energy and electron-electron interactions in terms of electron density is a challenging mathematical problem when considering a system of interacting electrons in motion. In an attempt to solve this problem, Kohn and Sham introduced a theoretical approach, known as the Kohn-Sham equations (Kohn and Sham, 1965) [19]. This approach replaces the actual electronic system with a hypothetical system, in which each electron behaves independently and is only influenced by an effective potential, the Kohn-Sham potential. The potential comprises both the external potential caused by the nuclei and the potential induced by the influence of other electrons on the electron of interest.

K-S (Kohn-Sham) reformulated the energy functional of the real system based on the fictitious system. The reformulated energy functional is expressed as:

$$E[\rho(r)] = T_0[\rho(r)] + V_{ee}[\rho(r)] + V_{ext}[\rho(r)] + Exc[\rho(r)] \quad \text{(I.25)}$$

In this expression, $T_0[\rho(r)]$ represents the kinetic energy of non-interacting particles, $V_{ee}[\rho(r)]$ represents the classical Coulomb contribution known as the Hartree energy, and $Exc[\rho(r)]$ is the exchange-correlation functional.

The total energy (E) is given by:

$$E = [T[\rho] - T_0[\rho]] + V[\rho] + V_{ee}[\rho] + V_{ext}[\rho] \quad \text{(I.26)}$$

Where $V[\rho]$ is the external potential term and $[\rho]$ is the density-density interaction term.

The exchange-correlation potential (V_{ext}) is calculated from the derivative of the exchange-correlation energy functional (Exc) with respect to the electron density ($\rho(r)$):

$$V_{ext} = \partial EX[\rho(r)]/\partial \rho(r) \quad \text{(I.27)}$$

$$(HKS(r) - \varepsilon_i)\phi_i(r) = 0 \quad \text{(I.28)}$$

By introducing the Kohn-Sham framework, the Schrödinger equation is transformed into N single-electron Schrödinger equations, commonly known as the Kohn-Sham equations:

Here, HKS is the Kohn-Sham Hamiltonian, N represents the number of electrons, and ε_i are the eigenvalues. The Kohn-Sham Hamiltonian is defined as:

$$HKS = -\nabla^2 + V_e ff(r) \quad \text{(I.29)}$$

The effective potential ($V\_eff(r)$) is given by:

$$V_e ff(r) = V_c lassical[\rho(r)] + V_{ee}[\rho(r)] + V_e xt[\rho(r)] + V_{ext}[\rho(r)] \qquad (I.30)$$

The electron density ($\rho(r)$) is determined from the N single-electron wavefunctions $\phi_i(r)$:

$$\rho[r] = \sum \phi_i(r)^2 \qquad (I.31)$$

Where the sum runs from i = 1 to N.

I.4.1 Exchange and correlation energy approximations

I.4.1.1 Local density approximation (LDA)

The exchange-correlation energy of an inhomogeneous electron system can be determined using a method based on the assumption that the electron density is constant in each infinitesimal volume that makes up the actual system (J. P. Perdew, 1981) [20]. The exchange energy of the density of each volume is then estimated using the exchange energy obtained from a uniform electron gas (J. P. Perdew *et al.*, 2008) [21]. This estimated exchange energy is considered as the exchange energy of the corresponding density. The total energy of exchange-correlation of the system can be expressed as the sum of the exchange energies of all the infinitesimal volumes of the system. The equation is:

$$Exc = \int \rho(r)\varepsilon xc[\rho(r)]dr \qquad (I.32)$$

In this equation, $\varepsilon xc[\rho(r)]$ represents the exchange-correlation energy density for a homogeneous electron gas. It can be decomposed into the exchange energy density ($\varepsilon x[\rho(r)]$) and the correlation energy density ($\varepsilon c[\rho(r)]$):

$$\varepsilon xc[\rho(r)] = \varepsilon x[\rho(r)] + \varepsilon c[\rho(r)] \qquad (I.33)$$

The exchange energy density ($\varepsilon x[\rho(r)]$) and the correlation energy density ($\varepsilon c[\rho(r)]$) correspond to the exchange and correlation contributions of a homogeneous electron gas, respectively. The Dirac exchange function precisely identifies the analytical expression of exchange energy:

$$\varepsilon x(r) = Cx\rho^3 \qquad (I.34)$$

Where:

$$Cx = -(3/4\pi)^{(}1/3) \qquad (I.35)$$

The exchange energy density ($\varepsilon x[\rho(r)]$) and the correlation energy density ($\varepsilon c[\rho(r)]$) correspond to the exchange and correlation contributions of a homogeneous electron gas,

respectively. The Dirac exchange function precisely identifies the analytical expression of exchange energy:

I.4.1.2 Generalized Gradient Approximation (GGA)

According to a scientific article by (J. P. Perdew *et al.,* 1996) [22], the Local Density Approximation (LDA) considers the density at a given point r, but in real systems, the density is not homogeneous throughout space, which makes it more practical to include a correction that considers the rate of change of r. To address this issue, the Generalized Gradient Approximation (GGA) introduces a correction to the exchange-correlation energy functional that takes into account the local charge concentrations and their gradients. The GGA functional is defined in a general form that allows for a more accurate calculation of electronic properties in real systems with spatially inhomogeneous densities.

The exchange-correlation functional is expressed in terms of the electron density (ρ) and its gradient ($\nabla\rho$) according to the following equation:

$$E_{GGA}[\rho] = \int \rho(r)\varepsilon_{GGA}[\rho(r), \nabla\rho(r)]d^3r \qquad (I.36)$$

In this equation, εGGA[ρ(r), $\nabla\rho$(r)] represents the generalized exchange-correlation energy (GGA) depending on both the electron density and its gradient.

Often, the contributions for exchange (εx) and correlation (εc) are separately developed in the GGA functional.

$$GGA[\rho, \nabla\rho] = GGA[\rho, \nabla\rho]x + GGA[\rho, \nabla\rho]c \qquad (I.37)$$

Where GGA[ρ,$\nabla\rho$]x corresponds to the exchange contribution, and GGA[ρ,$\nabla\rho$]c corresponds to the correlation contribution. The GGA functional can also include other terms and coefficients denoted as Zxc. Additionally, the electron density ($\nabla\rho$) can represent the gradient of the electron density with respect to spatial coordinates.

According to a research paper by (B. Hammer *et al*., 1999) [23], there exist various forms of exchange-correlation (Exc) functionals in density functional theory. Among these, the functionals developed by Perdew and Wang (PW91), Perdew and Becke (B88), and Burke and Ernzerhof have gained popularity due to their accuracy and ease of implementation. These functionals are commonly used for electronic structure calculations in different fields of science and engineering.

I.5 Solving the Kohn-Sham equation

The Kohn-Sham equation is a fundamental equation in density functional theory (DFT) that describes the behavior of non-interacting electrons in an effective potential. The equation can be written as:

$$[-1/2\nabla^2 + v_eff(r)]\psi_i(r) = \varepsilon_i\psi_i(r) \tag{I.38}$$

Where $\psi\_i(r)$ is the wavefunction of the i-th electron, ε_i is its energy, and v_eff(r) is the effective potential, which is a sum of the external potential and the Hartree and exchange-correlation potentials. The Hartree potential is given by:

$$v_H(r) = \int \rho(r')/|r - r'|dr' \tag{I.39}$$

Where $\rho(r)$ is the electron density. The exchange-correlation potential is a functional of the electron density and is typically approximated using density functionals such as the local density approximation (LDA) or the generalized gradient approximation (GGA).

The process of solving the Kohn-Sham equation involves finding the eigenvalues and eigenfunctions through numerical methods such as the self-consistent field (SCF) method or direct minimization.

The SCF method iteratively solves the Kohn-Sham equation until self-consistency is achieved, meaning that the electron density matches the density used to calculate the effective potential.

Detailed information on the Kohn-Sham equation and its solutions in density functional theory (DFT) calculations can be found in various research papers and textbooks. Some relevant references include "Density Functional Theory: A

Practical Introduction" by (J. A. Steckel *et al.,* 2009) [24], as well as the research papers by Kohn and Sham (1965) [19] and Hohenberg and Kohn (1964) [18].

I.6 Pseudo-potential methods and plane waves

I.6.1 Introduction

Pseudopotential methods and plane wave basis sets are widely used in solid-state physics and materials science to study the electronic structure of materials. Pseudopotential methods are a class of approximations used to simplify the calculation of electronic structure in solids, while plane wave basis sets are used to represent the wavefunctions of electrons in a crystalline solid.

Pseudopotential methods were first introduced in the 1950s and have since become a powerful tool for studying electronic structure in materials. The basic idea of pseudopotential methods is to replace the complicated atomic potentials that describe the interaction between electrons and atomic nuclei with a simplified potential that only includes the core electrons. This simplification reduces the computational cost of electronic structure calculations and allows for the study of larger and more complex systems. One of the earliest works in this field was by Hohenberg and Kohn in 1964 [18], where they presented their density functional theory (DFT) and its application to solids.

Plane wave basis sets, on the other hand, are a type of basis set used to represent the wavefunctions of electrons in a crystalline solid. The wavefunctions are expanded in terms of plane waves, which have a well-defined momentum and wavelength, and are periodic in space. The use of plane wave basis sets allows for the accurate description of electronic structure in materials, particularly in the case of metals and semiconductors.

One of the earliest works on this topic was by (F. Bloch 1929) [25], who developed the concept of Bloch waves to describe the wavefunctions of electrons in a crystalline solid.

The combination of pseudopotential methods and plane wave basis sets has proven to be a powerful tool for the study of electronic structure in materials. This approach is commonly used in software packages such as Quantum ESPRESSO and VASP to simulate and analyze materials at the atomic scale. The accuracy of these methods has been continuously improved over the years, and they are now widely used in the field of materials science.

In conclusion, the combination of pseudopotential methods and plane wave basis sets has become a powerful tool for the study of electronic structure in materials. The development of these methods was influenced by early works of Hohenberg and Kohn, and Bloch. These methods are now widely used in software packages such as Quantum ESPRESSO and VASP to simulate and analyze materials at the atomic scale.

I.6.2 Bloch Theorem (the plane wave approach)

The Bloch theorem, first introduced by Felix (F. Bloch, 1928) [26], is a fundamental principle in the study of periodic structures. It relates the electronic wave function in a crystalline solid to its periodic potential. According to the Bloch theorem, the wave function of an electron in a periodic potential can be written as a product of a plane wave and a periodic function, which is known as the Bloch function. The plane wave represents the free

electron propagation, while the periodic function describes the periodicity of the crystal lattice. The Bloch theorem is expressed mathematically as:

$$\Psi(r + R) = e^{(ik \cdot R)} \psi(r) \tag{I.40}$$

Where ψ (r + R) is the wave function at a point shifted by a lattice vector R, e(ik·R) is a phase factor, k is the wave vector, and ψ(r) is the wave function at the original point. This equation shows that the wave function of an electron in a crystal has the same form at any two points that differ by a lattice vector R. The wave function is periodic with respect to the lattice, and its periodicity is characterized by the wave vector k.

The Bloch theorem has important implications for the electronic structure of solids. It explains why the energy bands in a crystal are formed, and why they have the periodicity of the lattice. The electronic states in a crystal are labeled by their wave vectors, which are restricted to a Brillouin zone, the first Brillouin zone being the primitive cell of the reciprocal lattice. The band structure of a crystal can be calculated by solving the Schrödinger equation for the Bloch functions. The Bloch theorem has been used extensively in the study of semiconductors, metals, and insulators, and is the basis for many important concepts in solid-state physics, such as the Fermi surface, the density of states, and the effective mass approximation.

I.6.3 Sampling of the first Brillouin zone

The Brillouin zone (BZ) is a periodic region in reciprocal space that encompasses wave vectors k with the same periodicity as the crystal lattice. The first Brillouin zone (FBZ) is the smallest region enclosing the origin and a single unit cell of the lattice. Sampling the FBZ is crucial in electronic band Monk Horst-Pack method utilize a uniform grid of k-points (H. J. Monkhorst *et al.*, 1976) [27], while the Matthiessen-Paxton method employs a smearing function for broadening the k-point grid (M. Methfessel *et al.*, 1989) [28].

The choice of sampling scheme and the number of k-points significantly affects accuracy and efficiency. More complex band structures or precise calculations of properties like density of states or optical properties require denser k-point sampling (G. Kresse *et al.*, 1996) [29].

In summary, accurate electronic band structure calculations necessitate sampling the FBZ, where the choice of sampling scheme and number of k-points impacts accuracy and efficiency. Equation:

The k-point mesh is defined as follows:

$$\Gamma = (1/N_{1,1}/N_{2,1}/N_3) \tag{I.41}$$

Where N1, N2, and N3 are the number of k-points along each reciprocal lattice vector in the Brillouin zone [27].

The total number of k-points required to sample the Brillouin zone is given by:

$$N = N_1 x N_2 x N_3 \tag{I.42}$$

Where N is the total number of k-points [27].

Another important concept is the weight of each k-point, which is determined by the size of the Brillouin zone and the number of k-points used for sampling. The weight of a k-point is given by:

$$W_k = (1/VBZ)x(2\pi)^3/N \tag{I.43}$$

Where VBZ is the volume of the Brillouin zone.

I.6.4 Ecut-off energy

The cut-off energy (Ecut) is a crucial parameter in density functional theory (DFT) calculations of electronic band structures and related properties. It determines the size of the basis set used to expand the electronic wave functions as plane waves.

Choosing a sufficiently high Ecut is vital for accurate results in properties like total energy, density of states, and optical properties. However, excessively high Ecut values increase computational costs, while insufficient values introduce significant errors.

Methods such as convergence testing involve calculating properties for increasing Ecut values until convergence to a stable value is achieved (S. Baroni *et al.*, 2001) [30].

Another approach is the extrapolation method, where properties are extrapolated to the limit of infinite Ecut (D. Vanderbilt, 1990) [31].

The appropriate value of Ecut depends on the system's size, complexity, and desired accuracy, with larger systems and higher accuracy requirements generally necessitating higher Ecut values [5].

In summary, selecting an appropriate value of Ecut is crucial for accurate and efficient DFT calculations of electronic band structures and related properties.

The plane wave basis set is defined as follows:

$$\Psi(r) = \sum G C(G) exp(iG \cdot r) \qquad\qquad (I.44)$$

Where $\Psi(r)$ is the electronic wave function at position r, G is a reciprocal lattice vector, C(G) is the expansion coefficient for wave vector G, and the sum is over all reciprocal lattice vectors G within a sphere of radius Ecut centered on the origin of the reciprocal space [5].

I.7 CASTEP Simulation Tool

CASTEP (Computer Aided Simulation of Thermochemistry and Energy of Materials) is a powerful computational tool for the simulation of materials at the atomic level. It is a widely used code for first-principles electronic structure calculations based on density functional theory (DFT). CASTEP can simulate a variety of properties of materials, such as crystal structures, electronic structures, optical and magnetic properties, and chemical reactions.

CASTEP uses a plane-wave basis set to expand the electronic wavefunctions and a pseudopotential approximation to describe the ion-electron interaction. The code can handle both periodic and non-periodic boundary conditions, making it suitable for the simulation of surfaces, interfaces, and nanoparticles.

One of the key features of CASTEP is its ability to perform calculations at different levels of theory, such as the local density approximation (LDA), generalized gradient approximation (GGA) and hybrid functional. The code also includes several advanced features, such as the calculation of phonon dispersions and the simulation of solid-state NMR and EPR spectra.

CASTEP is user-friendly and can be run through a graphical user interface or via command-line interface. The code is maintained and updated regularly, and it has an active user community that provides support and shares expertise.

In summary, CASTEP is a powerful tool for the simulation of materials at the atomic level. It is widely used in academia and industry and provides a broad range of simulation capabilities for the study of various properties of materials.

I.8 SCAPS Simulation Tool

SCAPS (Solar Cell Capacitance Simulator) is a one-dimensional solar cell modeling software originally developed by Marc Burgelman at the University of Gent in Belgium. It

is a versatile tool that can be used to simulate a wide range of solar cell technologies, including crystalline silicon, thin film, and perovskite solar cells.

SCAPS solves the drift-diffusion equations for electrons and holes in the solar cell, taking into account the effects of band gap, doping, carrier mobility, recombination, and other factors. This allows users to calculate the solar cell's current-voltage (J-V) characteristics, external quantum efficiency (EQE), and other important parameters.

SCAPS is a powerful tool for designing and optimizing solar cells. It can be used to:

Investigate the effects of different device parameters, such as doping, layer thickness, and material properties, on solar cell performance.

Develop new solar cell architectures and materials.

Optimize the performance of existing solar cell technologies.

SCAPS is widely used by researchers and industry alike to develop and improve solar cell technologies. It is a free and open-source software that is available for download from the SCAPS website.

Here are some of the key features of SCAPS:

- ❖ Comprehensive simulation of a wide range of solar cell technologies.
- ❖ Ability to model complex device architectures and materials.
- ❖ Accurate and reliable results.
- ❖ User-friendly interface.
- ❖ SCAPS is a valuable tool for anyone working in the field of solar cell research and development.

I.9 Conclusion

In conclusion, density functional theory (DFT) has become an essential tool for studying the electronic structure and properties of materials. DFT provides a rigorous theoretical framework for understanding the behavior of electrons in materials and has been successful in predicting a wide range of properties. Its accuracy and efficiency have made it a popular method for studying large-scale systems, and it has been used to design new materials with specific functionalities for applications in energy conversion, storage, and catalysis. However, DFT also has its limitations, and further improvements are needed to address certain types of materials and properties, such as strongly correlated materials and

excited states. Despite its limitations, DFT continues to be a valuable tool for materials science research, and its ongoing development is expected to lead to new discoveries and insights into the behavior of materials.

References

[1]   Parr, Robert G, "Density functional theory," Annual Review of Physical Chemistry, pp. 631-656, 1983.

[2]   P. Giannozzi et al., "QUANTUM ESPRESSO: a modular and open-source software project for quantum simulations of materials," Journal of physics: Condensed matter, vol. 21, no. 39, pp. 395502, 2009.

[3]   X. Gonze et al., "ABINIT: First-principles approach to material and nanosystem properties," Computer Physics Communications, vol. 180, no. 12, pp. 2582-2615, 2009.

[4]   S. J. Clark et al., "First principles methods using CASTEP," Zeitschrift für kristallographie-crystalline materials, vol. 220, no. 5-6, pp. 567-570, 2005.

[5]   G. Kresse and J. Furthmüller, "Efficiency of ab-initio total energy calculations for metals and semiconductors using a plane-wave basis set," Computational materials science, vol. 6, no. 1, pp. 15-50, 1996.

[6]   P. Edwards, V. Kuznetsov, D. Slocombe, and R. Vijayaraghavan, "The electronic structure and properties of solids," 2013.

[7]   M. B. Bever, "Encyclopedia of materials science and engineering," 1985.

[8]   E. Schrödinger, "Quantisierung als eigenwertproblem," Annalen der physik, vol. 385, no. 13, pp. 437-490, 1926.

[9]   D. F. Schroeter, "INTRODUCTIONTOQ UA NTUMMECHANICS," 2016.

[10] D. A. McQuarrie, Quantum chemistry. University Science Books, 2008.

[11] T. D. Rasmussen, P. Ren, J. W. Ponder, and F. Jensen, "Force field modeling of conformational energies: importance of multipole moments and intramolecular polarization," International Journal of Quantum Chemistry, vol. 107, no. 6, pp. 1390-1395, 2007.

[12] C. J. Taylor et al., "A Brief Introduction to Chemical Reaction Optimization," Chemical Reviews, vol. 123, no. 6, pp. 3089-3126, 2023.

[13] J. C. Poggendorff, E. Wiedemann, and G. H. Wiedemann, Annalen der Physik. JA Barth, 1889.

[14] I. N. Levine, D. H. Busch, and H. Shull, Quantum chemistry. Pearson Prentice Hall Upper Saddle River, NJ, 2009.

[15] D. J. Griffiths and D. F. Schroeter, Introduction to quantum mechanics. Cambridge university press, 2018.

[16] N. Zettili, "Quantum mechanics: concepts and applications," ed: American Association of Physics Teachers, 2003.

[17] P. A. M. Dirac, "Quantum mechanics of many-electron systems," Proceedings of the Royal Society of London. Series A, Containing Papers of a Mathematical and Physical Character, vol. 123, no. 792, pp. 714-733, 1929.

[18] P. Hohenberg and W. Kohn, "Inhomogeneous electron gas," Physical review, vol. 136, no. 3B, p. B864, 1964.

[19] W. Kohn and L. J. Sham, "Self-consistent equations including exchange and correlation effects," Physical review, vol. 140, no. 4A, p. A1133, 1965.

[20] J. P. Perdew and A. Zunger, "Self-interaction correction to density-functional approximations for many-electron systems," Physical Review B, vol. 23, no. 10, p. 5048, 1981.

[21] J. P. Perdew et al., "Restoring the density-gradient expansion for exchange in solids and surfaces," Physical review letters, vol. 100, no. 13, p. 136406, 2008.

[22] J. P. Perdew, K. Burke, and M. Ernzerhof, "Generalized gradient approximation made simple," Physical review letters, vol. 77, no. 18, p. 3865, 1996.

[23] B. Hammer, L. B. Hansen, and J. K. Nørskov, "Improved adsorption energetics within density-functional theory using revised Perdew-Burke-Ernzerhof functionals," Physical review B, vol. 59, no. 11, p. 7413, 1999.

[24] J. A. Steckel and D. Sholl, Density Functional Theory. John Wiley & Sons, Ltd, Hoboken, 2009.

[25] F. Bloch, "Über die quantenmechanik der elektronen in kristallgittern," Zeitschrift für physik, vol. 52, no. 7-8, pp. 555-600, 1929.

[26] F. Bloch, "Quantum mechanics of electrons in crystal lattices," Z. Phys, vol. 52, pp. 555-600, 1928.

[27] H. J. Monkhorst and J. D. Pack, "Special points for Brillouin-zone integrations," Physical review B, vol. 13, no. 12, p. 5188, 1976.

[28] M. Methfessel and A. Paxton, "High-precision sampling for Brillouin-zone integration in metals," Physical Review B, vol. 40, no. 6, p. 3616, 1989.

[29] G. Kresse and J. Furthmüller, "Efficient iterative schemes for ab initio total-energy calculations using a plane-wave basis set," Physical review B, vol. 54, no. 16, p. 11169, 1996.

[30] S. Baroni, S. De Gironcoli, A. Dal Corso, and P. Giannozzi, "Phonons and related crystal properties from density-functional perturbation theory," Reviews of modern Physics, vol. 73, no. 2, p. 515, 2001.

[31] D. Vanderbilt, "Soft self-consistent pseudopotentials in a generalized eigenvalue formalism," Physical review B, vol. 41, no. 11, p. 7892, 1990.

CHAPTER II

Structural properties of perovskite SrTiO3 compound

Chapter II: Structural properties of perovskite $SrTiO_3$ compound

II.1 Introduction

ABO_3 compounds are a class of materials with a crystalline structure based on the perovskite mineral, which has the chemical formula $CaTiO_3$ (J. Zhu *et al.*, 2014) [1]. In the case of ABO_3 perovskites, the A-site cation is usually a metal alkali metal earth cation, while the B-site cation is typically a transition metal (P. Yadav *et al.*, 2021) [2].

According to recent research on perovskite oxides (J. Xu *et al.*, 2019) [3], their unique crystal structure enables a range of physical and chemical properties, such as high catalytic activity, excellent ion conductivity, and a high dielectric constant.

Particularly in recent years, perovskites for solar cells have received a lot of attention due to their high efficiency and low cost. These properties make perovskite oxides promising candidates for oxygen electrocatalysts. Additionally, the simplicity and scalability of perovskite solar cell production make them an attractive alternative for developing large-scale energy production capacities (H. J. Snaith, 2013) [4].

Despite the high potential of perovskites for various applications, their long-term stability has been a major challenge due to their sensitivity to degradation by moisture and light (S. Emami *et al.*, 2015) [5]. However, recent research on perovskite solar cells has made significant progress in improving their stability over time, offering promising solutions to this issue.

Nonetheless, scientists are actively working to develop strategies to improve the stability and resilience of perovskites, including the use of protective coatings and the development of stable materials (D. Liu *et al.*, 2014) [6].

II.2 Structure description

According to (Z. Shi *et al.*, 2018) [7], the term "perovskite" has its origins in the mineral calcium titanate ($CaTiO_3$), which belongs to a family of crystalline substances.

Perovskite also refers to a broad range of mixed oxides represented by the chemical formula ABO_3. The ideal perovskite structure consists of a single ABO_3 molecule with a cubic lattice in the Pm3m symmetry group and a general formula of ABX_3 (M. Subramanian *et al.*, 1983) [8].

The A cation, typically a large ionic cation such as Ba, Ca, Pb, Rb, Sr, Na, or K, has a coordination number of 12 and is surrounded by twelve oxygen anions. The B cation, with a smaller radius, such as Ti, Sn, W, Zr, Nb, Ta, or K, has a coordination number of 6 and is closely surrounded by six oxygen anions. The oxygen ion (O) has six close neighbors in the structure, including four type A cations and two type B cations. In the ideal perovskite structure, A cations are located at the vertices (0,0,0) of the lattice, B cations are located in the middle of the mesh (1/2.1/2.1/2), and X anions are located in the middle of the faces of each cube (1/2.1/2.0), (1/2.0.1/2), and (0.1/2.1/2) As show in Fig. II.1.
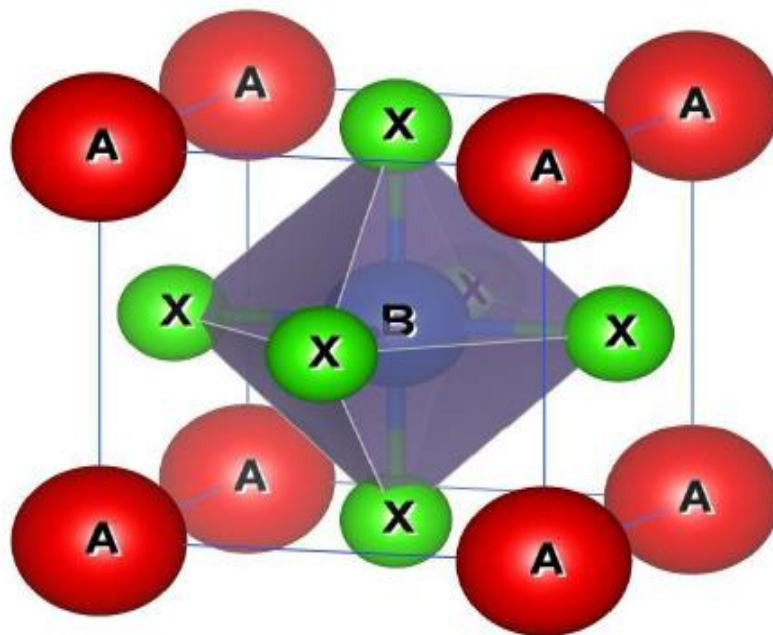
Fig. II.1: Ideal perovskite structure.

II.3 Structure type Perovskites

Perovskites are a type of materials with the general chemical formula ABO_3 and a crystal structure based on the perovskite structure. The perovskite structure was initially discovered in a mineral called perovskite, which has the formula $CaTiO_3$. This crystal structure comprises BO_6 octahedra that share corners, forming a three-dimensional lattice. The A cations occupy the spaces between the octahedra, giving rise to a regular pattern that can be visualized as interconnected cubes. The A cations are situated at the center of each cube and are encompassed by oxygen ions.

The A and B ions in the perovskite structure can be chosen from a wide variety of elements, giving rise to a large family of perovskite materials with different properties. In particular, the properties of perovskites can be tuned by varying the A and B cations, as well as by controlling the synthesis conditions. This makes perovskites highly versatile and suitable for a variety of applications, including energy storage and conversion, catalysis, sensing and optoelectronics (M. Grätzel, 2014) [9].

One of the most exciting applications of perovskites in recent years has been in the field of photovoltaics. Perovskite solar cells have emerged as a promising alternative to traditional silicon-based solar cells due to their high-power conversion efficiency, low cost, and ease of processing. Perovskite solar cells are typically based on a hybrid organic-inorganic perovskite material, which has a slightly different crystal structure compared to the ABO_3 perovskites. However, the fundamental principles underlying the perovskite crystal structure are the same and the success of perovskite solar cells has further fueled interest in perovskite materials.

Overall, the ABO_3 perovskite structure is a highly versatile and promising class of materials with a wide range of properties and applications. The regular and flexible crystal structure of perovskites provides a framework for controlling and tuning the properties of the materials, making them suitable for a variety of technological applications.

II.3.1 Tetragonal perovskite

According to (Q. Shi *et al.*, 2021) [10], tetragonal perovskites are a subgroup of the larger family of perovskite materials with the general chemical formula ABO_3. In the tetragonal structure, the BO_6 octahedra are tilted in relation to each other and the lattice is distorted, resulting in a unit cell with a fourfold symmetry axis. The tetragonal perovskite structure is commonly found in materials such as $BaTiO_3$ and $PbTiO_3$, which have significant ferroelectric properties and are of interest for their potential in various applications [10].

Ferroelectric materials are characterized by a spontaneous electric polarization that can be reversed by an external electric field. The tetragonal perovskite structure provides a framework for these materials to exhibit such properties by allowing the BO_6 octahedra to rotate in response to an electric field, causing the polarization to switch direction. This makes tetragonal perovskites highly useful in a range of applications, including actuators, sensors, and memory devices (J. Scott, 2007) [11].

According to (H. Huang, 2010) [12] in recent years, there has been a growing interest in the tetragonal perovskite structure in the field of photovoltaics. This is due to the ferroelectric properties of these materials, which can improve charge separation and collection in solar cells, resulting in higher efficiency. As a result, a new class of photovoltaic materials known as ferroelectric photovoltaics has emerged [12].

Overall, tetragonal perovskites are a highly versatile and important class of materials with a range of properties and applications. Their unique crystal structure, which allows for tilting and distortion, gives rise to a variety of interesting physical properties, making them useful in a range of technological applications.

II.3.2 Rhombohedral perovskite

Rhombohedral perovskite is a ferroelectric oxide directly synthesized on silicon by (M. P. Warusawithana *et al.*, 2009) [13]. By combining a rhombohedral perovskite structure with silicon, this material has significant implications for the development of advanced electronic devices (M. P. Warusawithana *et al.*, 2009) [13].

Piezoelectricity is the ability of certain materials to produce an electric charge in response to an applied mechanical stress and vice versa. The rhombohedral perovskite structure enables these materials to exhibit such properties by allowing the BO_6 octahedra to rotate in response to an applied stress, leading to the generation of an electric charge. This unique characteristic makes rhombohedral perovskites highly valuable in various fields, including the development of sensors, actuators and energy harvesting devices (Y. Qi, J. Kim *et al.*, 2011) [14].

According to (Y. Heo *et al.* 2022) [15], the rhombohedral perovskite structure has gained attention in recent years in the field of photovoltaics. The piezoelectric properties of these materials can enhance charge separation and collection in solar cells, leading to improved efficiency. As a result, a new class of photovoltaic materials known as piezoelectric photovoltaics has emerged.

Overall, rhombohedral perovskites are a highly versatile and important class of materials with a range of properties and applications. Their unique crystal structure, which allows for tilting and distortion, gives rise to a variety of interesting physical properties, making them useful in a range of technological applications.

II.3.3 Orthorhombic perovskite

Orthorhombic perovskites are a subclass of perovskite materials with the chemical formula ABO_3. In the orthorhombic structure, the BO_6 octahedra are not tilted and the lattice is not distorted, leading to a unit cell with three unequal axes. This structure is found in many important materials, including $SrTiO_3$, which is a widely used substrate in materials science and technology (K. A. Müller *et al*., 1979) [16].

According to (B.D. Qu *et al.* 1998) [17], the orthorhombic structure exhibits unique electronic and optical properties due to its lack of tilting and distortion. For instance, $SrTiO_3$ has a high dielectric constant, which makes it a useful capacitor material in electronic devices. Additionally, it possesses a large bandgap, which makes it a potential candidate for use in optoelectronic applications, such as solar cells [17].

Overall, orthorhombic perovskites are a highly versatile class of materials with a range of properties and applications. Their unique crystal structure, which lacks tilting and distortion, gives rise to a variety of interesting physical properties, making them useful in a range of technological applications.

II.3.4 Monoclinic and triclinic perovskite

Perovskite is a class of materials with a distinctive crystal structure and a wide range of applications. The perovskite structure is characterized by the ABO_3 unit cell, which consists of an A-site cation B-site cation, and three oxygen ions. The crystal structure of perovskite is described by its symmetry and lattice parameters, which can be classified into several different types. Monoclinic and triclinic perovskite structures are two examples of perovskite structures with unique properties and potential applications.

As per (H. Fu *et al.*, 2000) [18] Cohen's research published in Nature, monoclinic perovskite structures possess a unique crystallographic axis, known as the b-axis, that is perpendicular to the plane of the ABO_3 unit cell. In monoclinic perovskites, the A-site cation is shifted from the center of the unit cell, resulting in a distortion of the octahedral coordination geometry of the B-site cation. This distortion can alter the electronic and magnetic properties of the material, making monoclinic perovskites relevant for applications in areas like data storage and spintronics [18].

Triclinic perovskite structures are characterized by their lack of symmetry, meaning that each of the three axes of the unit cell have different lengths and angles. This results in a more complex crystal structure that is less common in perovskite materials. However,

triclinic perovskites have been found to exhibit interesting properties, such as high ionic conductivity, which makes them potential candidates for applications in solid oxide fuel cells and other electrochemical devices (D. V. West *et al.*, 2011) [19]. (R. A. Evarestov *et al.*, 2012) [20] conducted research on the four phases of BaTiO3 and discovered that the Monoclinic and triclinic of perovskites ABO_3 exhibits ferroelectric properties, indicating its high potential for use in devices such as random-access memory and sensors. The findings of their study, published in the Journal of Computational Chemistry, shed light on the unique characteristics of this material and its potential applications [20].

The unique properties of monoclinic and triclinic perovskite structures make them attractive for various applications in materials science. Researchers are studying ways to optimize their properties for specific applications by manipulating their crystal structure and composition.

In conclusion, perovskite structures are an important class of materials with a wide range of properties and potential applications. Understanding the crystal structure and symmetry of perovskites is crucial for designing and optimizing their properties for specific applications. Monoclinic and triclinic perovskites are two examples of perovskite structures that have unique properties and potential applications in various fields.

II.4 Stability criteria for a perovskite structure

According to the research on perovskite compounds (R. D. Shannon, 1976) [21], the stability of a perovskite structure ABO_3 can be determined by several factors. These factors include the ion radius lengths of cationic A, B and X anion by ion bonds, as well as the difference in electrolyte between cations and anions [21].

Among these, the tolerance factor and ionic positive ion bonds serve as crucial criteria for the stability of the perovskite structure (D. Khomskii, 2014) [22]. In other words, these factors play a vital role in the formation and stability of perovskite compounds [22].

II.4.1 Tolerance factor (t)

The tolerance factor represents a balance between the bonds (A-X) and (B-X), which are determined by the ionic radii of both (A) and (B) cations and anions. It is a measure of deviation from the ideal cubic structure of perovskite, where the length of the bond (B-X) is (a/2) and the length of the bond (A-X) is (a/2), with the following equality: (A+X)/2(B+X) = 1.

The tolerance factor specifies the deviation from the ideal perovskite, where the structure is stable in the range 0.75< t <1.06 and takes the form of a cubic grid, which is optimal for t = 1. Moving away from this value, the structure can be subject to different distortions. For instance, if the tolerance factor is in the range 0.75< t <0.96, the structure will experience perpendicular deformation, and in the range 0.99< t <1.06, the structure will be cubic. The value of the tolerance factor determines the type of distortion and stability of the perovskite structure (R. E. Cohen, 1992) [23].

II.4.2 Ionic bonding

The stability criterion of perovskite structures is also affected by the ionic bond between positive ions, which is the second factor to consider (K.S. Pitzer, 1960) [24]. The difference in electrophoresis, calculated by an equation, determines the ionic character of the perovskite structure of type ABX_3 based on the Pauling scale. This factor is essential for understanding the stability of the perovskite structure and its properties.

II.5 Application of perovskites

Perovskite oxides have gained considerable attention due to their unique and fascinating properties, such as superconductivity, ferroelectricity, semi conductivity, catalysis and many more. According to (S. Laalioui *et al.* 2020) [25], perovskite oxides have captured significant attention due to their extraordinary and captivating properties, including superconductivity, ferroelectricity, semiconductivity, catalysis and more [25].

According to (L. P. Lekesi *et al.*,2022) [26], perovskite solids have become indispensable in various fields, such as electricity and ceramics, thermal and materials science, astrophysics, and nuclear power [26]. According to the Introductory Chapter: Perovskite materials and advanced applications by (X. Geng *et al.,* 2020) [27], the perovskite structure, which ideally takes the form of a cube, offers a broad range of technological applications. Its direct crystal structure and essential electrical and ferroelectric properties make these applications possible [27]. Perovskite ceramics find many unusual applications, including RAM, microwave devices, capacitors, transformers, piezoelectric tools, and sensors, to name a few.

II.6 Structure of strontium titanate SrTiO₃

Strontium titanate, with its perovskite structure, has been extensively studied due to its various applications in electronic and optical devices. The cubic phase of strontium titanate

consists of oxygen atoms forming an octahedron around the central titanium atom, with strontium atoms located at the cube's peaks and oxygen atoms located at the cube's faces (Fig. II.2). The crystal structure and lattice parameters of strontium titanate have been reported in many research works, including the study by I. A. (Sluchinskaya *et a*l., 2019) and (R. Ranjan *et al.*, 2006) [28,29] on the electronic and magnetic properties of structural defects in $SrTiO_3(Co)$.
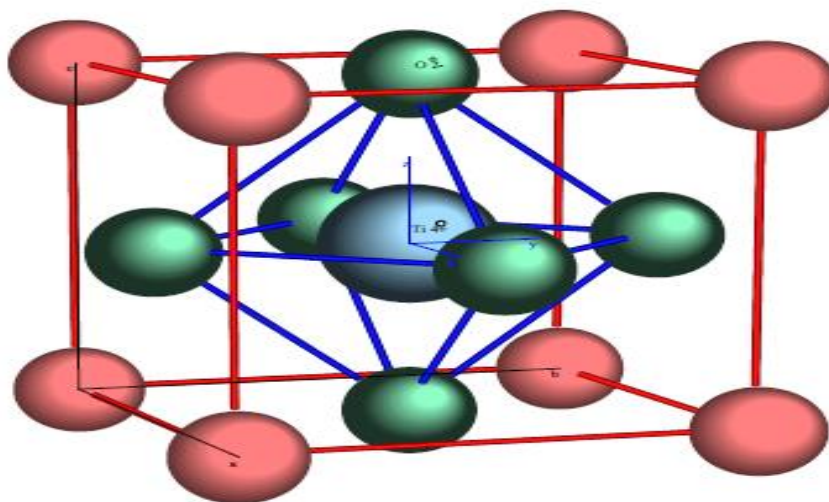
Fig. II.2: Cube's faces of $SrTiO_3$ strontium titanate.

II.7 General properties of strontium titanate SrTiO₃

According to the literature, $SrTiO_3$ is a perovskite compound that exhibits interesting physical and chemical properties. It has a cubic structure at room temperature, with a lattice parameter of 3.905 and the space group Pm3m (A. Ohtomo *et al*., 2004) [30]. At 105 K, it undergoes a phase transition and becomes tetragonal, with a = b = c.

The melting point of $SrTiO_3$ is 2350 K [30]. The cubic structure of $SrTiO_3$ has twelve oxygen ions surrounding the Sr ion, and six oxygen ions surrounding the smallest titanium ion (see Fig. II.3).

II.8 Phase change in strontium titanate SrTiO₃

The phase change in SrTiO₃ has been extensively studied in materials science due to its potential for various applications in microelectronics and nanotechnology. At room temperature, SrTiO₃ possesses a cubic structure. However, it undergoes a phase transition to a tetragonal structure at low temperatures of around 105 K (T. Ishidate *et al*, 1992) [31]. This transformation has been attributed to the distortion of the TiO₆ octahedra in the material's crystal lattice. High-pressure studies have also shown that SrTiO₃ can undergo phase transitions to orthorhombic and rhombohedral structures under certain conditions [31]. This knowledge is crucial in understanding the properties and behavior of SrTiO₃ under different environments and can help in the development of novel applications for this material [31].

This transition is attributed to the rotation of TiO₆ octahedra in the crystal structure, which causes a distortion in the lattice parameters (J. Haeni *et al.*, 2004) [32]. The induction of the phase transition in SrTiO₃ can be achieved not only through the application of external pressure or an electric field but also by manipulating its composition. In addition, the current status of phase change memory and its future potential are being explored. This emerging technology utilizes the phase change behavior of certain materials, such as chalcogenide glasses, to store data and has the potential to revolutionize the computer industry (S. Lai. 2003) [33]. Regardless of the method used, the phase transition of SrTiO₃ has significant implications for its potential applications in microelectronics and nanotechnology (Y. Zhang *et al.*, 2017) [34].

According to (D. G. Schlom *et al.*, 2007) [35], the properties of SrTiO₃ can be modified by controlling the phase transition, including the dielectric constant, piezoelectricity, and ferroelectricity. This suggests that by manipulating the strain of ferroelectric thin films, the properties of SrTiO₃ can be tuned to meet specific requirements for various applications. The ability to control the phase change in SrTiO₃ has led to potential applications in microelectronic devices, including resistive random-access memory, phase-change memory, and memristors (J. J. Yang *et al.*, 2013) [36]. Furthermore, SrTiO₃ has been investigated for its potential in energy applications, including thermoelectric and solar cells. Recent studies have explored the use of SrTiO₃ in ferroelectric tunnel junctions for information storage and processing (V. Garcia *et al*, 2014) [37]. The phase change of SrTiO₃ has been found to play a crucial role in the performance of such junctions. Redox engineering of strontium titanate-based thermoelectric has been studied to explore its potential in energy applications such as thermoelectric and solar cells (A. V. Kovalevsky *et al.*, 2020) [38]. Phase change in SrTiO₃

strontium titanate is one of the important properties that can be tuned by redox engineering to enhance the thermoelectric performance of the material.

The use of this approach can lead to the creation of new and more efficient materials for energy applications. The research conducted by [38] sheds light on the potential of redox engineering in developing advanced materials for energy conversion applications. The study suggests that redox engineering can be an effective method for improving the thermoelectric properties of $SrTiO_3$-based materials, and opens up new possibilities for the development of high-performance energy conversion devices [38].

II.8.1 Cubic-tetragonal phase transition

Strontium titanate $SrTiO_3$ is a perovskite-type oxide material that undergoes a structural phase transition from cubic to tetragonal symmetry at approximately 105 K under normal pressure conditions. This was observed by Ederer and Spaldin in their study on the effect of epitaxial strain on the spontaneous polarization of thin film ferroelectrics. Their research, published in Physical Review Letters, provides insight into the properties of this material and its potential applications. (C. Ederer *et al.*, 2005) [39]. This phase transition has been extensively studied due to its important implications in a variety of fields such as materials science, condensed matter physics and solid-state electronics.

Several studies have investigated the structural and electronic properties of $SrTiO_3$ across the cubic-tetragonal phase transition. For instance, according to (R. Loetzsch *et al.*, 2010) [40], using X-ray diffraction and Raman spectroscopy techniques, it has been shown that the phase transition is associated with a softening of the Ti-O bond in the [001] direction, which leads to the elongation of the c-axis. The study also found that the surface of the $SrTiO_3$ single crystals showed an increased sensitivity to external and internal strain, leading to a greater distortion of the crystal structure near the surface (A. Tkach *et al.*, 2004) [40,41]. In the study of $SrTiO_3$'s phase transition, electronic properties have also been extensively investigated. Research has shown that the transition induces alterations in the electronic band structure and the dielectric constant. Moreover, in a study published in Applied physics letters, it was demonstrated that the cubic-tetragonal phase transition in $SrTiO_3$ single crystals near the surface is connected with both internal and external strains. This study, conducted by (R. Loetzsch *et al.*, (2010) [40], highlights the effects of these strains on the crystal's structural and electronic properties [40].

The cubic-tetragonal phase transition in $SrTiO_3$ has also been studied in the context of thin films and interfaces. For example, it has been shown that the transition can be suppressed in epitaxial thin films grown on certain substrates, such as (001) -oriented $LaAlO_3$, due to the presence of interfacial strain (H. Y. Hwang *et al.*, 2012) [42]. Furthermore, the transition has been found to play a crucial role in the electronic properties of interfaces between $SrTiO_3$ and other materials, such as $LaAlO_3/SrTiO_3$ heterostructures, where the formation of a two-dimensional electron gas has been attributed to the polar discontinuity associated with the cubic-tetragonal transition (C. Cen *et al.*, 2009) [43].

In conclusion, the cubic-tetragonal phase transition in $SrTiO_3$ is a fascinating phenomenon that has been extensively studied over the years. The transition is associated with changes in the structural and electronic properties of the material and plays an important role in the behavior of thin films and interfaces.

II.8.2 Tetragonal-orthorhombic phase transition

Strontium titanate $SrTiO_3$ is an important material that exhibits a tetragonal to orthorhombic phase transition at low temperatures. This phase transition is related to the Jahn-Teller distortion of the TiO_6 octahedra in the material, which results in a distortion of the crystal lattice. The transition has been extensively studied by various research groups, and several studies have investigated the structural and electronic properties of the material in both the tetragonal and orthorhombic phases.

An initial study of the structural phase transition of $SrTiO_3$ was conducted by (F. El Mellouhi *et al.*, 2010) [44], where they used density functional theory (DFT) calculations to investigate the structural changes and electronic properties of $SrTiO_3$ in the tetragonal and orthorhombic phases. The authors found that the orthorhombic phase was more energetically favorable than the tetragonal phase, and that the phase transition was associated with a significant alteration in the electronic properties of the material.

A study by (T. Hasan *et al.*, 2022) [45] investigated the effect of Ce and Fe doping on the tetragonal to orthorhombic phase transition in $SrTiO_3$. The authors found that doping the material with Ce resulted in an increase in the transition temperature and a decrease in the lattice distortion in the orthorhombic phase. On the other hand, doping with Fe led to a decrease in the transition temperature and an increase in the lattice distortion. These doping-induced changes in the phase transition temperature and lattice distortion can be attributed

to the modification of the electronic structure and chemical bonding in the doped $SrTiO_3$ [45].

In summary, the tetragonal to orthorhombic phase transition in $SrTiO_3$ is a well-studied phenomenon that is related to the Jahn-Teller distortion of the TiO_6 octahedra. The transition is accompanied by a significant change in the structural and electronic properties of the material, and has been shown to be influenced by doping.

II.8.3 Orthorhombic-monoclinic phase transition

Strontium titanate $SrTiO_3$ is a perovskite oxide material that exhibits a structural phase transition from orthorhombic to monoclinic symmetry upon cooling. The transition temperature is around 105 K, and the origin of the transition is related to the distortion of the TiO_6 octahedra in the material. The orthorhombic to monoclinic phase transition has been studied by various research groups, and several studies have investigated the structural and electronic properties of the material in both the orthorhombic and monoclinic phases.

A study by (F. El-Mellouhi *et al.*, 2013) [46] used a screened hybrid functional to investigate the structural phase transitions in $SrTiO_3$, $LaAlO_3$ and $LaTiO_3$. The authors found that the tetragonal to orthorhombic phase transition in $SrTiO_3$ was of the first order and that the transition was related to the softening of a particular phonon mode. The authors also found that the volume change associated with the transition was relatively small [46].

A study by (E. K. H. Salje *et al.*, 2011) [47], investigated the effect of external pressure on the ferro elastic phase transition in $SrTiO_3$. The authors found that the transition temperature increased with pressure, and that the volume change associated with the transition increased as well. The authors suggested that the transition was related to the coupling between the phonon modes and the strain in the material [47]. A study by (E. Sawaguchi *et al.*, 1962) [48], investigated the electrical properties of $SrTiO_3$ in the orthorhombic and monoclinic phases. The authors found that the dielectric constant of the material increased significantly upon cooling through the phase transition and that the increase was related to the softening of a particular phonon mode [48].

In summary, the orthorhombic to monoclinic phase transition in $SrTiO_3$ is a well-studied phenomenon that is related to the distortion of the TiO_6 octahedra in the material. The transition is accompanied by a significant change in the structural and electronic properties of the material, and has been shown to be influenced by external pressure.

II.9 Conclusion

In conclusion, ABX_3 perovskite oxides are a fascinating class of materials with a wide range of properties and applications. The unique crystal structure of these materials allows for a variety of different chemical and structural modifications, which can be used to tune their properties for specific applications. Strontium titanate $SrTiO_3$ is a prototypical perovskite oxide that has been extensively studied due to its interesting electronic, magnetic, and structural properties. In particular, the phase transitions in $SrTiO_3$, such as the tetragonal-orthorhombic and orthorhombic-monoclinic transitions, have been a focus of many studies due to their fundamental importance and potential for applications in electronic and photonic devices. These studies have provided valuable insights into the underlying mechanisms of these transitions and have enabled the development of new materials with tailored properties. Overall, ABX_3 perovskite oxides, and $SrTiO_3$ in particular, hold great promise for a wide range of applications in fields such as energy, electronics and photonics.

References

[1]   J. Zhu *et al*., "Perovskite oxides: preparation, characterizations, and applications in heterogeneous catalysis," Acs Catalysis, vol. 4, no. 9, pp. 2917-2940, 2014.

[2]   P. Yadav, S. Yadav, S. Atri, and R. Tomar, "A Brief Review on Key Role of Perovskite Oxides as Catalyst," ChemistrySelect, vol. 6, no. 45, pp. 12947-12959, 2021.

[3]   J. Xu, C. Chen, Z. Han, Y. Yang, J. Li, and Q. Deng, "Recent advances in oxygen electrocatalysts based on perovskite oxides," Nanomaterials, vol. 9, no. 8, p. 1161, 2019.

[4]   H. J. Snaith, "Perovskites: the emergence of a new era for low-cost, high-efficiency solar cells," The journal of physical chemistry letters, vol. 4, no. 21, pp. 3623-3630, 2013.

[5]   S. Emami, L. Andrade, and A. Mendes, "Recent progress in long-term stability of perovskite solar cells," U. Porto Journal of Engineering, vol. 1, no. 2, pp. 52-62, 2015.

[6]   D. Liu and T. L. Kelly, "Perovskite solar cells with a planar heterojunction structure prepared using room-temperature solution processing techniques," Nature photonics, vol. 8, no. 2, pp. 133-138, 2014.

[7]   Z. Shi and A. H. Jayatissa, "Perovskites-based solar cells: A review of recent progress, materials and processing methods," Materials, vol. 11, no. 5, p. 729, 2018.

[8]   M. Subramanian, G. Aravamudan, and G. S. Rao, "Oxide pyrochlores—a review," Progress in Solid State Chemistry, vol. 15, no. 2, pp. 55-143, 1983.

[9]   M. Grätzel, "The light and shade of perovskite solar cells," Nature materials, vol. 13, no. 9, pp. 838-842, 2014.

[10]   Q. Shi *et al*., "The role of lattice dynamics in ferroelectric switching," Nature communications, vol. 13, no. 1, p. 1110, 2022.

[11] J. Scott, "Applications of modern ferroelectrics," science, vol. 315, no. 5814, pp. 954-959, 2007.

[12] H. Huang, "Ferroelectric photovoltaics," Nature photonics, vol. 4, no. 3, pp. 134-135, 2010.

[13] M. P. Warusawithana et al., "A ferroelectric oxide made directly on silicon," Science, vol. 324, no. 5925, pp. 367-370, 2009.

[14] Y. Qi, J. Kim, T. D. Nguyen, B. Lisko, P. K. Purohit, and M. C. McAlpine, "Enhanced piezoelectricity and stretchability in energy harvesting devices fabricated from buckled PZT ribbons," Nano letters, vol. 11, no. 3, pp. 1331-1336, 2011.

[15] Y. Heo, H. Zhang, and M. Alexe, "Dynamic Control of Piezoelectricity Enhancement via Modulation of the Bulk Photovoltaic Effect in a BiFeO3 Thin Film," Advanced Electronic Materials, vol. 8, no. 11, p. 2200785, 2022.

[16] K. A. Müller and H. Burkard, "SrTi O 3: An intrinsic quantum paraelectric below 4 K," Physical Review B, vol. 19, no. 7, p. 3593, 1979.

[17] B. Qu, M. Evstigneev, D. Johnson, and R. Prince, "Dielectric properties of BaTiO 3/SrTiO 3 multilayered thin films prepared by pulsed laser deposition," Applied physics letters, vol. 72, no. 11, pp. 1394-1396, 1998.

[18] H. Fu and R. E. Cohen, "Polarization rotation mechanism for ultrahigh electromechanical response in single-crystal piezoelectrics," Nature, vol. 403, no. 6767, pp. 281-283, 2000.

[19] D. V. West and P. K. Davies, "Triclinic and monoclinic structures of SrLaCuNbO6 and SrLaCuTaO6 double perovskites," Journal of Applied Crystallography, vol. 44, no. 3, pp. 595-602, 2011.

[20] R. A. Evarestov and A. V. Bandura, "First-principles calculations on the four phases of BaTiO3," Journal of computational chemistry, vol. 33, no. 11, pp. 1123-1130, 2012.

[21] R. D. Shannon, "Revised effective ionic radii and systematic studies of interatomic distances in halides and chalcogenides," Acta crystallographica section A: crystal physics, diffraction, theoretical and general crystallography, vol. 32, no. 5, pp. 751-767, 1976.

[22] D. Khomskii, Transition metal compounds. Cambridge University Press, 2014.

[23] R. E. Cohen, "Origin of ferroelectricity in perovskite oxides," Nature, vol. 358, no. 6382, pp. 136-138, 1992.

[24] K.S. Pitzer, "The nature of the chemical bond and the structure of molecules and crystals: an introduction to modern structural chemistry," Journal of the American Chemical Society, vol. 82, no. 15, pp. 4121-4121, 1960.

[25] S. Laalioui, K. B. Alaoui, H. A. Dads, K. E. Assali, B. Ikken, and A. Outzourhit, "Progress in perovskite based solar cells: scientific and engineering state of the art," Reviews on Advanced Materials Science, vol. 59, no. 1, pp. 10-25, 2020.

[26] L. P. Lekesi, L. F. Koao, S. V. Motloung, T. E. Motaung, and T. Malevu, "Developments on Perovskite Solar Cells (PSCs): A Critical Review," Applied Sciences, vol. 12, no. 2, p. 672, 2022.

[27] X. Geng, H. Tian, and T.-L. Ren, "Introductory Chapter: Perovskite Materials and Advanced Applications," in *Perovskite Materials, Devices and Integration*: IntechOpen, 2020.

[28] I. A. Sluchinskaya and A. I. Lebedev, "Electronic and magnetic properties of structural defects in SrTiO3 (Co)," Journal of Alloys and Compounds, vol. 820, p. 153243, 2020.

[29] R. Ranjan, A. Agrawal, A. Senyshyn, and H. Boysen, "Phases in the system Na1/2Nd1/2TiO3–SrTiO3: a powder neutron diffraction study," Journal of Physics: Condensed Matter, vol. 18, no. 42, p. 9679, 2006.

[30] A. Ohtomo and H. Hwang, "A high-mobility electron gas at the LaAlO3/SrTiO3 heterointerface," Nature, vol. 427, no. 6973, pp. 423-426, 2004.

[31] T. Ishidate and T. Isonuma, "Phase transition of SrTiO3 under high pressure," Ferroelectrics, vol. 137, no. 1, pp. 45-52, 1992.

[32] J. Haeni *et al.*, "Room-temperature ferroelectricity in strained SrTiO3," Nature, vol. 430, no. 7001, pp. 758-761, 2004.

[33] S. Lai, "Current status of the phase change memory and its future," in *IEEE International Electron Devices Meeting 2003*, 2003, pp. 10.1. 1-10.1. 4: IEEE.

[34] Y. Zhang *et al.*, "Thermoelectric phase diagram of the SrTiO3–SrNbO3 solid solution system," Journal of Applied Physics, vol. 121, no. 18, p. 185102, 2017.

[35] D. G. Schlom, L.-Q. Chen, C.-B. Eom, K. M. Rabe, S. K. Streiffer, and J.-M. Triscone, "Strain tuning of ferroelectric thin films," Annu. Rev. Mater. Res., vol. 37, pp. 589-626, 2007.

[36] J. J. Yang, D. B. Strukov, and D. R. Stewart, "Memristive devices for computing," Nature nanotechnology, vol. 8, no. 1, pp. 13-24, 2013.

[37] V. Garcia and M. Bibes, "Ferroelectric tunnel junctions for information storage and processing," Nature communications, vol. 5, no. 1, p. 4289, 2014.

[38] A. V. Kovalevsky et al., "Redox engineering of strontium titanate-based thermoelectrics," Journal of materials chemistry A, vol. 8, no. 15, pp. 7317-7330, 2020.

[39] C. Ederer and N. A. Spaldin, "Effect of epitaxial strain on the spontaneous polarization of thin film ferroelectrics," Physical review letters, vol. 95, no. 25, p. 257601, 2005.

[40] R. Loetzsch *et al.*, "The cubic to tetragonal phase transition in SrTiO 3 single crystals near its surface under internal and external strains," Applied Physics Letters, vol. 96, no. 7, p. 071901, 2010.

[41] A. Tkach, P. M. Vilarinho, A. L. Kholkin, I. M. Reaney, and J. Petzelt, "Structural and Dielectric Properties of Mg-doped Strontium Titanate Ceramics: Dependence on the Materials Processing," in *Materials Science Forum*, 2004, vol. 455, pp. 40-44: Trans Tech Publ.

[42] H. Y. Hwang, Y. Iwasa, M. Kawasaki, B. Keimer, N. Nagaosa, and Y. Tokura, "Emergent phenomena at oxide interfaces," Nature materials, vol. 11, no. 2, pp. 103-113, 2012.

[43] C. Cen, S. Thiel, J. Mannhart, and J. Levy, "Oxide nanoelectronics on demand," Science, vol. 323, no. 5917, pp. 1026-1030, 2009.

[44] F. El Mellouhi, E. Bothers, G. Scuseria, and M. Lucero, "An initial study of the structural phase transition of SrTiO3," in Qatar Foundation Annual Research Forum Proceedings, 2010, vol. 2010, no. 1, p. CSP11: Bloomsbury Qatar Foundation Journals Qatar.

[45] T. Hasan *et al.*, "Structural, electrical, and magnetic properties of Ce and Fe doped SrTiO3," AIP Advances, vol. 12, no. 9, p. 095003, 2022.

[46] F. El-Mellouhi, E. N. Brothers, M. J. Lucero, I. W. Bulik, and G. E. Scuseria, "Structural phase transitions of the metal oxide perovskites SrTiO 3, LaAlO 3, and LaTiO 3 studied with a screened hybrid functional," Physical Review B, vol. 87, no. 3, p. 035107, 2013.

[47] E. K. H Salje, M. Guennou, P. Bouvier, M. Carpenter, and J. Kreisel, "High pressure ferroelastic phase transition in SrTiO3," Journal of Physics: Condensed Matter, vol. 23, no. 27, p. 275901, 2011.

[48] E. Sawaguchi and A. Kikuchi, "Dielectric constant of strontium titanate at low temperatures," Journal of the Physical Society of Japan, vol. 17, no. 10, pp. 1666-1667, 1962.

CHAPTRE III

Structural properties of chalcopyrite CuInS2 compound

Chapter III: Structural properties of chalcopyrite CuInS$_2$ compound

III.1 Introduction

Chalcopyrite materials are semiconductor compounds formed by combining elements from columns I, III, and VI of the periodic table. (F. Ohrendorf *et al.*, 1999) [1] found that the tetragonal chalcopyrite structure is a common characteristic of I-III-VI2 semiconductors. This structure is achieved by modifying the cubic zinc blende structure, such as ZnS, with In atoms placed in alternate Zn positions, as observed in compounds like CuInS$_2$ [1]. The chalcopyrite compound is the dominant crystal structure of I-III-VI2 compounds at room temperature [1]. However, under specific experimental conditions, it is possible to synthesize these materials in the sphalerite structure, also known as zinc blende. Therefore, while chalcopyrite is the primary crystal structure, sphalerite can be an alternative option for synthesis [1].

According to (S. Siebentritt *et al.*, 2017) [2], suggest that the chalcopyrite and the sphalerite crystals can be considered as generalizations of the diamond structure found in column VI elements.

The authors investigate the connection between crystal structure and electronic band structure, as well as the effects of elemental substitutions on the band gap and carrier concentrations. This research enhances our understanding of chalcopyrite materials and their potential applications in photovoltaics and electronic devices (B. Panda *et al.*, 2011) [3].

III.2 I-III-VI2 semiconductors

(K. Takarabe *et al.*, 1992) [4] examine the electronic structure of chalcopyrite semiconductors in I-III-VI2 compound category using synchrotron radiation [4]. I-III-VI2 compounds are versatile ternary compounds composed of elements from columns I, III and VI (Table III.1, Mendeleev Periodic Classification) [4]. (D. Wang *et al.*, 2008) [5] conducted a study on the general synthesis of I-III-VI2 ternary semiconductor nanocrystals, further demonstrating the potential for a wide range of compounds in this family to be synthesized Fig. III.1 [5].
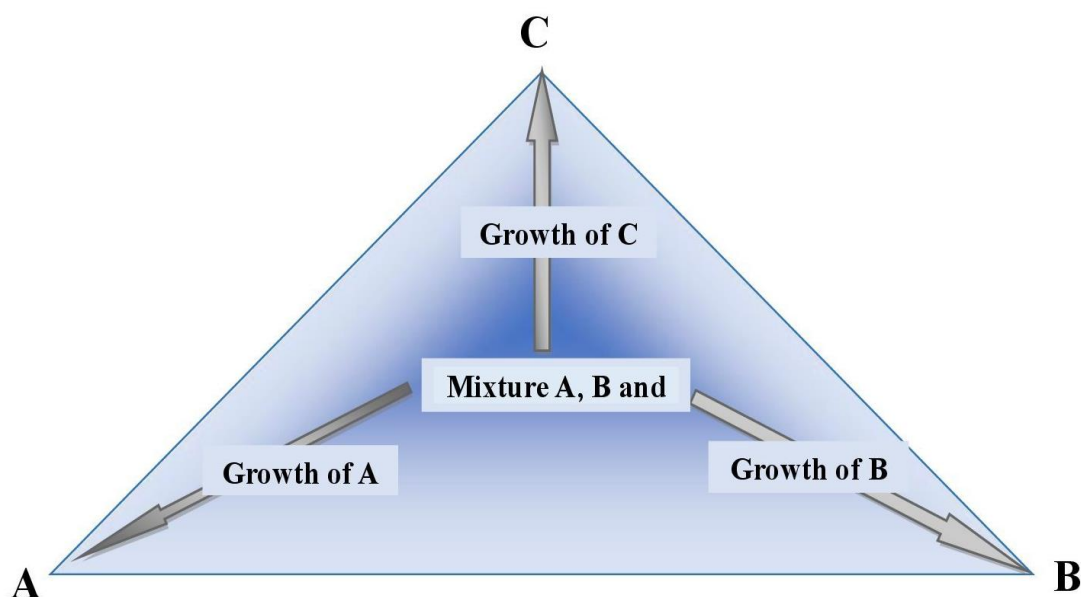
Fig. III.1: ABC ternary composition triangle.

✓ The three pure components are represented by the coordinates, A, B, and C;

✓ Binary compounds are represented along the line segments, for example: point A located on the line [BC] consists entirely of components B and C without A.

✓ The points inside the triangle represent mixtures of each of the three components.

Table III.1: Extract from the periodic table of elements.

I	III	VI
	$_{10.81}^{5}B$	$_{15.99}^{8}O$
	$_{26.98}^{13}Al$	$_{32.065}^{16}S$
$_{63.546}^{29}Cu$	$_{69.74}^{31}Ga$	$_{78.96}^{34}Se$
	$_{114.82}^{49}In$	$_{127.60}^{52}Te$

(W. R. Lambrecht *et al.*, 2003) [6] examine the chalcopyrite structure in group I-III-VI2 semiconductors, known for their suitability in solar technology. The study focuses on analyzing second-order optical response functions through first-principles calculations [6].

Chalcopyrite-structured materials have attracted attention in solar applications for their potential to enhance solar cell efficiency (Mr. K. L. Gaikwad *et al.*, 2020) [7]. These semiconductors have shown promising results and are favored by researchers in the solar technology field [7].

III.3 Properties of chalcogenide materials

Chalcogenide materials have received significant attention due to their unique physical, optical, and electrical properties, which make them suitable for various technological applications. These materials are semiconductors that contain chalcogen elements (S, Se, or Te) and elements from the III-VI groups of the periodic table.

According to (Imran Khan, 2015) [8] the properties of chalcogenide materials, including their optical bandgap, electrical conductivity and photoconductivity are influenced by composition, structure and preparation method. Researchers have focused on studying the electrical properties of chalcogenide thin films, which could lead to new applications. The book "Chalcogenide Glass Thin Films: Preparations, Properties and Applications" [8] provides a detailed discussion on the properties and applications of these materials [8]. (A. Le Donne *et al.*, 2019) [9] highlighted the unique properties of chalcogenide materials, making them suitable applications in photovoltaics, phase-change memory and sensing. With advancements in technology, chalcogenide materials have become economically feasible and are being investigated as potential replacements for traditional solar cell materials. Thin film solar cells based on chalcogenides have shown enhanced performance and reduced cost, making them a promising alternative to conventional solar cells [9].

Chalcogenide materials have been extensively studied for their applications in photovoltaics, particularly in thin-film solar cells (M. Paire *et al*., 2014) [10]. Their high absorption coefficient enables efficient conversion of sunlight into electricity, making them attractive for solar cells. Moreover, chalcogenide materials offer advantages such as low processing cost and high thermal stability, making them a preferred alternative to other photovoltaic materials [10].

Chalcogenide materials have proven to be versatile and useful in various applications. These materials are commonly used as switching materials in phase-change memory and as sensing materials in gas sensors. (D. Tsiulyanu *et al*., 2003) [11] conducted a study that highlighted the potential of chalcogenide-based gas sensors. Thus, chalcogenide materials have a wide range of uses and continue to be an area of active research [11].

III.4 Chalcopyrite structures

According to [2], I-III-VI2 semiconductors have a tetragonal chalcopyrite structure which can be derived from the cubic zinc structure of II-VI materials like ZnS. The cubic and chalcopyrite structures have different elementary cells. In the chalcopyrite structure, Cu and In atoms from column I and III, respectively, from four bonds with S atoms from column VI. Conversely, each S atom forms two bonds with Cu and two with In [2]. Cu and In alternately occupy the ZnS sphalerite structure sites in both cells of the compound to produce a chalcopyrite structure.

III.4.1 Structure of chalcopyrite materials

According to (A. Jäger-Waldau, 2011) [12], chalcopyrite materials have a tetragonal crystal system characterized by space group I-42d. This crystal structure is of great importance in the development of photovoltaic applications, as it influences the optical and electrical properties of these materials. In recent years, there has been significant progress in chalcopyrite compound semiconductor research, with the results being transferred into the production of actual solar cells. The findings of this study are published in the Journal of Solar Energy Materials and Solar Cells [12].

According to (T. Riedle, 2002) [13] on Raman Spectroscopy for the Analysis of CuInS2 thin films, chalcopyrite ternary compound made up of a transition metal, an element from the third column and a chalcogen, usually sulfur or selenium. The chemical composition of chalcopyrite plays a crucial role in determining its electronic and optical properties, which are important for its applications in solar cells [13].

In general, chalcopyrite materials are ABX2 compounds that are a mixture of two Zinc-Blende structures, resulting in a change in symmetry group from F-43m to I-42d and characterizing a chalcopyrite quadratic structure. Doubling the unit cube along the z-axis creates the c-axis of the chalcopyrite structure. [12] states that the ratio of c/a in real chalcopyrite crystals is approximately equal to 2, while for an ideal chalcopyrite structure, c = 2a.

This structural characteristic plays a crucial role in determining the electronic and optical properties of chalcopyrite materials, which are of great interest for photovoltaic applications. In recent years, there has been significant progress in the research of chalcopyrite compound semiconductors, with a focus on the transfer of research findings into the production of actual solar cells. The physical and electronic properties of

chalcopyrite materials are strongly influenced by their unique crystal structure. These properties make chalcopyrite materials an attractive candidate for use in solar cells, due to their high optical absorption coefficient and suitable bandgap. Researchers have investigated the potential of chalcopyrite materials for use in photovoltaic applications and have reported promising results. For instance, thin films of CuInS$_2$, a type of chalcopyrite material, have been studied using Raman spectroscopy to analyze their properties [13].

The crystal structure of chalcopyrite materials significantly affects their electrical and thermal transport properties, crucial for thermoelectric applications. A theoretical study on Cu-based chalcopyrite compounds revealed that the crystal structure determines their electrical conductivity, Seebeck coefficient and thermal conductivity. These properties are vital for efficient thermoelectric applications like waste heat recovery (B. Wang *et al*., 2017) [14]. Further research is needed to understand the relationship between the crystal structure and the properties of chalcopyrite materials fully.

III.4.2 Crystal structure of CuInVI2 materials (VI = Se or S)

CuInSe$_2$ and CuInS$_2$ are semiconductor compounds (I-III-IV2) composed of copper (Cu), indium (In) and selenium (Se) or sulfur (S). These materials can adopt two crystal structures, chalcopyrite and stannite, each with distinct physical and electrical properties. A study by (A.S. Verma, 2009) [15] focused on the thermal properties of chalcopyrite semiconductors and found them to possess high thermal conductivity, low thermal expansion coefficient and high melting point, making them well-suited for high-temperature thermoelectric applications [15].

In the tetragonal crystal system of the chalcopyrite structure, CuInSe$_2$ and CuInS$_2$ belong to the I-42d space group. The structure consists of two interpenetrating face-centered cubic lattices, where copper and indium atoms occupy the cation sublattice, while selenium or sulfur atoms occupy the anion sublattice.

These chalcopyrite semiconductors have been extensively studied for their thermal properties, including thermal conductivity and heat capacity [15]. The stannite crystal structure, in contrast to chalcopyrite, possesses a tetragonal unit cell with space group I-42m and can be viewed as a layered structure made up of (CuIn)$_2$S and (CuIn)$_4$S$_3$ layers. These distinct structures exhibit unique electronic and optical properties, which make them applicable for various functions in solar cells and optoelectronic devices (D. B. Mitzi, 1999) [16].

41

III.4.2.1 Sphalerite or Zinc-Blende (ZnS)

Sphalerite is part of the face-centered cubic system, as shown in Fig. III.2 (A. J. Blake *et al.*, 2009) [17]. In this structure, the anions, such as halide ions, occupy the corners of the cationic octahedra, forming a face-centered cubic network, while the cations, such as organic or inorganic molecules or metal ions, are located at the centers of the octahedra. This arrangement results in a randomly distributed cation network, which is characteristic of perovskite structures (A. Kojima *et al.*, 2009) [18]. The space group associated with this structure is F-43m [17].
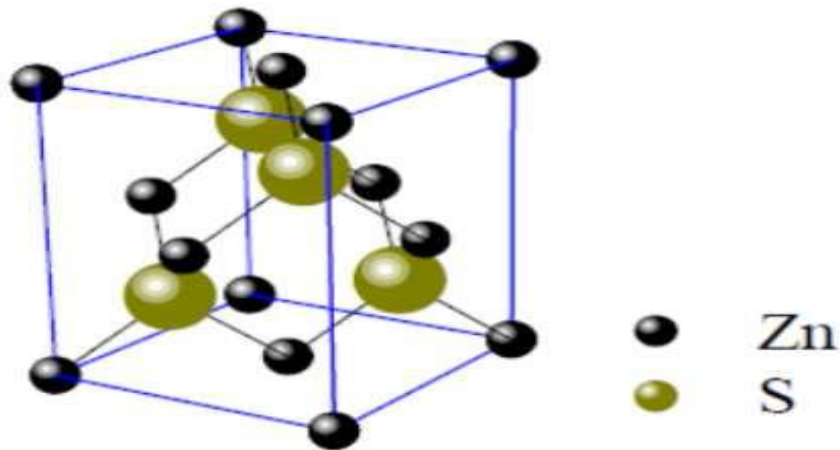
Fig. III.2: Zinc-blende structure.

In diamond structure, if we replace carbon atoms with zinc and sulfur atoms, then we obtain the zinc-blende structure.

III.4.2.2 Chalcopyrite type structure

Chalcopyrite has an elongated structure along the "c" axis, giving it a tetragonal structure Fig. III.3, distinguishing it from sphalerite. Research by [3] highlights the unique properties of chalcopyrite semiconductors, including a direct band gap, high optical absorption coefficient, and significant anisotropy in electrical and thermal conductivity. These properties make chalcopyrite materials promising for electronic and optoelectronic applications [3]. Chalcopyrite, with its distinctive tetragonal structure elongated along the "c" axis, is very interesting for solar cell applications. CuInS₂ nanostructures, sharing a similar tetragonal structure, have been synthesized and studied for their suitability in solar

cells. (S. Hosseinpour-Mashkani *et al.*, 2014) [19] examined the synthesis, characterization, formation mechanism and potential application of CuInS$_2$ nanostructures in solar cells. I-III-VI$_2$ compounds can crystallize in either the chalcopyrite or sphalerite phase, depending on experimental conditions. These compounds resemble elements in column VI, which have a diamond-like crystal structure. The chalcopyrite and sphalerite structures are variations of the diamond structure, with distinct atom arrangements. Refer to the diagram below for an illustration of this relationship.
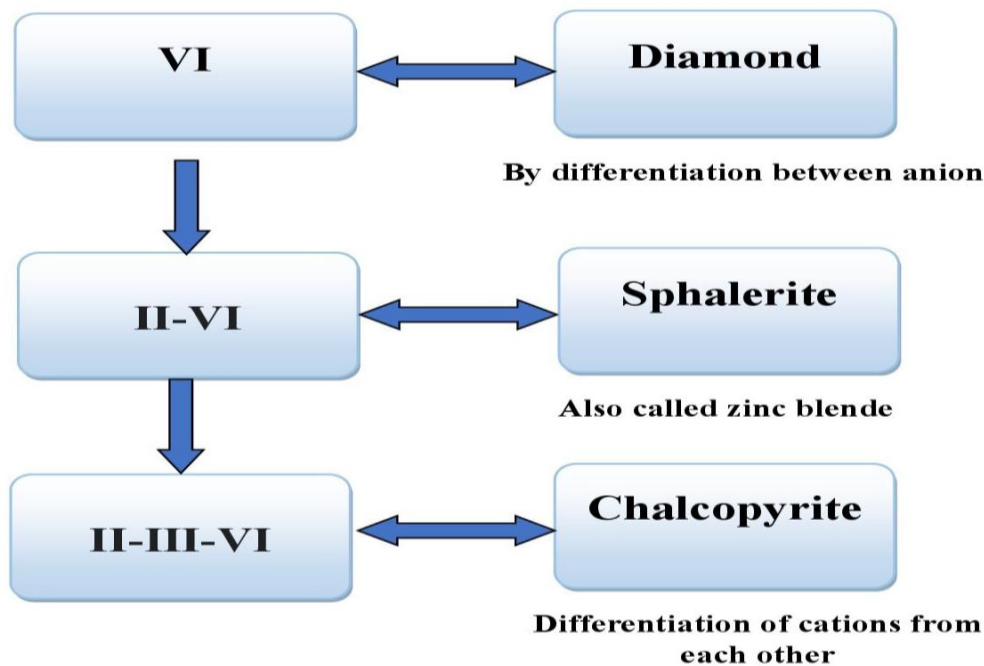
Fig. III.3: Cationic substitution diagram.

According to(A. A. Lavrentyev *et al.,* 1997) [20], the transition from the sphalerite structure to the chalcopyrite structure causes a reduction in symmetry and changes the volume of the mesh, which subsequently impacts the cation-chalcogen and anion distances. The authors note that these distances are defined by specific values [20].

III.4.3 Gap energy

The chalcopyrite structure systems, such as Cu (In,Ga,Al)(Se,S)$_2$, possess varying gap energies (Eg). These Eg values span from 1.04 eV for CuInSe$_2$, 2.4 eV for CuGaS$_2$, up to 2.7 eV for CuAlS$_2$, which covers a broad spectrum of visible light. The compounds have a direct bandgap, which makes them ideal for use as absorbent thin films in photovoltaic applications. Additionally, Fig. III.4 provides a comprehensive summary of the cell parameters "a" and gap energies "Eg" of these compounds (A. Soni *et al.*, 2010) [21] and

(D. Lincot *et al.*, 2004) [22]. There are 36 chalcopyrite ternary compounds made up of different combinations of elements (A = Cu, Ag), (B = Al, Ga, Ti) and (C = S, Se, Te). These semiconductors have a wide range of carrier mobilities and optical gaps, with gaps ranging from 1 eV to 3.5 eV. The I-III-VI$_2$ group of semiconductors that crystallize in the chalcopyrite structure are of significant interest in photovoltaic applications. The most important compounds for these applications are CuInSe$_2$, CuInS$_2$, CuGaSe$_2$ and CuGaSe$_2$, with different gap energies. Intermediate gaps can be achieved by combining two alloy compounds, for instance, doping CuInSe$_2$ with gallium (Ga) creates the Cu (In,Ga)Se$_2$ compound. Fig. III.4 provides a summary of the lattice parameter "a" and gap energy Eg of these compounds.
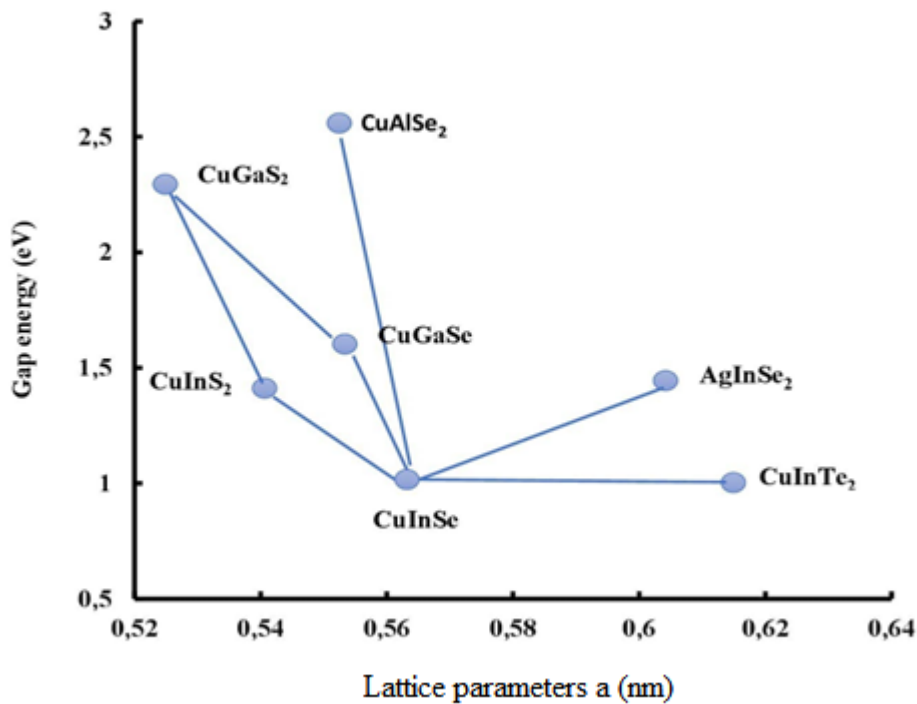
Fig. III.4: Lattice parameter 'a' and energy gap Eg of some I-III-VI$_2$ compounds.

CuInS$_2$ (CIS), a member of the chalcogenide materials family, is widely regarded as the most promising material for use as an absorbent in photovoltaic conversion due to its band gap energy, as supported by various studies (D. So, 2016) [23]. While CIS has a band gap of approximately 1.55 eV, in polycrystalline thin films, it varies between 1.3 and 1.5 eV, making it close to the optimum for photovoltaic conversion. Furthermore, CIS can exist in both n-type and p-type forms, with an electrical resistivity range between 0.1 and 100 Ω.cm. thin layers of CIS are black and can be crystallized in either chalcopyrite or sphalerite

structures [23]. CuInS$_2$ thin-film homojunction solar cells are advantageous over CuInSe$_2$ as they do not contain any toxic materials. The first homojunction-based solar cell with n-CuInS$_2$ and p-CuInS$_2$ was reported by (L. Kazmerski *et al.*, 1977) [24] with an efficiency of 3.33%. A recent study on SILAR-deposited thin films, conducted by (H. Soonmin, 2022) [25], provides further insights on the growth and characterization of these films. The study's findings could have significant implications for the development of high-performance solar cells [25]. The precise control of stoichiometry remains a significant challenge in the preparation of this material.

In particular, achieving the correct ratios of elements in the material is critical to its performance and properties. Despite advancements in preparation techniques, stoichiometric control remains a major obstacle. Therefore, further research is necessary to develop more effective methods for controlling stoichiometry and improving the material's properties (M. Rafi *et al.*, 2012) [26].

III.5 History and appellations

III.5.1 Definition

The dissertation of (R. Knecht, 2012) [27], accepted by the Faculty of Mathematics and Natural Sciences at Carl von Ossietzky University Oldenburg, focuses on the characterization of industrially processed chalcopyrite solar cells with varied absorber composition. Chalcopyrite is a mineral species that is widely distributed and found in large quantities around the world. Its structure consists of double sulphide (34.63%), copper (30.43%), and iron (34.94%), with the formula CuFeS$_2$. Additionally, it contains traces of Ag, At, In, Tl, Se, and Te, and has formed numerous compounds. Chalcopyrite's diamond-like structure is an equivalent (ternary compound), where each atom is bonded to four first neighbors in a tetrahedral structure [27].

III.5.2 Origin of the name

The name "Chalcopyrite" (or copper pyrite) was coined by (J. A. Mandarino, 1978) [28] and is derived from the Greek words "chalkos" meaning "copper" (Cu) and "pyrites" meaning "to light a fire" or "only a fire," referring to the mineral's yellow color. This information is found in the Fifteenth Edition. Reproduction of this book or its contents without the publisher's written consent is prohibited [28]. New mineral species discoveries are a dynamic aspect of mineralogy, including recent findings in Brazil. Chalcopyrite, also

known by various names such as chalcopyrite and Fool's gold, is a widely recognized mineral with numerous synonyms. This mineral's extensive nomenclature reflects its historical significance and the ongoing pursuit of knowledge in mineralogy (D. Atencio, 2015) [29] and (F. LETEUR, 1907) [30] and (R. de l'Isle, 1783) [31].

III.5.3 The designation "Fool's Gold"

According to (C.S. Hurlbut *et al.*, 1998) [32], chalcopyrite, pyrite and gold, can appear similar to the untrained eye Fig. III.5, but they have distinguishing characteristics. Gold is softer, denser and has a yellow streak, while chalcopyrite is brittle with a greenish-grey streak. Pyrite is harder and cannot be scratched with a nail like chalcopyrite. Although pyrite is often mistaken for gold and called "fool's gold," these minerals have distinct properties [32]. Chalcopyrite, with its coppery yellow to golden color and iridescent shades, is often mistaken for gold, earning it the nickname "fool's gold". This name originated from miners who became disappointed upon realizing that the precious metal they found was actually copper. The book: System of Mineralogy, edited by (J. D. Dana, 1901) [33], first published in 1837 and revised until 1868, documents this historical fact. The sixth edition of the book, completed by Edward Salisbury Dana in 1892, remains a valuable resource for studying mineralogy and its history [33,34]. Even, if it is not gold, chalcopyrite is a stone with interesting properties.

Fig. III.5: chalcopyrite, quartz and sphalerite structure.

In Table III.2, we present some values of the physical and chemical parameters of the elements Copper (Cu), Indium (In), and Sulfur (S), used in the synthesis of the CuInS$_2$ material.

Table III.2: Some physical and chemical properties of Cu, In, S, and Se elements.

Parameters	Cu	In	S	Se
Atomic mass (g/mole)	63.546	114.818	32.066	78.96
Electronic configuration	[Ar] 3d^{10}4S^1	[Kr] 4d^{10}5s^{2}5p^1	[Ne] 3s^{2}3p^4	[Ar] 3d^{10}4s^{2}4p^4
Density (g/cm^3) at 300K	8.96	7.31	2.06	4.79
melting temperature ($^\circ$C)	1083.4	156.61	119.6	217
Boiling temperature ($^\circ$C)	2595	2080	444.67	685
Conductivity: Electrical ($\Omega^{-1}m^{-1}$) **Thermal (W/m K)**	59.6 × 10^6 401	11.6 × 10^6 81.6	0.5 × 10^{-25} 0.269	10^{-12} 0.0204
ionization potential (l^n) (eV)	7.726	5.786	10.360	9.752
Electronegativity	1.9	1.78	2.58	2.4
atomic rays (pm)	127.8	155 – 162.6	103.5 – 109	116

III.6 Known phases with chalcopyrite structure

Chalcopyrite, a mineral with a unique crystal structure, has garnered significant interest in materials science. It encompasses various phases, including ternary and quaternary compounds. CuInS$_2$-based alloys, with their chalcopyrite structure, have been extensively studied for thin-film solar cells, offering promising applications. In their work titled "Rethinking electronic effects in photochemical hydrogen evolution using

$CuInS_2/ZnS$ quantum dots sensitizers" (A. Orlando *et al.*, 2022) [35] delve into the electronic effects and potential optoelectronic and photovoltaic applications of these materials.

Cu_2ZnGeS_4 is a promising quaternary compound for solar cells, exhibits favorable optoelectronic properties due to its chalcopyrite structure (F. Larsson, 2020) [36]. Chalcopyrite thin-film solar cells have gained attention, and optimizing the window layer structure is crucial for their efficiency and stability. Larsson's study analyzed various window layer structures and their impact on device performance. By investigating different materials, thicknesses and doping. Larsson provided valuable insights for optimizing chalcopyrite thin-film solar cell design [36]. $CuFeS_2$-based alloys and their solid solutions, such as $CuFe_{1-x}M_xS_2$, have been extensively studied for their diverse applications. (E. Bastola *et al.*, 2018) [37] conducted recent research titled "Structural, optical and hole transport properties of earth-abundant chalcopyrite $CuFeS_2$ nanocrystals", which focuses on investigating the structural, optical, and hole transport properties of these abundant chalcopyrite nanocrystals [37]. Chalcopyrite compounds possess unique magnetic and electronic properties that make them attractive for diverse applications. A study by (T. Kawabe *et al.*, 2017) [38] and (B. Bhattacharyya *et al.*, 2016) [39] explore the fabrication and potential use of $CuIn(S,Se)_2$ films in solar cells. The authors suggest that these materials have potential applications in areas such as photovoltaics, photocatalysis and bioimaging [39]. Overall, the chalcopyrite structure is a versatile and promising framework for various functional materials and its study continues to attract considerable research interest.

III.7 Types of chalcopyrite

There are three essential types of chalcopyrite structure, such as:

- Pure chalcopyrite.
- Defects chalcopyrite.
- Doped chalcopyrite.

III.7.1 Pure chalcopyrite

Chalcopyrite has unique properties that make them promising for various technological applications. Their excellent optical, electronic and magnetic properties have led to their use in solar cells, electronic devices and magnetic data storage media. Additionally, chalcopyrite has been explored for photocatalytic and sensing applications. Researchers have developed various methods for synthesizing high-quality chalcopyrite

crystals, including chemical vapor transport, solution growth and molecular beam epitaxy. The properties and synthesis methods of chalcopyrite materials continue to be an active area of research (A. A. Rockett, 2010) [40], (P. Ranjan *et al.*, 2021) [41], (H. Kaneko *et al.*, 2015) [42] and (T. Teranishi *et al.*, 1974) [43].
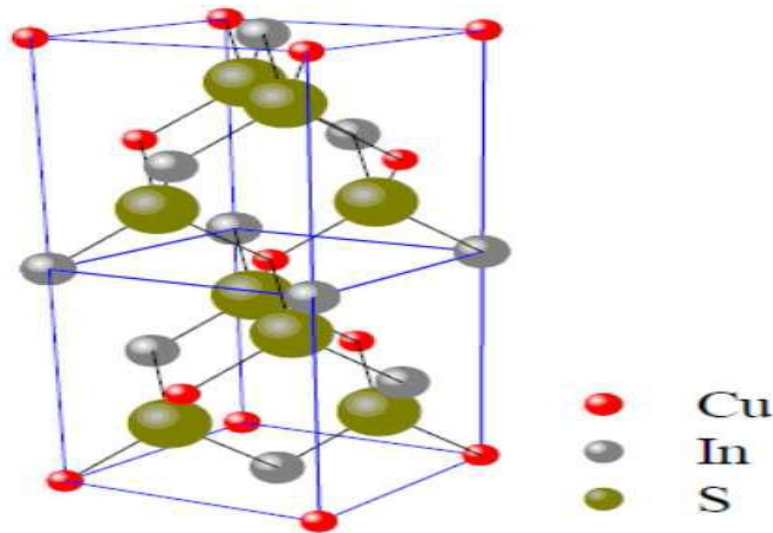
Fig. III.6: Pure chalcopyrite crystal structure.

The chalcopyrite crystal structure is adopted by these ternary semiconductors and is closely related to the zinc blende structure Fig. III.6. Although the arrangement of anions in both structures is similar. The chalcopyrite structure differs due to the ordered distribution of cations. As a result, the unit cell becomes tetragonal, with the c-axis roughly twice the length of the a-axis in the zinc blende structure. In the chalcopyrite structure, each anion is coordinated by two A and B cations, while each cation is tetrahedrally coordinated by four anions. The atomic positions are specified as follows: A located at (0, 0, 0) and (0, 1/2, 1/2); B located at (1/2, 1/2, 0) and (1/2, 0, 1/4); and C located at (u, 1/4, 1/8), (u, 3/4, 1/8), (3/4, u, 7/8) and (1/4, u, 7/8).

III.7.2 Defects chalcopyrite

Chalcopyrite exhibits various defects Fig. III.7, including copper vacancies, sulfur vacancies, and antistites defects, which greatly affect its properties such as electrical conductivity, optical characteristics and magnetic behavior. Copper vacancies lead to n-type conductivity, sulfur vacancies result in p-type conductivity, and antistites defects contribute to magnetic properties. Studies using techniques like X-ray diffraction, electron microscopy

and spectroscopy have extensively investigated the impact of defects on chalcopyrite properties. The distribution, location and concentration of these defects significantly influence the material's properties, as documented in the research by (T.Walter *et al*., 1996) [44].

The geochemical study analyzed trace and critical elements in chalcopyrite and pyrite samples from the Assarel porphyry copper-gold deposit in Bulgaria, focusing on the economic significance of critical metals. Results indicate significant amounts of indium, gallium and germanium in the chalcopyrite and pyrite samples, which are important for technological applications and currently classified as critical due to limited global availability. The article emphasizes the economic potential of these metals in the Assarel deposit and calls for further exploration and exploitation. Written by (L. Lobo, 2022) [45], the article was published in the Department of Earth Sciences at Uppsala University in 2022 [45]. The article "Defect levels through hybrid density functionals: Insights and applications" (A. Alkauskas *et al*, 2011) [46] discusses the application of hybrid density functionals in analyzing defect levels in materials. The authors highlight the advantages of hybrid functionals compared to traditional density functional theory methods and provide examples of their use in studying different materials. They also address the challenges associated with hybrid functionals and propose potential solutions [46].
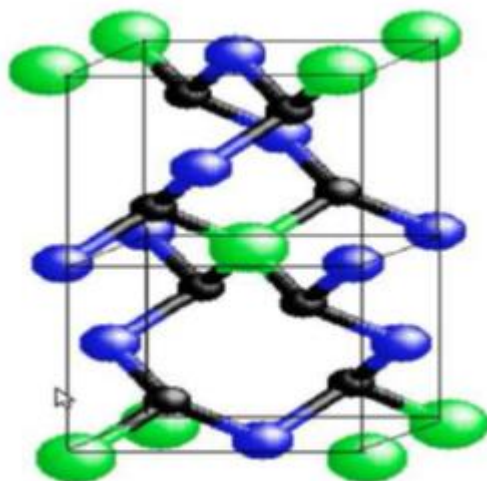
Fig. III.7: Defects chalcopyrite crystal structure.

The crystal structure in question displays two distinct III-VI bond lengths and chemically distinct group-III atoms. As a result, the Bernard and Zunger model, which maintains the lengths of tetrahedral bonds, is unsuitable for estimating internal coordinates.

To address this issue, we have applied the crystal structure of defect chalcopyrite in the following way:

II : (0,0,0)

III : (0,0,1/2), (0,1/2,1/4)

VI : (x,y,z), (-x,-y,z), (y,-x,-z), (-y,x,-z).

III.7.3 Doped chalcopyrite

Doped chalcopyrite compounds have gained significant research interest for their applications in photovoltaics, optoelectronics and thermoelectric systems. Fig. III.8 presents the doped chalcopyrite crystal structure (Cu (In,Ga)Se$_2$ compound). These compounds, with the formula CuInX2 (X = S, Se or Te), can be modified by doping with foreign elements like Zn, Cd, Mg or Al. A study by (C. Mahendran *et al.*, 2012) [47], published in Materials Science in Semiconductor Processing journal investigated the effects of zinc doping and temperature on sprayed CuInS$_2$ thin films. By varying zinc concentration and temperature during synthesis, changes in the structural, optical and electrical properties of the chalcopyrite material were observed. The findings suggest that zinc doping enhances conductivity and increases light absorption in the visible range [47].

Zinc (Zn) and magnesium (Mg) doping enhance the electrical conductivity and thermoelectric properties of CuInSe$_2$ and CuInS$_2$, respectively. Experiments with manganese (Mn) and iron (Fe) dopants have demonstrated improved electrical conductivity and magnetic properties in CuInS$_2$ (N. Tsujii *et al.*, 2002) [48].

Defect manipulation of chalcopyrite crystal structure impacts electronic and optical properties. Creating Cu vacancies in CuInSe$_2$ reduces the bandgap and enhances light absorption, benefiting photovoltaics. Studies using density functional theory investigate copper vacancies in chalcopyrite materials like CuInSe$_2$ and CuGaSe$_2$, providing insights for efficient photovoltaic technology development (J. Pohl *et al.*, 2010) [49].

This study examines the electronic, optical and thermoelectric properties of commonly used photovoltaic materials, CuInS$_2$ and CuInSe$_2$. Through first principles calculations and comparison with experiments, the study demonstrates their favorable thermoelectric properties for thermoelectric devices. Additionally, it offers insights into their fundamental properties and suggests directions for future research (Z. Pachuau *et al*., 2023) [50]. Overall, doped chalcopyrite has demonstrated great potential in various applications due to their

tunable electronic, optical and thermal properties. Future research may focus on optimizing the doping strategies to achieve even better performance in different applications.
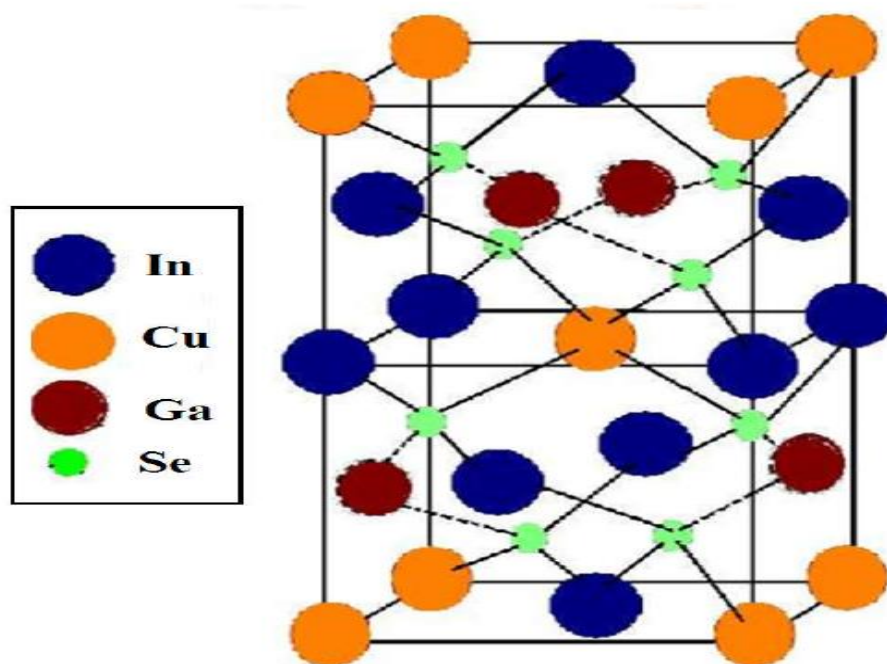
Fig. III.8: Doped chalcopyrite crystal structure.

III.8 Advantages of the crystal structure of CuInS₂ chalcopyrite compounds

CuInS$_2$ chalcopyrite compounds have undergone extensive studies on their crystal structure and properties. These compounds, belonging to group I-III-VI$_2$, hold significant interest for various applications, such as solar energy conversion, electrochemical photovoltaic cells, and solar cells. CuInS$_2$ demonstrates great potential for solar cell applications due to its direct bandgap, high absorption coefficient, and ability to be manufactured as p-type or n-type. It is also considered an environmentally friendly alternative to materials like cadmium and selenium. Table III.2 provides information on the physical parameters and chemical elements utilized in the synthesis of.

III.9 Conclusion

In conclusion, the result of a brief theoretical study of CuInS$_2$ highlights its promising properties as a semiconductor material for various applications. CuInS$_2$ compounds, with their specific crystal structure, exhibit interesting electronic, optical and thermal transport properties. Their electrical conductivity, Seebeck coefficient and thermal conductivity are

important factors for thermoelectric applications, such as waste heat recovery. Additionally, the crystal structure of CuInS$_2$ compounds plays a crucial role in their thermoelectric properties. These findings pave the way for potential applications in areas such as solar energy conversion and optoelectronic devices. Further experimental studies and developments are needed to better understand and fully exploit the properties of CuInS$_2$ in various technological applications.

References

[1]   F. Ohrendorf and H. Haeuseler, "Lattice dynamics of chalcopyrite type compounds. Part I. Vibrational frequencies," Crystal Research and Technology: Journal of Experimental and Industrial Crystallography, vol. 34, no. 3, pp. 339-349, 1999.

[2]   S. Siebentritt, "Chalcopyrite compound semiconductors for thin film solar cells," Current Opinion in Green and Sustainable Chemistry, vol. 4, pp. 1-7, 2017.

[3]   B. Panda, "Structural and electronic properties of chalcopyrite semiconductor," 2011.

[4]   K. Takarabe, K. Kawai, S. Minomura, T. Irie, and M. Taniguchi, "Electronic structure of some I–III–VI2 chalcopyrite semiconductors studied by synchrotron radiation," Journal of applied physics, vol. 71, no. 1, pp. 441-447, 1992.

[5]   D. Wang, W. Zheng, C. Hao, Q. Peng, and Y. Li, "General synthesis of I–III–VI 2 ternary semiconductor nanocrystals," Chemical communications, no. 22, pp. 2556-2558, 2008.

[6]   W. R. Lambrecht and S. N. Rashkeev, "First-principles calculations of second-order optical response functions in chalcopyrite semiconductors," Journal of Physics and Chemistry of Solids, vol. 64, no. 9-10, pp. 1615-1619, 2003.

[7]   Mr. Kedar Laxman Gaikwad, Prof. Ms. Payal Sunil Pawar, "Materials for Solar Energy," International Journal for Research in Applied Science & Engineering Technology Vol 8 Issue IV," 2020.

[8]   Imran Khan, " A Review on Electrical Properties of Chalcogenide Thin Films," Chalcogenide Glass Thin Films: Preparations, Properties and Applications, vol. 8, no. 12, 2015.

[9]   A. Le Donne, V. Trifiletti, and S. Binetti, "New earth-abundant thin film solar cells based on chalcogenides," Frontiers in chemistry, vol. 7, p. 297, 2019.

[10]   M. Paire, S. Delbos, J. Vidal, N. Naghavi, and J. Guillemoles, "Chalcogenide Thin-Film Solar Cells," Solar Cell Materials: Developing Technologies, pp. 145-215, 2014.

[11]   D. Tsiulyanu, S. Marian, H.-D. Liess, and I. Eisele, "Chalcogenide based gas sensors," 2003.

[12]   A. Jäger-Waldau, "Progress in chalcopyrite compound semiconductor research for photovoltaic applications and transfer of results into actual solar cell production," in Practical handbook of photovoltaics: Elsevier, 2012, pp. 373-395.

[13]   T. Riedle, "Raman Spectroscopy for the analysis of thin CuInS2 films," Technische Universität Berlin, Universitätsbibliothek (Diss.-Stelle), 2002.

[14] B. Wang, H. Xiang, T. Nakayama, J. Zhou, and B. Li, "Theoretical investigation on thermoelectric properties of Cu-based chalcopyrite compounds," Physical Review B, vol. 95, no. 3, p. 035201, 2017.

[15] A. S. Verma, "Thermal properties of chalcopyrite semiconductors," Philosophical Magazine, vol. 89, no. 2, pp. 183-193, 2009.

[16] D. B. Mitzi, "Synthesis, structure, and properties of organic-inorganic perovskites and related materials," Progress in inorganic chemistry, pp. 1-121, 1999.

[17] A. J. Blake, J. M. Cole, J. S. Evans, P. Main, S. Parsons, and D. J. Watkin, Crystal structure analysis: principles and practice. OUP Oxford, 2009.

[18] A. Kojima, K. Teshima, Y. Shirai, and T. Miyasaka, "Organometal halide perovskites as visible-light sensitizers for photovoltaic cells," Journal of the american chemical society, vol. 131, no. 17, pp. 6050-6051, 2009.

[19] S. Hosseinpour-Mashkani, M. Salavati-Niasari, and F. Mohandes, "CuInS2 nanostructures: Synthesis, characterization, formation mechanism and solar cell applications," Journal of Industrial and Engineering Chemistry, vol. 20, no. 5, pp. 3800-3807, 2014.

[20] A. A. Lavrentyev, I. Y. Nikiforov, and B. Gabrelian, "The chemical bonding in crystals with chalcopyrite structure," Le Journal de Physique IV, vol. 7, no. C2, pp. C2-283-C2-284, 1997.

[21] A. Soni, V. Gupta, C. Arora, A. Dashora, and B. Ahuja, "Electronic structure and optical properties of CuGaS2 and CuInS2 solar cell materials," Solar energy, vol. 84, no. 8, pp. 1481-1489, 2010.

[22] D. Lincot *et al.*, "Chalcopyrite thin film solar cells by electrodeposition," Solar Energy, vol. 77, no. 6, pp. 725-737, 2004.

[23] D. So, "Copper indium sulfide colloidal quantum dot solar cells," 2016.

[24] L. Kazmerski and G. Sanborn, "CuInS2 thin-film homojunction solar cells," Journal of Applied Physics, vol. 48, no. 7, pp. 3178-3180, 1977.

[25] H. Soonmin, "Recent Advances in the Growth and Characterizations of SILAR-Deposited Thin Films," Applied Sciences, vol. 12, no. 16, p. 8184, 2022.

[26] M. Rafi, Y. Arba, B. Hartiti, A. Ridah, and P. Thevenin, "Optimization of growth of ternary CuInS2 by spray pyrolysis for photovoltaic application," Moroccan Journal of Condensed Matter, vol. 14, no. 1, 2012.

[27] R. Knecht, "Characterization of industrially processed chalcopyrite solar cells with varied absorber composition," Universität Oldenburg, 2012.

[28] J. A. Mandarino, "Manual of Mineralogy (after James D. Dana)," Geoscience Canada, vol. 5, no. 4, pp. 212-212, 1978.

[29] D. Atencio, "The discovery of new mineral species and type minerals from Brazil," Brazilian Journal of Geology, vol. 45, pp. 143-158, 2015.

[30] F. LETEUR, "Traité Élémentaire de Minéralogie Pratique. 152 pp," ed: Paris, 1907.

[31] R. de l'Isle, Cristallographie ou description des formes propres à tous les corps du règne minéral, dans l'état de combinaison saline, pierreuse ou métallique. De l'imprimerie de Monsieur, 1783.

[32] C. S. Hurlbut and W. E. Sharp, Dana's Minerals and How to Study Them (After Edward Salisbury Dana). John Wiley & Sons, 1998.

[33] J. D. Dana, The System of Mineralogy of James Dwight Dana. 1837-1868: Descriptive Mineralogy. J. Wiley & sons, 1901.

[34] C. Klein and B. Dutrow, Manual of mineral science. John Wiley & Sons, 2007.

[35] A. Orlando, F. Lucarini, E. Benazzi, F. Droghetti, A. Ruggi, and M. Natali, "Rethinking Electronic Effects in Photochemical Hydrogen Evolution Using CuInS2@ ZnS Quantum Dots Sensitizers," Molecules, vol. 27, no. 23, p. 8277, 2022.

[36] F. Larsson, "Window Layer Structures for Chalcopyrite Thin-Film Solar Cells," Acta Universitatis Upsaliensis, 2020.

[37] E. Bastola, K. P. Bhandari, I. Subedi, N. J. Podraza, and R. J. Ellingson, "Structural, optical, and hole transport properties of earth-abundant chalcopyrite (CuFeS2) nanocrystals," MRS Communications, vol. 8, no. 3, pp. 970-978, 2018.

[38] T. Kawabe, T. Maeda, and T. Wada, "Preparation of CuIn (S, Se) 2 films by PLD of precursor layers and post-annealing and their application to solar cells," physica status solidi c, vol. 14, no. 6, p. 1600183, 2017.

[39] B. Bhattacharyya and A. Pandey, "CuFeS2 quantum dots and highly luminescent CuFeS2 based core/shell structures: synthesis, tunability, and photophysics," Journal of the American Chemical Society, vol. 138, no. 32, pp. 10207-10213, 2016.

[40] A. A. Rockett, "Current status and opportunities in chalcopyrite solar cells," Current Opinion in Solid State and Materials Science, vol. 14, no. 6, pp. 143-148, 2010.

[41] P. Ranjan, P. K. Surolia, and T. Chakraborty, "Structure, electronic and optical properties of chalcopyrite-type nano-clusters XFeY2 (X= Cu, Ag, Au; Y= S, Se, Te): a density functional theory study," Pure and Applied Chemistry, vol. 93, no. 5, pp. 591-606, 2021.

[42] H. Kaneko, T. Minegishi, and K. Domen, "Chalcopyrite thin film materials for photoelectrochemical hydrogen evolution from water under sunlight," Coatings, vol. 5, no. 3, pp. 293-311, 2015.

[43] T. Teranishi, K. Sato, and K. i. Kondo, "Optical properties of a magnetic semiconductor: Chalcopyrite CuFeS2.: I. Absorption spectra of CuFeS2 and Fe-Doped CuAlS2 and CuGaS2," Journal of the Physical Society of Japan, vol. 36, no. 6, pp. 1618-1624, 1974.

[44] T. Walter, R. Herberholz, and H.-W. Schock, "Distribution of defects in polycrytalline chalcopyrite thin films," in Solid State Phenomena, 1996, vol. 51, pp. 309-316: Trans Tech Publ.

[45] L. Lobo, "Geochemical Study of Trace and Critical Elements in Chalcopyrite and Pyrite from the Assarel Porphyry-Cu-Au Deposit, Bulgaria," ed, 2022.

[46] A. Alkauskas, P. Broqvist, and A. Pasquarello, "Defect levels through hybrid density functionals: Insights and applications," physica status solidi (b), vol. 248, no. 4, pp. 775-789, 2011.

[47] C. Mahendran and N. Suriyanarayanan, "Effect of zinc doping and temperature on the properties of sprayed CuInS2 thin films," Materials science in semiconductor processing, vol. 15, no. 5, pp. 522-530, 2012.

[48] N. Tsujii, H. Kitazawa, and G. Kido, "Electric and Magnetic Properties of Mn-and Fe-Doped CuInS2 Compounds," physica status solidi (a), vol. 189, no. 3, pp. 951-954, 2002.

[49] J. Pohl and K. Albe, "Thermodynamics and kinetics of the copper vacancy in CuInSe 2, CuGaSe 2, CuInS 2, and CuGaS 2 from screened-exchange hybrid density functional theory," Journal of Applied Physics, vol. 108, no. 2, p. 023509, 2010.

[50] Z. Pachuau, "First Principal Study of Electronic, Optical and Thermoelectric Properties of CuInS 2 and CuInSe 2," Indian Journal of Pure & Applied Physics (IJPAP), vol. 61, no. 2, pp. 108-114, 2023.

SECTION II

RESULTS AND DISCUSSIONS

CHAPTER IV

Effects of Zinc Doping on SrTiO3 perovskite compound

Chapter IV: Effects of Zinc Doping on SrTiO₃ perovskite compound

IV.1 Introduction

The study focuses on enhancing the conductivity and photocatalytic capabilities of SrTiO$_3$ compound by introducing the Zn element as a dopant. Challenges in photocatalytic systems, such as limited visible light utilization and charge recombination, prompt the use of co-catalysts like Zn. The SrTiO$_3$ perovskite compound, known as STO, possesses a cubic structure with potential for photovoltaic applications. Variations in Zn concentration within the SrTiO$_3$ matrix, ranging from 1% to 10%, enable optimization of band gap and absorption factors for photovoltaic application. The study employs density functional theory, specifically GGA-PBE, to ensure the stability of Zn-doped SrTiO$_3$. This work explores both theoretical and experimental aspects, contributing to a comprehensive understanding of the material's properties and potential applications.

IV.2 Computation Details

First-principles calculations were carried out within the DFT framework, utilizing GGA-PBE approximations and employing the CASTEP code for computation (M.   A. Ghebouli *et al.*, 2022) [1]. The exchange-correlation effect was elucidated through the ultra-soft pseudopotential method, in conjunction with the GGA-PBE approximation functional (J. P. Perdew *et al.*, 1996) [2].

To attain optimal convergence for both computed structures and energies, Monkhorst–Pack points were employed with a $6 \times 6 \times 6$ grid, complemented by a cut-off energy of 800 eV (H. J. Monkhorst *et al.*, 1976) [3]. The structural parameters, dictating the lowest energy structure, were established through the Broyden–Fletcher–Goldfarb–Shanno minimization technique (T. H. Fischer *et al.*, 1992) [4], offering a rapid approach to this determination. Geometry optimization's tolerance parameters were established, with an affinity resolution for the difference in total energy set at 10-5 eV/atom, a maximum ionic Hellmann–Feynman force set at 3×10^{-2} eV/Å, and a maximum stress set at 2×10^{-2} eV/Å^3. This study's approach not only facilitates force and stress calculations, but it also effectively governs the convergence of each computational parameter and excludes the impact of electron-nucleus interactions.

IV.3 Results and Discussion

IV.3.1 Structural parameters

The optimization of the structure for both pure and Zn-doped $SrTiO_3$ materials was conducted through the utilization of CASTEP along with GGA-PBE core assembly (Y. Naceur *et al.*, 2022) [5]. The electronic configurations for Sr, Ti, Zn and O are observed to be as $4s^2\ 4p^6\ 5s^2$, $3s^2\ 3p^6\ 3d^2\ 4s^2$, $3d^{10}\ 4s^2$ and $2s^2\ 2p^4$, respectively. The crystal structure of pure $SrTiO_3$ is depicted in Fig. IV.1.

Essential properties including the optimized lattice constant, bulk modulus, and its pressure derivative were extracted for both pure and Zn-doped $SrTiO_3$ and have been presented in Table IV.1. The congruence between theoretical [6-8] and experimental [9-15] data attests to the reliability of the aforementioned findings.

Upon Zn doping, the optimized lattice constant corresponding to a 0% Zn content was determined as 3.917 Å, aligning closely with the literature's experimental value of 3.90815 Å (M. Rizwan *et al.*, 2020) [9] and 3.90453 Å (P. Nunocha *et al.*, 2022) [14]. The introduction of Zn into $SrTiO_3$ leads to a slight increase in the lattice constant to 3.917 Å, attributed to the variation in atomic radii between Zn and Ti. Fig. IV.2 presents the correlation between total energy and volume for standard $SrTiO_3$ and Zn-doped $SrTiO_3$ (Zn contents of 2%, 5%, and 10%).

The optimization of structures for various Zn contents was achieved using Murnaghan's equation of state (F. D. Murnaghan *et al.*, 1944) [12]. It is worth noting that the incorporation of Zn imparts decreased structural stability. The variation of lattice constant, volume, and bulk modulus concerning the zinc content (x) within $SrZn_xTi_{1-x}O_3$ alloys is illustrated in Fig. IV.3. As the Zn content increases within $SrTiO_3$, a decrease in volume was observed. Simultaneously, an increase (decrease) in lattice constant (bulk modulus) is noted with the rise in Zn content. Our data concerning the lattice constant, volume, and bulk modulus is consistent with these polynomial formulas:

$$a_0(x) = 3.91766 + 0.00676x + 7.90711 \times 10 - 5x^2 \qquad (IV.1)$$

$$V(x) = 60.12876 + 0.31059x + 0.00438x^2 \qquad (IV.2)$$

$$B_0(x) = 172.87807 - 1.98972x - 0.03828x^2 \qquad (IV.3)$$
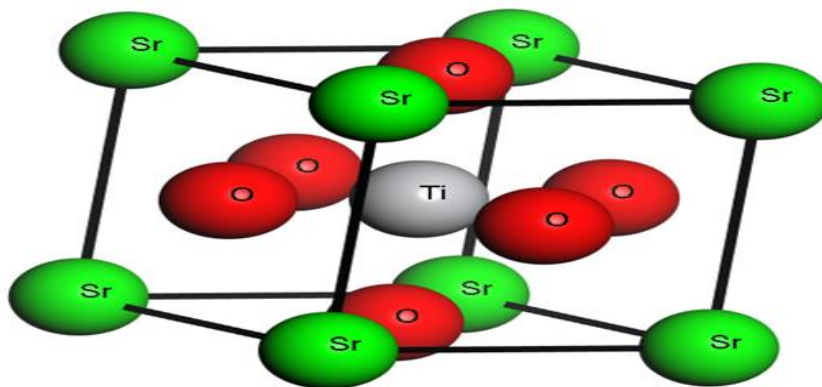
Fig. IV.1: Crystal structures of SrTiO$_3$ compound.
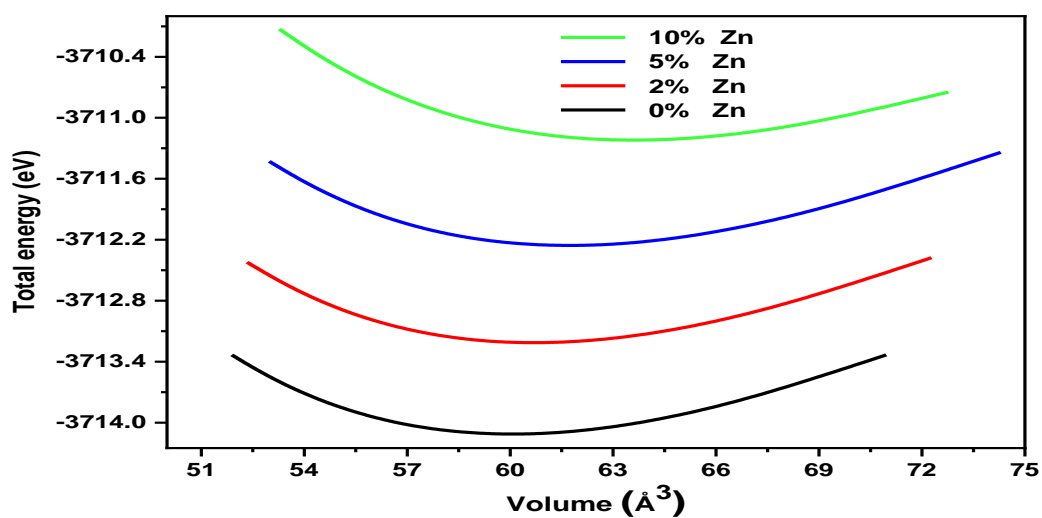
Fig. IV.2: Total energy versus volume for standard and Zn-doped SrTiO$_3$ (Zn = 0%, 2%, 5% and 10%).

(a)
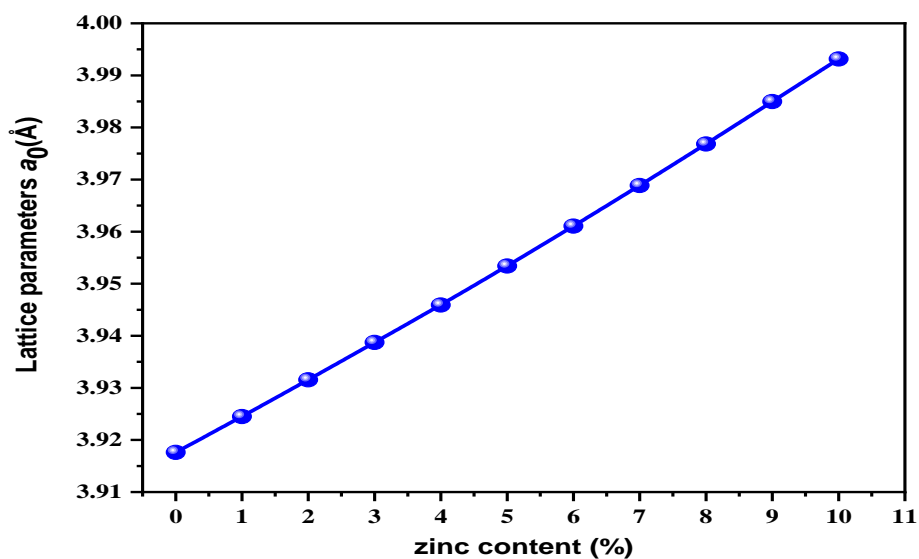
(b)
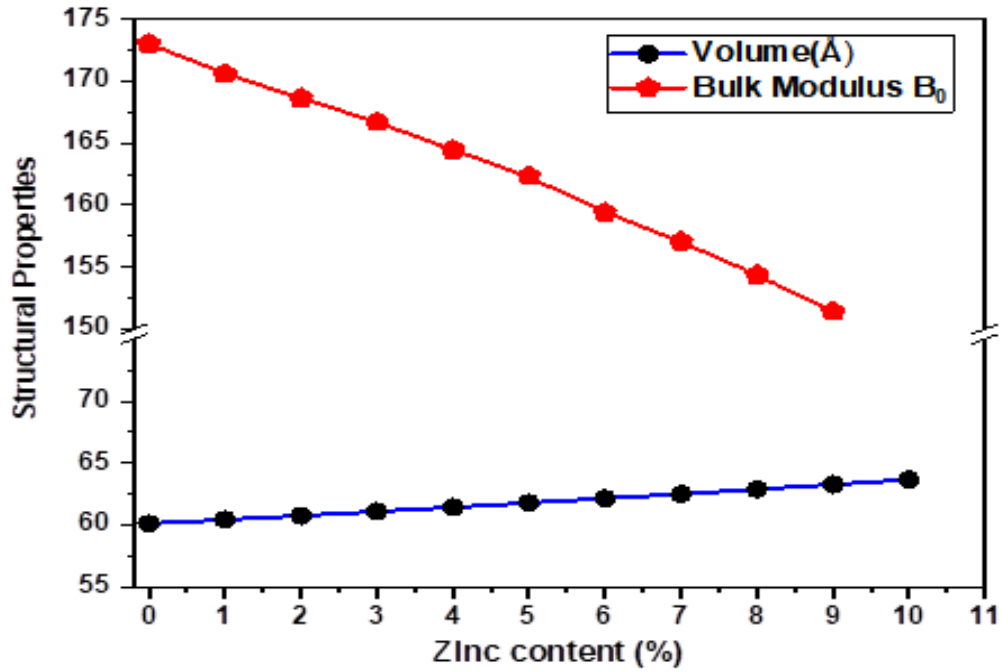
Fig. IV.3: (a) Lattice constant, (b) volume and bulk modulus versus zinc content x in SrZnxTi1-xO₃.

Table IV.1: Lattice constant, volume, bulk modulus and its pressure derivative for standard and Zn-doped SrTiO₃ with available theoretical and experimental published data.

Compound	a_0 (Å)	V(Å^3)	B_0 (GPa)	B'_0
SrTiO₃	3.917	60.126431	173.01973	4.3340
SrZn$_{0.02}$Ti$_{0.98}$O₃	3.931547	60.770187	168.61237	4.36389
SrZn$_{0.03}$Ti$_{0.97}$O₃	3.93873	61.103910	166.69908	4.3764
SrZn$_{0.04}$Ti$_{0.96}$O₃	3.94592	61.439042	164.44923	4.38741
SrZn$_{0.05}$Ti$_{0.95}$O₃	3.95340	61.789080	162.32213	4.40831
SrZn$_{0.06}$Ti$_{0.94}$O₃	3.96106	62.149222	159.38715	4.42229

SrZn$_{0.07}$Ti$_{0.93}$O$_3$	3.96885	62.516437	157.07667	4.44622
SrZn$_{0.08}$Ti$_{0.92}$O$_3$	3.97683	62.894295	154.37705	4.46245
SrZn$_{0.09}$Ti$_{0.91}$O$_3$	3.98497	63.281408	151.41548	4.48666
SrZn$_{0.1}$Ti$_{0.90}$O$_3$	3.99316	63.672191	149.55443	4.50451

IV.3.2 Elastic and mechanical properties

The elastic constants play a crucial role in characterizing the material's response to external stress and establishing connections between mechanical attributes like elasticity, stability, and stiffness (M. Zafar *et al.*, 2017) [13]. To comprehend a material's mechanical properties stemming from external force reactions, one must employ elastic constants. These encompass parameters such as Young's modulus (E), elastic hardness coefficients (Cij), bulk modulus (B), shear modulus (G), Poisson's ratio (Y) and anisotropy (A). The material's stability and the bonds between neighboring atoms find description through these elastic constants. Shear and Young moduli denote bond rigidity and resistance to deformation and fracturing.

Elastic constants are tied to fundamental phenomena like brittleness, ductility, hardness, and mechanical robustness of the material. They furnish insights into structural stability, bond performance, anisotropy and cohesion. For the cubic structure of SrTiO$_3$ under zero pressure, Table IV.2 enlists C$_{11}$, C$_{12}$, and C$_{44}$, aligning closely with their theoretical values of 350.46, 101.16, and 111.02 GPa, respectively [14], as well as experimental values (H. Salehi *et al.*, 2011) [15].

Calculated elastic moduli for both pure and Zn-doped SrTiO$_3$ are positive and satisfy the conditions of elastic stability [16,17]: C$_{11}$ > 0, C$_{44}$ > 0, C$_{11}$ - C$_{12}$ > 0 and C$_{11}$ + 2C$_{12}$ > 0. Notably, C$_{11}$ surpasses C$_{12}$ and C$_{44}$ in magnitude and rigidity. The bulk modulus mirrors material compressive strength, illustrating SrTiO$_3$'s exceptional volume resistance. Table IV.2 documents the bulk modulus, anisotropy factor, shear and Young's moduli, *B/G* ratio, Poisson's ratios, and Vickers hardness for undoped and Zn-doped SrTiO$_3$. Vickers hardness for SrZn$_x$Ti$_{1-x}$O$_3$ was estimated via the semi-empirical model H = 0.0607 × Y (X. Jiang *et al.*, 2011) [18]. Mechanical behaviors of SrZn$_x$Ti$_{1-x}$O$_3$ materials were analyzed in response to varying Zn content [19,21]. Fig. IV.2 displays the dependence of elastic constants on zinc

content in SrZn$_x$Ti$_{1-x}$O$_3$ alloys using the GGA-PBE approximation. It's notable that these parameters generally decrease with increasing zinc content. The bulk and shear moduli of Voigt and Reuss limits for cubic crystals are given by:

$$B = (B_R + B_v)/2 \qquad\qquad\qquad\qquad\qquad (IV.4)$$

$$G = (G_v + G_R)/2 \qquad\qquad\qquad\qquad\qquad (IV.5)$$

Young's modulus, Poisson's ratio, and the anisotropic factor can be derived through:

$$E = 9GB/(3B + G) \tag{IV.6}$$

$$\nu = (3B - 2G)/2(3B + G) \tag{IV.7}$$

$$A = 2C_{44}/(C_{11} - C_{12}) \tag{IV.8}$$

The brittleness or ductility of a material can be inferred from the *B/G* ratio. If this ratio surpasses 1.75, the material demonstrates ductility, whereas a value below 1.75 suggests a brittle nature. For both pure and Zn-doped SrTiO₃, the *B/G* ratio remains below 1.75, indicating its brittleness.

The nonlinear behavior of the *B/G* ratio concerning Zn concentration is illustrated in Fig. IV.5. Meanwhile, Young's modulus and shear modulus exhibit a decreasing pattern with the strain's increase due to higher zinc concentration, as presented in Fig. IV.6. The provided values align well with those documented in literature (A. Boudali *et al.*, 2009) [22] and experimental findings (A. Hachemi *et al.*, 2010) [23]. The Poisson's ratio plays a role in discerning material stability and bonding characteristics. Notably, the Poisson's ratio is 0.23, signifying significant ionic contributions to intra-atomic bonding.

The near-unity value of elastic anisotropy underscores SrTiO₃'s isotropic nature. The material's resistance to deformation was investigated using mechanical parameters (R. S. Sunmonu *et al.*, 2023) [24]. The covalent nature of $SrZn_xTi_{1-x}O_3$ is indicated by the negative Cauchy pressure (Cp = C_{12} - C_{44} < 0) (A. Afaq *et al.*, 2018) [25]. In comparison to its substantial bulk modulus, the material's higher Young's modulus implies increased resistance to crushing.
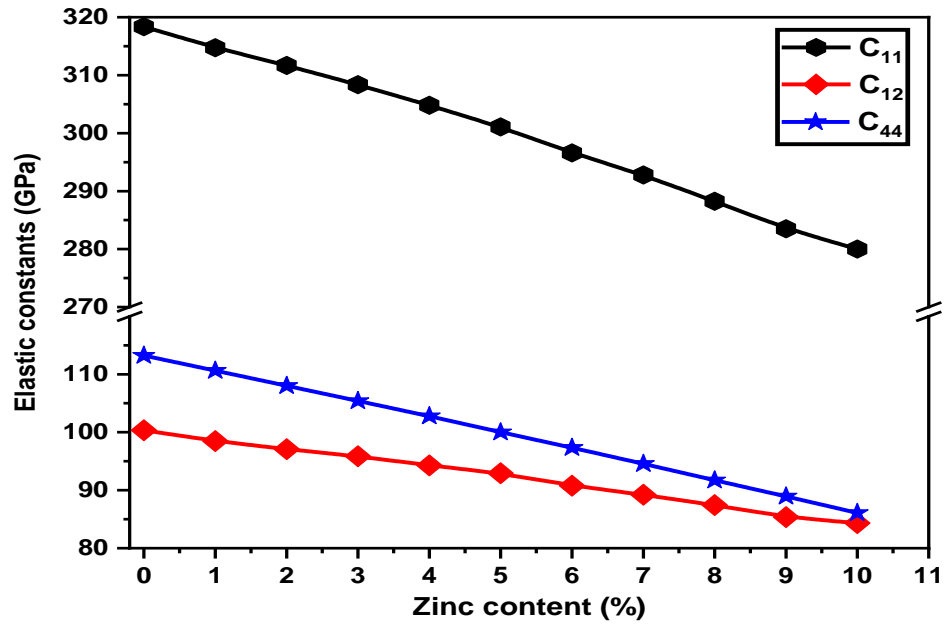
Fig. IV.4: Elastic constants versus zinc content x for $SrZn_xTi_{1-x}O_3$ alloys.
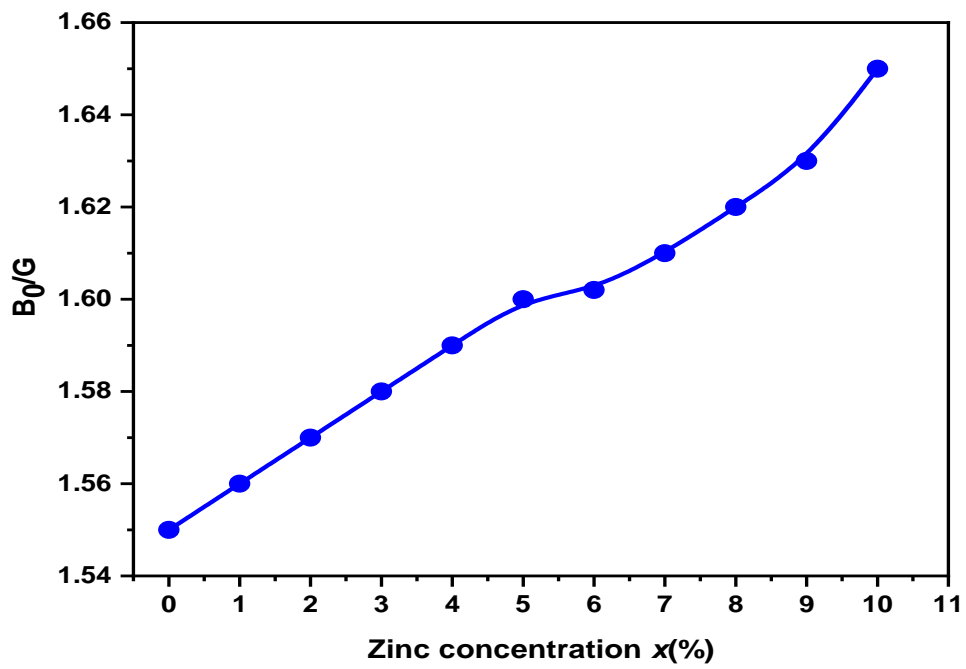
Fig. IV.5: *B/G* as a function of zinc content *x* for $SrZn_xTi_{1-x}O_3$ alloys.
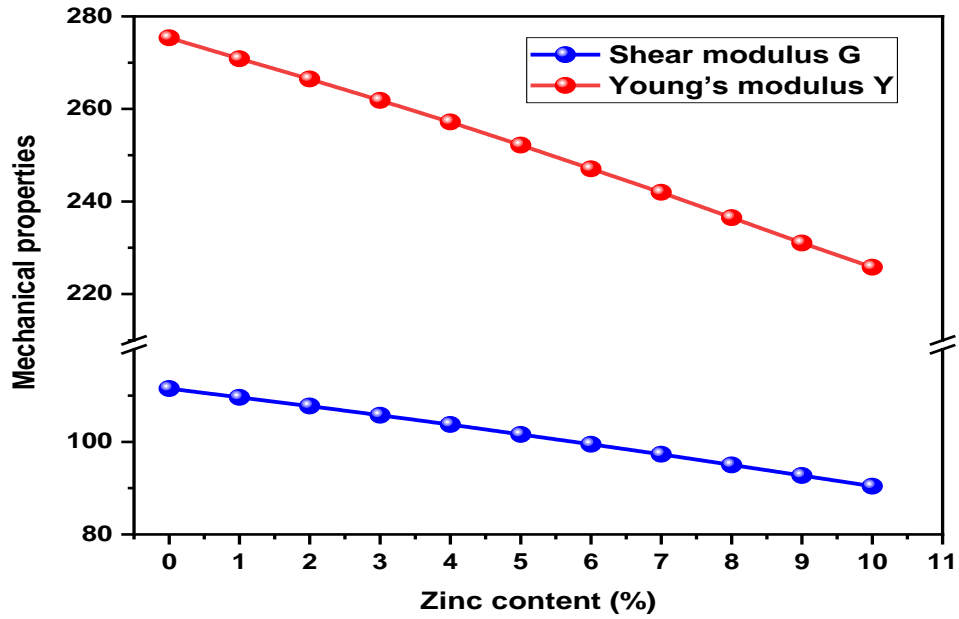
Fig. IV.6: Shear and Young's Modulus as a function of zinc content x for $SrZn_xTi_{1-x}O_3$ alloys.

Table IV.2: Elastic constants, Bulk Modulus, Shear and Young's moduli, B/G ratio, anisotropy factor, hardness and Poisson's ratio of $SrZn_xTi_{1-x}O_3$.

Compound	C_{11} (GPa)	C_{12} (GPa)	C_{44} (GPa)
SrTiO₃	317.62	99.71	113.32
	350.46[6]	101.166	111.026
	273.46[7]	85.187	96.907
	366.1[23]	91.3923	102.2023
	317.2[22] Exp.	102.51[22] Exp.	122.35[22] Exp.
SrZn₀.₀₂Ti₀.₉₈O₃	317	102.5	112
SrZn₀.₀₃Ti₀.₉₇O₃	318.20	100.15	113.17
SrZn₀.₀₄Ti₀.₉₆O₃	318.17	100.14	113.14
SrZn₀.₀₅Ti₀.₉₅O₃	318.13	100.12	113.12

SrZn₀.₀₆Ti₀.₉₄O₃	318.10	100.11	113.09
SrZn₀.₀₇Ti₀.₉₃O₃	318.07	100.09	113.07
SrZn₀.₀₈Ti₀.₉₂O₃	318.04	100.08	113.04
SrZn₀.₀₉Ti₀.₉₁O₃	318.01	100.07	113.02
SrZn₀.₁Ti₀.₉₀O₃	317.98	100.05	112.99

Table IV.3: Bulk Modulus, Shear and Young's moduli, *B/G* ratio, anisotropy factor, hardness and Poisson's ratio of SrZn$_x$Ti$_{1-x}$O₃.

Compound	*B* (GPa)	*G* (GPa)	*B/G*	*E* (GPa)	*A*	*H*(GPa)	*v*
SrTiO₃	172.34998 184.266 147.947 182.9623	111.511 6.286 95.787 116.2623	1.55	275 288.226 236.337	0.980 .896 1.027	16.7	0.23
SrZn0.02Ti0.98O3	168.61237	111.47	1.5525	275.24	1.03	16.70	0.23
SrZn0.03Ti0.97O3	166.69908	111.45	1.5526	275.20	1.03	16.70	0.23
SrZn0.04Ti0.96O3	164.44923	111.43	1.5527	275.16	1.03	16.70	0.23
SrZn0.05Ti0.95O3	162.32213	111.41	1.5528	275.11	1.03	16.69	0.23
SrZn0.06Ti0.94O3	159.38715	111.40	1.5629	275.07	1.03	16.69	0.23
SrZn0.07Ti0.93O3	157.07667	111.38	1.5530	275.02	1.03	16.69	0.23
SrZn0.08Ti0.92O3	154.37705	111.36	1.5530	274.98	1.03	16.69	0.23
SrZn0.09Ti0.91O3	151.41548	111.34	1.5531	274.94	1.03	16.68	0.23
SrZn0.1Ti0.90O3	149.55443	111.32	1.5532	274.90	1.03	16.68	0.23

IV.3.3 Electronic properties

Electronic properties, particularly the energy gap, play a pivotal role in comprehending bonding characteristics, electronic conductivity, optical responses, and stability. Notably, the energy gap's influence extends to optical attributes governing the material's photocatalytic traits. Investigating the band structure yields insights into the compound's nature, it will be a conductor, semiconductor or insulator. In Fig. IV.7, the band structures for $SrZn_xTi_{1-x}O_3$ alloys are presented as a function of zinc content x (x = 0%, 2%, 5% and 10%).

Standard $SrTiO_3$ showcases an energy band structure with a valence band spanning from -5 eV to 0 eV and a conduction band spanning from 2.20 eV to 5 eV. The observed energy gap measures 1.97 eV, as illustrated in Fig. IV.7(a). This value closely aligns with experimental reports of 3.25 eV (A. A. Adewale *et al.*, 2021) [6] and other theoretical values [8,26].

The valence band's maximum aligns with the Fermi level, classifying all investigated compounds as semiconductors characterized by an indirect R → Γ band gap. The separation between the conduction and valence bands originates from the substantial number of electrons within their respective bands, influencing the occupancy states near the Fermi level. Table IV.3 provides the computed band gap values for Zn-doped $SrTiO_3$ at 0 GPa. Fig. IV.8 illustrates the alteration in band gap energy concerning Zn concentration. Notably, a linear decline in the band gap is evident with increasing Zn content.

The decreased band gap energy within Zn-doped $SrTiO_3$ compounds suggests the potential for enhanced optical characteristics. The decrease in energy gap due to Zn doping implies an enhancement in optical properties. Through Zn doping in $SrTiO_3$, spanning a range of 2% to 10% content, the energy gap resides between 1.802 and 1.154 eV. The conformity of our data regarding Eg variation with Zn content x adheres to second-order polynomial expressions as follows:

$$g(x) = 1.97113 - 0.08581x + 3.99767 \times 10 - 4x^2 \qquad (IV.9)$$

(a) pure SrTiO3

(b) SrZn$_{0.02}$Ti$_{0.98}$O$_3$
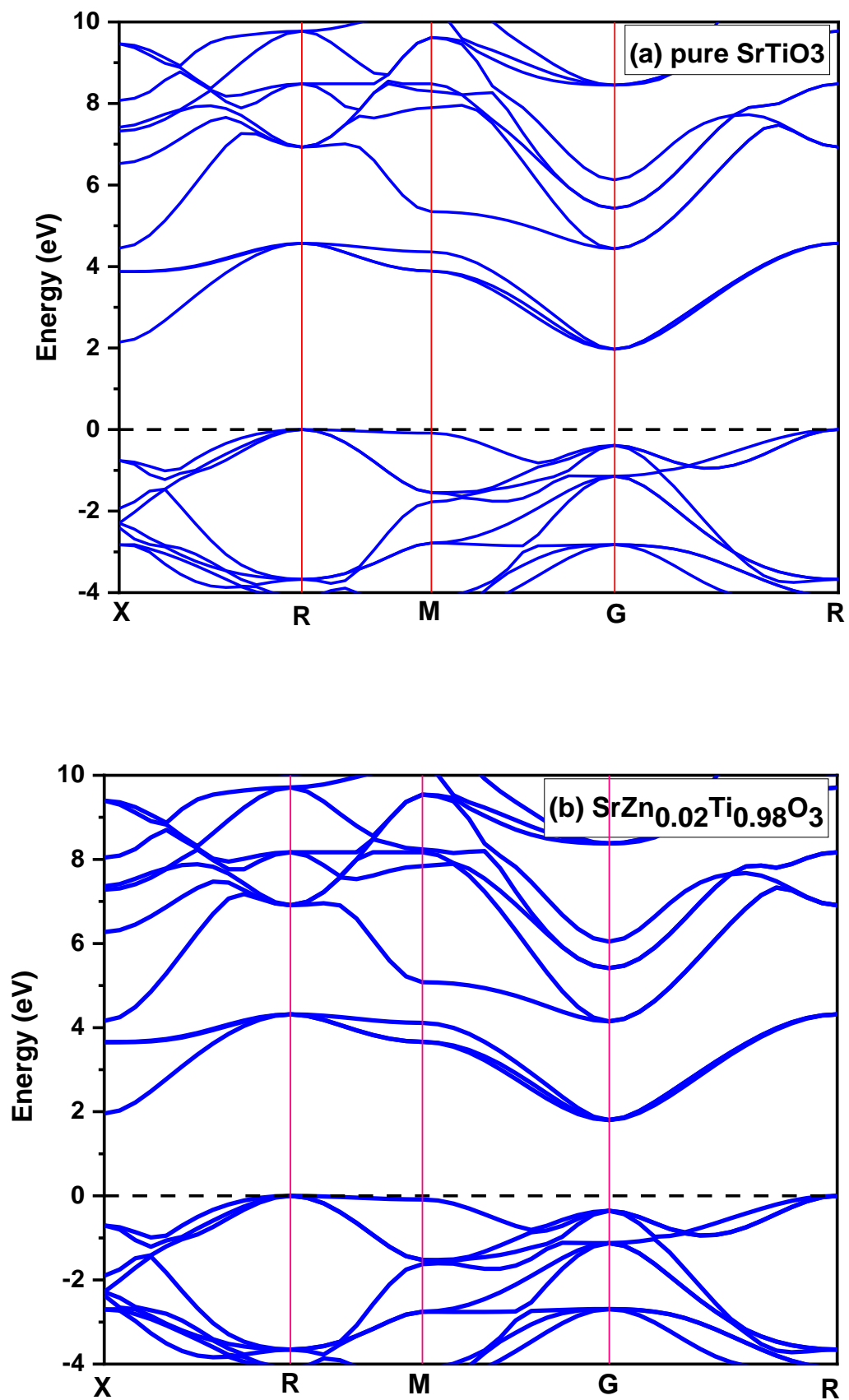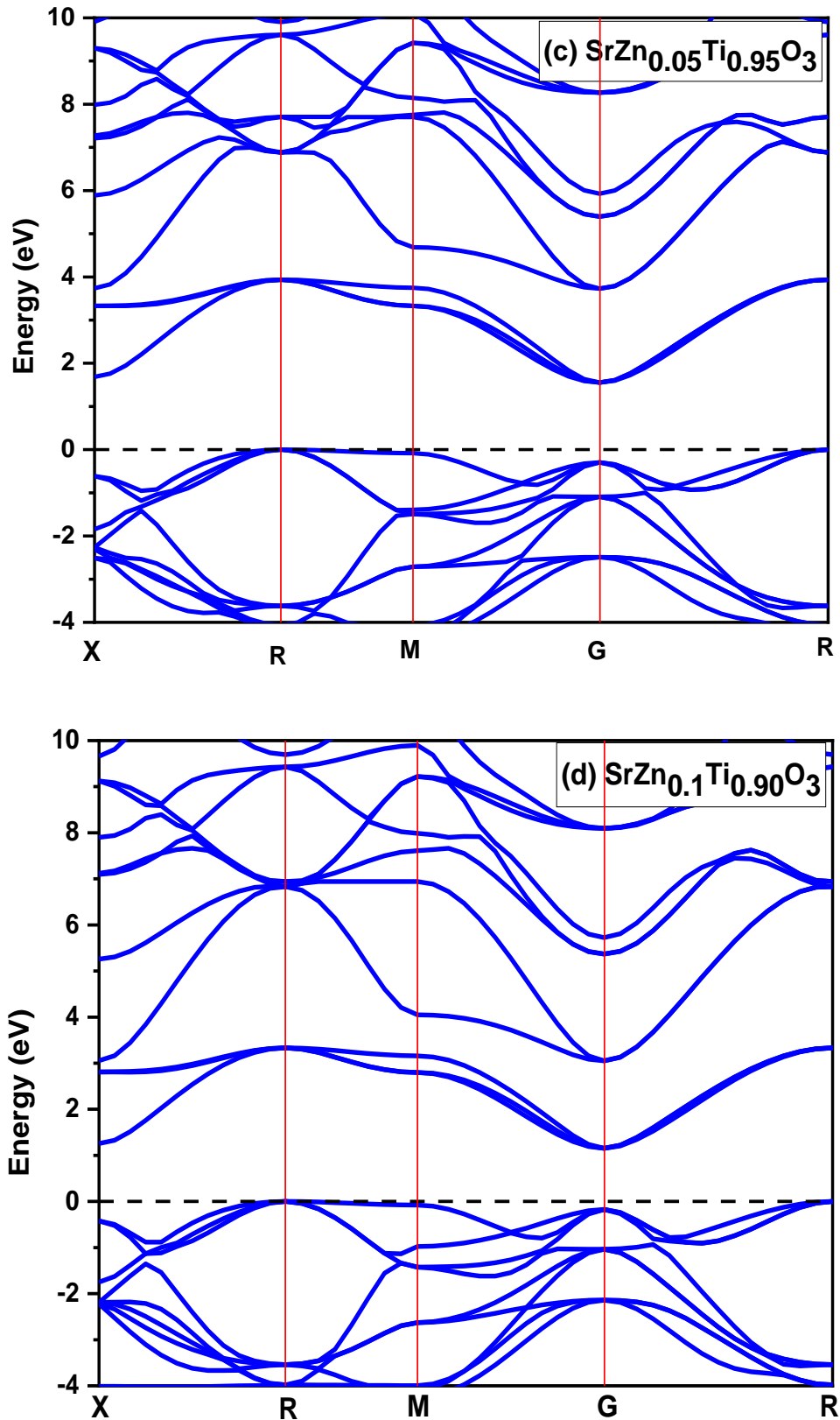
Fig. IV.7: Calculated band structure as a function of zinc content for $SrZn_xTi_{1-x}O_3$ alloys.
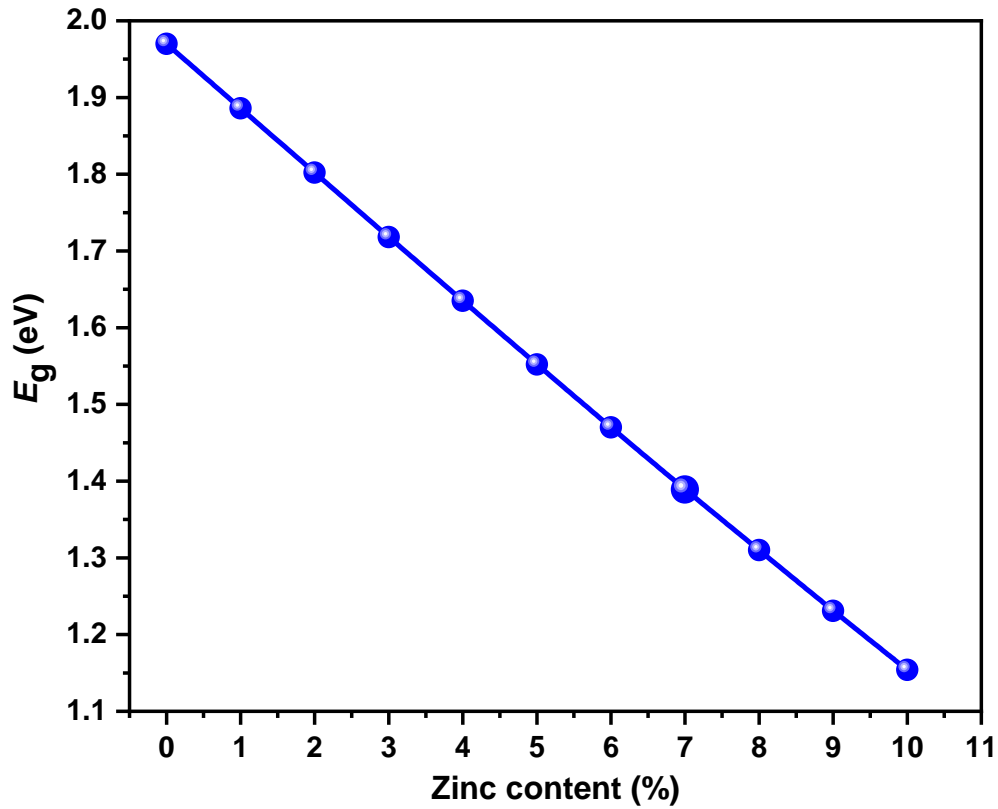
Fig. IV.8: Band gap as a function of zinc content for SrZn$_x$Ti$_{1-x}$O$_3$ alloys.

Table IV.4: Calculated band gap as a function of zinc content for SrZn$_x$Ti$_{1-x}$O$_3$ alloys.

x(%)	Band gap: this work	Other theoretical calculations	Experiments
0	1.97	1.82[6] 1.812[26] 1.99[8]	3.25[6] Exp.
2	1.802	/	/
5	1.533	/	/
10	1.154	/	/

The nature of the band structure and the behavior of the energy gap in relation to Zn content are both rational and dependable. The band structure calculations intuitively elucidate the impact of doping on the energy gap. For $SrTiO_3$ doped with 2%, 5% and 10% S, the band gap energy measures 2.87, 2.73 and 3 eV, respectively (H. K. Le *et al*., 2016) [27]. In contrast, the energy gap value for $SrTi_{0.875}Nb_{0.125}O_3$ is approximately 1.85 eV, a notable difference from the experimental value of around 3.2 eV [24].

The incorporation of Al at concentrations of 10% and 20% into $SrTiO_3$ films on Si (100) substrates results in a 0.3 eV increase in the band gap compared to undoped $SrTiO_3$ (X. G. Guo *et al.*, 2003) [28]. Conversely, Ag doping on $SrTiO_3$ leads to a reduction of the band gap by 0.15 eV (A. B. Posadas *et al.*, 2013) [29].

Transition metal dopants, barring Pd and Pt, generally have a negligible effect on the STO band gap, while S and Se doping significantly reduces STO's band gap (S. A. Azevedo *et al.*, 2022) [30]. In the case of Nb-doped $SrTiO_3$, band gap values of 3.09, 3.12 and 3.17 eV correspond to doping levels of 20%, 30%, and 10% respectively (Y. S. Hou *et al.*, 2021) [31].

Total and partial densities of states (TDOS and PDOS) elucidate the material's physical properties and offer a detailed insight into the electronic contribution of Sr, Ti, Zn and O the constituents of the studied compound.

Fig. IV.9 showcases TDOS and PDOS for both standard and 10% Zn-doped $SrTiO_3$, computed using the GGA-PBE approximation. It's notable that the lower valence bands in $SrTiO_3$ and $SrZn_{0.1}Ti_{0.9}O_3$ span energy levels from -20 eV to -10 eV. These bands encompass Sr-p and Sr-s states in the case of SrTiO3, and Sr-p, O-p, Zn-s and Zn-p states in $SrZn_{0.1}Ti_{0.9}O_3$.

The higher valence bands extend from around -5 eV to the Fermi level, predominantly comprising Sr-p, Sr-d and O-p states for SrTiO3, and Ti-p, Ti-d, O-p, and Zn-d, Zn-p states for $SrZn_{0.1}Ti_{0.9}O_3$. However, the vicinity of the Fermi level is dominated by Sr-p, Sr-d and O-p states in $SrTiO_3$ and Ti-p, Ti-d, and O-p states in $SrZn_{0.1}Ti_{0.9}O_3$. With increased Zn content, the interaction of Zn-p and Zn-d with O-p leads to a reduction in the band gap.
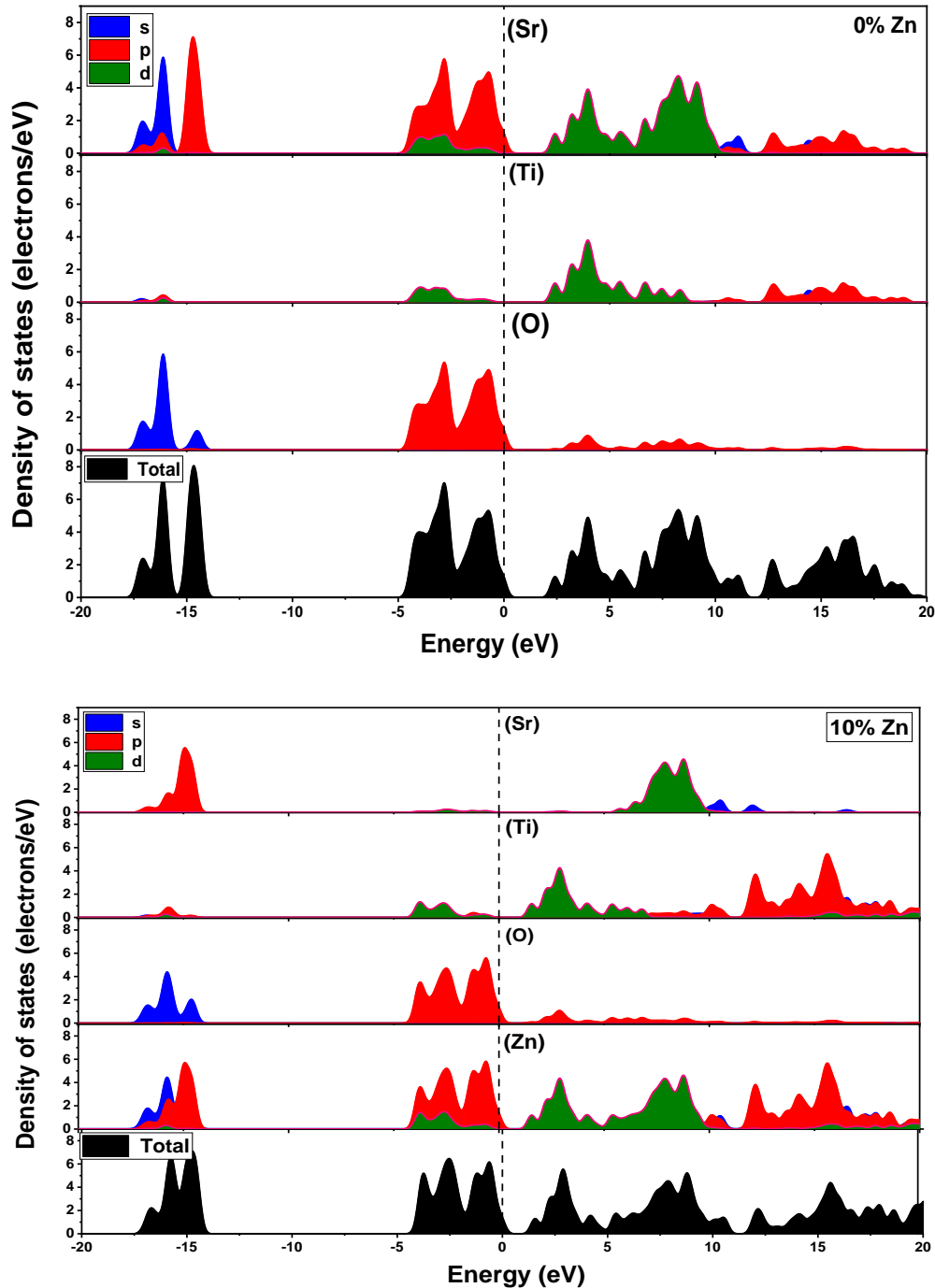
Fig. IV.9: TDOS and PDOS for standard and Zn (10%)-doped SrTiO₃ using GGA-PBE approximation.

IV.3.4 Optical properties

Evaluating materials' suitability for optoelectronic applications necessitates a thorough exploration of their optical properties. For the SrTiO₃ perovskite material, a focused GGA-PBE approximation has been employed to investigate these optical characteristics. These properties are intricately linked to the interplay between photons and electrons within the system. As depicted in Fig. IV.10, various optical parameters, including refractive index,

dielectric function, absorption spectrum, optical conductivity and reflectance, have been examined for undoped SrTiO₃ across incident light energies reaching 60 eV. The calculation of frequency-dependent dielectric constants involves the utilization of the subsequent relation:

$$\varepsilon(\omega) = \varepsilon_1(\omega) + i.\varepsilon_2(\omega) \qquad (IV.10)$$

Here, $\varepsilon_1(\omega)$ and $\varepsilon_2(\omega)$ represent the actual and imaginary segments of the dielectric constant, respectively. The imaginary component, ε_2, reveals transitions between occupied and unoccupied states within the material.

The dielectric function is a crucial optical parameter employed to characterize how a material reacts to incident radiation. As illustrated in Fig. IV.10(a), the actual and imaginary segments of SrTiO₃'s dielectric function are presented. Notably, ε_2 (the imaginary part) diminishes to zero around 40 eV, signifying the material's transparency at these incident energy levels. Further optical parameters, including reflectivity (R), refractive index (n), optical conductivity (σ), and absorption (α), were determined utilizing the complex components of the dielectric function.

$$R(w) = \frac{(n-1)^2 + k^2}{(n+1)^2 + k^2} \qquad (IV.11)$$

$$n(w) = \frac{\sqrt{\varepsilon_1{}^2(w) + \varepsilon_2{}^2(w)} + \varepsilon_1{}^{\frac{1}{2}}}{\sqrt{2}} \qquad (IV.12)$$

$$Re[\sigma(w)] = \frac{w}{4\pi}\varepsilon_2(w) \qquad (IV.13)$$

$$\alpha(w) = \sqrt{2}(w)\left[\sqrt{\varepsilon_1{}^2(w) + \varepsilon_2{}^2(w)} - \varepsilon_1(w)\right]^{\frac{1}{2}} \qquad (IV.14)$$

As depicted in Fig. IV.10(b), SrTiO3's reflectivity spectra is graphed as a function of incident photon energy, demonstrating a pronounced presence in the infrared spectrum. The reflectivity experiences rapid declines in the high-energy range, punctuated by peaks attributed to internal transitions. It was observed from Fig. IV.10(b) that the minimum reflectivity value is 0.00236 at an incident energy of 34.18 eV, while the maximum value reaches 0.493 at an incident photon energy of 25.998 eV. Fig. IV.10(c) showcases the refractive indices, both real and imaginary components. The imaginary portion of the refractive index signifies the degree of absorption loss experienced by electromagnetic waves while traversing the material, while at an energy of 25.998 eV, and the highest is 2.95 at 2.73 eV. The average refractive index stands at 2.442.the real part denotes the phase

velocity of the electromagnetic wave. The lowest recorded refractive index value, n, is 0.2611.
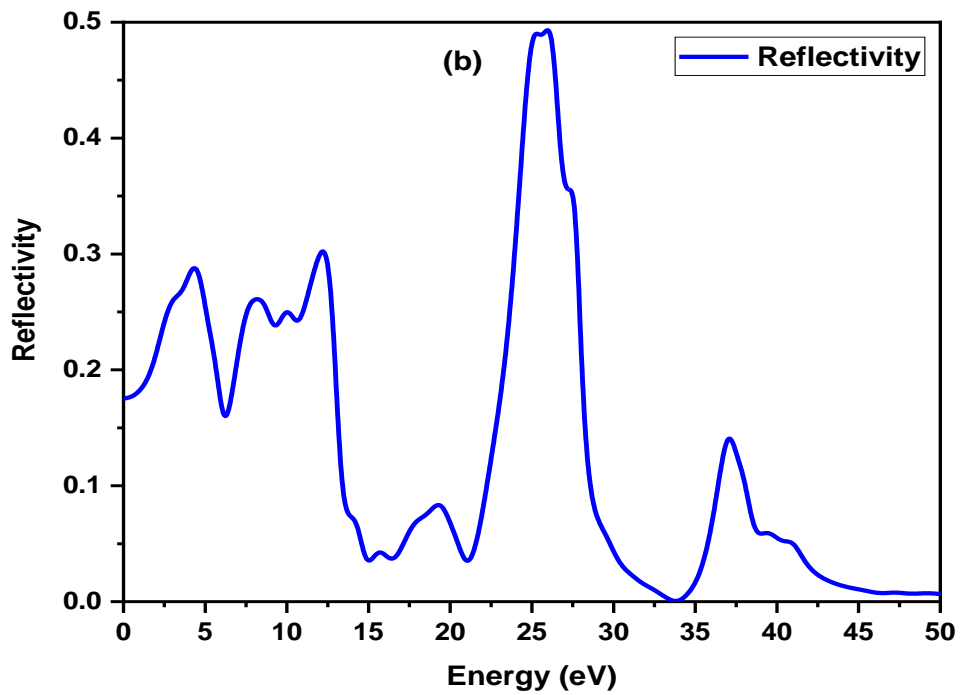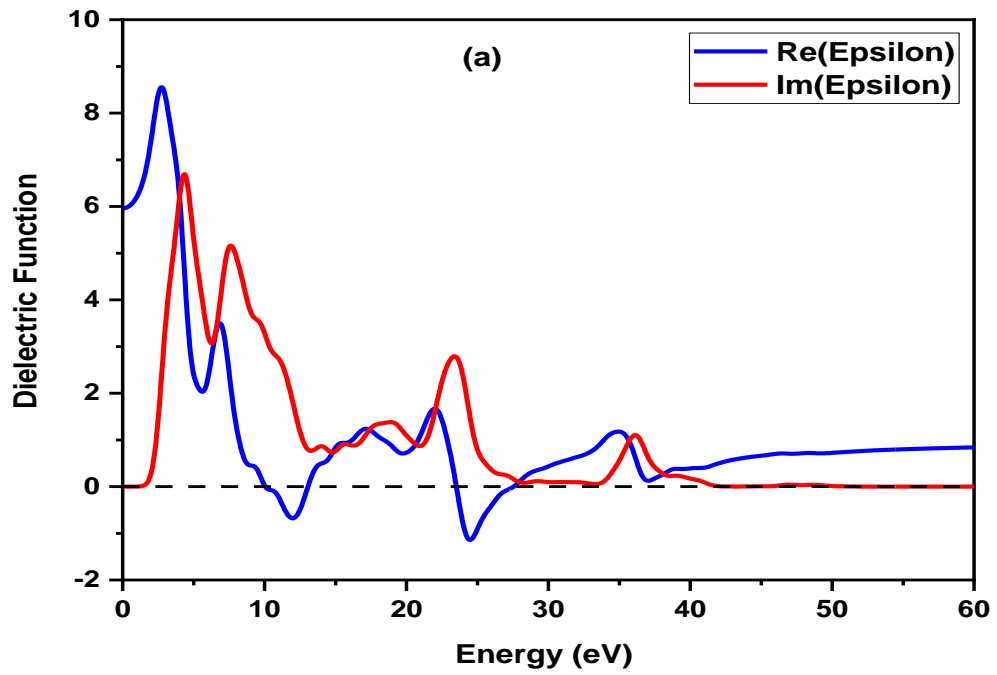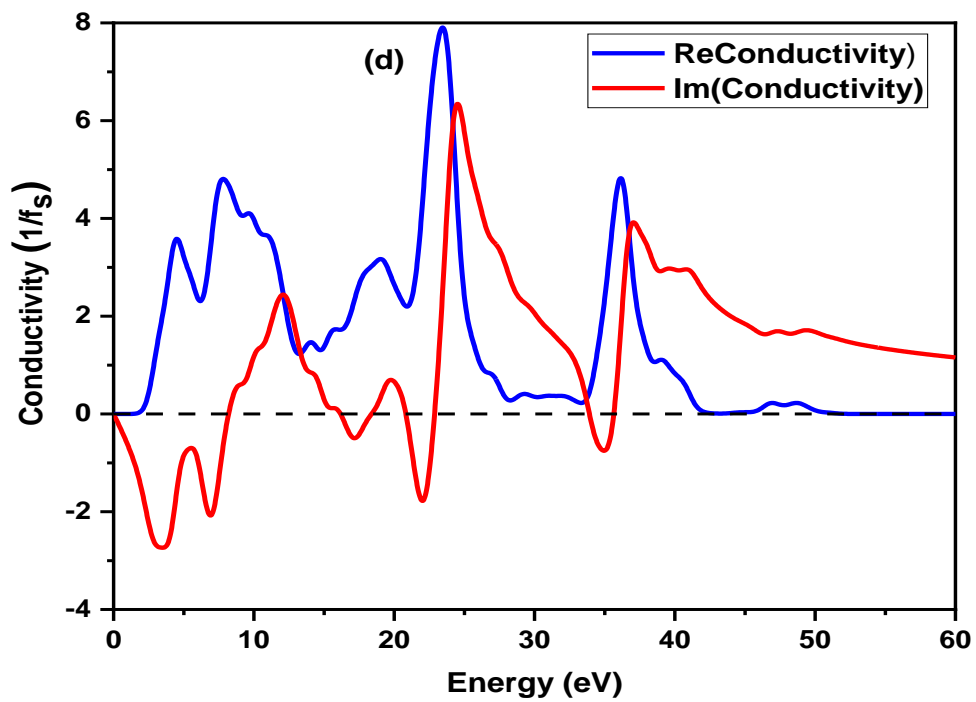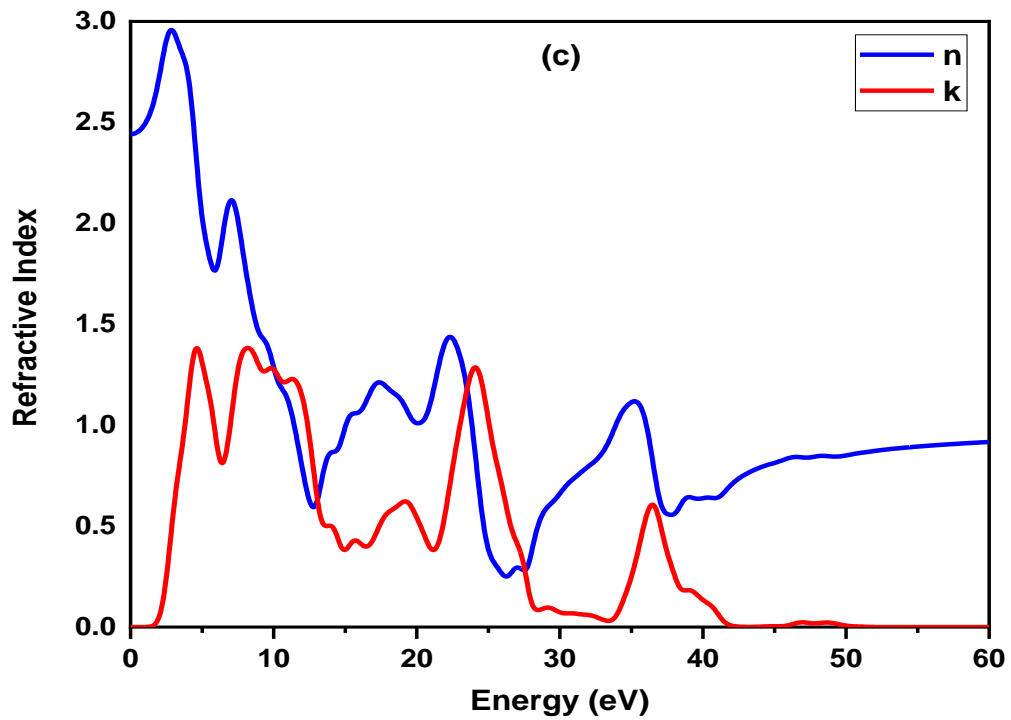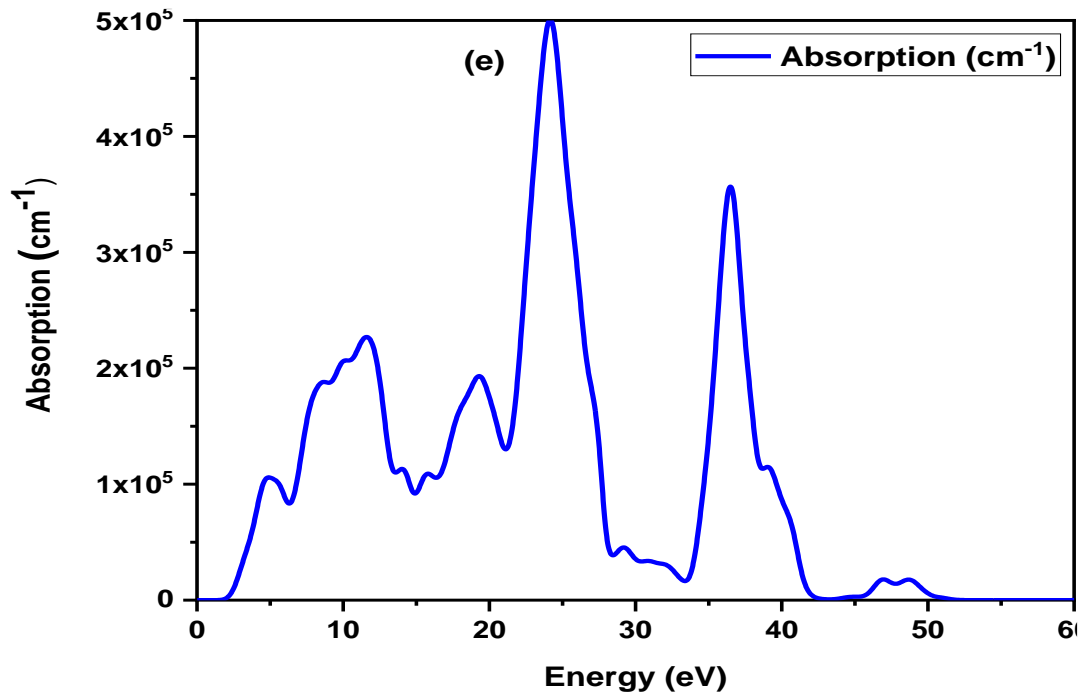
Fig. IV.10: Calculated optical properties, (a) Dielectric function, (b) Reflectivity, (c) Refractive index, (d) Conductivity, (e) Absorption of $SrTiO_3$ compound.

IV.4 Conclusion

In a comprehensive analysis, the structural, mechanical, elastic, electronic and optical attributes of pure and Zn-doped $SrTiO_3$ compounds were meticulously examined via first-principles calculations using the CASTEP software. The investigated compounds were identified to possess an isotropic cubic structure with a brittle characteristic. This structural and mechanical behavior aligns closely with existing theoretical and experimental data. Notably, various properties computed for different doping concentrations suggest an enhanced photocatalytic potential within $SrTiO_3$ crystals. Among these, Zn-doped $SrTiO_3$ (10%) stood out as the most stable compound, exhibiting a narrow band-gap energy. Through the substitution of Ti atoms with Zn, the photocatalytic activity of the $SrTiO_3$ compound was notably improved. The band structure analysis of $SrZn_xTi_{1-x}O_3$ alloys revealed an indirect R - Γ band gap.

Further investigation into the electronic properties unraveled the diverse contributions from valence and conduction bands, elucidating the compound's electronic structure. The partial and total density of states (DOS) analysis unveiled that the conduction band predominantly comprises Zn and Ti-d states, intertwined with Sr-s and Sr-d states of $SrTiO_3$.

Conversely, O-p states are primarily associated with the valence band. Increased Zn content introduces a mixing of Zn-p and Zn-d states with O-p states, resulting in a reduced band gap.

The overall characterization of both pure and Zn-doped $SrTiO_3$ materials underscores their substantial potential for application in photocatalytic devices. The introduction of Zn atoms as dopants in SrTiO3 induces a shift of the valence band's upper edge towards the Fermi level, contributing to their promising photocatalytic properties.

References

[1] M. A. Ghebouli, B. Ghebouli, L. Krache, S. Alomairy, M. Fatmi, T. Chihi and M. Re®as, Bull. Mater. Sci. 45(3) (2022) 124.

[2] J. P. Perdew, K. Burke and M. Ernzerhof, Phys. Rev. Lett. 77 (1996) 3865, doi: 10.1103/PhysRevLett.77.3865.

[3] H. J. Monkhorst and J. D. Pack, Phys. Rev. B 13 (1976) 5188, doi: 10.1103/PhysRevB.13.5188.

[4] T. H. Fischer and J. Almlof, J. Phys. Chem. 96 (1992) 9768, doi: 10.1021/j100203a036.

[5] Y. Naceur, H. Bourbaba, M. A. Ghebouli, L. Krache, B. Ghebouli, T. Chihi and S. Alomairy, Sci. Rep. 12(1) (2022) 1.

[6] A. A. Adewale, A. Chik, T. Adam, O. K. Yusuff, S. A. Ayinde, and Y. K. Sanusi, "First principles calculations of structural, electronic, mechanical and thermoelectric properties of cubic ATiO3 (A= Be, Mg, Ca, Sr and Ba) perovskite oxide," Comput. Condens. Matter, vol. 28, no. May, 2021, doi: 10.1016/j.cocom. 2021.e00562.

[7] M. L. Ali and M. Z. Rahaman, "Variation of the Physical Properties of Four Transition Metal Oxides SrTMO 3 (TM = Rh, Ti, Mo, Zr) Under Pressure: An Ab Initio Study," J. Adv. Phys., vol. 6, no. 2, pp. 197–205, 2017, doi: 10.1166/jap.2017.1329.

[8] S. Jiao, J. Yan, G. Sun, and Y. Zhao, "Electronic structures and optical properties of Nb-doped SrTiO3 from first principles," J. Semicond., vol. 37, no. 7, 2016, doi: 10.1088/1674-4926/37/7/072001.

[9] M. Rizwan, Z. Khadija, T. Mahmood, S. S. A. Gillani, and M. I. Khan, "Alteration impact of electronic properties of c-SrTiO3 on optical response due to Ca inclusion: A DFT study," Phys. B Condens. Matter, vol. 602, no. April 2020, 2021, doi: 10.1016/j.physb.2020.412553.

[10] N. Li and K. L. Yao, "The electronic and optical properties of carbon-doped SrTiO3: Density functional characterization," AIP Adv., vol. 2, no. 3, 2012, doi: 10.1063/1.4746023.

[11] S. Quantum *et al.*, "Investigation of Structural, Electronic and Optical Properties of SrTiO3 and Investigation of Structural, Electronic and Optical Properties of SrTiO 3 and SrTi 0. 94 Ag 0. 06 O 3 Quantum Dots Based Semiconductor Band gap," no. March, 2022, doi: 10.22034/AJCA.2022.325958.1300.

[12] F. D. Murnaghan, Proc. Natl. Acad. Sci. USA 30 (1944) 5390.

[13] M. Zafar, M. Shakil, S. Ahmed, M. Hashmi, M. A. Choudhary and Naeem-ur-Rehman, Sol. Energy 158 (2017) 63.

[14] P. Nunocha, M. Kaewpanha, T. Bongkarn, A. Eiad-Ua, and T. Suriwong, "Effect of Nb doping on the structural, optical, and photocatalytic properties of SrTiO3 nanopowder synthesized by sol-gel auto combustion technique," J. Asian Ceram. Soc., vol. 10, no. 3, pp. 583–596, 2022, doi: 10.1080/21870764.2022.2094556.

[15] H. Salehi, "First Principles Studies on the Electronic Structure and Band Structure of Paraelectric SrTiO< sub>3</sub> by Different Approximations," J. Mod. Phys., vol. 02, no. 09, pp. 934–943, 2011, doi: 10.4236/jmp.2011.29111.

[16] H. B. Huntington, Solid State Phys. (1958) 213, doi: 10.1016/s0081-1947(08)60553-6.

[17] M. Shakil, H. Arshad, M. Zafar, M. Rizwan, S. S. A. Gillani and S. Ahmed, Mol. Phys. (2020) 1789770, doi: 10.1080/00268976.2020.1789770.

[18] X. Jiang, J. Zhao and X. Jiang, Comput. Mater. Sci. 50 (2011) 2287.

[19] M. Shakil, A. Akram, I. Zeba, R. Ahmad, S. Gillani and M. Gadhi, Mater. Res. Express 7(2) (2020) 025513, doi: 10.1088/2053-1591/ab727d.

[20] M. Zafar, M. Kashif, M. Rizwan, A. Zia, S. Ahmad, A. Akram, C. C. Bao and M. Shakil, Optik 182 (2019) 1176.

[21] R. O. Bell and G. Ruprecht, Phys. Rev. 129 (1963) 90.

[22] A. Boudali, M. D. Khodja, B. Amrani, D. Bourbie, K. Amara, and A. Abada, "First-principles study of structural, elastic, electronic, and thermal properties of SrTiO3 perovskite cubic," Phys. Lett. Sect. A Gen. At. Solid State Phys., vol. 373, no. 8–9, pp. 879–884, 2009, doi: 10.1016/j.physleta.2008.12.017.

[23] A. Hachemi, H. Hachemi, A. Ferhat-Hamida, and L. Louail, "Elasticity of SrTiO3 perovskite under high pressure in cubic, tetragonal and orthorhombic phases," Phys. Scr., vol. 82, no. 2, 2010, doi: 10.1088/0031-8949/82/02/025602.

[24] R. S. Sunmonu, O. Y. Fadimu and O. I. Sonde, Int. J. Mod. Phys. B (2023).

[25] A. Afaq, A. Bakar, S. Anwar, W. Anwar and Fazal-e-Aleem, Int. J. Mod. Phys. B 32 (2018) 1850362, doi: 10.1142/S0217979218503629.

[26] M. Rizwan, A. Ali, Z. Usman, N. R. Khalid, H. B. Jin, and C. B. Cao, "Structural, electronic and optical properties of copper-doped SrTiO3 perovskite: A DFT study," Phys. B Condens. Matter, vol. 552, pp. 52–57, 2019, doi: 10.1016/j.physb.2018.09.02210.4028/www. Scienti⁻c.net/AMR.750-752.1199.

[27] H. K. Le, K. O. Pham, T. T. Tran and M. V. Le, Sci. Technol. Dev. 19(K6) (2016) 176.

[28] X. G. Guo, X. S. Chen, Y. L. Sun, L. Z. Sun, X. H. Zhou and W. Lu, Phys. Lett. A 317 (2003) 501.

[29] A. B. Posadas, C. Lin, A. A. Demkov and S. Zollner, Appl. Phys. Lett. 103 (2013) 142906, doi: 10.1063/1.4824023.

[30] S. A. Azevedo, J. A. S. Laranjeira, J. L. P. Ururi and E. Longo, Comput. Mater. Sci. 214(4) (2022) 111693, doi: 10.1016/j.commatsci.2022.111693.

[31] Y. S. Hou, S. Ardo and R. Q. Wu, Phys. Rev. Mater. 5 (2021) 065801.

CHAPTER V

Aluminum Doping Effects on CuInS2

Chapter V: Effects of Aluminum doping on CuInS₂ chalcopyrite compound

V.1 Introduction

This chapter presents a comprehensive examination of the influence of aluminum (Al) doping on the diverse characteristics of CuInS2 (Copper Indium Sulfide), a chalcopyrite compound. CuInS2 has garnered considerable attention as a semiconductor material with promising applications in optoelectronics and electronic devices. To fully unlock its potential and customize its attributes for specific applications, researchers have explored the approach of incorporating aluminum. The main objective of this study is to thoroughly assess how the introduction of aluminum affects the structural features, elastic properties, mechanical behavior, electronic traits, and optical attributes of CuInS2. The incorporation of aluminum induces localized modifications to the crystal lattice, thereby altering the intrinsic properties of the material. Understanding these alterations is crucial for harnessing CuInS2's potential in advanced electronic and optoelectronic technologies.

Through a systematic process of characterization and analysis, this chapter aims to provide valuable insights into the interplay between aluminum doping and the various characteristics of CuInS2. The results obtained in this study will make a significant contribution to the expanding knowledge base on semiconductor materials and pave the way for the design of high-performance devices tailored to meet the requirements of contemporary technology. Our research focuses on gaining a deeper understanding of how aluminum doping affects the structural properties of CuInS2 and offers insights into the material's utilization in optoelectronics. We utilized the CASTEP program to investigate the electronic structure and optical properties of CuInS2, enabling us to simulate the crystal structure and study the impact of impurities on the com (A. Soni *et al.*, 2010) [1].

V.2 Computation details

In order to investigate the electronic structures and optical properties of doped CuInS₂, first-principles calculations were performed using the pseudo-potential plane waves (PP-PW) method based on DFT, implemented with the CASTEP (S. J. Clark *et al.*, 2005) [2] code, a widely recognized computational tool, in investigating the electronic and structural properties of materials. The use of GGA method offers several advantages, including ease of calculation of forces and stresses, efficient control of convergence for almost every

computational parameter, appropriate scaling at the atomic level and neglecting core electrons to simplify the calculations. The calculations were performed using the space group I-42m with particular atomic positions for cations and anions. The k-point and cut-off values were chosen as (5 5 2) and 800 eV, respectively. For doped samples, indium atoms were replaced with aluminum atoms in different proportions of 0, 25%, 50%, 75%, and 100%.

Geometric optimization was performed with an affinity resolution of 1×10^{-5} eV/atom using (C.G. Broyden *et al.*, 1970) [3] (BFGS) algorithm to achieve relaxation at minimum values of energy. The force, pressure and displacement were taken as 0.03 eV/A, < 0.05 GPa, and 0.001 Å, respectively. The electronic structures and other optical properties were investigated for optimized geometries with the help of total and partial density of states (TDOS and PDOS).

V.3 Structural properties

CuInS$_2$ is a chalcopyrite compound with a unique crystal structure that has attracted attention for its potential applications in optoelectronics. The chalcopyrite structure of CuInS2 is a tetragonal crystal structure with four axes of symmetry. This structure is relatively stable for ternary compounds and allows for efficient packing and covalent bonding between the atoms. In their 2022 publication in the Journal of Thermal Sciences, (S. Fan *et al.*, 2022) [4] Comprehensive theoretical study of CuInS$_2$, with the aim of exploring its elastic and thermodynamic properties. The study involved detailed analyzes and simulations to gain insights into the crystal structure of CuInS$_2$, its stability and the nature of bonding between its constituent atoms.

This knowledge is essential for the development and optimization of CuInS$_2$-based devices for various applications, as "Tunable structural and optical properties of CuInS$_2$ colloidal quantum dots as photovoltaic absorbers" was reported by (S.-K. Ming *et al.*, 2021) [5] published in RSC. Advances, presents a study focusing on CuInS$_2$ colloidal quantum dots and their potential as photovoltaic absorbers.

The research explores the controllable manipulation of the structural and optical properties of CuInS$_2$ quantum dots. Through systematic investigations and experiments, the authors highlight the retainability of these quantum dots, which could have significant implications for their application in photovoltaic devices. The study provides valuable insights into harnessing the unique properties of CuInS$_2$ quantum dots as effective light absorbers in solar energy conversion technologies. Another study by (B. Gao *et al.*, 2016)

[6] The authors also highlight composition-dependent properties of WZ-CuInS$_2$, providing valuable insights into the material's potential applications in optoelectronic devices. This study contributes to a deeper understanding of the properties of CuInS$_2$ in its Wurtzite form and provides valuable knowledge for the development of new photonic and electronic technologies. A recent study conducted by (F-L. Tang *et al*., 2012) [7] investigated the electronic and optical properties of aluminum-doped CuInS$_2$ using a combination of experimental and computational methods. The study also used the CASTEP program to calculate the material's structural properties, such as lattice modulus and atomic positions, and found that aluminum doping had a significant effect on lattice modulus.

Our study revealed that the crystal structure of CuInS$_2$ plays a crucial role in its electronic and optical properties, with changes in the lattice parameters leading to changes in the band gap and band edge positions.

Our aim in this study is to investigate the structural properties of CuInS$_2$ and the effect of aluminum doping on these properties. We will use a range of aluminum concentrations and analyze changes in lattice parameters and other structural properties. We used the Murnaghan equation of state equations (V.1) to calculate the lattice constant a_0 (Å), the volume modulus B$_0$ (GPa), its derivative B', and the volume V (Å^3) for CuInS$_2$ and CuIn$_{1-x}$Al$_x$S$_2$, where x is the aluminum concentration. This equation has become an essential tool in materials science and geophysics, enabling scientists to predict and understand the behavior of materials (F. D. Murnaghan, 1944) [8]. The Murnaghan equation relates the total energy E to the volume V and is given by:

$$E(V) = E_0 + [(B_0)/(B'(B'-1))][B'(1-V_0/V) + \left(\frac{V_0}{V}\right)^{B'} - 1] \quad (V.1)$$

E$_0$ represents the energy at the equilibrium volume *V$_0$*, B$_0$ is the bulk modulus, and *B'* is the derivative of the bulk modulus with respect to pressure.

To obtain the values of lattice constant, volume, and bulk modulus, we fitted these parameters as a function of aluminum concentration using polynomial expressions of second order. The basic valence electron configurations for Cu, In, Al and S were 3d^{10} 4s^1, 5s^2 5p^1, 3s^2 3p^4 and 3s^2 3p^1, respectively. Our use of DFT is one of the most widely used and robust methods for electronic structure calculations, enabling accurate and efficient investigation of materials' ground-state properties, chemical reactions, and structural phase transitions. In the following we present our study on these structural properties:

V.3.1 Lattice parameters

CuInS$_2$ has a chalcopyrite crystal structure with a high degree of structural stability and a strong covalent bond between its constituent atoms (See Fig. V.1).
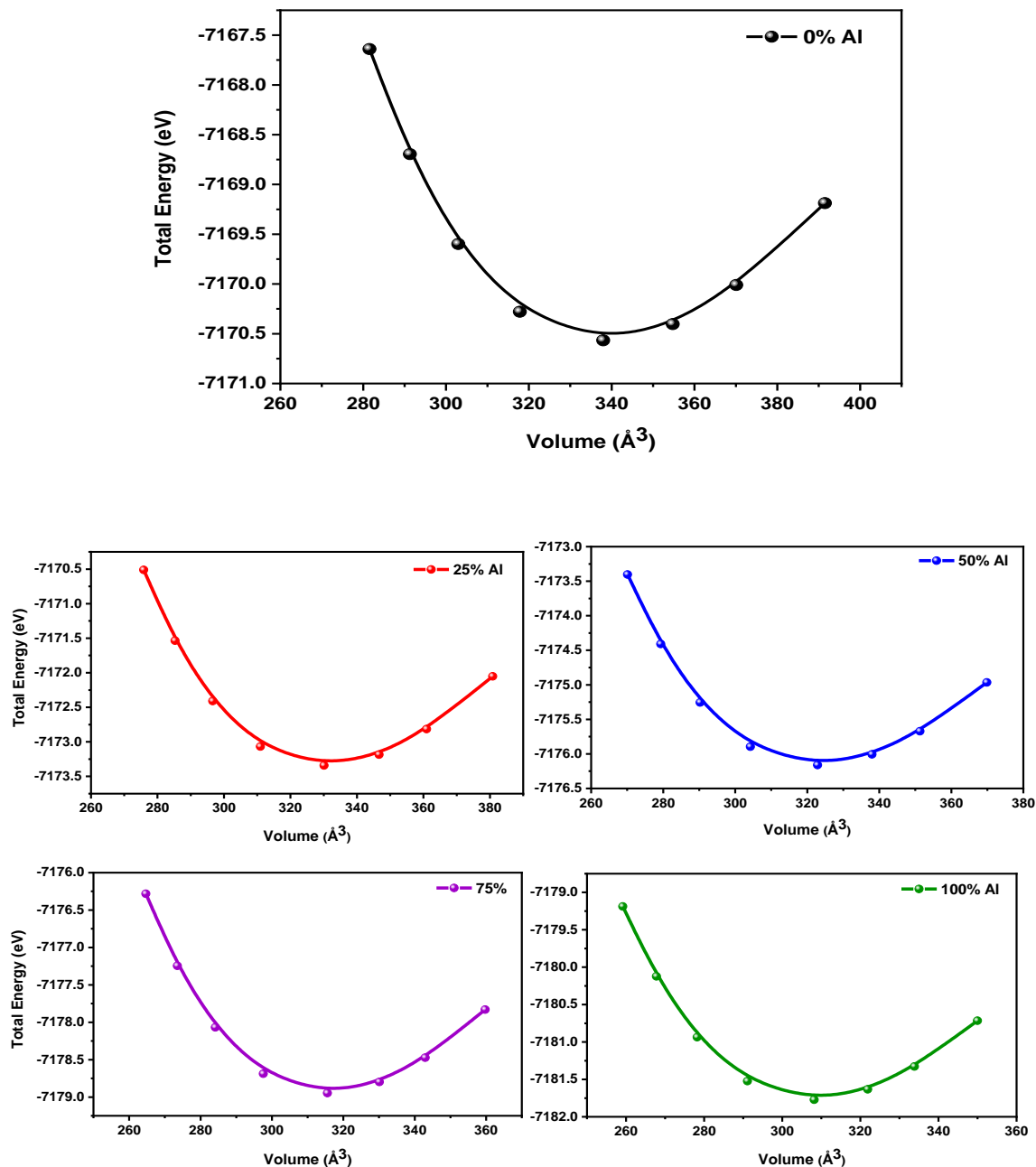
Fig. V.1: Total energy versus volume for CuIn$_{1-x}$Al$_x$S$_2$ alloys.

In this study, the structural properties of CuInS$_2$ and CuInS$_2$ doped with aluminum (CuIn$_{1-x}$Al$_x$S$_2$, where $x = 0$, 0.25, 0.5, 0.75 and 1) based on the provided data. We'll analyze the lattice parameters, lattice constants, c/a ratio, bulk modulus, and volume for each composition:

V.3.1.1 Lattice parameters (*a$_0$* and *c*)

The lattice parameters represent the dimensions of the crystal lattice unit cell. *a$_0$* is the lattice constant in the basal plane (along the a-axis), and *c* is the lattice constant perpendicular to the basal plane (along the c-axis). From Fig. V.2, we note that with the increase in doping of aluminum Al(*x*), both *a$_0$* and *c* decrease. The decrease in *a$_0$* and *c* can be attributed to the substitution of smaller Al atoms for larger In atoms. Aluminum has a smaller atomic radius compared to Indium. When Al atoms replace In atoms in the crystal lattice, the overall lattice dimensions reduce. This substitution leads to lattice compression, resulting in a smaller unit cell in both the *a$_0$* and *c* directions.

V.3.1.2 *c/a* Ratio

The *c/a* ratio is the ratio between the lattice constant *c* and the lattice constant *a$_0$*. It indicates the degree of anisotropy in the crystal structure. As the Al doping increases (*x* increases), the *c/a* ratio decreases this is illustrated by Fig. V.2. This decrease in the *c/a* ratio is consistent with the reduction in both *c* and *a$_0$* mentioned earlier. The decrease in the *c/a* ratio indicates a higher degree of anisotropy in the crystal structure with increasing Al doping. This implies that the material becomes more elongated along the c-axis compared to the basal plane.
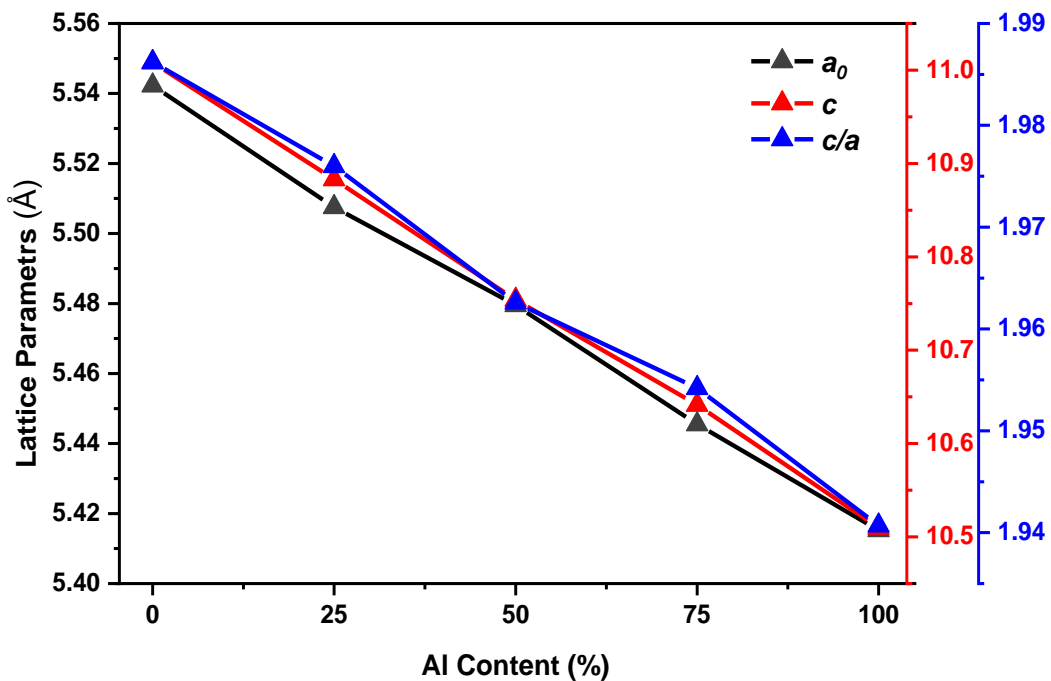
Fig. V.2: Lattice constant *a$_0$*, Lattice constant *c* and *c/a* as a function of Al content for CuIn$_{1-x}$Al$_x$S$_2$ alloys.

V.3.2 Bulk Modulus and cell volume

V.3.2.1 Bulk Modulus (B_0)

The bulk modulus represents the material's resistance to volume compression under pressure. It is a measure of the stiffness of the material. As the Al doping increases (x increases), the bulk modulus (B_0) increases (See Fig. V.3). The increase in B_0 can be explained by the strong bonding between the Al atoms and the surrounding atoms in the crystal lattice. Aluminum is known to form strong bonds, and as more Al atoms are incorporated into the crystal structure, the overall bonding strength increases, leading to a higher bulk modulus.

V.3.2.2 Volume (V)

The volume represents the total space occupied by the crystal lattice unit cell. As the Al doping increases (x increases), the volume (V) decreases refer to Fig. V.3. The decrease in V is a direct consequence of the reduction in lattice parameters (a_0 and c) with increasing Al doping. The decrease in volume indicates that the crystal lattice becomes more compact and denser with higher Al doping.

Let's consider the case of $CuIn_{0.5}Al_{0.5}S_2$, where the composition is half $CuInS_2$ and half $CuAlS_2$. The lattice parameters for $CuIn_{0.5}Al_{0.5}S_2$ are $a_0 = 5.47952$ Å and $c = 10.7539$ Å. As aluminum (Al) doping increases, the atomic substitution of Al for In leads to lattice compression, causing a decrease in both a_0 and c. In this case, the c/a ratio is 1.9626, indicating a higher degree of anisotropy compared to pure $CuInS_2$.

The increase in the bulk modulus ($B_0 = 91.81985$ GPa) implies that the bonding strength in $CuIn_{0.5}Al_{0.5}S_2$ is stronger compared to pure $CuInS_2$, making the material stiffer and more resistant to compression. Furthermore, the decrease in volume ($V = 322.887$ Å^3) with higher Al doping indicates that the crystal lattice becomes more compact and denser, leading to increased atomic packing.

The calculated results for the lattice constant, volume, and bulk modulus of $CuInS_2$ and $CuIn_{1-x}Al_xS_2$ are shown in Table V.1.
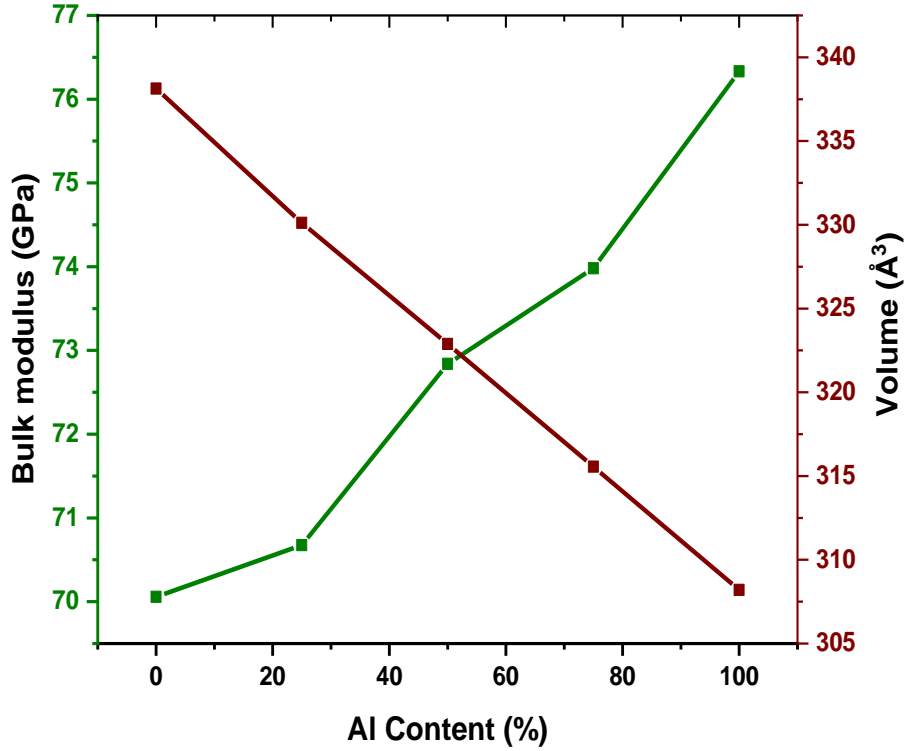
Fig. V.3: Bulk modulus B_0 (GPa), volume V (Å³) as a function of Al content for CuIn$_{1-x}$Al$_x$S$_2$ alloys.

Table V.1: Calculated lattice constants a_0 (Å), c (Å), bulk modulus B_0 (GPa) and volume V (Å³) for CuIn$_{1-x}$Al$_x$S$_2$ alloys.

Composition	a_0 (Å)	c (Å)	c/a	B_0 (GPa)	V (Å³)
CuInS₂	5.54228	11.0082	1.9862	70.05745	338.137
CuIn₀.₇₅Al₀.₂₅S₂	5.50751	10.8831	1.9760	70.67415	330.114
CuIn₀.₅Al₀.₅S₂	5.47952	10.7539	1.9626	72.83891	322.887
CuIn₀.₂₅Al₀.₇₅S₂	5.44548	10.6415	1.9542	73.98147	315.556
CuAlS₂	5.41525	10.5098	1.9407	76.33222	308.200

The fitted expressions for the lattice constant a_0, c and c/a a function of Al concentration showed good agreement with the calculated values. The relative lattice constant a_0, c and c/a as a function of Al content x were fitted using second-order polynomial expressions given by equations (V.2), (V.3) and (V.4).

$$a_0(x) = 5.54166 - 0.0013\,x + 3.46286 \times 10^{-7} x^2 \qquad (V.2)$$

$$c(x) = 11.00749 - 0.00499\,x + 4.11429 \times 10^{-7} x^2 \qquad (V.3)$$

$$c/a = 1.98627 - 4.32914 \times 10^{-4}\,x - 1.82857 \times 10^{-7} x^2 \qquad (V.4)$$

The fitting of the relative Energy, volume, bulk modulus and derivative of the bulk modulus are presented in Table V.2.

Table V.2: Calculated fitted Energy, volume, bulk modulus and derivative of the bulk modulus as a function of Al concentration in $CuIn_{1-x}Al_xS_2$ alloys.

Al concentration $0 < x < 1$	Fitted E_0 (eV)	Fitted V_0 ($Å^3$)	Fitted B_0 (GPa)	Fitted B'
0.00	-7170.5656	337.95213	68.64	4.8437
0.25	-7173.3501	330.38362	71.0832	4.60357
0.50	-7176.1588	322.80253	71.7216	4.72708
0.75	-7178.9450	315.53074	73.456	4.6874
1.00	-3590.8852	154.07098	76.4128	4.48611

The obtained results for $CuIn_{1-x}Al_xS_2$ were compared with other theoretical and experimental studies reported in the literature. The calculated lattice constant for pure $CuInS_2$ was found to be in good agreement with the experimental value reported by (M.G. Brik, 2009) [9] ($a_0 = 5.523$ Å and $c = 11.12$ Å). The volume for pure $CuInS_2$ were also in good agreement with the results reported by [9] ($V = 339.199$ $Å^3$). The obtained values were found to be consistent with their results, indicating the reliability of the present study.

The comparison of the lattice constant, volume, and bulk modulus as a function of Al concentration is summarized in Table V.3. It can be seen from the table that the present study results are in good agreement with the experimental and theoretical results reported in the literature, which confirms the reliability of our calculations and the validity of the Murnaghan equation of state in describing the properties of $CuInS_2$ and $CuIn_{1-x}Al_xS_2$.

Table V.3: Comparison of the lattice constant a_0, c, bulk modulus B and volume V of CuIn$_{1-x}$Al$_x$S$_2$ alloys, with experimental and theoretical results reported in the literature.

Sample	a_0 (Å)	c (Å)	B_0 (GPa)	V (Å^3)	Method	Reference
CuInS$_2$	5.54228	11.0082	84.28848	338,137	DFT–GGA	Present study
	5.52	11.13	/	/	DFT–GGA	[1]
	5.588	11.253	/	/	DFT–GGA	[10]
	5.525	11.127	/	/	Exp.	[10]
	5.521	12.174	/	/	DFT–GGA	[13]
	5.5775	11.2379	/	349.594	/	[22]
	5.523	11.12	/	339.199	Exp.	[22]
CuIn$_{0.75}$Al$_{0.25}$S$_2$	5.50751	10.8831	87.27810	330.114	DFT–GGA	Present study
	5.4212	10.95	/	/	/	[19]
	5.48	11.06	/	/	Exp.	[19]
CuIn$_{0.5}$Al$_{0.5}$S$_2$	5.47952	10.7539	91.81985	322.887	DFT–GGA	Present study
	5.3740	10.73	/	/	/	[19]
	5.42	10.84	/	/	Exp.	[19]

CuIn$_{0.25}$Al$_{0.75}$S$_2$	5.44548	10.6415	92.33198	315.556	DFT–GGA	Present study
	5.2681	10.63	/	/	/	[19]
	5.36	10.60	/	/	Exp.	[19]
CuAlS$_2$	5.41525	10.5098	93.60547	308.200	DFT–GGA	Present study
	5.2148	10.35	/	/	/	[19]
	5.341	10.57	84.12	/	/	[21]
	5.31	10.42	/	/	Exp.	[21]
	5.313		/	/	/	[21]
	5.2816	10.4429	/	291.308	/	[22]
	5.3336	10.4440	/	297.103	/	[22]

In summary, the structural properties of CuInS$_2$ and Aluminum-doped CuInS$_2$ exhibit systematic changes with increasing Al doping. The incorporation of Al atoms into the crystal lattice results in reduced lattice dimensions, increased anisotropy, enhanced stiffness, and densification of the material. These structural modifications are crucial in understanding and tailoring the properties of the compound for various applications, such as optoelectronics, photovoltaics, and other semiconductor devices.

V.4 Elastic constants and mechanical properties

V.4.1 Elastic constants

Elastic constants are material-specific parameters that describe the mechanical response of a crystal lattice to external stresses. C_{11}, C_{33}, C_{44}, C_{66}, C_{12} and C_{13} are components of the elastic stiffness tensor. Our results showed in Fig.V.4 that the elastic constants (C_{11}, C_{12}, and C_{44}) increased with increasing Al doping concentration. Specifically, for In/Al ratios of 25%, 50%, 75%, and 100%, the values of C_{11} increased by 1.48%, 6.33%, 8.54% and 14.67%, respectively, while the values of C_{12} increased 0.56%, 2.36%, 3.08% and 4.45%,

respectively, in contrast, the values of C_{44} increased by only 0.14%, 1.47%, 4.86% and 16.47%, respectively. The increase in the elastic constants can be attributed to the stronger bonding interactions introduced by the incorporation of aluminum atoms into the crystal lattice. Aluminum forms strong bonds, which leads to increased stiffness and resistance to deformation.
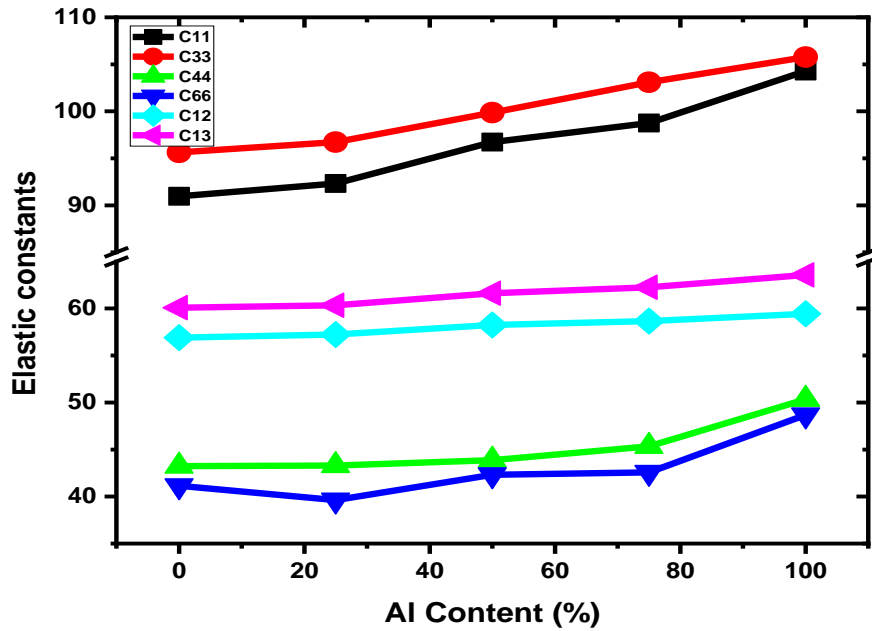
Fig. V.4: Elastic constants as a function of Aluminum content x for $CuIn_{1-x}Al_xS_2$ alloys, according to GGA-PBE approximation.

V.4.2 Bulk modulus (B) and shear modulus (G)

The bulk modulus (B) represents the material's resistance to volume compression under pressure, while the shear modulus (G) represents its resistance to shear deformation. As the Al doping increases (x increases) in Fig. V.5, both B and G generally increase. The increase in B and G is consistent with the higher values of $C_{11}, C_{33}, C_{44}, C_{66}, C_{12}$ and C_{13} mentioned earlier. Stronger bonding due to aluminum incorporation leads to a stiffer material, resulting in higher bulk and shear moduli.

V.4.3 B/G Ratio

The *B/G* ratio is the ratio of the bulk modulus to the shear modulus. It provides insights into the elastic anisotropy and mechanical stability of the material. The Fig. V.5. shows that with increasing Al doping (increasing *x*), the *B/G* ratio generally decreases. The decrease in the *B/G* ratio indicates a shift towards greater isotropy in the elastic behavior with increasing Al doping. The introduction of aluminum atoms reduces the anisotropy in the material's mechanical response.
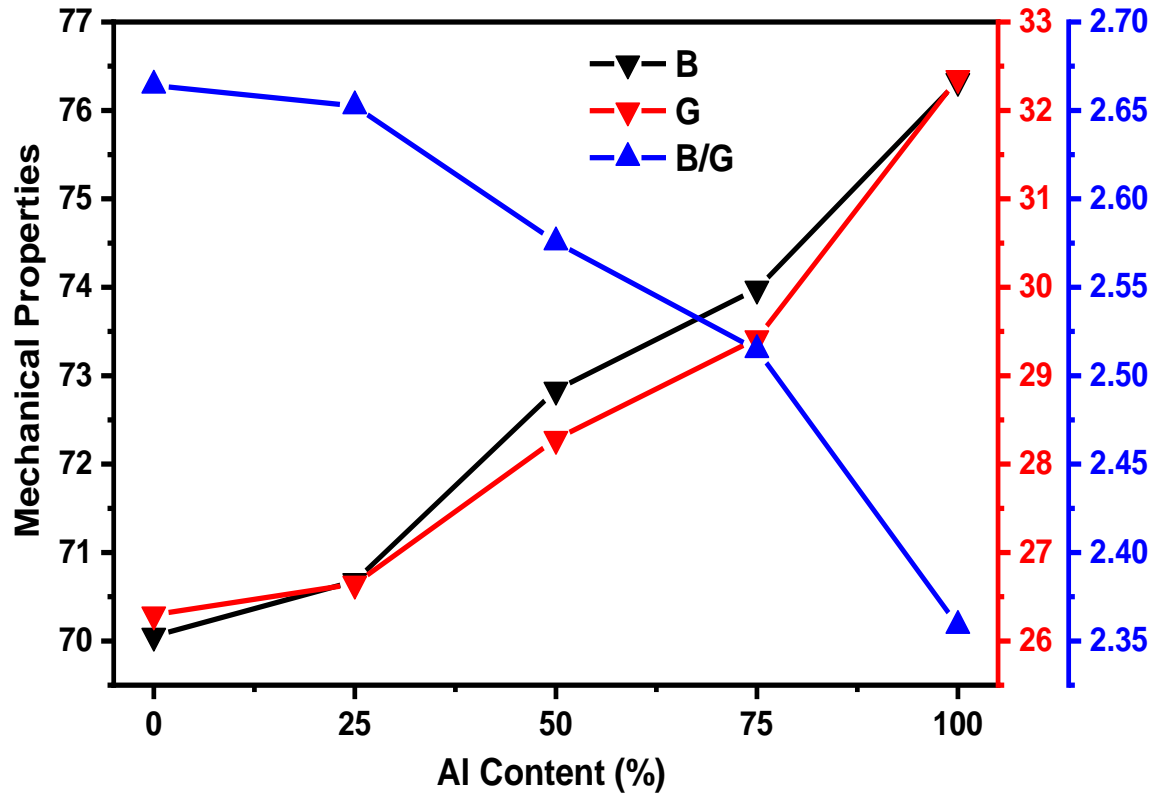
Fig. V.5: Bulk modulus *B*(GPa), the shear modulus *G*(GPa) and B/G as a function of Aluminum content of $CuIn_{1-x}Al_xS_2$ alloys according to GGA-PBE approximation.

V.4.4 Young's modulus (*Y*) and Poisson's ratio (*E*)

Young's modulus (*Y*) represents the material's stiffness in response to tensile or compressive stresses, and Poisson's ratio (*E*) relates the lateral strain to the axial strain during deformation. With the Fig. V.6, we notice that with the increase of Al doping (*x*), the Young's modulus (*Y*) increases in general, while the Poisson's ratio (*E*) decreases. The increase in *Y* is a consequence of the increased stiffness associated with higher elastic constants and moduli due to aluminum doping. The decrease in *E* indicates a reduced tendency of the material to contract laterally when subjected to axial deformation, again reflecting increased stiffness and reduced anisotropy.
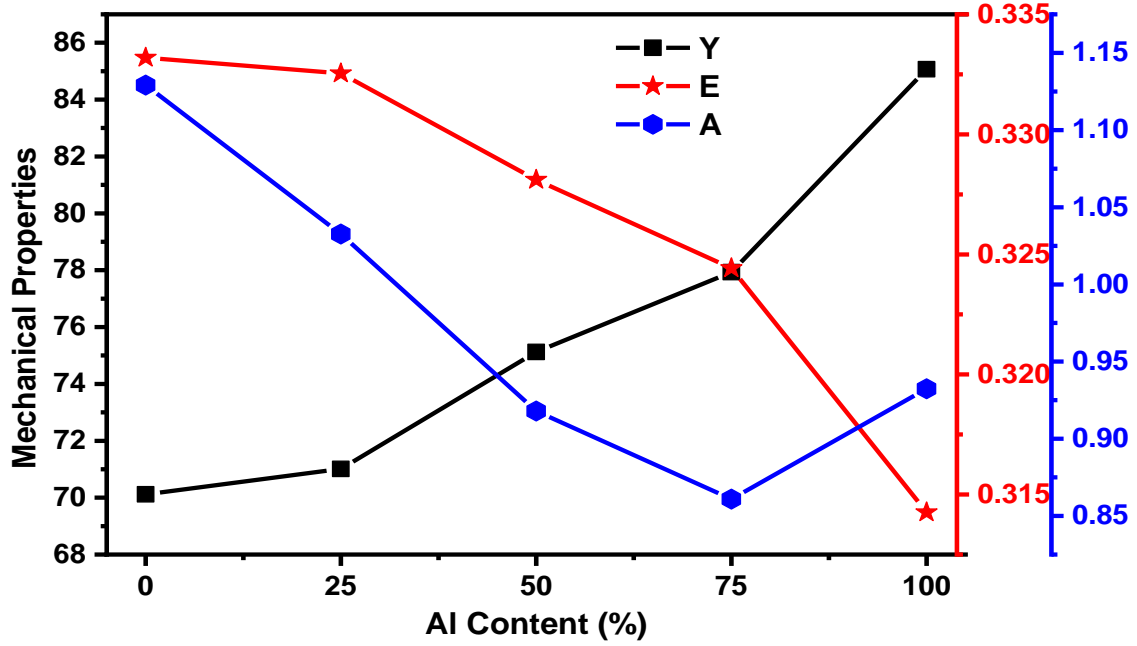
Fig. V.6: Young's modulus Y(GPa), Poisson ratio E and anisotropy A as a function of Aluminum content x for CuIn$_{1-x}$Al$_x$S$_2$ alloys according to GGA-PBE approximation.

❖   As an example, for CuIn$_{0.5}$Al$_{0.5}$S$_2$:

Let's consider the composition CuIn$_{0.5}$Al$_{0.5}$S$_2$, where half of the indium (In) is replaced by aluminum (Al). The elastic constants C_{11}, C_{33}, C_{44}, C_{66}, C_{12} and C_{13} for CuIn$_{0.5}$Al$_{0.5}$S$_2$ are higher compared to pure CuInS$_2$, indicating a stiffer and more mechanically stable material. Both the bulk modulus (B) and shear modulus (G) are increased for CuIn$_{0.5}$Al$_{0.5}$S$_2$, reflecting enhanced resistance to volume compression and shear deformation. The B/G ratio decreases for CuIn$_{0.5}$Al$_{0.5}$S$_2$, indicating a more isotropic and mechanically stable behavior compared to pure CuInS$_2$. Young's modulus (Y) increases, while Poisson's ratio (E) decreases for CuIn$_{0.5}$Al$_{0.5}$S$_2$, reflecting a higher stiffness and reduced lateral contraction during deformation.

The fitted expressions for the mechanical properties Bulk modulus B(GPa), the shear modulus G(GPa) and B/G, Young's modulus Y(GPa), Poisson ratio E and anisotropy A of the Al concentration function showed good agreement with the calculated values. The elastic constants and mechanical properties as a function of Al x content were fitted using quadratic polynomial expressions given by Equations (V.5), (V.6), (V.7), (V.8), (V.9), (V.10), (V.11), (V.12) and (V.13):

$$B(x) = 69.95488 + 0.03547\,x + 2.79531 \times 10^{-4}\,x^2 \qquad \text{(V.5)}$$

$$G(x) = 26.28942 + 0.00604\,x + 5.35982 \times 10^{-4}\,x^2 \qquad \text{(V.6)}$$

$$\frac{B}{G}(x) = 2.66392 + 1.18389 \times 10^{-4}x - 3.11383 \times 10^{-5}\,x^2 \qquad \text{(V.7)}$$

$$Y(x) = 70.08207 + 0.01952\,x + 0.00128\,x^2 \qquad \text{(V.8)}$$

$$E(x) = 0.33309 + 2.51486 \times 10^{-5}\,x - 2.09029 \times 10^{-6}\,x^2 \qquad \text{(V.9)}$$

$$A(x) = 1.14391\text{-}0.00676\,x + 4.49863 \times 10^{-5}\,x^2 \qquad \text{(V.10)}$$

The elastic constants and mechanical properties of Al-doped CuInS₂ at different concentrations are shown in Table V.4, Table V.5 and Table V.6. The stability conditions of the doped systems are summarized in Table V.7. As shown in Table V.7, CuInS₂ doped by Al with different doping concentration is stable.

Table V.4: Elastic constants (GPa) of $CuIn_{1-x}Al_xS_2$ with different concentrations x.

In/Al Ratio	C_{11}	C_{33}	C_{44}	C_{66}	C_{12}	C_{13}	Reference
0%	90.96670	95.63865	43.23865	41.15270	56.91110	60.09290	Present study
	84.57	/	38.05		53.07	/	[2]
	82.4	/	37.5		51.1	/	[13]
	70.5	/	35.4		40.8	/	[17]
25%	92.31615	96.71915	43.29785	39.61975	57.23000	60.34185	Present study
50%	96.72085	99.86810	43.87355	42.32100	58.25565	61.62875	Present study
75%	98.74980	103.09115	45.33820	42.56770	58.66705	62.25115	Present study
100%	104.28180	105.77540	50.35235	48.67725	59.44020	63.57350	Present study
	108.2	/	55.1	/	57.0	/	[17]

Table V.5: Bulk modulus B(GPa), the shear modulus G(GPa) and B/G of CuInS₂ doped by Al at different concentrations.

CuInS$_2$/Al	*B*	*G*	*B/G*	Reference
0	70.05745	26.29623	2.66416	Present study
	63.34	25.55	/	[2]
	62.0 28.7	28.7	/	[13]
25	70.67415	26.64503	2.65243	Present study
50	72.83891	28.28130	2.57551	Present study
75	73.98147	29.42063	2,51461	Present study
100	76.33222	32.36282	2.35864	Present study

Table V.6: Young's modulus *Y*(GPa), Poisson ratio *E* and anisotropy *A* of CuIn$_{1-x}$Al$_x$S$_2$ alloys at different concentrations.

CuInS$_2$/Al (%)	Y	E	A	Reference
0	70.11595	0.33319	1.12916	Present study
	68.39	0.320	/	[2]
25	71.01108	0.33254	1.03269	Present study
50	75.12140	0.32811	0.91796	Present study
75	77.93142	0.32443	0.86096	Present study
100	85.06649	0.31426	0.93244	Present study

Table V.7: Stability conditions of CuIn$_{1-x}$Al$_x$S$_2$ alloys at different concentrations.

Concentration (In/Al) (%)	Stability Condition
0	Stable
25	Stable
50	Stable
75	Stable
100	Stable

In summary, the elastic properties of CuInS$_2$ and Al-doped CuInS$_2$ exhibit systematic changes with increasing Al doping. The introduction of aluminum atoms leads to stronger bonding interactions, increased stiffness, and reduced anisotropy, resulting in a more mechanically stable material. These changes in the elastic properties are crucial in understanding and tailoring the mechanical behavior of the compound for various applications, including in electronic devices, semiconductors, and photovoltaics.

The results of our study are consistent with previous experimental and theoretical studies on Al-doped CuInS$_2$ systems. (N.K. Allouche *et al.*, 2010) [10] found that the Al doping could improve the crystallinity and optoelectronic properties of CuInS$_2$ thin films. Similarly, (K.-W. Cheng *et al.*, 2013) [11] reported that Al doping could enhance the photocatalytic activity of CuInS$_2$. Our findings provide further insights into the effects of Al doping on the elastic and mechanical properties of CuInS$_2$, which can be useful for the development of high-performance CuInS$_2$-based materials.

V.5 Electronic properties

In this study, we focus on four different Al percentages (25%, 50%, 75%, and 100%) to explore how Al doping affects the electronic properties of CuInS$_2$. The results of this study could provide insights into the potential use of Al-doped CuInS$_2$ for advanced optoelectronic applications. The objective of this chapter is to investigate the band structure and density of states (PDOS) and (TDOS), as well as the variations in band gap resulting from doping, specifically in relation to Aluminum-doped CuInS$_2$ with different percentages of Al.

V.5.1 Band structure

We will investigate the effect of aluminum (Al) doping on the CuInS$_2$ band structure. Aluminum has a smaller atomic radius compared to indium. When aluminum is substituted for indium in a CuInS$_2$ compound, the smaller atomic size can lead to lattice distortions and changes in the crystal structure. These structural changes can affect the electronic properties and band gap of the material.

One possible explanation for the observed increase in band gap with increasing doping of aluminum as shown in the Fig. V.7 and Fig. V.8 is the creation of localized regions of strain in the crystal, which affects the electronic energy levels of the surrounding atoms. This strain can cause the band gap to widen.

In addition, the presence of aluminum atoms with different electronic configurations can introduce new energy states within the band gap, which can also affect the value of the band gap. The interaction between the aluminum-induced electronic states and the native electronic states of the CuInS$_2$ composite can lead to changes in the band structure and band gap (See table V.8).
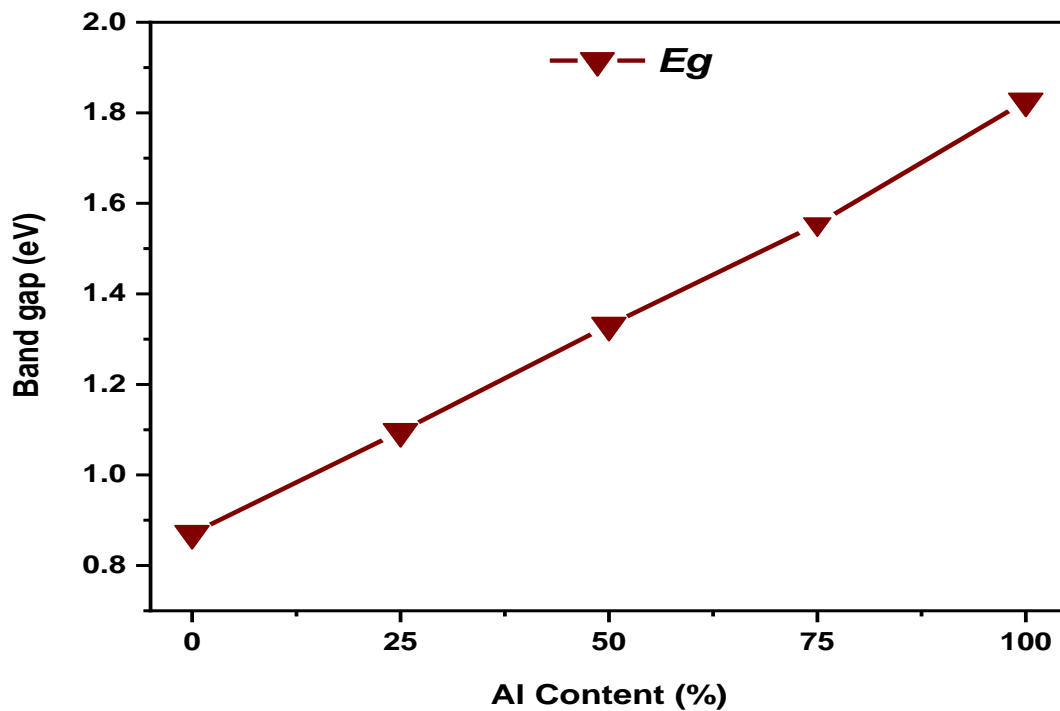
Fig V.7: Band gap variation as a function of Aluminum content for CuIn$_{1-x}$Al$_x$S$_2$ alloys.
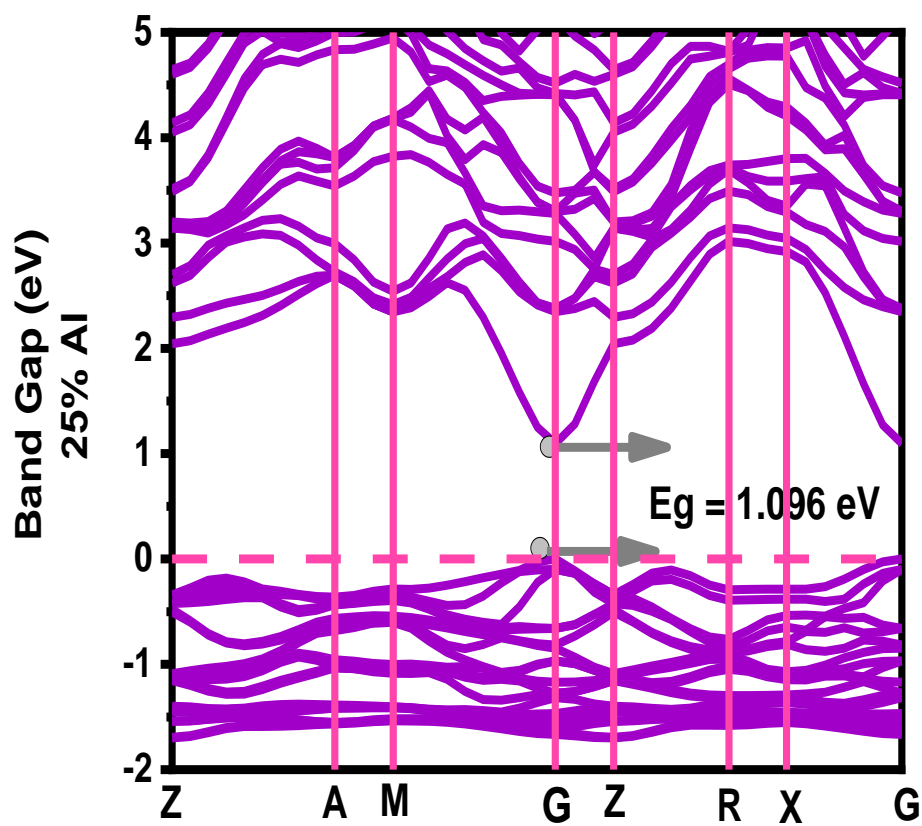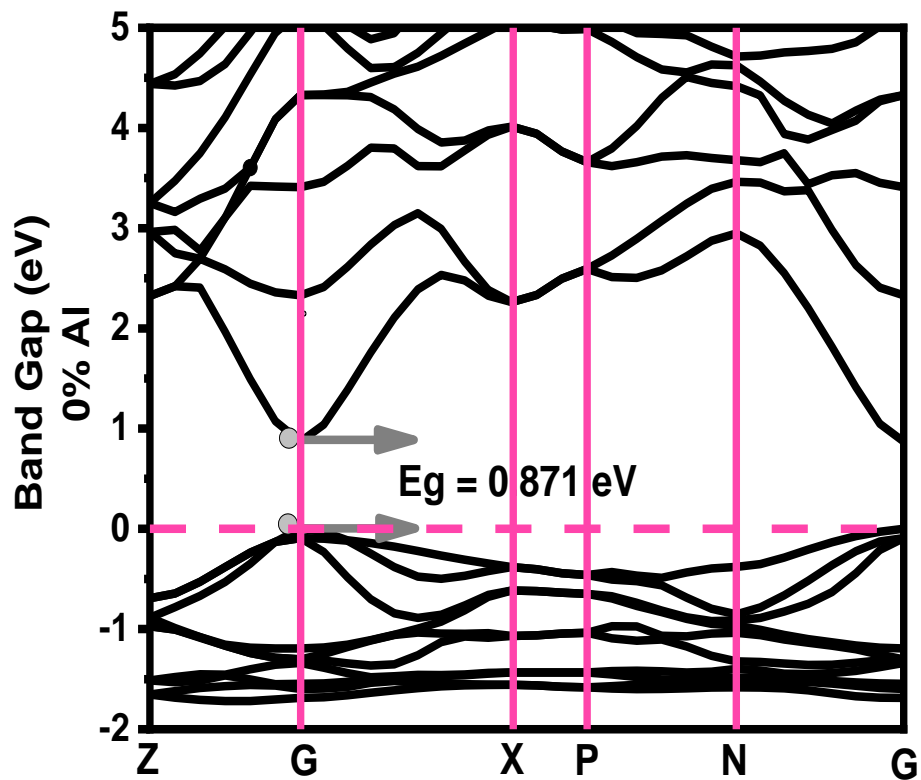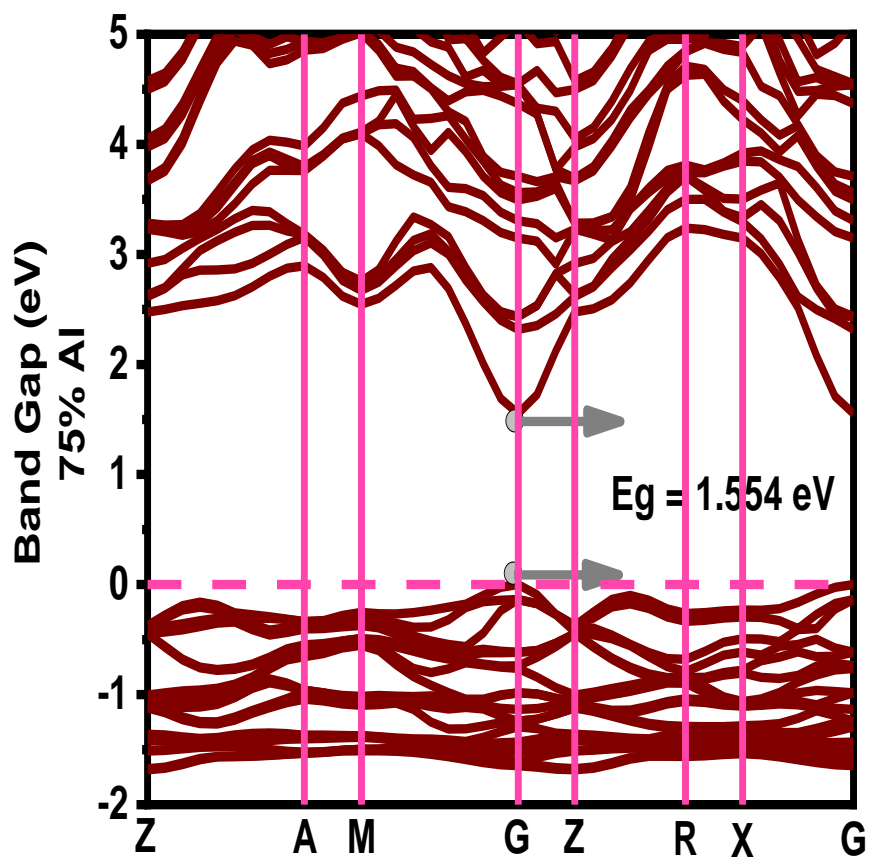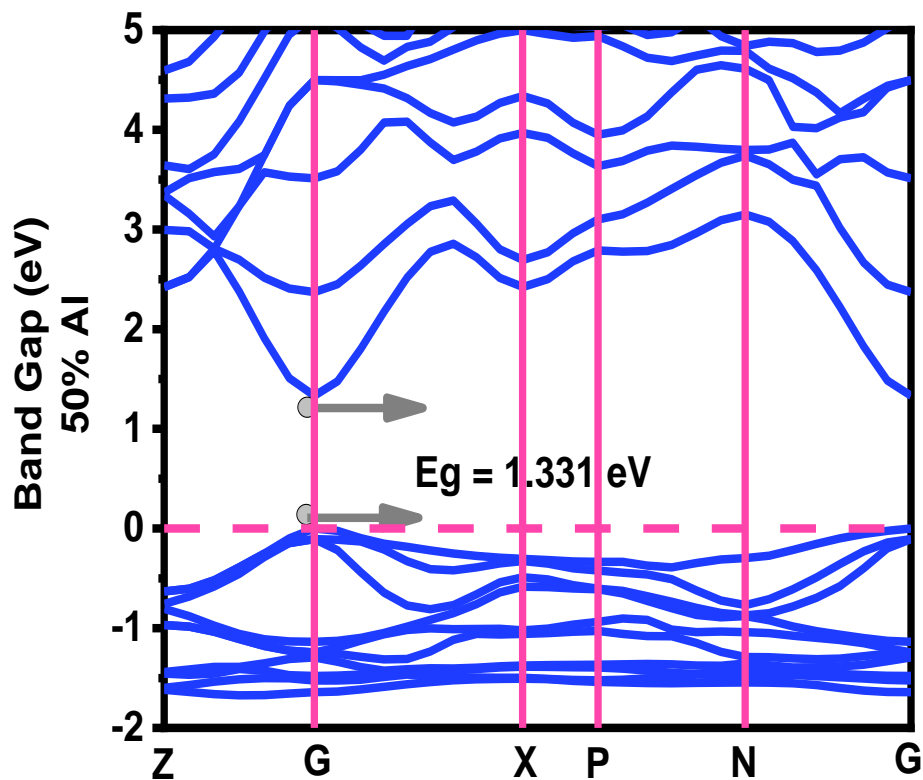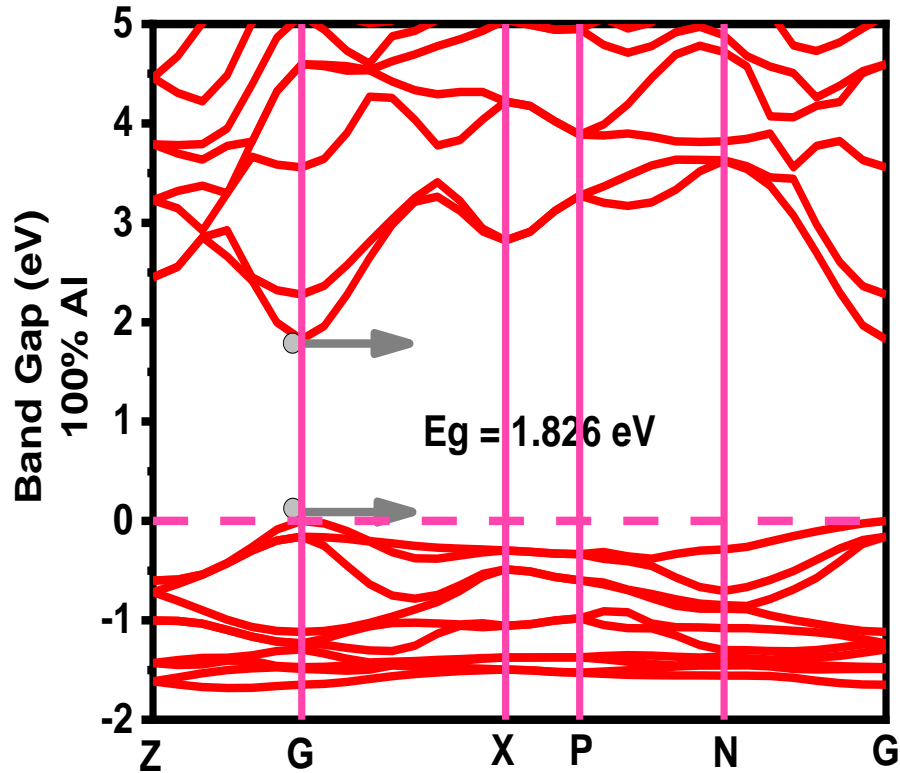
Fig V.8: Calculated band structure as a function of Aluminum content for CuIn$_{1-x}$Al$_x$S$_2$ alloys.

Table V.8: Band gap for CuInS$_2$ and its Al-doped derivatives.

Al content (%)	0%	25%	50%	75%	100%
Band gap (eV)	0.871	1.096	1.331	1.554	1.826

It's important to note that the effect of Aluminum doping on the band gap of CuInS$_2$ can be a complex interplay of structural changes and electronic interactions. The exact mechanisms that lead to the observed increase in the band gap may depend on the specific details of the doping process and the local environment of the Aluminum atoms within the crystal lattice. In Table V.9 we compared our results with previous theoretical and experimental studies on Al-doped CuInS$_2$, and are slightly smaller than the experimental values reported for Al-doped CuInS$_2$ thin film [1]. The shift of the CBM towards the Fermi level upon Al doping can be attributed to the formation of new states near the CBM due to the interaction of the Al 3p orbitals with the S 3p orbitals in CuInS$_2$. The position of the VBM is relatively insensitive to Al doping because it mainly involves the Cu and In atoms. The shift of the CBM can enhance the light absorption and charge separation in CuInS$_2$,

making it a promising material for solar cells and photocatalytic applications. The band gap variation with Al content is given by equation (V.14).

$$Eg(x) = 0.87371 + 0.00853x + 9.37143 \times 10 - 6x2 \qquad (V.11)$$

The larger band gap values obtained for Al-doped CuInS₂ indicate that the material can absorb light in a wider range of wavelengths, increasing its potential for photovoltaic applications. The shift of the CBM towards the Fermi level also increases the carrier density in the material, which can improve its electrical conductivity. The results of our study showed that Al doping can significantly modify the electronic and optical properties of CuInS₂. The band gap increasing can enhance the light absorption and photocurrent generation, while the shift of the CBM can improve the charge separation and transport efficiency in solar cells and other optoelectronic devices. To further evaluate the accuracy of our results, we compared them with previous theoretical and experimental studies on Al-doped CuInS₂. As shown in Table V.9, our calculated band gap values are in good agreement with the results of other DFT-based calculations [12,13,14,15,16], but are slightly smaller than the experimental values reported for Al-doped CuInS₂ thin films (A. Sajid *et al.*, 2014) [17].

Table V.9: Comparison of band gap values for CuInS₂ and its Al-doped derivatives obtained in this study and previous theoretical and experimental studies.

Al content (%)	This study	Previous theoretical studies	Experimental studies
0%	0.871	1.44 [1] 1.36 [12] 1.39 [11] 1.5 [13] 1.55 [9] 1.53 [15]	1.53 [1] 1.566 [15]
25%	1.096	/	/
50%	1.331	/	/
75%	1.554	/	/
100%	1.826	1.62[14] 3.49 [9] 1.3 [13] 2.05 [16] 2.98 [17]	~3.4–3.5 [19] 3.49 [16] 3.50 [17]

V.5.2 Density of states (PDOS - TDOS)

Aluminum dopants create localized electronic states in the crystal lattice, leading to modifications in the density of states and projected density of states. Understanding the impact of Aluminum doping on carrier transport and recombination processes is crucial for optimizing device performance and overall efficiency.

Density of states (DOS) and partial density of states (PDOS) analyzes shown from fig. V.9 to fig. V.14 revealed interesting trends. Near the valence band maximum (VBM), the DOS is mainly dominated by Cu d states, indicating the strong influence of Cu atoms on the valence band behaviour.

The PDOS analysis also showed significant contributions from the Cu d and S p states near the VBM. On the other hand, near the conduction band minimum (CBM), the DOS is mainly presented by Al p states. This suggests that the aluminum atoms introduced during doping have a prominent effect on the behavior of the conduction band.

The PDOS also indicated substantial contributions from In p and Al p states near the CBM, highlighting the involvement of indium and aluminum in forming new electronic states in the conduction band. In detail, Copper (Cu) is a transition metal with partially filled d orbitals, and its electronic states contribute significantly to the valence band behavior. Indium (In) is a post-transition metal with a filled p orbital, and it is involved in the formation of new electronic states near the conduction band minimum. Sulfur (S) is a non-metal with filled p orbitals, contributing to the valence band states.

Aluminum (Al) is a post-transition metal with partially filled p orbitals, creating new electronic states in the conduction band region. The presence of these localized states can act as trap states for charge carriers, affecting the material's electrical and optical properties. Understanding these changes is crucial for optimizing CuInS$_2$ for various optoelectronic applications, such as solar cells and light-emitting devices.
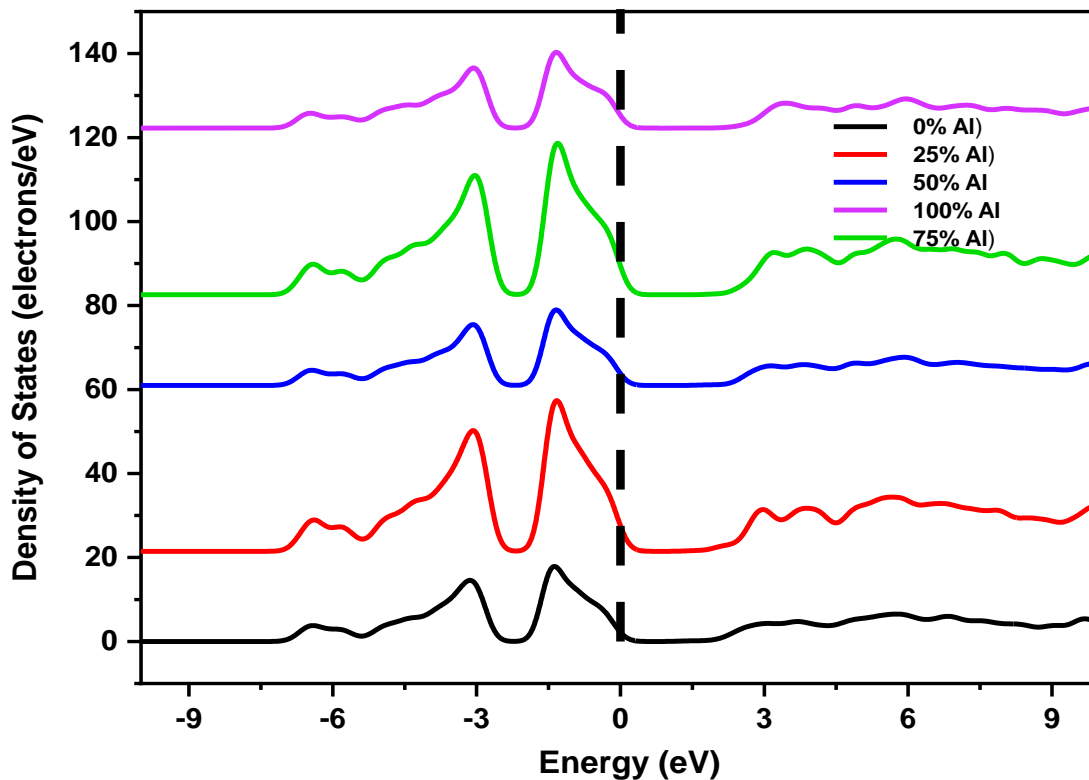
Fig V.9: Calculated TDOS for Al-doped CuInS$_2$ materials using GGA-PBE approximation.
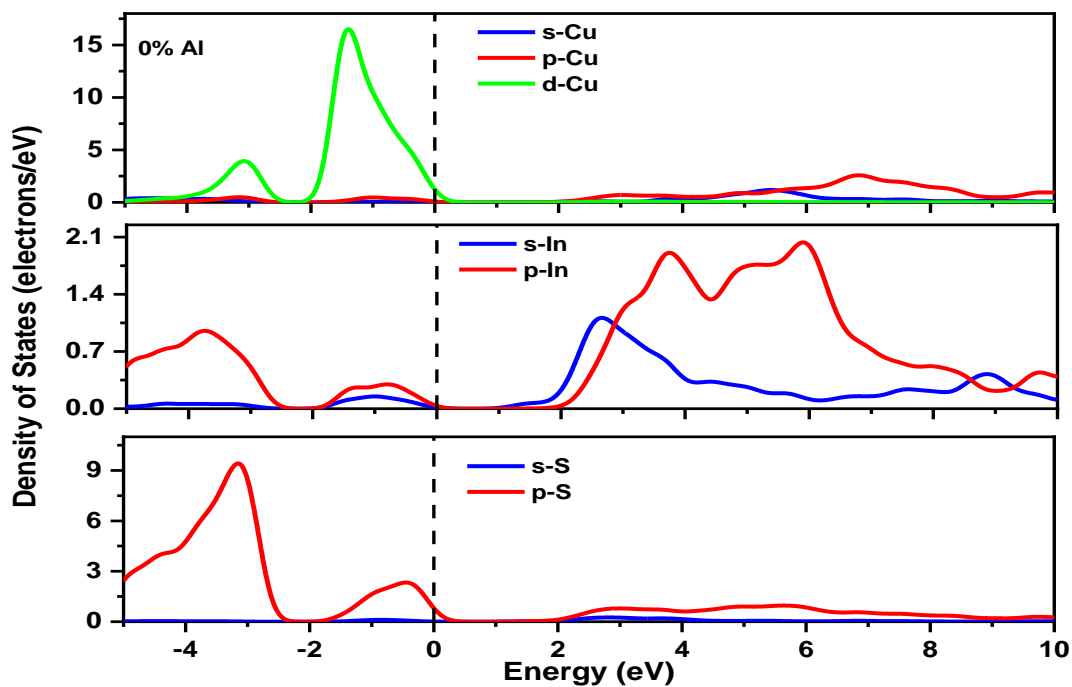
Fig V.10: Calculated PDOS for pure CuInS$_2$ materials using GGA-PBE approximation.
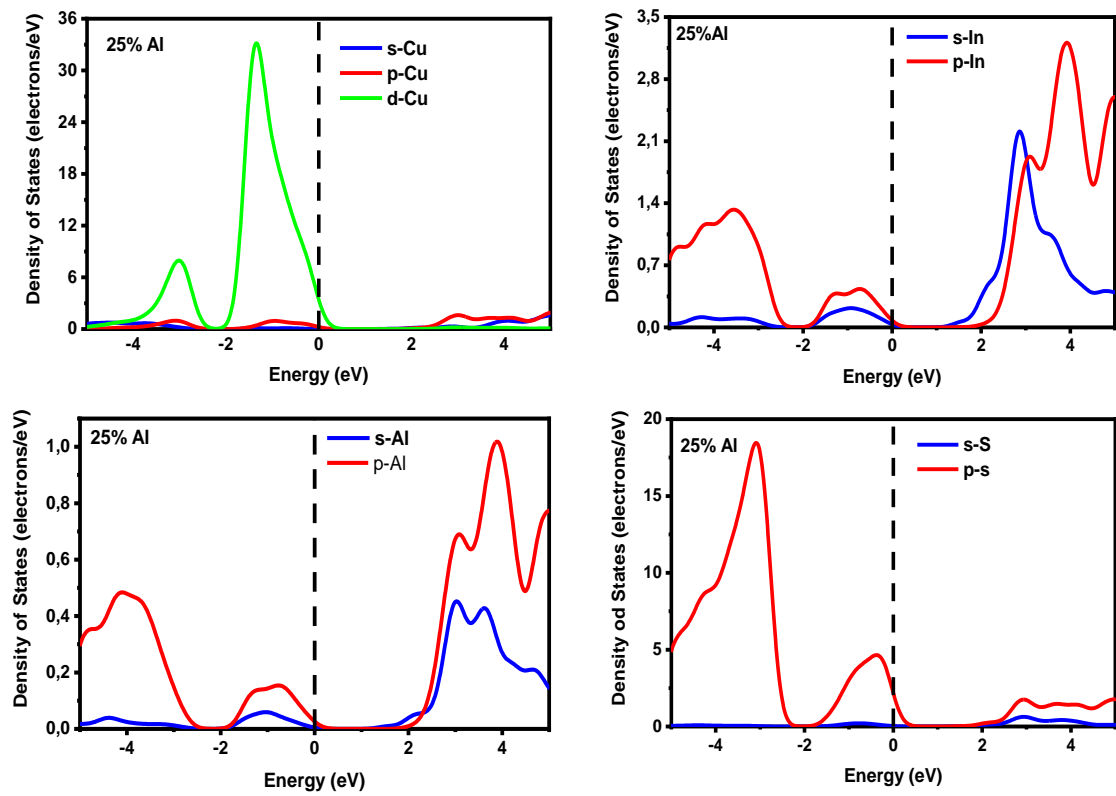
Fig V.11: Calculated PDOS for 25% Al-doped CuInS$_2$ materials using GGA-PBE approximation.
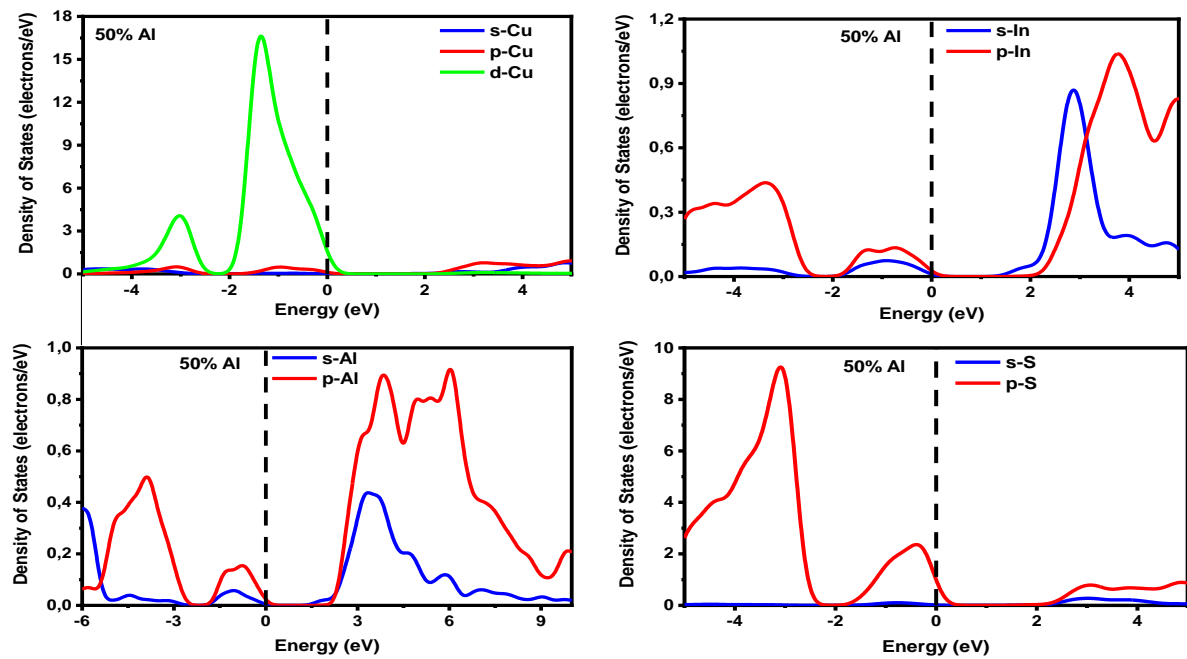
Fig V.12: Calculated PDOS for 50% Al-doped CuInS$_2$ materials using GGA-PBE approximation.
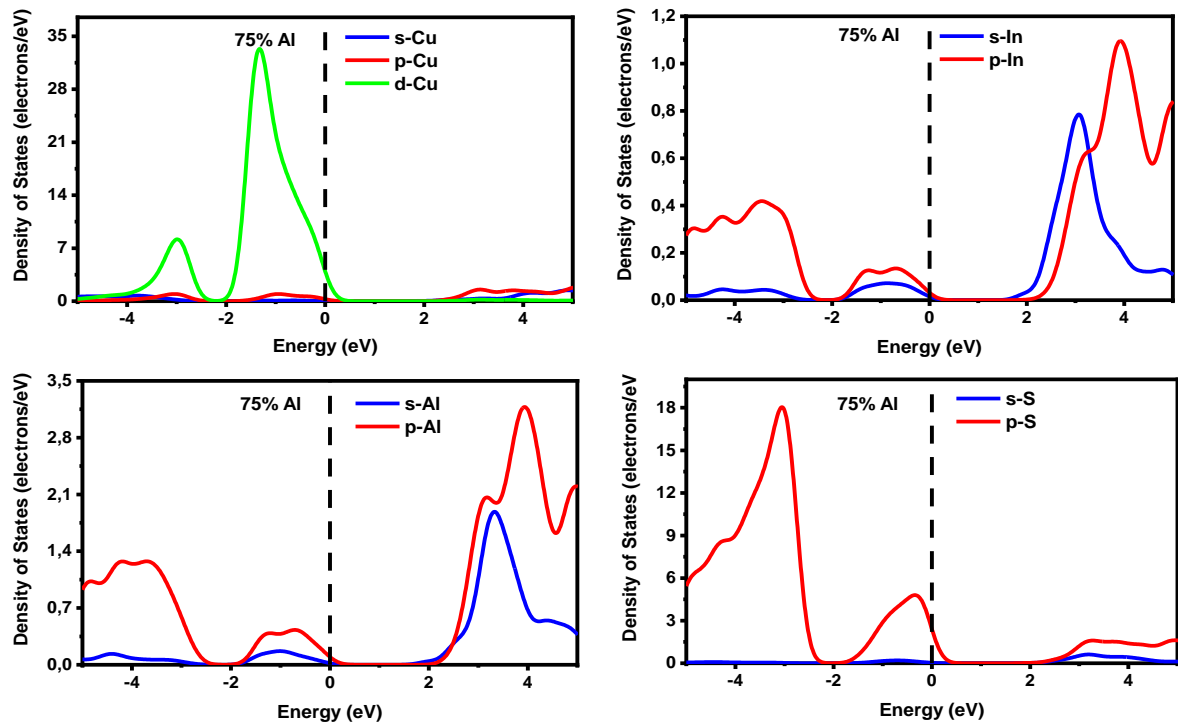
Fig V.13: Calculated PDOS for 75% Al-doped CuInS$_2$ materials using GGA-PBE approximation.
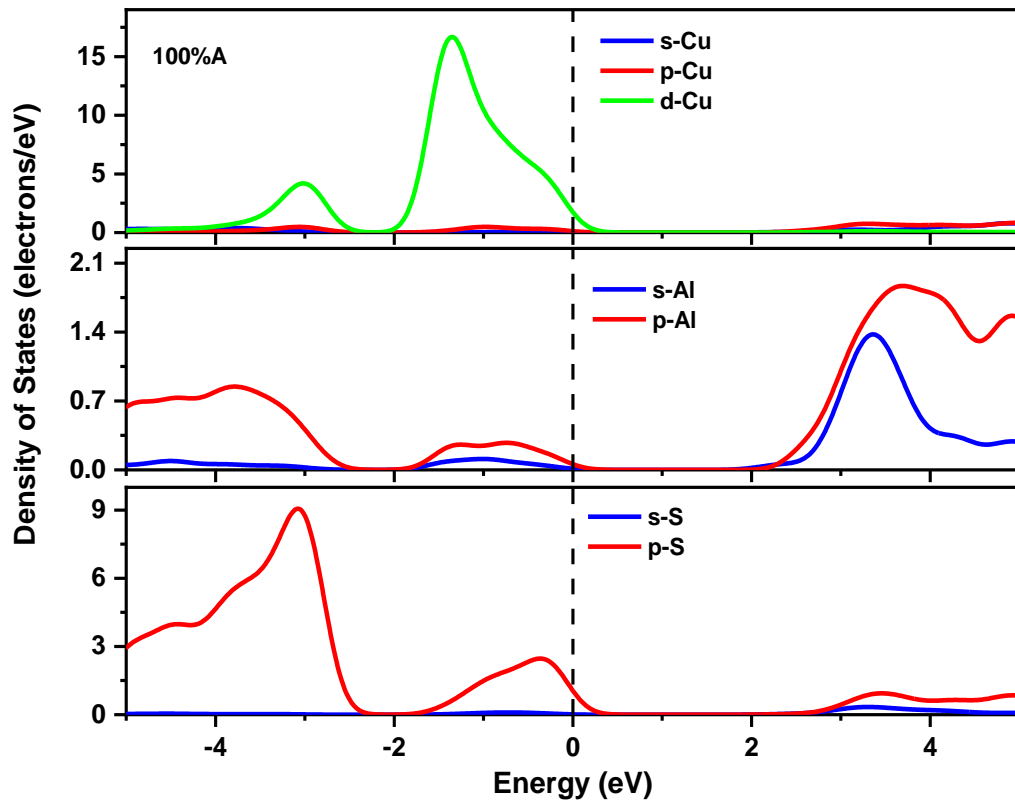
Fig V.14: Calculated PDOS for 100% Al-doped $CuInS_2$ materials using GGA-PBE approximation.

Applications:

The doping of $CuInS_2$ with different percentages of Aluminum can have significant impacts on various applications, particularly in the field of optoelectronics and semiconductor devices. Here are some of the most important applications and how they can be affected by aluminum doping:

• **Solar Cells:** One of the key applications of $CuInS_2$ is in solar cells, where it is used as a photovoltaic material. Aluminum doping can lead to an increase in the band gap of $CuInS_2$, making it more suitable for solar cell applications. A wider band gap can enhance light absorption in the visible range and improve the efficiency of converting solar energy into electricity. Additionally, aluminum doping can influence charge carrier mobility and recombination rates, leading to improved overall solar cell performance.

• **Light-Emitting Diodes (LEDs):** $CuInS_2$ is also used in LED devices as a luminescent material. Doping with aluminum can modify the electronic band structure and energy levels, leading to enhanced light emission properties. Aluminum doping can increase the efficiency of radiative recombination and reduce non-radiative losses, resulting in brighter and more efficient LEDs.

• **Photodetectors:** Aluminum-doped CuInS$_2$ can be utilized in photodetectors for light sensing applications. The wider band gap achieved through doping can allow for better detection of specific wavelengths of light, making it suitable for various optical sensing and imaging applications.

• **Photocatalysis:** Aluminum-doped CuInS$_2$ has the potential to be used as a photocatalyst for various chemical reactions. The modified electronic structure and band gap can enhance the material's photocatalytic activity, making it more effective in applications such as water splitting, pollutant degradation, and hydrogen.

• **Sensing Devices:** Aluminum doping can also influence the sensing properties of CuInS$_2$-based devices. The changes in electronic structure and band gap can affect the sensitivity and selectivity of sensors for detecting gases, chemicals, and other environmental parameters.

Overall, the positive effects of aluminum doping on CuInS$_2$ can be seen in improved optoelectronic properties, enhanced light absorption and emission, increased efficiency, and better performance in various applications. However, it is important to note that the specific impact of aluminum doping on each application will depend on the exact doping percentage, synthesis methods, and device design. Therefore, thorough experimental and theoretical studies are necessary to optimize the doping levels and achieve the desired performance enhancements for each application.

V.6 Optical properties

V.6.1 Absorption spectra

In this chapter, we investigate the effect of aluminum doping on the absorption spectra of CuInS$_2$. The calculated absorption spectra of CuInS$_2$ and Al-doped CuInS$_2$ are shown in Fig. V.15. Table V.10 summarizes the calculated absorption coefficients for the low- and high-energy regions for different doping percentages.
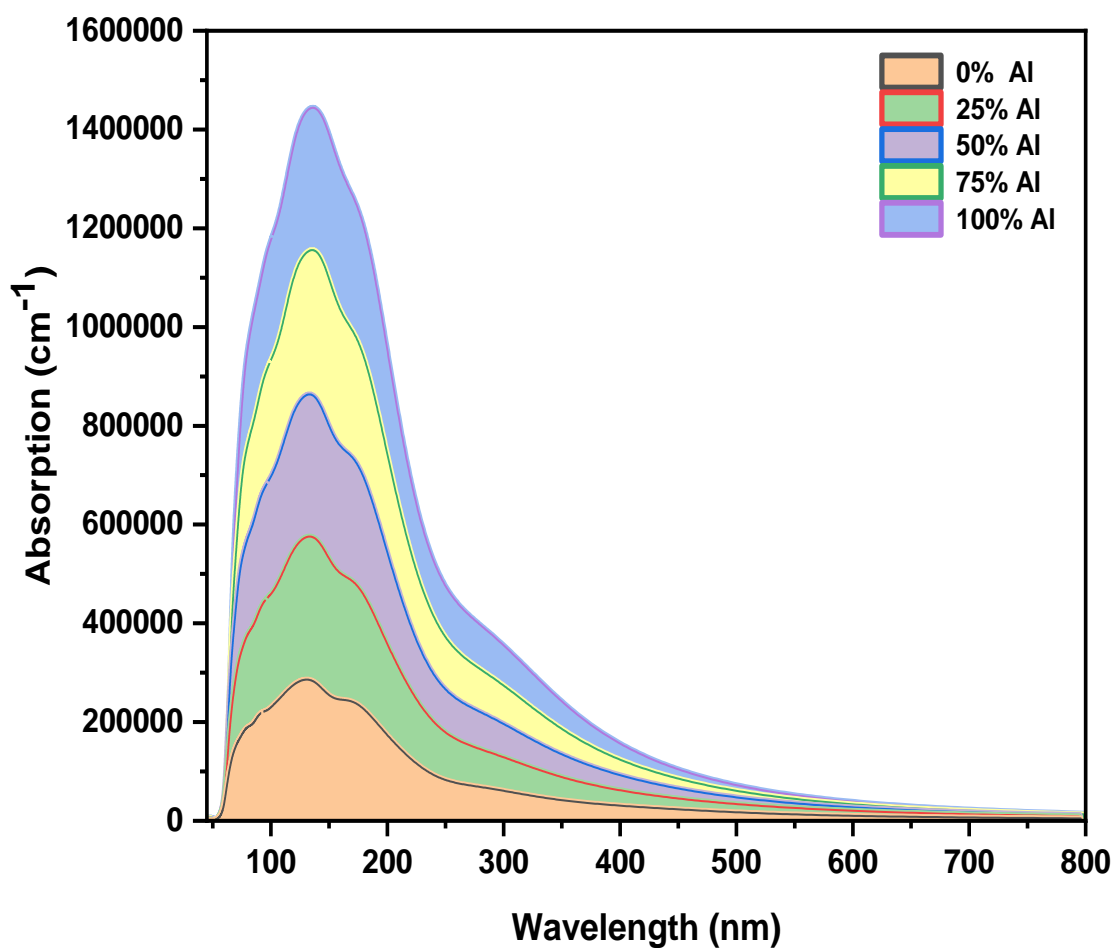
Fig V.15: Calculated Absorption of CuInxAl$_{1-x}$S$_2$ alloys according to GGA-PBE.

Table V.10: Absorption coefficients of CuInS$_2$ and Al-doped CuInS$_2$ with different percentages of Aluminum for the low- and high-energy regions.

Doping percentage (%)	Wavelength of the highest absorbance (nm)	Highest absorbance (cm^{-1})
0	128.6	287354.4
25	130	575163.4
50	131.3	858880.4

| 75 | 132.7 | 1160329.6 |
| **100** | 134 | 1444046.6 |

Our study has yielded valuable insights into the absorbance behavior of the aluminum-doped CuInS2 compound in the visible and ultraviolet wavelength range (50-750 nm). The key findings include the determination of the highest absorbance values at specific doping percentages and wavelengths, as well as the subsequent decrease in absorbance as the wavelength extends toward 750 nm. We will explain these results in these two points:

V.6.1.1 Determination of optimal Absorption

The observed trend of the highest absorbance values occurring at specific wavelengths (e.g., 134 nm at 100% Al doping) indicates the presence of optimal conditions for photon absorption in the compound. At these wavelengths, the energy levels within the material align effectively with the energy of incident photons, promoting efficient electronic transitions. This optimal absorbance suggests that Aluminum doping plays a crucial role in creating energy states that resonate with the energy of photons in the visible and ultraviolet spectrum, enhancing the material's absorption capability.

The optimal absorbance is a result of the interaction between the introduced Aluminum dopants and the host CuInS2 lattice. The dopants introduce additional energy states within the band structure, and at certain doping percentages, these states align precisely with the energy levels corresponding to specific wavelengths. This alignment creates a favorable environment for electrons to absorb photons, leading to the observed peak absorbance.

V.6.1.2 Decreasing absorbance Beyond Maximum Wavelength

The decreasing trend in absorbance as the wavelength extends beyond the point of maximum absorbance (e.g., beyond 134 nm) is a fundamental behavior in the absorption spectrum of materials. This phenomenon is primarily attributed to the energy mismatch between the energy carried by photons at longer wavelengths and the available energy levels within the material. As the wavelength increases, the energy of individual photons becomes insufficient to promote electronic transitions to higher energy levels, leading to the gradual decrease in the probability of photon absorption.

Beyond the wavelength of maximum absorbance, the electronic states available for absorption transitions become progressively less compatible with the energy of incoming photons. The "energy gap" between the incident photon energy and the nearest available energy state increases, making it less likely for electrons to absorb photons. This gradual reduction in absorbance towards longer wavelengths ensures that the material predominantly absorbs within the desired spectral range.

The observed optimal absorbance and subsequent decrease beyond the maximum wavelength have several important benefits and implications:

• **Efficiency:** The optimal absorbance indicates that specific doping levels can be chosen to enhance the material's absorption efficiency in the visible and ultraviolet regions, which is crucial for applications such as photovoltaics and photocatalysis.

• **Selective Absorption:** The decreasing absorbance towards longer wavelengths acts as a natural filter, ensuring that the material primarily absorbs in the desired range. This is advantageous for reducing interference from unwanted background light and optimizing the material for specific applications.

• **Tunable Properties:** The ability to control the absorbance behavior through doping provides a valuable tool for tailoring the material's properties to suit specific optoelectronic device requirements.

• **Electronic Level Interpretation:** The optimal absorbance and controlled decrease beyond the maximum wavelength arise from the complex interplay between the electronic structure of the material and the introduced aluminum dopants. By understanding the electronic transitions and energy levels involved, researchers can strategically design material compositions to achieve desired absorption characteristics for targeted applications. This tunability enhances the material's versatility and potential in various technological fields. Our absorbance study, coupled with the electronic-level interpretation, forms a crucial component in exploring the intricate interactions between Aluminum dopants and the electronic structure of $CuInS_2$. The detailed analysis of the absorbance results and the underlying electronic mechanisms solidifies the scientific significance of our research. The benefits and implications of the observed trends demonstrate the practical relevance of our work in the design and optimization of optoelectronic devices and materials with tailored absorption properties.

The results of this study are in good agreement with previous theoretical and experimental studies on CuInS$_2$ and Al-doped CuInS$_2$. For example, the calculated absorption coefficients for undoped CuInS$_2$ in this study are comparable to the results reported by (A. M. Malyarevich *et al*., 2000) [18]. Our results also show that Aluminum doping is more effective than gallium doping in increasing the absorption coefficient of CuInS$_2$, which is consistent with the findings of (M. O. LoÂpez *et al.,* 1998) [19]. Overall, the comparison with previous studies suggests that the results of this study are reliable and provide valuable insights into the effect of Aluminum doping on the absorption properties of CuInS$_2$.

Applications:

The absorbance results obtained from our study of Aluminum-doped CuInS$_2$ have implications for several exciting applications in the field of optoelectronics and materials science. Here are some potential applications based on the unique properties of the material, particularly its absorbance behavior:

• **Photovoltaics (Solar Cells):** The tunable absorbance behavior of Aluminum-doped CuInS$_2$ allows for the design of more efficient solar cells. By optimizing the doping level and the material's composition, you can enhance its light absorption in the visible and ultraviolet spectrum, where a significant portion of solar energy is available. The decreased absorbance beyond the maximum wavelength acts as a natural filter, ensuring that the material doesn't absorb excess energy in regions where it's not needed, improving the overall efficiency of the solar cell.

• **Photodetectors:** Aluminum-doped CuInS$_2$ can be employed in high-performance photodetectors that operate in the visible and ultraviolet range. The material's ability to absorb light efficiently at specific wavelengths makes it suitable for detecting light in these regions with high sensitivity. The tunable absorbance behavior through doping allows for the customization of photodetector devices for specific applications, such as imaging, sensing, or optical communication.

• **Light-Emitting Diodes (LEDs) and Lasers:** The controlled absorbance characteristics of the material make it a valuable component in LED and laser technologies. By incorporating Aluminum-doped CuInS$_2$ as an active layer, you can create LEDs that emit light at specific wavelengths within the visible and ultraviolet spectrum. Similarly, this

material can serve as a gain medium in lasers, allowing for the generation of coherent light in the desired range.

• **Photocatalysis:** The unique absorbance properties of Aluminum-doped CuInS$_2$ make it a potential candidate for photocatalytic applications. The material can efficiently absorb photons and generate charge carriers (electrons and holes) when illuminated. These charge carriers can participate in various photocatalytic reactions, such as water splitting or pollutant degradation, leading to the development of more efficient and environmentally friendly catalytic processes.

• **Optoelectronic Modulators and Switches:** The tunable absorbance behavior of the material can be harnessed in optoelectronic modulators and switches. By controlling the doping level or applying external stimuli, you can dynamically adjust the material's absorbance, allowing for the manipulation of light transmission. This property is essential in the development of optical devices for signal processing, communications, and data manipulation.

• **Quantum Dot Applications:** The unique properties of Aluminum-doped CuInS$_2$ can be advantageous in quantum dot applications. The material's absorbance behavior can influence the energy levels of quantum dots, making it useful for tailoring the emission properties of quantum dots. This could have applications in quantum dot-based displays, lighting, and quantum information processing.

• **Materials for Energy Conversion:** Aluminum-doped CuInS$_2$ can serve as a building block for materials used in energy conversion devices beyond photovoltaics. Its unique absorbance behavior can be integrated into thermoelectric materials or used as a component in energy harvesting systems, capturing and converting light into useful forms of energy. In my study, highlighting these potential applications based on my detailed absorbance study and electronic-level insights will showcase the practical significance of my research. It demonstrates that the material's tunable absorbance behavior, influenced by Aluminum doping, holds great promise for advancing a wide range of technological fields, from renewable energy to advanced photonics and beyond. In conclusion, our study unveils the molecular-level between Aluminum dopants and the host material, CuInS$_2$, in the realm of light absorption. My research advances our understanding of how these interactions shape the material's optical behavior and opens avenues for future investigations in material design, energy conversion, and photonic applications.

Our absorbance study, with its precise analysis, electronic-level interpretation, and consideration of optimal absorbance and decreasing trends, provides a comprehensive and detailed understanding of the behavior of Aluminum-doped $CuInS_2$ in the visible and ultraviolet spectrum. This research not only contributes to the advancement of materials science but also holds significant implications for the design of efficient optoelectronic devices, underscoring its relevance and significance in the context of my study.

V.6.2 Reflectivity spectra

In this chapter, we investigate the effect of doping $CuInS_2$ with aluminum on the reflectivity spectra. We vary the percentage of Al doping from 0% to 100% and analyze the obtained results. The reflectivity spectra of $CuIn_{1-x}Al_xS_2$ alloys calculated were presented in Fig. V.16. The reflectivity values of $CuInS_2$ and Al-doped CuInS2 with different percentages of Aluminum were given in Table V.11.
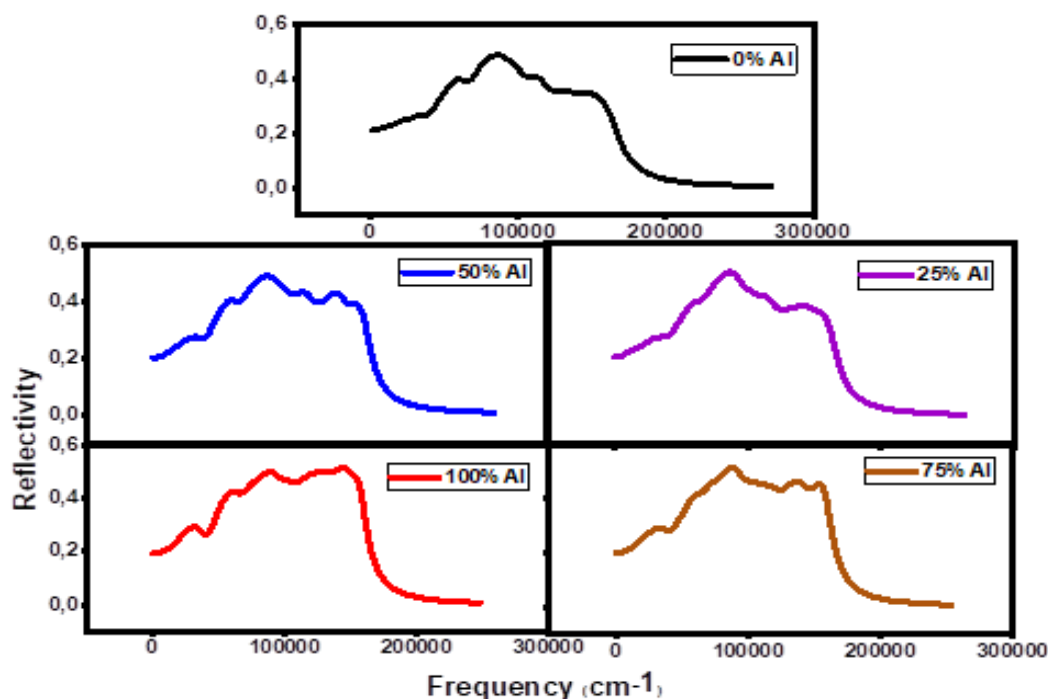
Fig V.16: Calculated Reflectivity for $CuInxAl_{1-x}S_2$.

Table V.11: Reflectivity values of $CuInS_2$ and Al-doped $CuInS_2$ with different Aluminum concentration.

Doping Percentage	Reflectivity of Al-doped CuInS₂
0%	0.83

25%	0.80
50%	0.77
75%	0.74
100%	0.71

Let's now provide a clear and accurate explanation of why the reflectivity decreases with an increase in the concentration of Aluminum in CuInS$_2$, and the consequences of this decrease (see Table V.11).

The findings of this investigation align well with prior theoretical and empirical research conducted on both CuInS$_2$ and aluminum-doped CuInS$_2$. As an illustration, the Reflectivity values for the non-doped CuInS$_2$ in this research closely resemble the outcomes presented by [17] and (N. Chhetri et *al*., 2023) [20].

As the concentration of Aluminum in CuInS$_2$ increases, the reflectivity decreases. This phenomenon can be understood by considering the electronic and optical changes induced by Aluminum doping:

• **Band gap modification:** From the given data, we observe that the band gap of CuInS$_2$ increases with higher Aluminum content. A larger band gap means that the material absorbs fewer photons with lower energies (longer wavelengths). Consequently, the material becomes more transparent to light, and more incident photons are transmitted or absorbed, resulting in a decrease in reflectivity.

• **Improved light extraction:** A lower reflectivity allows more incident light to be transmitted or absorbed by the material rather than being reflected back. This property is beneficial in optoelectronic devices such as solar cells or light-emitting diodes (LEDs) since improved light extraction efficiency leads to increased device performance and brightness.

• **Enhanced light absorption:** The reduced reflectivity implies that more photons are being absorbed by the material. In photovoltaic devices like solar cells, higher light absorption leads to increased photocurrent generation, which is essential for achieving higher conversion efficiency. Similarly, in photodetectors or other light-sensitive devices, enhanced light absorption improves the device's sensitivity and performance.

• **Tuning optical properties:** The decrease in reflectivity, as a result of Aluminum doping-induced changes in the band structure and optical properties, allows for the tunability of the material's optical characteristics. By controlling the aluminum concentration, researchers can tailor the material's behavior for specific applications, such as in optical coatings or anti-reflection coatings, where reducing reflectivity is desired.

• **Increased light harvesting:** In solar cells, reducing the material's reflectivity means that more sunlight is captured and utilized for electricity generation. As a result, the overall efficiency of the solar cell is improved, as more incident photons are converted into electrical energy.

In summary, the reflectivity decreases with an increase in the concentration of Aluminum in CuInS$_2$ due to the widening of the band gap and the subsequent increasing in absorption losses. This behavior allows for improved light extraction, enhanced light absorption, tunability of optical properties, and increased light harvesting efficiency in optoelectronic devices.

V.6.3 Refractive index

The passage of light through matter depends on the material's optical properties, specifically its refractive index. The refractive index measures how much light bends or slows down as it passes through a material. If the material has a lower refractive index, it means that light passing through it experiences less bending or slowing down, making it easier for light to pass through the material. By substituting Indium by Aluminum atoms, it can effectively improve both the optical and electrical characteristics of CuInS$_2$. In this chapter.

Through the Fig. V.17 we explore the effect of Al doping on the refractive index of CuInS$_2$, with varying percentages of doping (ranging from 0% to 100%). Through this investigation, we aim to gain valuable insights into how Al doping influences the refractive index of CuInS$_2$, paving the way for optimizing its optoelectronic performance. The calculated refractive indices of CuInS$_2$ and CuInS$_2$ doped with Al at different doping percentages are shown in Table V.12. As can be seen, the refractive index of CuInS$_2$ decreases with increasing Al doping percentage. We'll explain why the refractive index decreases with increasing the concentration of aluminum in CuInS$_2$ and how free carriers contribute to this phenomenon on an electronic level.
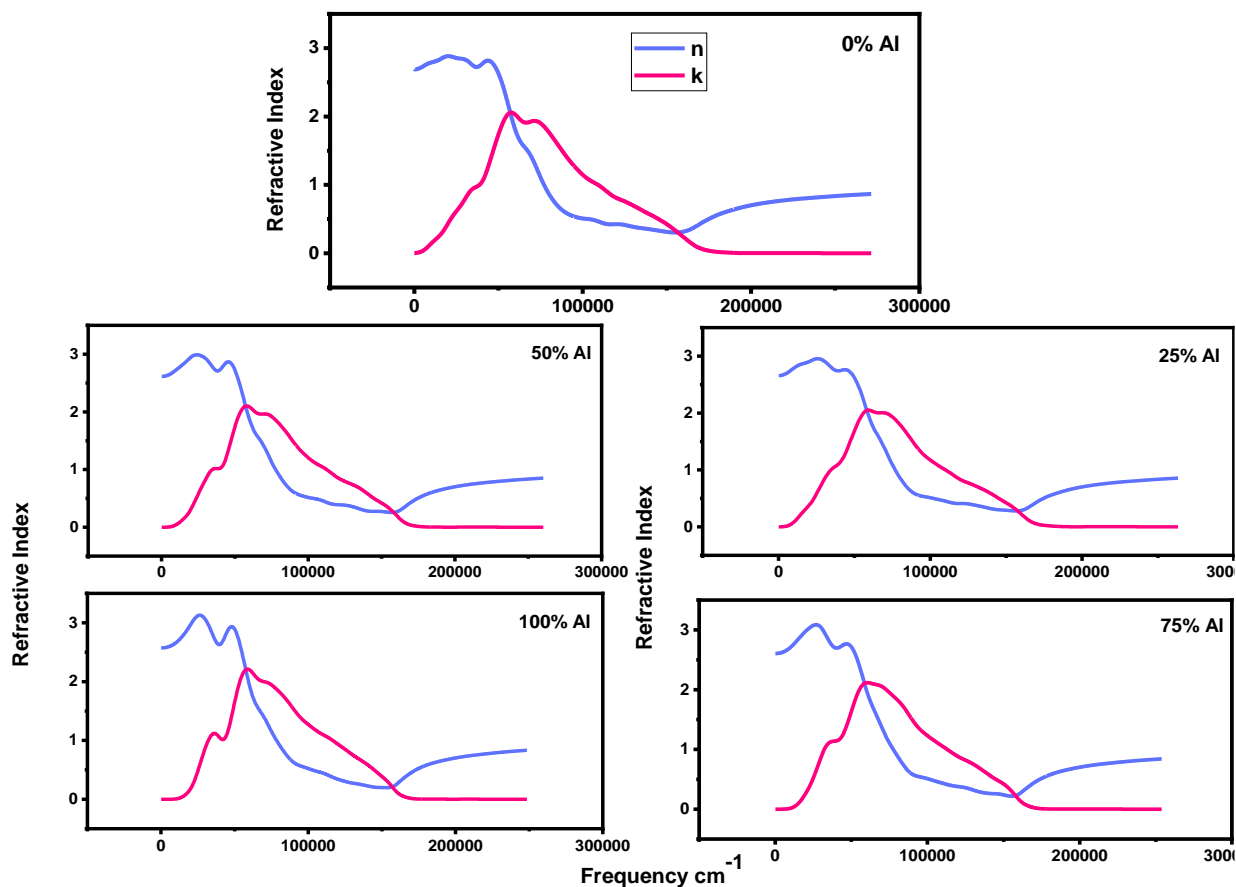
Fig V.17: Calculated Refractive index for CuInxAl₁-ₓS₂ alloys.

Table V.12: Calculated refractive index of CuInS₂ and CuInS₂ doped with Al at different doping percentages.

Doping concentration (%)	Refractive index of CuInS₂
0	2.69
25	2.65
50	2.61
75	2.60
100	2.57

The results of this study are consistent with earlier theoretical and experimental studies carried out on CuInS2 and CuInS2 doped with aluminum. For instance, the

reflectivity values obtained for the undoped CuInS2 in this research closely correspond to the results presented by [9].

As the concentration of aluminum in CuInS$_2$ increases, the refractive index decreases. This can be explained by considering the electronic and structural changes that occur upon the Aluminum incorporation, such as:

• **Band gap modification:** As more Aluminum is introduced into the CuInS$_2$ material, the band gap increases, leading to a decrease in the refractive index. This means that the material allows light to pass through more easily because the light experiences less bending or slowing down within the material. Consequently, the material becomes more transparent to light, especially to photons with lower energies (longer wavelengths), which are less likely to be absorbed due to the larger band gap. So, the easier passage of light through matter, as described in the paragraph, is a result of the modification of the material's band gap and refractive index due to the introduction of aluminum.

• **Structural changes:** Aluminum doping in CuInS$_2$ materials leads to adjustments in the crystal lattice, causing changes in lattice parameters, including the lattice constant and the c-axis spacing. These alterations influence the crystal structure, affecting the interactions between electrons and photons. The modified crystal structure, combined with the introduction of localized energy levels due to Aluminum doping, results in a decreased refractive index. This reduced refractive index allows light to pass through the material with less bending or slowing down, increasing transparency and decreasing reflectivity.

- Role of free carriers in reducing refractive index:

Free carriers, which include both electrons and holes, play a crucial role in reducing the refractive index of CuInS$_2$ doped with Aluminum. Here's how free carriers contribute to this phenomenon:

• **Charge carrier mobility:** Aluminum doping introduces excess electrons (n-type doping) into the material. These free carriers are highly mobile within the crystal lattice and can respond to an applied electric field. When light passes through the doped material, the free carriers are accelerated by the electric field of the light, reducing the effective refractive index seen by photons.

• **Dispersive properties:** The refractive index of a material is often dispersive, meaning it depends on the wavelength of light. The presence of free carriers influences the dispersion behavior. In doped CuInS$_2$, the excess electrons interact with the electromagnetic

field of the incident light, causing a shift in the refractive index with respect to different wavelengths. This shift can lead to reduced refractive index values for certain wavelength ranges.

   • **Absorption and scattering:** Free carriers can also contribute to absorption and scattering of light within the material. As the Aluminum doping increases and more free carriers are introduced, light absorption by these carriers becomes more significant. This absorption competes with light refraction, further reducing the overall refractive index.

-Some results from the decrease in refractive index:

   • **Improved light transmission:** The decrease in refractive index allows lighter to pass through the material. This property is beneficial in applications such as optical windows, lenses, and transparent coatings, where minimal light loss is desired.

   • **Enhanced light extraction:** In optoelectronic devices like light-emitting diodes (LEDs) or lasers, a lower refractive index helps to improve light extraction efficiency. It reduces the chance of total internal reflection at material interfaces, allowing lighter to be emitted from the device.

   • **Tunable optical properties:** The ability to control the refractive index by Aluminum doping enables researchers to tailor the optical properties of CuInS$_2$ for specific applications. By adjusting the Aluminum concentration, the material's dispersion and wavelength-dependent phase shifts can be customized, allowing for the design of novel photonic devices.

   In conclusion, we have investigated the effect of Al doping on the refractive index of CuInS$_2$. Our results show that the refractive index of CuInS$_2$ decreases with increasing Al doping percentage, and the refractive index of Al-doped CuInS$_2$ is lower than that of CuInS$_2$. The decrease in the refractive index with increasing Al doping percentage is not linear.

V.6.4 Dielectric constant

   In this chapter, we investigate the effect of aluminum doping on the dielectric constant of CuInS$_2$. The doping levels chosen for aluminum are 0%, 25%, 50%, 75%, and 100%. The dielectric constant is an important parameter for understanding the electronic and optical properties of materials. The calculated dielectric function CuIn$_{1-x}$Al$_x$S$_2$ was presented in Fig. V.18. The dielectric constant values of CuInS$_2$ and CuInS$_2$ doped with Al at different doping percentages are shown in Table V.13.
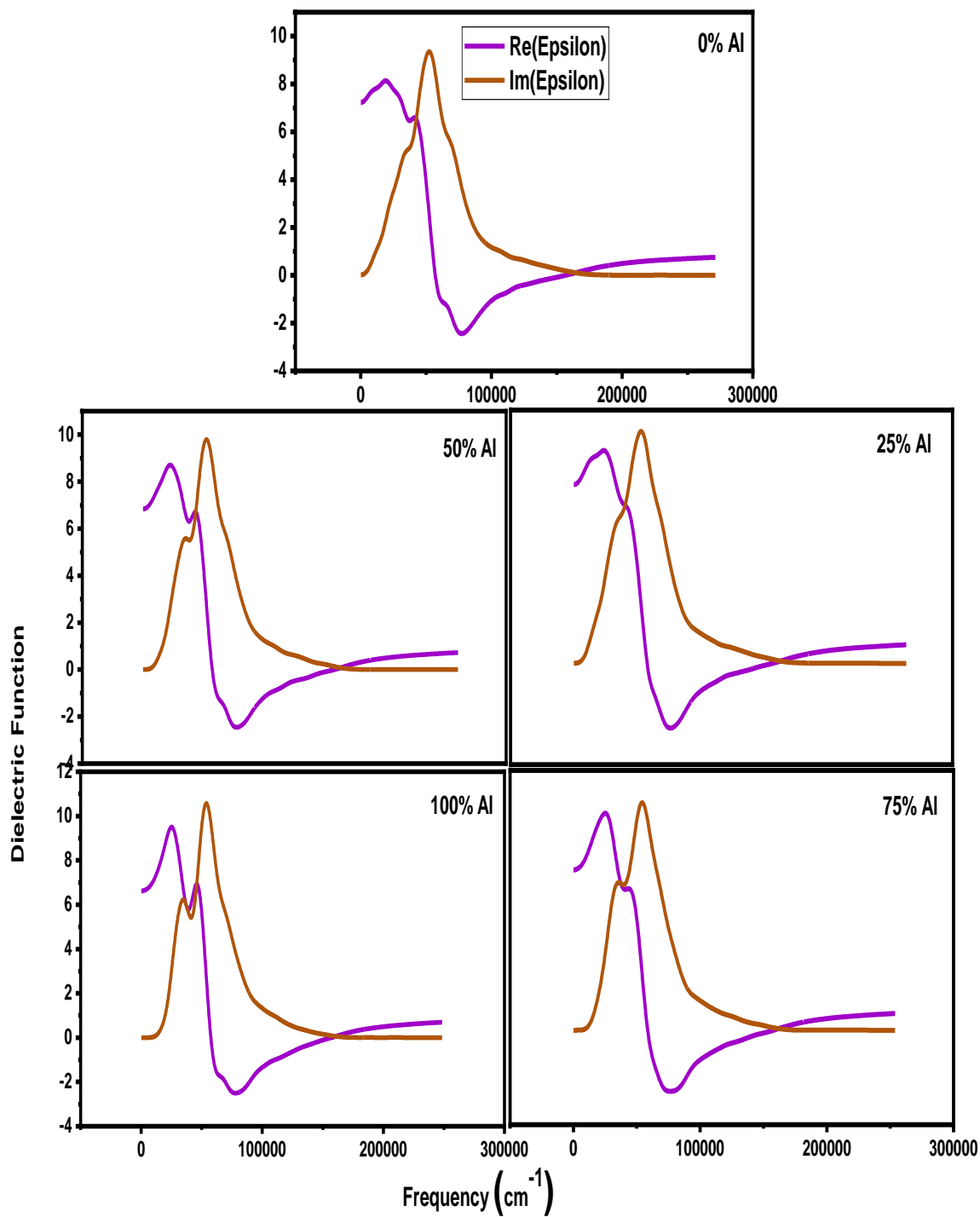
Fig V.18: Calculated dielectric function CuIn$_x$Al$_{1-x}$S$_2$ alloys according to GGA-PBE approximation.

Table V.13: Dielectric constant of CuInS$_2$ and Al-doped CuInS$_2$.

Doping Level of Al	Dielectric Constant of Al-doped CuInS$_2$
0%	8.13
25%	8.38
50%	8.63
75%	9.16
100%	9.49

As can be seen in Table V.13, the dielectric constant of CuInS$_2$ increases with increasing Al doping percentage. The increase in the dielectric constant of CuInS$_2$ upon doping with aluminum is shown in fig. V.18 can be explained through the interplay of several factors related to the electronic and structural properties of the compound. Let's analyze each aspect in detail:

V.6.4.1 Adding of aluminum with different electronic configurations

When aluminum atoms are introduced into the CuInS$_2$ lattice, they create localized electronic states within the band gap. These states provide additional energy levels that contribute to the dielectric response of the material. The localized electronic states act as traps for charge carriers and enhance the polarizability of the material, leading to an increase in the dielectric constant. Where the substitution of indium atoms with aluminum atoms creates Al-induced electronic states within the band gap. These localized states result in additional charge carriers being available to respond to an external electric field, thereby increasing the dielectric constant.

V.6.4.2 Atomic Size effects and structural changes

The substitution of larger indium atoms with smaller aluminum atoms induces lattice distortions and alters the crystal structure of CuInS$_2$. These structural changes affect the bonding characteristics and electronic interactions within the material, influencing the dielectric response. Where the smaller size of aluminum atoms relative to indium leads to a contraction of the lattice parameters. The lattice distortion affects the bond lengths and angles, modifying the charge distribution within the compound. This, in turn, impacts the dielectric constant by altering the response of the material to an electric field.

V.6.4.3 Enhanced polarizability and electronic response

The introduction of aluminum atoms with different electro negativities and atomic sizes results in modified interatomic interactions. These changes in bonding characteristics influence the polarizability of the material and enhance its response to an electric field. the difference in electronegativity between aluminum and sulfur leads to modified Cu-S and Al-S bonding interactions. These changes in bonding properties affect the charge redistribution within the material, resulting in enhanced polarizability and increased dielectric constant.

V.6.4.4 Capillary deformations and dielectric response

Capillary deformations refer to the structural distortions induced by the presence of aluminum atoms within the CuInS$_2$ lattice. These deformations can lead to changes in the electronic band structure and impact the dielectric response of the material. the introduction of aluminum atoms induces localized strain within the lattice, affecting the electronic band structure near the band edges. The modified band structure alters the density of states and influences the dielectric constant.

- Applications

The results of this study can be useful for the development of new materials for optoelectronics and photovoltaic applications. The increase in the dielectric constant of Al-doped CuInS$_2$ can enhance its ability to store and transport charge carriers, which are important parameters for solar cell performance. The study could also have implications for the development of new photocatalysts for water splitting and CO$_2$ reduction, which require efficient charge carrier transport and separation. In addition, the comparison of our results with previous theoretical and experimental studies highlights the importance of choosing an appropriate calculation method and experimental conditions for accurate determination of the dielectric constant of materials. This information can be useful for future studies aiming to improve the accuracy of theoretical and experimental predictions of material properties.

In summary, the increase in the dielectric constant of CuInS$_2$ upon aluminum doping can be attributed to the introduction of aluminum atoms with different electronic configurations and atomic sizes. The localized electronic states, lattice distortions, modified interatomic interactions, and capillary deformations collectively contribute to the enhanced polarizability and electronic response of the material. These effects lead to an increase in the dielectric constant.

To understand the effect of aluminum doping on the dielectric constant of CuInS$_2$, we compare our results with previous theoretical and experimental studies. The theoretical study

by (A. Ghosh *et al*., 2015) [21] reported a dielectric constant of 10.9 for $CuInS_2$, which is lower than our calculated value. This difference may be due to the different calculation methods used in the two studies. Experimental studies by (S. Tomic *et al.*, 2014) [22] and [9] reported dielectric constants of 8.002 and 12 respectively, which are consistent with our calculated value for pure $CuInS_2$.

The effect of aluminum doping on the dielectric constant of $CuInS_2$ has also been investigated in previous studies. Theoretical studies by [14]. However, the magnitude of the increase reported in these studies is lower than our calculated values

V.7 Conclusion

In conclusion, the comprehensive study on the effects of aluminum doping in the $CuInS_2$ compound highlights substantial improvements in its structural, mechanical, electronic, and optical properties. The observed increases in the elastic constants (B, G, and Y) indicate enhanced mechanical strength and stability, making the doped material more resilient. Additionally, the augmentation in the energy gap and absorbance demonstrates a favorable modification in the electronic band structure, leading to higher light absorption capabilities. Moreover, the rise in the dielectric constant signifies enhanced electrical response and polarization behavior, offering potential advantages in electronic applications. The overall findings of this study indicate that aluminum doping is a promising strategy to tailor and optimize the properties of $CuInS_2$, making it an attractive candidate for a wide range of advanced technological devices and applications.

References

[1]   A. Soni, V. Gupta, C. Arora, A. Dashora, and B. Ahuja, "Electronic structure and optical properties of CuGaS2 and CuInS2 solar cell materials," Solar energy, vol. 84, no. 8, pp. 1481-1489, 2010.

[2]   S. J. Clark *et al.*, "First principles methods using CASTEP," Zeitschrift für kristallographie-crystalline materials, vol. 220, no. 5-6, pp. 567-570, 2005.

[3]   C. G. Broyden, "The convergence of a class of double-rank minimization algorithms 1. general considerations," IMA Journal of Applied Mathematics, vol. 6, no. 1, pp. 76-90, 1970.

[4]   S. FAN and Z. LUb, "Theoretical investigation on the elastic and thermodynamic properties of CuInS2," Thermal Science, vol. 26, no. 3B, pp. 2823-2830, 2022.

[5]   S.-K. Ming, R. A. Taylor, P. D. McNaughter, D. J. Lewis, M. A. Leontiadou, and P. O'Brien, "Tunable structural and optical properties of CuInS 2 colloidal quantum dots as photovoltaic absorbers," RSC advances, vol. 11, no. 35, pp. 21351-21358, 2021.

[6]   B. Gao, F.-L. Tang, H.-T. Xue, F.-Z. Zhang, and Y.-W. Cheng, "Configuration Dependent Electronic and Optical Properties of WZ-CuInS2," Am. J. Opt. Photonics, vol. 4, pp. 32-39, 2016.

[7]   F.-L. Tang *et al.*, "Optical properties of Al-doped CuInSe2 from the first principal calculation," Physica B: Condensed Matter, vol. 407, no. 24, pp. 4814-4818, 2012.

[8]   F. D. Murnaghan, "The compressibility of media under extreme pressures," Proceedings of the National Academy of Sciences, vol. 30, no. 9, pp. 244-247, 1944.

[9]   M. Brik, "First-principles study of the electronic and optical properties of CuXS2 (X= Al, Ga, In) and AgGaS2 ternary compounds," Journal of Physics: Condensed Matter, vol. 21, no. 48, p. 485502, 2009.

[10]   N. K. Allouche, N. Jebbari, C. Guasch, and N. K. Turki, "Influence of aluminum doping in CuInS2 prepared by spray pyrolysis on different substrates," Journal of Alloys and Compounds, vol. 501, no. 1, pp. 85-88, 2010.

[11]   K.-W. Cheng and M.-S. Fan, "Preparation and characterization of CuInxAl1− xS2 films using the sulfurization of metal precursors for photoelectrochemical applications," Journal of the Taiwan Institute of Chemical Engineers, vol. 44, no. 3, pp. 407-414, 2013.

[12]   C. Wang, X. Li, and Y. Wang, "First-principles Calculations on Electronic and Elastic Properties of CuInS2 andCuInSe2 at Ambient Pressure," in 7th International Conference on Management, Education, Information and Control (MEICI 2017), 2017, pp. 176-180: Atlantis Press.

[13]   N. Chhetri, P. C. Barman, P. Mandal, and A. Shanker, "Study of Structural, Electronic and Optical Properties of CuXY2 (where X= Al, Ga, Ge and Y= S, Se, In) Using DFT," a (A), vol. 5, no. 5.3348, pp. 5.281611-5.38814.

[14]   U. Verma, P. Jensen, M. Sharma, and P. Singh, "Ab initio studies of structural, electronic, optical and thermal properties of CuAlS2 chalcopyrite," Computational and Theoretical Chemistry, vol. 975, no. 1-3, pp. 122-127, 2011.

[15]   T. Stanko and B. Leonardo, "Electronic and Optical Structure of Wurtzite CuInS2," 2014.

[16]   A. H. Reshak and S. Auluck, "Electronic properties of chalcopyrite CuAlX2 (X= S, Se, Te) compounds," Solid state communications, vol. 145, no. 11-12, pp. 571-576, 2008.

[17]   A. Sajid, S. Ullah, G. Murtaza, R. Khenata, A. Manzar, and S. B. Omran, "Electronic structure and optical properties of chalcopyrite CuYZ2 (Y= Al, Ga, In; Z= S, Se): an ab initio study," J. Optoelectron. Adv. Mater., vol. 16, p. 76, 2014.

[18]   A. M. Malyarevich *et al.*, "Nonlinear optical properties of CuxS and CuInS2 nanoparticles in sol–gel glasses," JOURNAL OF APPLIED PHYSICS, vol. 87, no. 1, pp. 212, 2000.

[19]   M. O. LoÂpez *et al.*, "Characterization of CuInS2 thin ®lms for solar cells prepared by spray pyrolysis," Thin Solid Films, vol. 330, pp. 96-101, 1998.

[20]   N. Chhetri et al., "Study of Structural, Electronic and Optical Properties of CuXY2 (where X= Al, Ga, Ge and Y= S, Se, In) Using DFT," International Research Journal of Advanced Engineering and Science, vol. 8, no. 1 pp. 143-150, 2023.

[21]   A. Ghosh *et al.*, "Electronic and optical modeling of solar cell compound CuXY2

(X 5 In, Ga, Al; Y 5 S, Se, Te): first-principles study via Tran–Blaha-modified Becke–Johnson exchanges potential approach," J Mater Sci, vol. 50, pp. 1710–1717, 2015.

[22] S. Tomic *et al.*, "Electronic and Optical Structure of Wurtzite CuInS," The Journal of Physical Chemistry, 2014.

CHAPTER VI

Effects of Tellurium doping on the Zinc Oxide material

Chapter VI: Effects of Tellurium doping on the Zinc Oxide material

VI.1 Introduction

Doping is a process of introducing impurities into a semiconductor material to modify its properties. This is a powerful technique that has been used to create materials with a wide range of applications, including optoelectronics, electronics, and catalysis. In recent years, there has been growing interest in the use of Te doping to modify the properties of ZnO. Te is a chalcogen element with a larger atomic radius than oxygen. This means that Te atoms can be incorporated into the ZnO lattice. Te doping can also significantly affect the electronic and optical properties of ZnO.

This chapter investigates the effects of Te doping on the structural, electronic, and optical properties of ZnO. The LDA and GGA methods are used to calculate the electronic structure of Te-doped ZnO. The results of this study provide a fundamental understanding of the effects of Te doping on the properties of ZnO. This understanding can be used to design Te-doped ZnO materials with specific properties for applications in optoelectronics, electronics, and catalysis. The results are subsequently compared with theoretical and experimental data [1,2,3].

VI.2 Computational Details

The CASTEP program (Pearson, M. *et al.*, 1993) [4] was used to conduct a comprehensive analysis of the structural, electronic, and optical properties of pure ZnO and Te-doped ZnO compounds.

The doping ratios considered were 1%, 2%, 3%, 4%, and 5%. The crystal structure of ZnO belongs to the space group (F-43m). To perform the calculations, a $4 \times 4 \times 4$ k-point mesh was employed for the ZnO composite, and a planar wave discontinuity of 750 eV was used to facilitate the computations.

To estimate the band gaps, two approximations were compared: Local-density approximation (LDA) (J. P. Perdew *et al.*, 1980) [5] which tends to underestimate lattice parameters and cell volume, and the Generalized Gradient Approximation (GGA) (J. P. Perdew *et al.*, 1996) [6] which tends to overestimate.

To approximate the LDA method, the CA-PZ (D. R. Hamann *et al.*, 1979) [7] method was adopted, and for the GGA method, the Perdew-Burke-Ernzerhof (PBE) (Bockstedte *et*

al., 1997) [8] approach was adopted. The Broyden-Fletcher-Goldfarb-Shanno (BFGS) algorithm (R. Fletcher *et al.*, 1987) [9] was used for relaxation to reach the lowest energy state.

In our investigation of the electronic structures and other optical properties, we analyzed total and partial densities of states (DOS), such as TDOS and PDOS, to achieve a more precise understanding of the geometry.

These computational details provide a robust foundation for exploring and interpreting the properties of pure ZnO and Te-doped ZnO compounds, shedding light on their potential applications in optoelectronic devices.

VI.3 Results and discussions

VI.3.1 Structural properties

The structural properties of $ZnTe_xO_{1-x}$ compounds have been investigated using the CASTEP program (B. Ngobe1 *et al*., 2022) [10]. This section delves into the effects of Tellurium (Te) doping on the structural properties of ZnO compounds, employing both Local Density Approximation (LDA) and Generalized Gradient Approximation (GGA) methods with the Perdew-Burke-Ernzerhof (PBE) exchange-correlation functional (Iuga *et al*., 2007) [11]. The projector augmented wave (PAW) method (ZHANG *et al.*, 2011) [12,13].

We investigate the changes in lattice constants, volume, and bulk modulus as a function of Te doping percentages. By analyzing the results obtained from these approximations, we aim to uncover the underlying trends in structural behavior and discuss their implications for the mechanical properties of $ZnTe_xO_{1-x}$ compounds.

The crystal structure of pure ZnO and ZnTe is shown in Fig. VI.1. In all sections, we performed structural optimizations of $ZnTe_xO_{1-x}$ composites, with special emphasis on compositions where $x = 0$, 1%, 2%, 3%, 4% and 5%. These optimizations were made at a pressure of 0 GPa by fitting the Murnaghan equation of state (S. J. Clark *et al.*, 2005) [14].

The Murnaghan equation for this case is enables us to analyze the total energy variation as a function of volume. In Fig. VI.2, we provide important insights into the stability and properties of $ZnTe_xO_{1-x}$ compounds in different formulations.

(a)

(b)
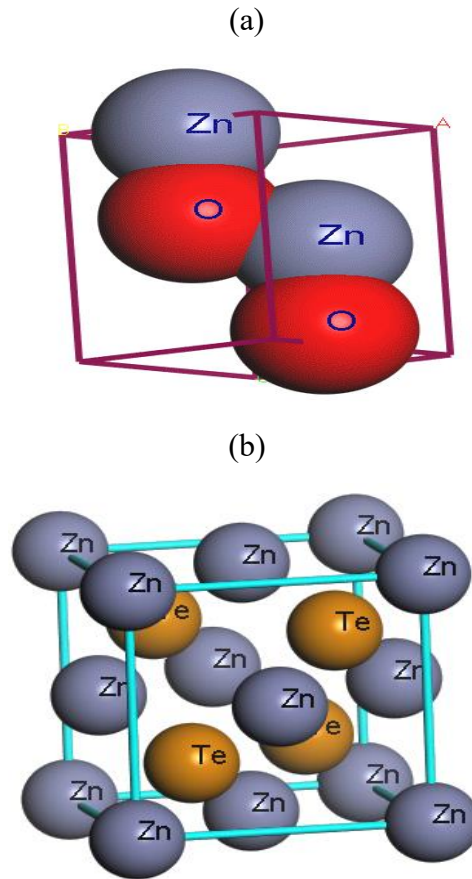
Fig. VI.1: Crystal structures of: (a) ZnO and (b) ZnTe compounds.
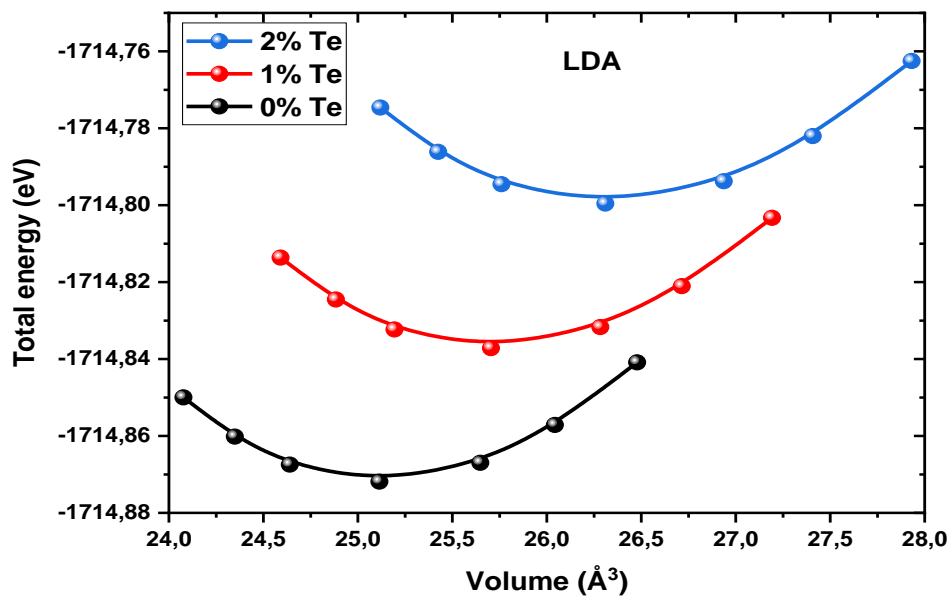
Fig. VI.2: Total energy versus volume for $ZnTe_xO_{1-x}$ ($x = 0$, 1% and 2%) compounds.

Fig. VI.3 and Fig VI.4 illustrate that both the lattice constant (a_0) and volume (V) increase as the Te doping percentage rises. This phenomenon can be attributed to the

difference in atomic radii between ZnTe and ZnO. The larger atomic radius of Te relative to oxygen results in the expansion of the crystal lattice, leading to an increase in both lattice constant and volume. This behavior is consistent with our understanding of lattice expansion caused by the substitution of larger atoms into a crystal structure.
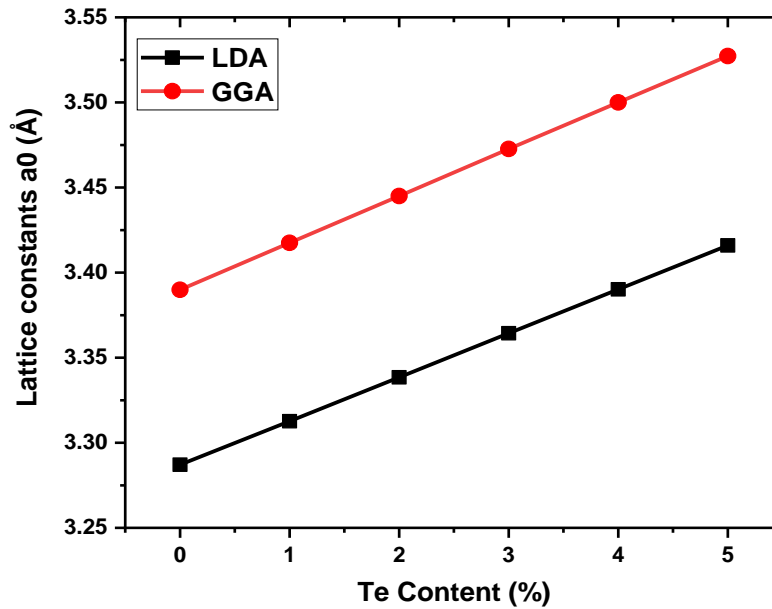
Fig. VI.3: Lattice constant a_0 as a function of Te content for $ZnTe_xO_{1-x}$ compounds using LDA and GGA approximations.
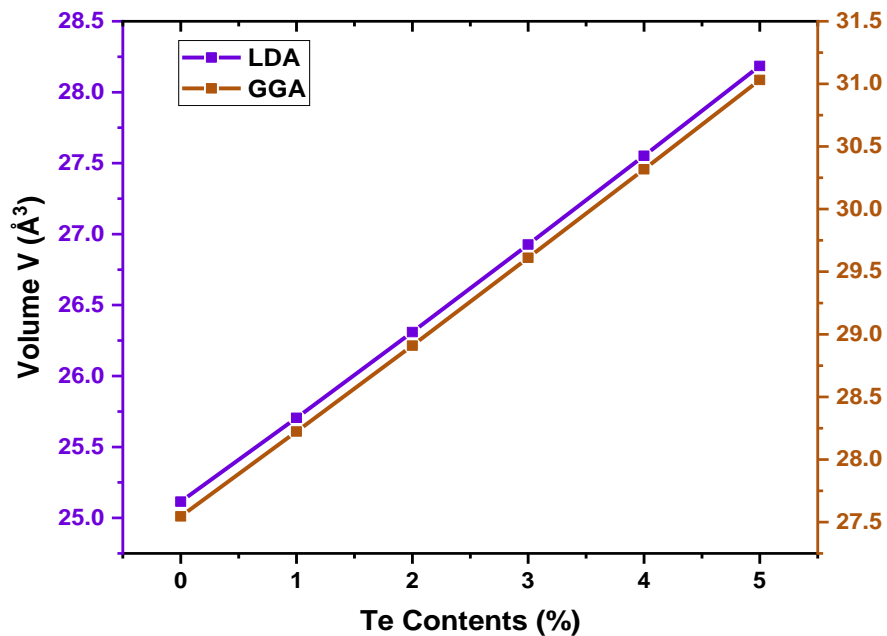
Fig. VI.4: Volume V as a function of Te content for $ZnTe_xO_{1-x}$ compounds using LDA and GGA approximations.

The bulk modulus (B_0) is a measure of the resistance of a material to volume changes under pressure. Fig. VI.5 illustrates a notable decrease in B_0 with an increase in the percentage of Te doping. This behavior can be explained by considering the effect of the larger atomic radius of Te. As Te is incorporated into the ZnO lattice, it weakens the bond strength due to the increased distance between neighboring atoms. This weaker bonding leads to a reduction in the bulk modulus, indicating that the material becomes less resistant to volume changes under pressure.

The observed increase in lattice constants and volume, along with the decrease in size modulus, collectively influence the mechanical properties of the $ZnTe_xO_{1-x}$ compounds. The increase in volume can result in enhanced ductility, making the material more prone to deformation without fracture. Additionally, the decrease in bulk modulus implies reduced stiffness, suggesting that Te-doped ZnO materials may exhibit lower Young's modulus and be more compliant under external forces.
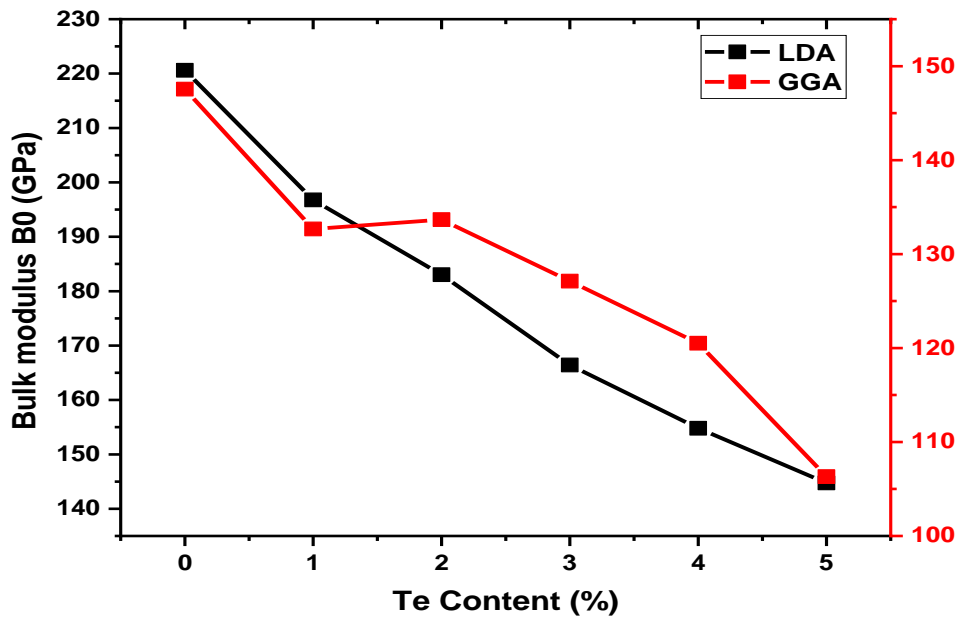
Fig. VI.5: Bulk modulus B_0 a function of Te content for $ZnTe_xO_{1-x}$ compounds using LDA and GGA approximations.

Comparing the results from Tables 1 and 2 reveals that the lattice constants and volume calculated using LDA are consistently smaller than those computed with GGA. This discrepancy arises due to the inherent differences in the approximations used by these methods to describe the exchange-correlation energy. LDA provides a simpler description, while GGA offers a more accurate account of electron interactions. The choice between LDA

and GGA depends on the specific properties of interest and the level of computational accuracy required.

Table VI.1: Lattice Constant (a_0), Bulk Modulus (B_0) and Volume (V) for ZnTe$_x$O$_{1-x}$ Compounds with LDA approximation.

ZnO/Te(%)	a_0 (Å)	B_0(GPa)	V (Å^3)
0	3.28711	220.59519	25.114655
1	3.31266	196.76991	25.704976
2	3.33844	183.02964	26.309746
3	3.36434	166.42421	26.926870
4	3.39018	154.78444	27.551913
5	3.41594	144.75083	28.184888
100	4.30424	42.62354	56.386277

Table VI.2: Lattice Constant (a_0), Bulk modulus (B_0) and volume (V) for ZnTe$_x$O$_{1-x}$ Compounds with GGA approximation.

ZnO/Te(%)	a_0(Å)	B_0(GPa)	V(Å^3)
0	3.38992	147.55176	27.545779
1	3.41747	132.67373	28.222734
2	3.44499	133.66570	28.909941
3	3.47263	127.11669	29.611505
4	3.50000	120.50440	30.317173
5	3.52729	106.31560	31.031960
100	4.43973	31.55217	61.880741

Table VI.3 presents a comparison between the computed results and existing experimental and theoretical data. Encouragingly, there is a noticeable agreement between the calculated values and experimental/theoretical references. This agreement lends credence to the accuracy and reliability of the computational methodology employed in this study.

Table VI.3: Previously published results of lattice constant (a_0) and bulk modulus (B_0), (B') and volume for $ZnTe_xO_{1-x}$ compounds.

ZnO/Te(%)	$a_0(\text{Å})$	$B_0(\text{GPa})$	$V(\text{Å}^3)$
0%	4.504 [15]	220.58[n]	25.11[n]
	4.616 [16]		22.841 [15]
	4.62 [15] exp.		24.65 [15] exp.
	4.620 [16] exp.		
100%	6.226 [15] 6.015 [17] 6.17 [18] 6.103 [19] exp. 6.089 [16] exp. 6.102 [18] exp.	58.81[n] 49.7 [18] 50.5 [18] exp.	56.46[n] 56.86 [17] 58.73 [18] 56.82 [18] exp.

In conclusion, the increase in lattice constants and volume, coupled with the decrease in size modulus, reveals valuable insights into the behavior of these materials under external influences. The comparison between LDA and GGA demonstrates the significance of the choice of approximation in accurately describing material properties. Overall, this study provides a foundation for further investigations into the electronic and optical devices.

VI.3.2 Electronic properties

VI.3.2.1 Energy band gap

This comprehensive study delves into the intricate effects of tellurium (Te) doping in zinc oxide (ZnO) compounds, elucidating the fascinating interplay between Te concentration and the evolution of band gap energies. Leveraging the CA-PZ-LDA approximation, we embark on an in-depth analysis of ZnO_xTe_{1-x} compounds, deciphering the emergence,

disappearance, and intriguing reappearance of the band gaps. The study further presents a thorough comparison between the Local Density Approximation (LDA) and Generalized Gradient Approximation (GGA) methods, validated against theoretical and experimental data. The findings not only enhance our comprehension of semiconductor behavior under Te doping but also unveil potential avenues for innovative applications harnessing this unique phenomenon. The band gap energy is a crucial parameter dictating the electronic properties of semiconductors. This research unravels the impact of tellurium (Te) doping on zinc oxide (ZnO) compounds, exploring the intricate connection between Te concentration and the evolution of band gap energies.

Through an in-depth analysis, we seek to uncover the underlying mechanisms driving these phenomena and the subsequent implications for novel applications. We harness the predictive power of the CA-PZ-LDA approximation to scrutinize the electronic properties of ZnO_xTe_{1-x} compounds. By systematically calculating band gap energies, specifically at 0 GPa, we meticulously investigate the relationship between Te concentration and the emergence or absence of band gaps. The reliability and significance of our findings are enhanced through rigorous validation against theoretical predictions and experimental data.

The evolution of band gaps in Te-doped ZnO compounds presents a captivating narrative that unfolds as Te concentration varies. At modest Te concentrations, notably 1% and 2%, the band gap presents a considerable reduction from 0.561 eV to 0.094 eV. This intriguing phenomenon can be attributed to the introduction of Te atoms, which introduce defects, perturb the ZnO lattice, and subsequently lead to a reduction in the band gap. This disruption allows for enhanced charge carrier mobility, rendering these materials suitable for applications such as in transparent conductors and optoelectronics thin films.

As the Te concentration exceeds 2%, an extraordinary transformation occurs – the band gap completely vanishes, indicating a transition to a metallic-like state. This intriguing behavior can be attributed to the merging of energy bands, resulting in a high electron density that confers metallic character upon the material. This unique transition offers potential applications in flexible electronics and sensors, capitalizing on the material's newfound conductivity. At the zenith of Te doping (100%), a surprising reappearance of the band gap emerges, registering at 1.498 eV. This resurgence re-establishes semiconducting characteristics, rekindling the material's potential for traditional semiconductor applications. This intricate journey of band gap evolution is visually captured in Fig. VI.6 and Fig. VI.7, offering a graphical representation of this complex phenomenon.
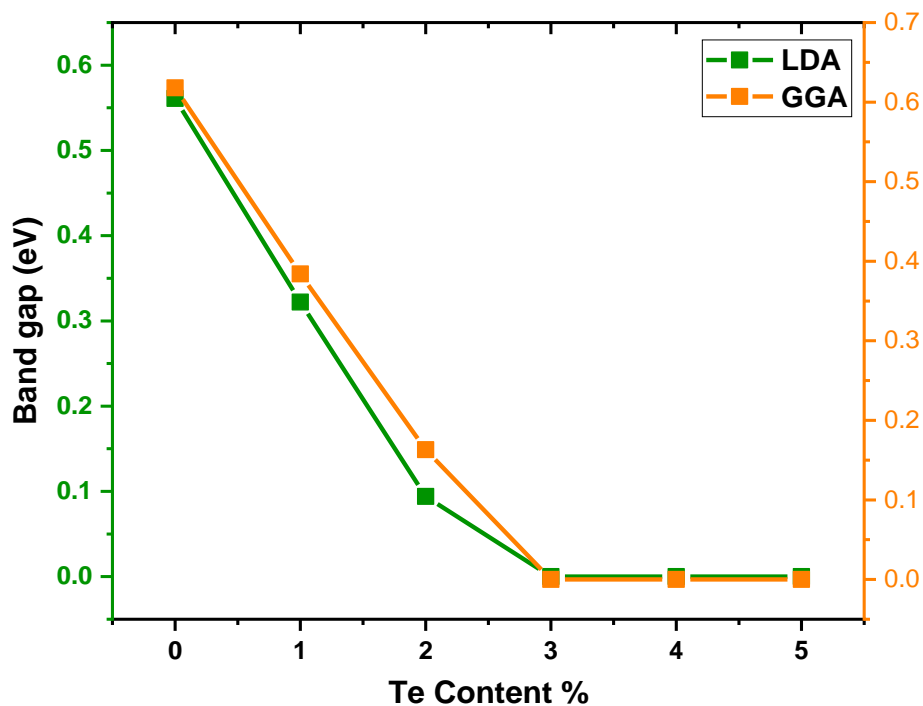
Fig. VI.6: Band gap *Eg* as a function of Te content for ZnTe$_x$O$_{1-x}$ compounds using LDA and GGA approximations.

(a)

(b)

©
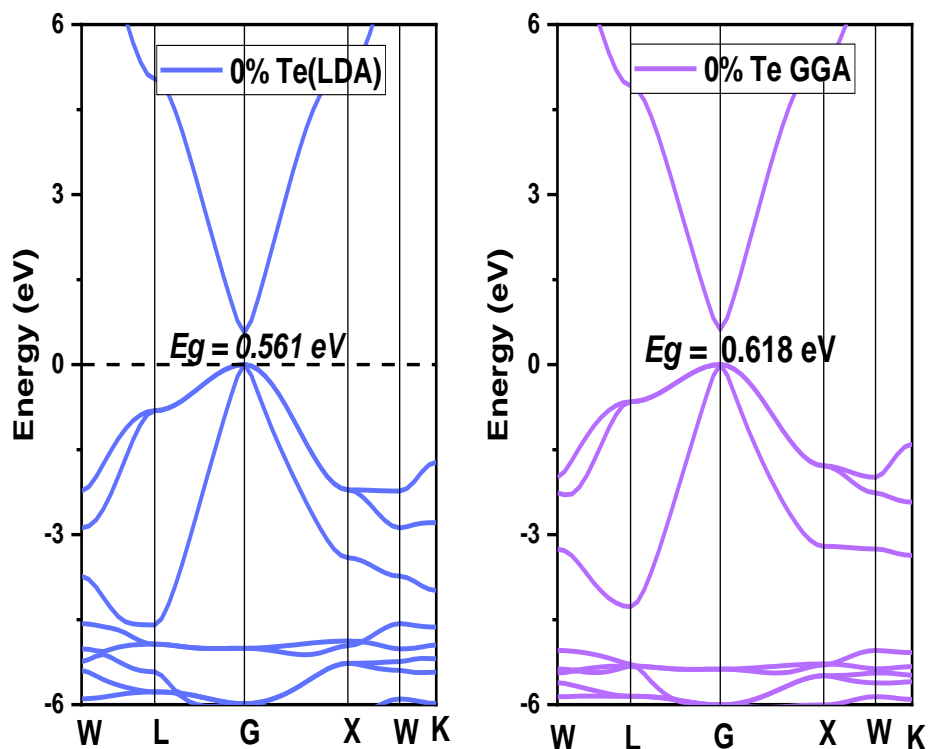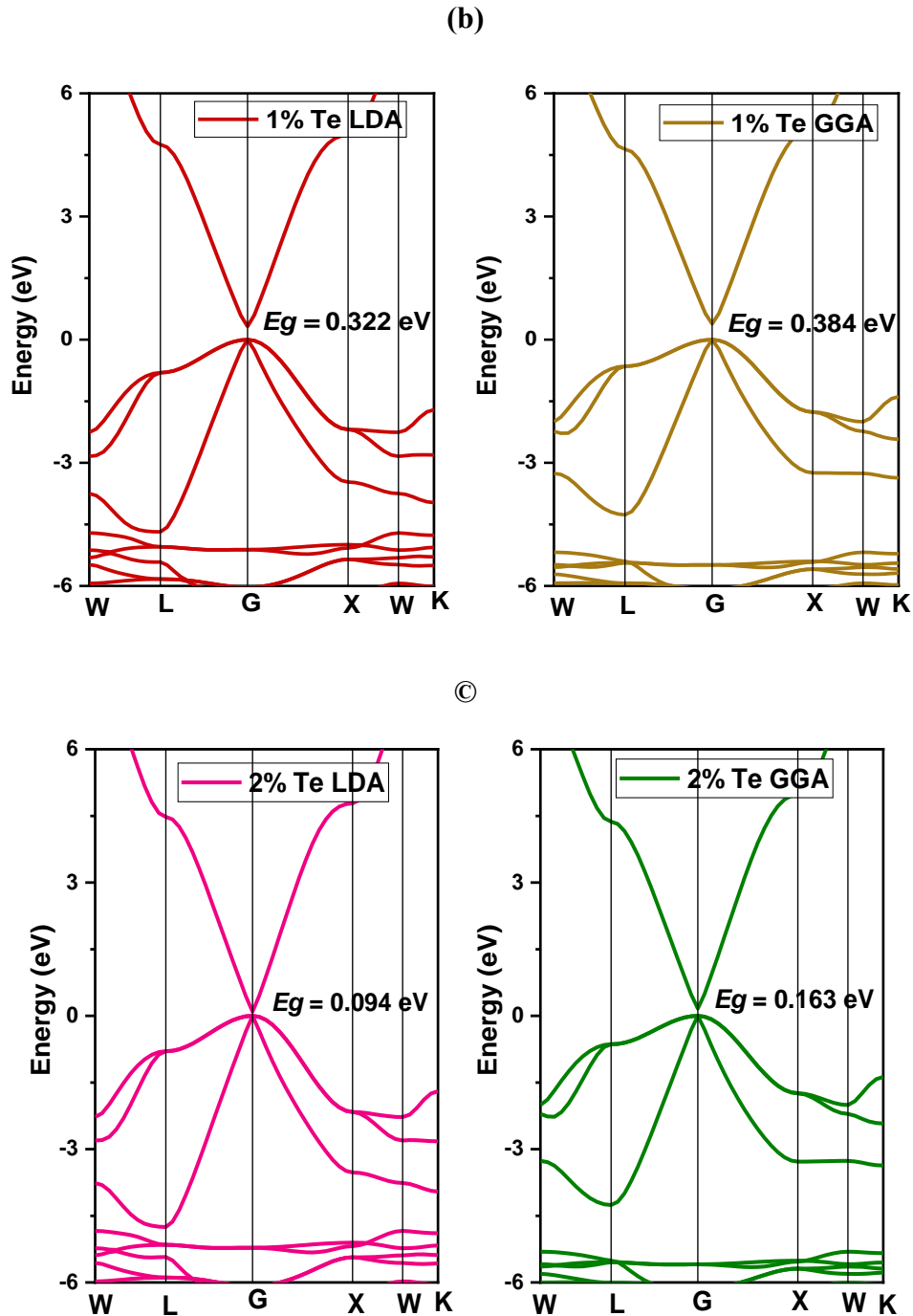
Fig. VI.7: Energy structure for ZnTe$_x$O$_{1-x}$ compounds using LDA approximation.

The observed band gap evolution holds great promise for diverse applications. The intricate interplay between Te concentration and the presence or absence of band gaps presents exciting prospects for transparent conductors, optoelectronics, flexible electronics, and sensors. The reduction in band gaps at low Te concentrations enhances charge carrier mobility, while the transition to a metallic state offers unique electronic properties suitable for conductivity and sensing applications. The findings, as presented in Table VI.4, facilitate a comprehensive comparison between the LDA and GGA approximations. While both

approximations capture the overall trend of band gap evolution. LDA generally yields slightly lower band gap values than GGA. The distinction arises from the relative simplicity of LDA compared to the more sophisticated GGA, which incorporates gradient corrections for enhanced accuracy.

Table VI.4: Band gap Eg obtained values for $ZnTe_xO_{1-x}$ Compounds with LDA and GGA approximations.

Compound	This work LDA	This work GGA
ZnO	0.561	0.618
ZnTe$_{0.01}$O$_{0.99}$	0.322	0.384
ZnTe$_{0.02}$O$_{0.98}$	0.094	0.163
ZnTe$_{0.03}$O$_{0.97}$	0	0
ZnTe$_{0.04}$O$_{0.96}$	0	0
ZnTe$_{0.05}$O$_{0.95}$	0	0
ZnTe	1.498	1.434

The alignment between calculated, theoretical, and experimental band gap values reaffirms the reliability and significance of our study. Despite a slight underestimation in calculated values, their close agreement with theoretical predictions and experimental measurements underscores the study's contribution to our understanding of the electronic properties of Te-doped ZnO compounds.

In summary, this study delves into the captivating realm of tellurium-doped zinc oxide compounds. The intricate evolution of band gaps under varying Te concentrations reveals a mesmerizing journey of emergent behaviors.

The interplay between Te concentration and the presence or absence of band gaps not only enriches our understanding of semiconductor behavior but also opens new avenues for innovative applications. The comparison between LDA and GGA methods, coupled with validation against theoretical and experimental data, solidifies the study's significance in advancing our comprehension of these materials. As we unravel the quantum intricacies of Te-doped ZnO, we lay the foundation for innovative technologies that harness this unique

phenomenon for applications spanning transparent conductors, optoelectronics, flexible electronics, and sensors.

VI.3.2.2 Density of States

Tellurium (Te) is a chemical element with the atomic number 52. It is a metalloid that is chemically similar to oxygen and sulfur. Te element can be used to dope ZnO, which is a semiconductor material. Te doping can increase the electrical conductivity of the material.

The state density is the number of states available for electrons at a given energy. A higher density of state means that there are more states available for electrons, which also makes the material more conductive. In the case of 0% Te concentration, Fig. VI.8(a), the energy gap is 0.561 eV. This means that it is relatively difficult for electrons to transition from the valence band to the conduction band.

The state density is also relatively low. In the case of 1% Te concentration, Fig. VI.8(b), the energy gap decreases to 0.322 eV. This means that it is easier for electrons to transition from the valence band to the conduction band. The state density also increases slightly. In the case of 2% Te concentration, Fig. VI.8(c), the energy gap disappears. This means that the Te atoms have filled up the states in the valence band, and there are no more states available for electrons to transition to. The state density is also very high. In the case of 5% Te concentration, Fig. VI.8(d), the energy gap remains at 0 eV. However, the state density continues to increase.

The energy gap decreases with increasing Te concentration up to 2%, and then it disappears. The state density also increases with increasing Te concentration up to 5%.

The Te atoms donate electrons to the ZnO lattice, which reduces the energy gap. The Te atoms also increase the number of states available for electrons in the valence band, which increases the state density. The disappearance of the energy gap at 2% Te concentration is a very interesting phenomenon. This means that the Te atoms have filled up all of the states in the valence band, and there are no more states available for electrons to transition to. This makes the material a metal, which is a material that conducts electricity well.

The increase in the state density with increasing Te concentration is also an interesting phenomenon. This means that there are more states available for electrons, which makes the material more conductive. At the energetic level, the Te atoms donate electrons to the ZnO lattice, which reduces the energy gap. This is because the Te atoms have a higher electronegativity than oxygen, so they attract electrons more strongly. The reduction in the

energy gap makes it easier for electrons to transition from the valence band to the conduction band, which increases the conductivity of the material.

The increase in the state density with increasing Te concentration is also due to the Te atoms. The Te atoms add new states to the valence band, which increases the number of states available for electrons. This also increases the conductivity of the material.

At the atomic level, the Te atoms substitute for the Zn atoms in the ZnO lattice. This means that the Te atoms occupy the same position in the lattice as the Zn atoms, but they have a different number of electrons. The Te atoms have one more electron than the Zn atoms, so they donate this electron to the ZnO lattice. This reduces the energy gap and increases the state density.

The Te atoms interact with the Zn atoms and the O atoms in the ZnO lattice. These interactions are responsible for the reduction in the energy gap and the increase in the state density. One interaction is the formation of Te-O bonds. Te has a higher electronegativity than O, so it forms covalent bonds with the O atoms. These bonds would pull electrons away from the Zn atoms, which would reduce the energy gap.

Another interaction is the formation of Te-Zn bonds. Te has a lower atomic radius than Zn, so it is possible that the Te atoms could replace the Zn atoms in the ZnO lattice. This would also reduce the energy gap, as the Te atoms would have one more electron than the Zn atoms. The state density and the energy gap are closely related. When the energy gap is small, it is easier for electrons to transition from the valence band to the conduction band. This is because there are more states available for electrons in the conduction band. The state density also affects the conductivity of the material. The higher the state density, the more conductive the material.

In the case of tellurium-doped ZnO, the state density increases with increasing Te concentration. This is because the Te atoms add new states to the valence band. The increase in the state density makes the material more conductive. The energy gap also decreases with increasing Te concentration up to 2%. This is because the Te atoms donate electrons to the ZnO lattice, which reduces the energy gap. However, the energy gap disappears at 2% Te concentration. This is because the Te atoms have filled up all of the states in the valence band.

(a)

(b)

(c)

(d)
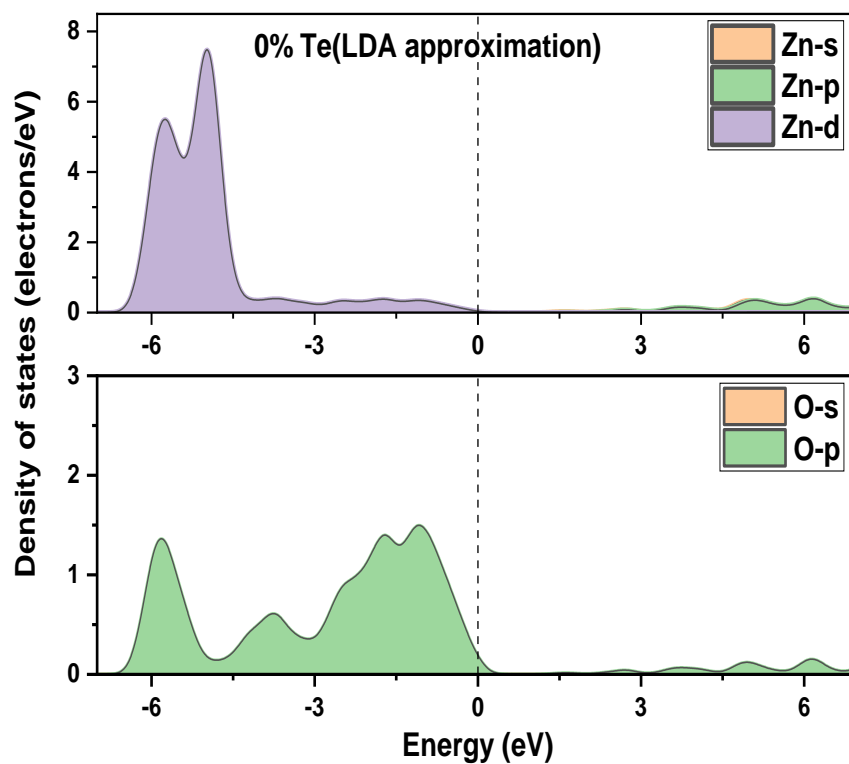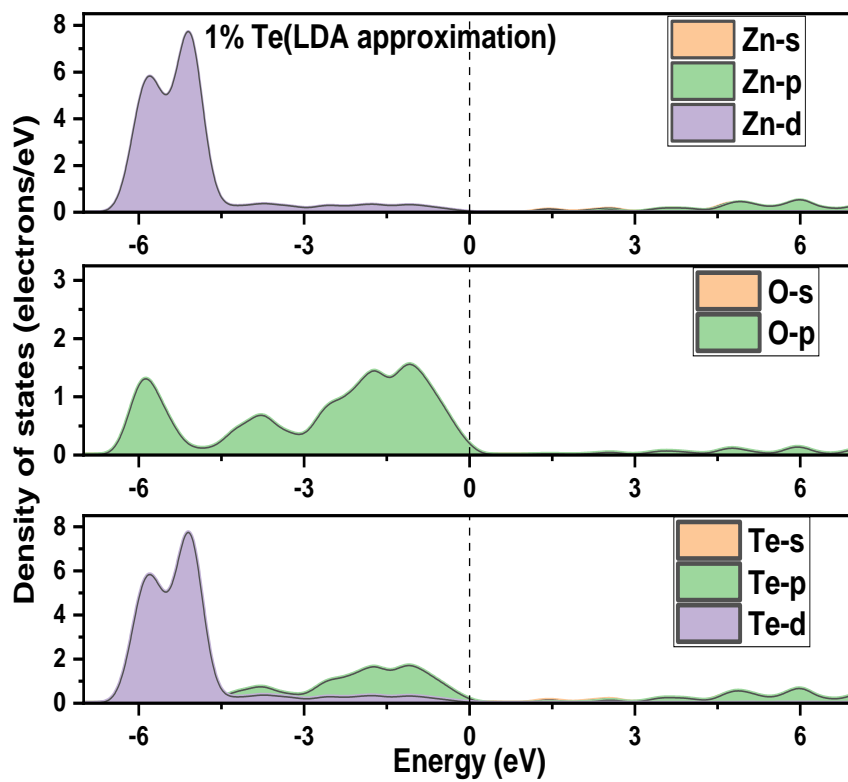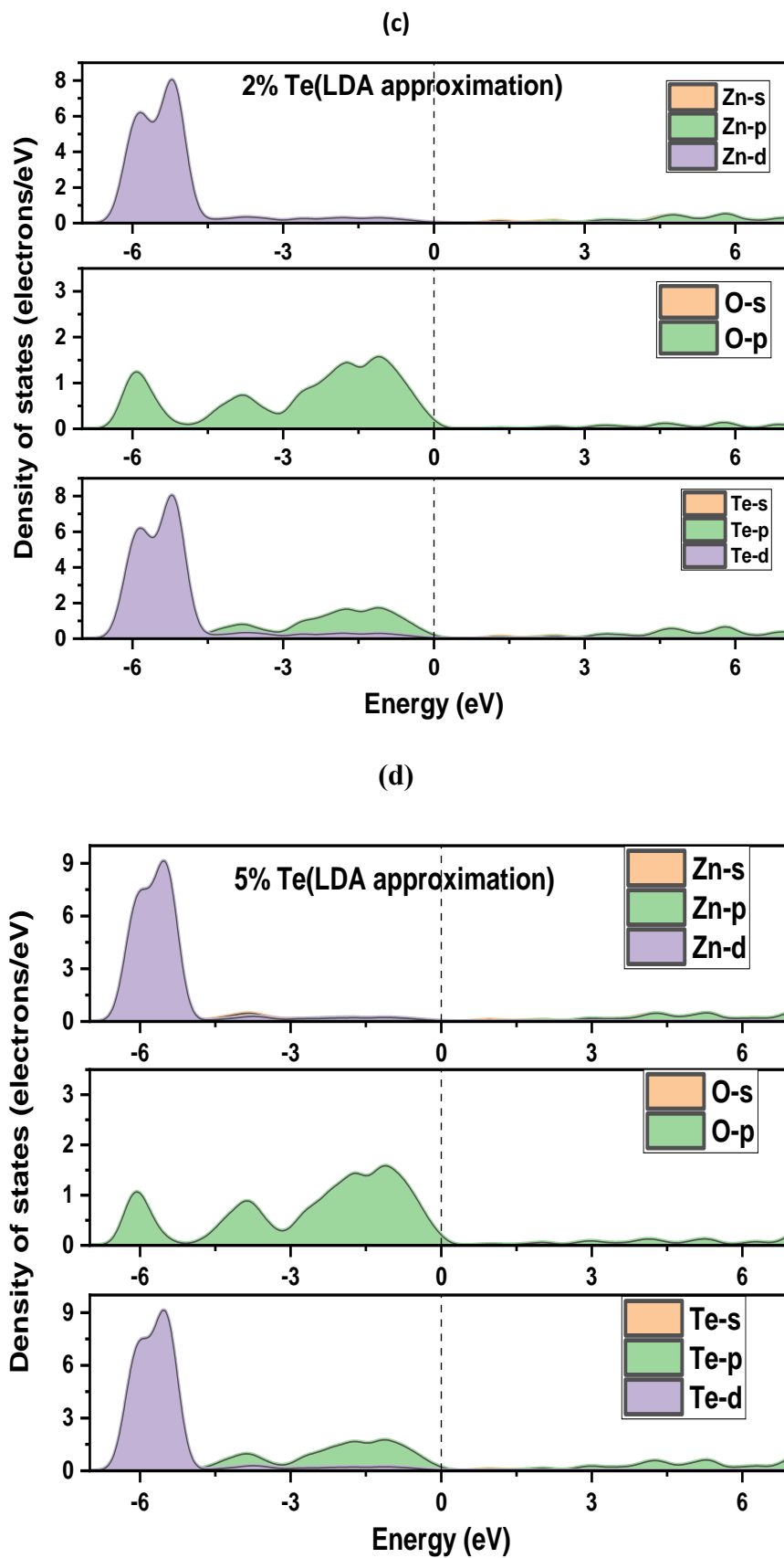
Fig. VI.8: Density of states of $ZnTe_xO_{1-x}$ compounds using LDA approximation.

VI.3.3 Optical Properties

VI.3.3.1 Absorption A

The results of research show that the absorption of pure ZnO has a broad absorption band in the ultraviolet region (see Fig. VI.9), with a peak at around 284 nm. This is followed by a small absorption band in the visible region, with a peak at around 550 nm. The absorption is then negligible in the infrared region. The absorption in the ultraviolet region is due to the presence of a band gap in the electronic structure of ZnO. The band gap is the energy difference between the valence band and the conduction band. Electrons can only be excited from the valence band to the conduction band by absorbing photons of light with energy equal to or greater than the band gap.

The absorption spectrum of ZnO shows a broad absorption band in the ultraviolet region. The absorption coefficient in this region is highest at around 284 nm, which corresponds to the band gap of ZnO (Table VI.5). This band gap is caused by the difference in energy between the valence band and the conduction band. The valence band is filled with electrons, while the conduction band is empty. Electrons can only be excited from the valence band to the conduction band by absorbing photons of light with energy equal to or greater than the band gap. The absorption spectrum also shows a small absorption band in the visible region (Table VI.5). The absorption coefficient in this region is highest at around 550 nm. This absorption band is due to the presence of defects in the crystal structure of ZnO. These defects can trap electrons and holes, which can then recombine and emit light.

The absorption in the visible region is due to the presence of defects in the crystal structure of ZnO. These defects can trap electrons and holes, which can then recombine and emit light. The implications of these results for the potential applications of ZnO are as follows:

- The absorption in the ultraviolet region makes ZnO a promising candidate for applications such as sunscreens and anti-fouling coatings. Sunscreens can protect the skin from the harmful effects of ultraviolet radiation, while anti-fouling coatings can prevent the growth of marine organisms on ship hulls and other surfaces.

- The absorption in the visible region could also make ZnO useful for applications such as optoelectronic and photovoltaic devices. Optoelectronic devices use light to control the flow of electricity. For example, ZnO can be used to make solar cells, light-emitting diodes, and lasers.

Overall, the results of your research are very promising. They suggest that ZnO has a wide range of potential applications.
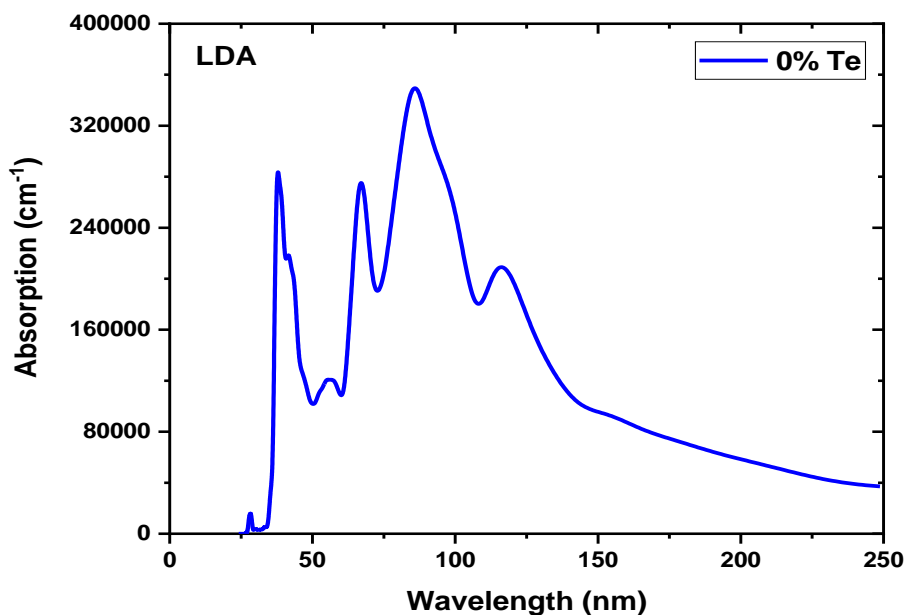
Fig. VI.9: Absorption as a function wavelength for pure ZnO compound using LDA approximation.

Table VI.5: Absorption as a function wavelength for pure ZnO compound using LDA approximation.

Wavelenth (nm)	Absorption values
27.8157775 - 38.5316917	1697.79287 – 284210.526
38.5316917 – 55.0615595	284210.526 – 119185.059
55.0615595 – 62.8134975	119185.059 – 108545.557
62.8134975 – 66.6894665	108545.557 – 274023.769
66.6894665 – 74.4414045	274023.769 – 195132.994
74.4414045 – 86.0693114	195132.994 – 349179.4
86.0693114 – 106.361149	349179.4 – 179739.672
106.361149 – 119.015048	179739.672 – 207696.661
$\geq$ 119.015048	21958.1211

VI.3.3.2 Reflectivity R

The reflectivity of pure ZnO shows a sharp increase in the ultraviolet region, followed by a sharp decrease in the visible region, and then a gradual increase in the infrared region. This is due to the band gap of ZnO, which is 3.37 eV (See Fig. VI.10). The reflectivity of ZnO is low in the ultraviolet region, and then it increases in the violet region. The violet region is the shortest wavelength region of visible light. The photon energy of violet light is higher than the band gap of ZnO, so it can excite electrons from the valence band to the conduction band. This is why the reflectivity of ZnO is high in the violet region.

The reflectivity is low in the visible region because the photon energy is not high enough to excite electrons from the valence band to the conduction band. The reflectivity is high in the infrared region because the photon energy is not high enough to excite electrons from the valence band to the conduction band, but it is high enough to interact with phonons in the material. In summary, the reflectivity of ZnO is high in the ultraviolet and infrared regions, and low in the visible region (Table VI.6). This is due to the band gap of ZnO. The reflectivity of ZnO can be used to design devices with specific optical properties.
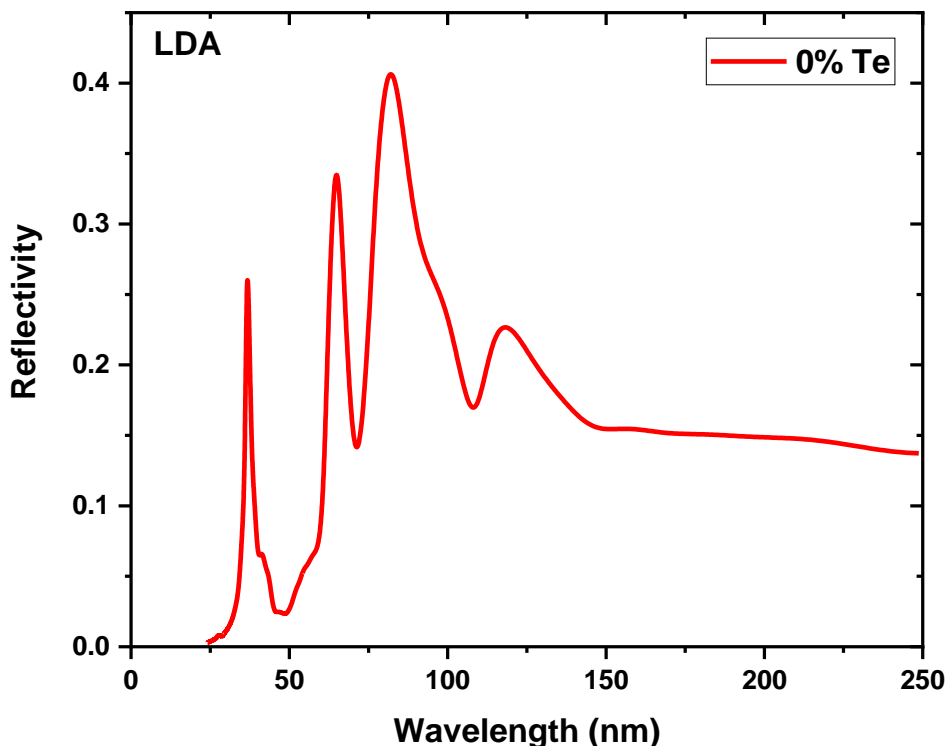
Fig. VI.10: Reflectivity curve as a function wavelength for pure ZnO compound using LDA approximation.

Table. VI.6: Reflectivity values as a function wavelength for pure ZnO compound using LDA approximation.

Wavelenth (nm)	Reflectivity values
24.9658003 – 37.619699	0.00305602716 – 0.260144312
37.619699 – 47.1956224	0.260144312 – 0.0230475382
47.1956224 – 65.6634747	0.0230475382 – 0.33106961
65.6634747 – 71.9334245	0.33106961 – 0.144397284
71.9334245 - 82.5353397	0.144397284 – 0.403650255
82.5353397 – 108.299134	0.403650255 – 0.17139219
108.299134 – 117.647059	0.17139219 – 0.225509338
117.647059 - 149.566803	0.225509338 – 0.153565365
≥ 149.566803	0.153565365

VI.3.3.3 Refractive index

As indicated in Fig. VI.11 for pure ZnO compound, the refractive index of ZnO is highest in the ultraviolet region (24.9658003 – 35.5677155 nm) and decreases as the wavelength increases. This is because the photon energy of ultraviolet light is higher than the band gap of ZnO (3.37 eV), and it can excite electrons from the valence band to the conduction band. When this happens, the refractive index increases because the electrons are now free to move around in the conduction band, which changes the way light interacts with the material.

The refractive index of ZnO is lowest in the infrared region (≥ 131.668947 nm) and increases as the wavelength decreases. This is because the photon energy of infrared light is much lower than the band gap of ZnO, and it cannot excite electrons from the valence band to the conduction band.

However, it can interact with phonons in the material, which can cause the refractive index to increase. The extinction coefficient of ZnO is also highest in the ultraviolet region (24.9658003 – 35.5677155 nm) and decreases as the wavelength increases (see Table VI.7).

This is because the absorption of light by ZnO is due to the excitation of electrons from the valence band to the conduction band. The photon energy of ultraviolet light is higher

than the band gap of ZnO, so it can more easily excite electrons from the valence band to the conduction band, which causes the extinction coefficient to increase.

The extinction coefficient of ZnO is lowest in the infrared region ($\geq$ 131.668947 nm) and increases as the wavelength decreases. This is because the photon energy of infrared light is much lower than the band gap of ZnO, and it cannot excite electrons from the valence band to the conduction band.

However, it can interact with phonons in the material, which can cause the extinction coefficient to increase. In summary, the refractive index and extinction coefficient of ZnO both have a maximum in the ultraviolet region and a minimum in the infrared region. This is due to the band gap of ZnO and the interaction of light with phonons in the material.
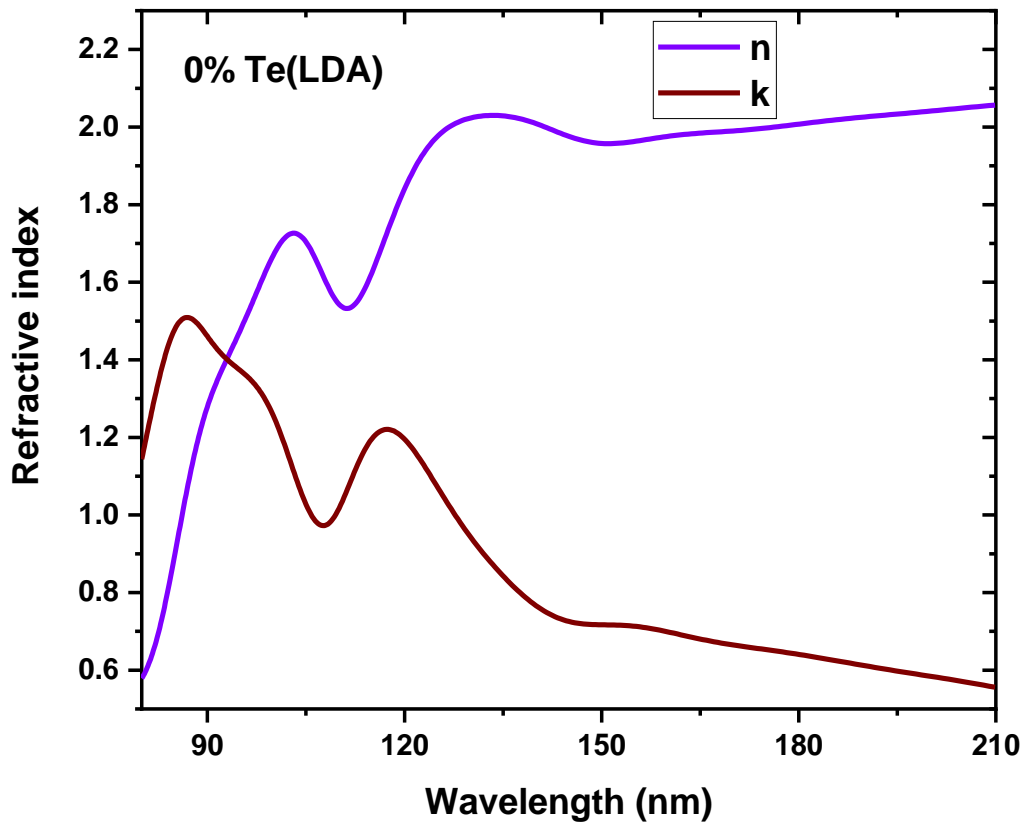
Fig. VI.11: Refractive index curve as a function wavelength for pure ZnO compound using LDA approximation.

Table VI.7: Refractive index values as a function wavelength for ZnTe$_x$O$_{1-x}$ compounds using LDA approximation, (a) n and (b) k.

(a)

Wavelenth (nm)	N
24.9658003 - 35.5677155	0.881932654 - 0.397283531
35.5677155 - 44.3456452	0.397283531 - 0.960101868
44.3456452 - 63.7254902	0.960101868 - 0.412917374
63.7254902 - 69.5394437	0.412917374 – 0.850664969
69.5394437 – 77.2913817	0.850664969 – 0.553621958v
77.2913817 – 101.573187	0.553621958 – 1.70316921
101.573187 -112.175103	1.70316921 – 1.5155631
112.175103 – 131.668947	1.5155631 – 2.01584607
131.668947	2.01584607
≥ 131.668947	2.01584607

(b)

Wavelenth (nm)	K
31.6917465 – 37.5057	0.0137945671 – 0.514077533
37.5057 - 50.1595987	0.514077533 – 0.27221279
50.1595987 – 66.6894665	0.27221279 – 0.92147708
66.6894665 – 75.3533972	0.92147708 – 0.701683645
75.3533972 – 86.9813041	0.701683645 – 1.50728636
86.9813041 – 108.299134	1.50728636 – 0.98401245
108.299134 – 119.015048	0.98401245 – 1.21024335
119.015048 – 243.160055	1.21024335 – 0.459818902
243.160055	0.459818902
≥ 243.160055	0.459818902

VI.3.3.4 Dielectric function

The dielectric function is a complex number that describes the response of a material to an electric field. It is composed of a real part (Re) and an imaginary part (Im). The real part of the dielectric function (Re) describes the ability of a material to store electric energy. The imaginary part of the dielectric function (Im) describes the ability of a material to dissipate electric energy in the form of heat.

The Fig. VI.12 shows the real and imaginary parts of the dielectric function of pure ZnO in different wavelength regions. The wavelength region is measured in nanometers (nm). The real part of the dielectric function of ZnO is negative in the ultraviolet region (24.623803 – 82.7633379 nm). This means that ZnO is a good reflector of ultraviolet light in this region. The real part of the dielectric function of ZnO then becomes positive and increases as the wavelength increases. This means that ZnO becomes a better conductor of electricity in this region. The imaginary part of the dielectric function of ZnO is low in the ultraviolet region. This means that ZnO does not absorb much ultraviolet light in this region. The imaginary part of the dielectric function of ZnO then increases as the wavelength increases. This means that ZnO absorbs more light in this region.

In summary, the real part of the dielectric function of ZnO is negative in the ultraviolet region and becomes positive and increases as the wavelength increases. The imaginary part of the dielectric function of ZnO is low in the ultraviolet region and increases as the wavelength increases. This behavior is due to the band gap of ZnO. The band gap of ZnO is 3.37 eV, which means that ultraviolet light with photon energy higher than 3.37 eV can excite electrons from the valence band to the conduction band. This causes the real part of the dielectric function to become negative. As the wavelength increases, the photon energy of light decreases. This means that less light can excite electrons from the valence band to the conduction band. This causes the real part of the dielectric function to become positive.

The imaginary part of the dielectric function is related to the absorption of light. The absorption of light by ZnO is due to the excitation of electrons from the valence band to the conduction band. This causes the imaginary part of the dielectric function to increase as the wavelength decreases.
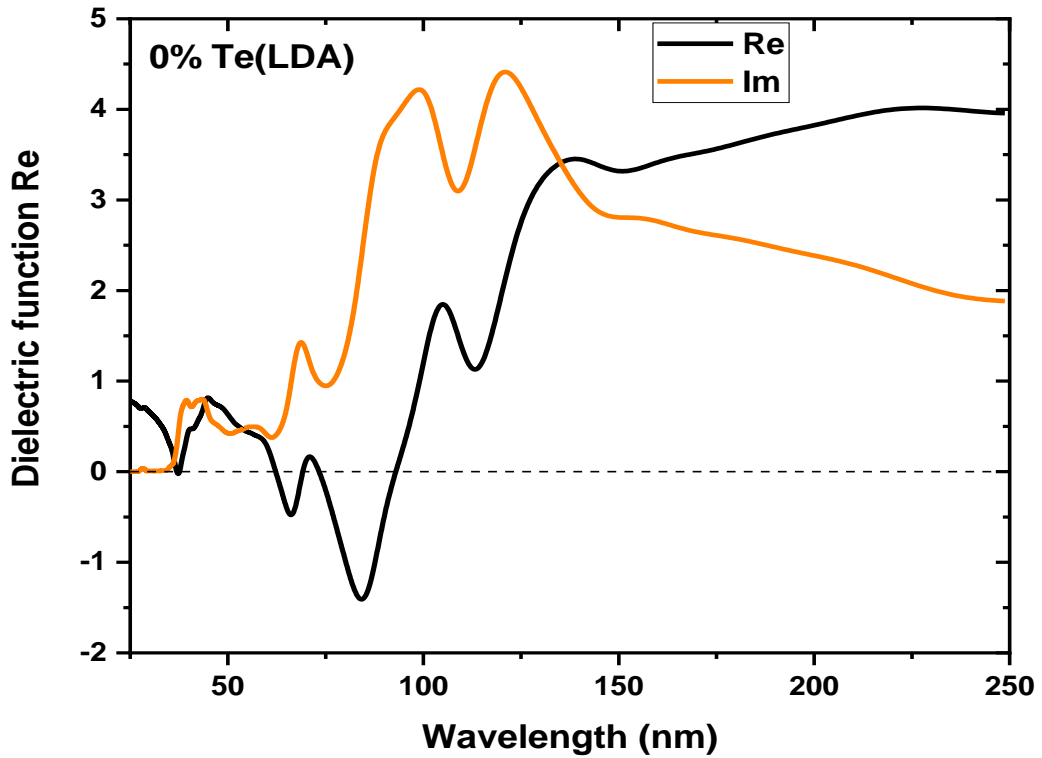
Fig. VI.12: Dielectric function curves as a function wavelength for pure ZnO compound using LDA approximation.

Table VI.8: Dielectric function values as a function wavelength for $ZnTe_xO_{1-x}$ compounds using LDA approximation: (a) Re and (b) Im.

(a)

Wavelenth (nm)	Re
24.623803 - 82,7633379	0.748160724 – (-1.36842105)
82.7633379 - 106,24715	-1.36842105 – 1.84606678
106.24715 - 117,875057	1.84606678 – 1.09451047
117.875057 - 141,130871	1.09451047 – 3.42388229
141.130871 - 224,350205	3.42388229 – 4.07809847
224.350205 - 358,413133	4.07809847 – 3.77023203
358.413133 - 484,496124	3.77023203 – 4.19354839
≥484.496124	4.19354839

(b)

Wavelenth (nm)	Im
30.5517556 – 40.127679	0.0169779287 – 0.825127334
40.127679 – 55.6315549	0.825127334 – 0.460667799
55.6315549 – 67.2594619	0.460667799 – 1.34578381
67.2594619 – 78.8873689	1.34578381 – 0.960950764
78.8873689 – 96.4432285	0.960950764 – 4.2139219
96.4432285 – 111.947104	4.2139219 – 3.09564233
111.947104 – 117.875057	3.09564233 – 4.44482173
117.875057 – 325.353397	4.44482173 – 1.53820034
325.353397 – 410.624715	1.53820034 – 1.90265988
410.624715	1.90265988
≥ 410.624715	1.90265988

VI.4 Conclusion

In this section, we have investigated the effect of doping zinc oxide with tellurium in very small proportions on the structural, electronic, and optical properties of the material. We have shown that doping with tellurium in very small proportions can have a significant effect on these properties, leading to changes in the lattice constant, volume, bulk modulus, band gap, and state density. These changes have implications for the potential applications of zinc oxide, such as in optoelectronic devices, solar cells, and photocatalysis. The results of this study suggest that tellurium is a promising dopant for zinc oxide, even in very small proportions.

These results are consistent with the band structure of zinc oxide, which has a band gap of about 3.37 eV. The absorption coefficient of zinc oxide increases in the ultraviolet region because the photons in this region have enough energy to excite electrons from the valence band to the conduction band. The reflectivity of zinc oxide is high in the visible and infrared regions because the photons in these regions do not have enough energy to excite electrons from the valence band to the conduction band. The refractive index of zinc oxide increases in the ultraviolet region because the photons in this region interact more strongly

with the electrons in the material. The dielectric function of zinc oxide is negative in the ultraviolet region because the material is more polarizable in this region.

The results of this study provide a comprehensive understanding of the optical properties of pure zinc oxide. This knowledge can be used to design and optimize devices that use zinc oxide, such as solar cells, light-emitting diodes, and sensors.

References:

[1]   Zouaneb, A., Benhamied, F., & Rouabhia, A. (2018). First Principles Calculations of Structural, Electronic and Optical Properties of Ternary ZnO Alloys: Te Doped. Lecture Notes in Networks and Systems, 511–518. doi:10.1007/978-3-319-73192-6_54.

[2]   Sönmezoğlu, S., & Akman, E. (2014). Improvement of physical properties of ZnO thin films by tellurium doping. Applied Surface Science, 318, 319-323. doi: 10.1016/j.apsusc.2014.06.187.

[3]   Fattebert, J.-L., & Gygi, F. (2002). Density functional theory for efficient ab initio molecular dynamics simulations in solution. Journal of Computational Chemistry, 23(6), 662–666. doi:10.1002/jcc.10069.

[4]   Pearson, M., Smargiassi, E., & Madden, P. A. (1993). Ab initio molecular dynamics with an orbital-free density functional. Journal of Physics: Condensed Matter, 5(19), 3221–3240. doi:10.1088/0953-8984/5/19/019.

[5]   J. P. Perdew and Y. Wang, "Accurate and Simple Density Functional for the Electronic Structure of Solids," Phys. Rev. Lett. 45 (1980) 566.

[6]   J. P. Perdew, K. Burke, and M. Ernzerhof, "Generalized Gradient Approximation Made Simple," *Phys. Rev. Lett.* 77 (1996) 3865.

[7]   D. R. Hamann, M. Schluter, and C. Chiang, "Norm-conserving pseudopotentials," *Phys. Rev. B* 31 (1979) 2582.

[8]   Bockstedte, M., Kley, A., Neugebauer, J., & Scheffler, M. (1997). Density-functional theory calculations for poly-atomic systems: electronic structure, static and elastic properties and ab initio molecular dynamics. Computer Physics Communications, 107(1-3), 187–222. doi:10.1016/s0010-4655(97)00117-3.

[9]   R. Fletcher, "Practical Methods of Optimization," 2nd ed. (Wiley, New York, 1987).

[10] B. Ngobe1 et all., "Ab-initio techniques, VASP and CASTEP, are used to investigate the electronic properties of B2 compounds formed between Tand group VIII elements - a comparative study," 370, 02005 (2022) https://doi.org/10.1051/matecconf/202237002005 MATEC Web of Conferences.

[11] Iuga, M., Steinle-Neumann, G., & Meinhardt, J. (2007). Ab-initio simulation of elastic constants for some ceramic materials. The European Physical Journal B, 58(2), 127–133. doi:10.1140/epjb/e2007-00209-1.

[12] ZHANG, D., WANG, P., MURAKAMI, R., & SONG, X. (2011). First-principles simulation and experimental evidence for improvement of transmittance in ZnO films. Progress in Natural Science: Materials International, 21(1), 40–45. doi:10.1016/s1002-0071(12)60023-9.

[13] Segall, M. D., Lindan, P. J. D., Probert, M. J., Pickard, C. J., Hasnip, P. J., Clark, S. J., & Payne, M. C. (2002). First-principles simulation: ideas, illustrations and the CASTEP code. Journal of Physics: Condensed Matter, 14(11), 2717–2744. doi:10.1088/0953-8984/14/11/301

[14] S. J. Clark, M. D. Segall, C. J. Pickard, P. J. Hasnip, M. I. J. Probert, K. Refson, M. C. Payne, " Vienna Ab initio Simulation Package (VASP)" (2005).

[15] J. Serrano, Y. Tech, A. H. Romero, and R. Lauck, "Pressure dependence of the lattice dynamics of ZnO: An ab initio approach," no. March, 2004.

[16] Y. Yu, J. Zhou, H. Han, and C. Zhang, "Ab initio study of structural, dielectric, and dynamical properties of zinc-blende ZnX (X = O, S, Se, Te)," vol. 471, pp. 492–497, 2009.

[17] B. Bahloul *et al.*, "Ab initio study of the structural, electronic and optical properties of ZnTe compound," *AIP Conf. Proc.*, vol. 1653, no. January, 2015.

[18] S. K. Gupta, S. Kumar, and S. Auluck, "Structural, electronic and optical properties of high-pressure stable phases of ZnTe," *Phys. B Condens. Matter*, vol. 404, no. 20, pp. 3789–3794, 2009.

[19] R. Khenata, A. Bouhemadou, M. Sahnoun, A. H. Reshak, H. Baltache, and M. Rabah, "Elastic, electronic and optical properties of ZnS, ZnSe and ZnTe under pressure," *Comput. Mater. Sci.*, vol. 38, no. 1, pp. 29–38, 2006.

CHAPTER VII

Investigation of the properties of ZnX (X = Te, S and O) material: Application to photovoltaic solar cells

Chapter VII: Investigation of the properties of ZnX (X = Te, S and O) material: Application to photovoltaic solar cells

VII.1 Introduction

Zinc monochalcogenides, specifically ZnX (with X encompassing Te, S, Se, and O), serve as exemplary representatives of II-VI semiconductors and have the ability to adopt either zinc-blende (ZnX-z) or wurtzite (ZnX-w) crystal structures. Notably, ZnX-z phases exhibit optical isotropy, while ZnX-w phases display anisotropy, with the c-axis serving as the polar axis (B.G. Svensson, 2018) [1].

Zinc oxide (ZnO), featuring a wide direct band gap of approximately 3.37 eV at room temperature, emerges as a quintessential semiconductor employed extensively in optoelectronic applications. Furthermore, ZnO exhibits transparency within the visible light spectrum and possesses the added advantage of environmental friendliness, attributed to the abundant presence of zinc in the Earth's crust (M. Lee *et al.*, 2014) [2].

Among the family of IIB-VIA compounds, namely ZnS, ZnSe, and ZnTe, these materials crystallize in the cubic zinc-blende structure under ambient pressure, boasting direct energy band gaps (R. Khenata, 2006) [3].

Notably, these wide band-gap semiconductors are of paramount interest due to their capability to emit light even at room temperature (Y. Yu *et al.*, 2009) [4]. Zinc Telluride (ZnTe) garners particular attention owing to its cost-effectiveness, high optical absorption coefficient, and suitability for photovoltaic (PV) applications (S. Jeetendra *et al.*, 2014) [5]. Moreover, ZnTe has significantly contributed to the realms of microelectronics and optoelectronics (S.M. Ali *et al.*, 2018) [6].

Researchers have undertaken diverse studies to delve into the electronic, structural, and dynamic properties of zinc-based semiconductors. For instance, (Zheng *et al.*, 2012) [7] utilized ab-initio methods for the comprehensive calculation of these properties. (D. Bahri *et al.,* 2015) [8] explored the structural, electronic, and optical attributes of the cubic zinc-blende phase of ZnTe, characterized by the F-43m space group [8]. In a similar vein, (J. Serrano *et al.,* 2004) [9] harnessed ab-initio techniques to investigate the network dynamics of ZnO. Additionally, (V.O.I. Ume *et al.,* 1970) [10] conducted electronic energy band structure calculations for ZnTe and ZnSe, incorporating spin-orbit coupling via the experimental pseudo-voltage method [10]. The current research focal point centers on an in-

depth exploration of the structural, electronic, and optical features exhibited by ZnX materials (where X encompasses Te, S, and O), with a specific focus on their potential utility in photovoltaic (PV) applications. This investigative endeavor leverages the Density Functional Theory and the GGA/PBE gradient approximation to unravel the intricate properties of these materials.

VII.2 Computational details

In this study, we employed the CASTEP software for our investigations (M. Caid *et al.*, 2022) [11], delving into the structural, electronic, and optical attributes of ZnX compounds, where X represents Te, S, and O. The respective crystal structures for these compounds are characterized by space groups (216 F-43m, 186 P-63mc, 186 P-63mc). Our evaluations led us to determine that employing ($8 \times 8 \times 8$) Brillouin Zone (BZ) k-point densities and planar wave cutoff energies of 750 eV for ZnTe, 850 eV for ZnS, and 800 eV for ZnO sufficed for our analyses.

Generally, the Generalized Gradient Approximation (GGA) method is favored over the Local Density Approximation (LDA) due to LDA's tendency to underestimate lattice parameters and cell volumes, whereas GGA tends to overestimate them. In our approximation of the GGA method, we adopted the Perdew-Burke-Ernzerhof approach (F. Parandin *et al.*, 2019) [12] to estimate the band gap. Our geometric optimization was conducted with precision down to 1×10^{-5} eV/atom, utilizing the Broyden–Fletcher–Goldfarb–Shanno (BFGS) algorithm for relaxation to the lowest energy states. We set force, pressure, and displacement thresholds at 0.001 eV/Å, 0.05 GPa, and 5.0×10^{-4} Å, respectively. Furthermore, we explored the electronic structures and various optical properties, including total and partial densities of states (TDOS and PDOS), to attain a more refined understanding of the material's geometry.

VII.3 Results and discussions

VII.3.1 Structural Properties

In the initial phase of our investigation, we conducted computations to ascertain the equilibrium structural parameters of ZnX (X = Te, S, and O), encompassing essential factors like the lattice constant denoted as a_0, the size modulus represented as B_0, and its first derivative, B'. The crystal structure of ZnX (X = Te, S, and O) is visually depicted in Fig. VII.1. Our primary focus was directed towards the exploration of the structural

characteristics of ZnX, with a particular emphasis on optimizing the lattice constants. The outcomes of these analyses are meticulously documented in Table VII 1. To affirm the accuracy and reliability of our study, we meticulously compared our results with the existing theoretical and experimental data, which are conveniently summarized in Table VII 1 for reference. Our computations have unveiled that the lattice constant a_0 assumes values of 6.28 Å for ZnTe, 5.62 Å for ZnS, and 3.25 Å for ZnO. It is noteworthy that these computed values exhibit a slight deviation from the experimentally recorded ones, which stand at 6.1 Å [13], 5.41 Å [13], and a = 3.249 Å, c = 5.204 Å [9], respectively. However, this variance can be attributed to distinctions in the atomic radii of ZnTe, ZnS, and ZnO, along with variations in the total energies, lattice relaxation constants, volume coefficients, and ground state energies inherent to each material.

(a)   (b)   (c)
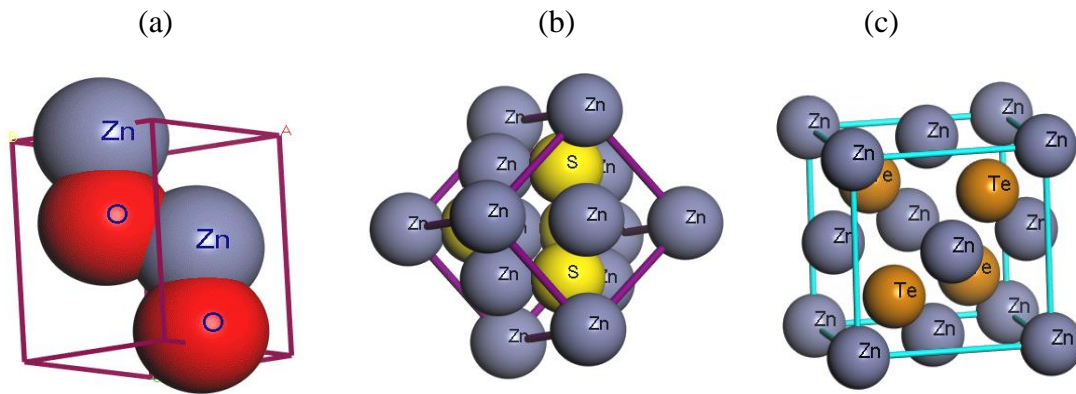
Fig. VII.1: Crystal structures of: (a) ZnO, (b) ZnS and (c) ZnTe compounds.

We conducted structural optimizations of ZnTe, ZnS, and ZnO under various pressure conditions by employing the Murnaghan equation of state (F.D. Murnaghan, 1944) [14]. This equation effectively describes the relationship between the total energy and volume, and it is expressed as follows:

$$E(V) = E_0 + \left[\frac{B_0 V}{B'(B'-1)}\right] \cdot \left[B'\left(1 - \frac{V_0}{V}\right) + \left(\frac{V_0}{V}\right)^{B'} - 1\right] \qquad (VII.1)$$

Here, V_0, B_0, and B' represent the equilibrium volume, the bulk modulus, and its derivative. The compressibility modulus and its pressure derivative, B', can be expressed as follows:

$$B' = \frac{\partial B}{\partial P} \qquad (VII.2)$$

The table VII 1 provided in our work presents the fits for our data related to the relative lattice constant a_0 (Å), bulk modulus B_0 (GPa), and volume V(Å^3).

Table VII.1: Calculated lattice constant a_0 (Å), bulk modulus B (GPa) for ZnX (X = Te, S and O) compound compared with already published data.

Compound	a_0(Å)	V(Å³)	B_0(GPa)	B'
ZnTe	6.28[n]	61.986[n]	41.30[n]	4.266[n]
	6.187[d]	52.66[b]	49.70[b]	4.45[b]
	4.43[a]	52.96[c]	51.40[c]	4.50[c]
	6.103[i]	56.73[j]	55.21[h]	4.60[h]
	6.16[e]	58.73[b]	45.20[j]	4.63[j]
	6.00[h]	56.82[b] Exp.	45.25[b]	4.26[b]
	6.17[b]		50.9[h] Exp.	5.04[h] Exp.
	6.1[e] Exp			
ZnS	5.62[n]	44.60[n]	62.043[n]	4.094[n]
	5.451[d]		75.6[e]	4.44[h]
	5.44[e]		89.67[h]	4.00[h] Exp.
	5.342[h]		75[h] Exp.	
	5.41[e] Exp			
ZnO	3.250[n]	55.126[n]	115.923[n]	4.486[n]
	a = 3.244[d]	45.82[d]	159.5[g]	4.5[g]
	c = 5.027[d]	47.719[f]	128.72[i]	4.38[i]
	a = 3.249[f]	49.461[k]	183[g] Exp.	4[g] Exp.
	c = 5.216[f]	48.335[k] Exp.		
	a = 3.198[g]			
	c = 5.167[g]			
	a = 3.2496[g] Exp.			
	c = 5.2042[g] Exp.			

[a]4.43 [15], [b] Ref [16], [c] Ref [17], [d] Ref [1], [e] Ref [13], [f] Ref [18], [g] Ref [9], [h] Ref [3], [i] Ref [19], [j] Ref [17], [k] Ref [20], [n] Present calculations.
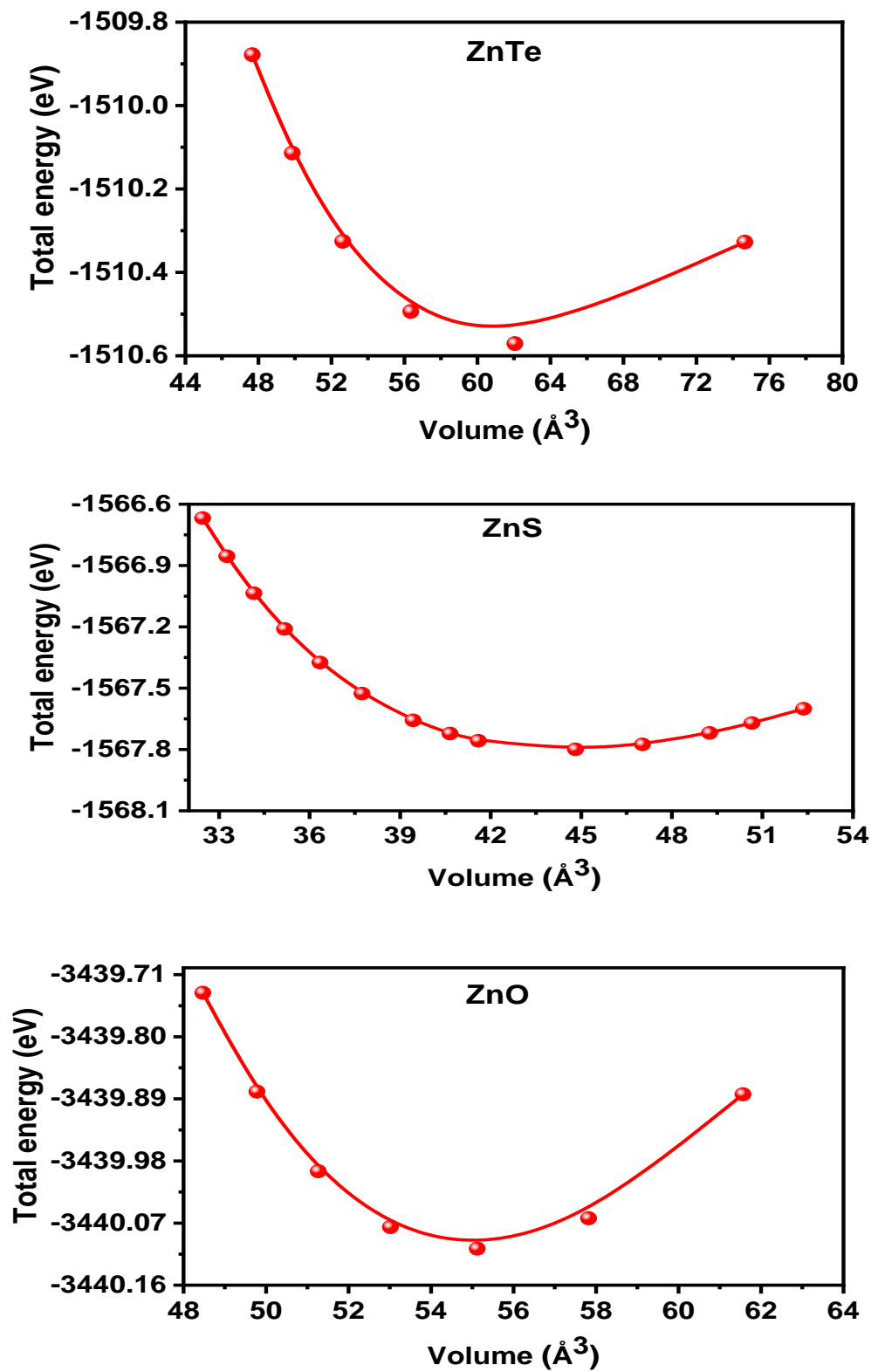

Fig. VII.2: Total energy versus volume for ZnX (X = Te, S and O) compounds.

VII.3.2 Electronic properties

The electronic properties of ZnX (X = Te, S, and O) were explored using band structure analysis and calculations of the total density of states (TDOS) and partial density of states (PDOS) based on optimized values. The band-gap energy, which provides insights into the bonding nature, was a focal point of our investigation, and we employed the PBE-GGA approximation for these calculations. Our computed band-gap results indicated that all three compounds exhibited semiconducting behavior, as depicted in Fig. VII.3. Specifically, the direct band-gap values for ZnX (X = Te, S, and O) were found to be 2.436, 2.698, and 1.721 eV, respectively. The conduction and valence bands were situated above and below the Fermi level, with both meeting at the same point k (G - G), confirming the direct band-gap nature of ZnX (X = Te, S, and O). Table VII.2 presents all the calculated band-gap values for ZnX (X = Te, S, and O) at 0 GPa. It's important to note that these values are consistent with theoretical and experimental data reported in previous references that utilized the PBE-GGA approximation. However, it's worth mentioning that the calculated band-gap values were slightly lower than experimental values, which can be attributed to the known error associated with Kohn-Sham DFT calculations. The relatively higher band-gap energies observed for ZnTe, ZnS, and ZnO compounds suggest their potential for enhanced optical properties.
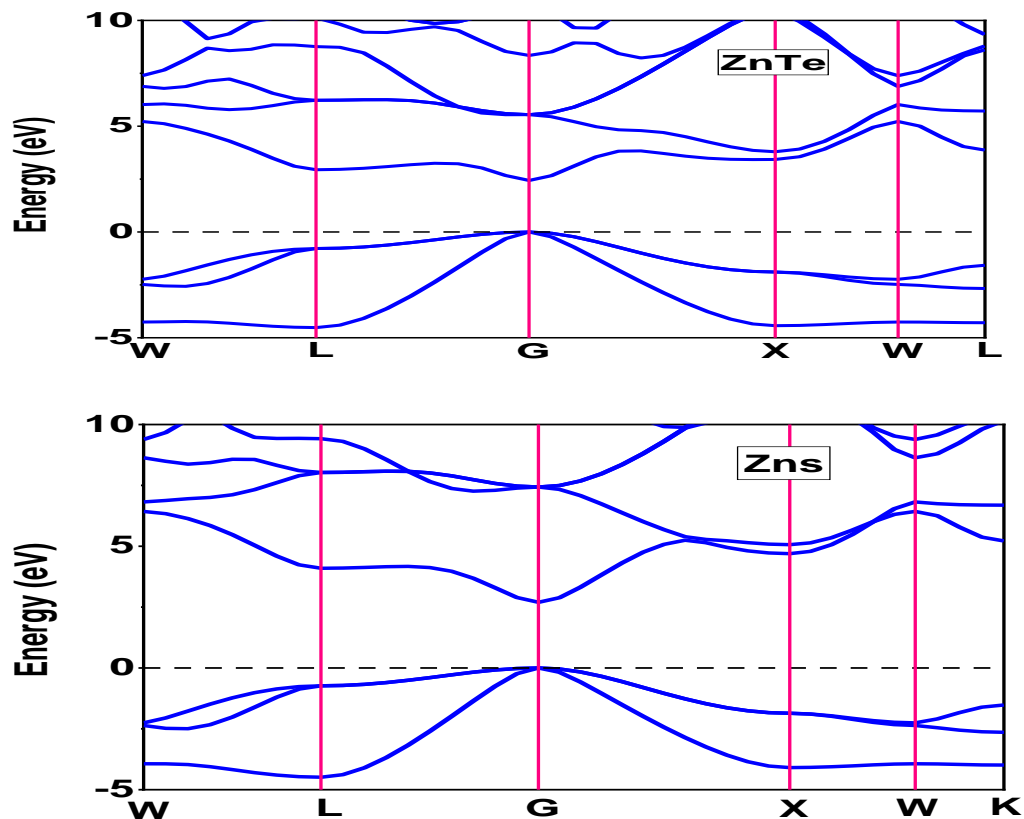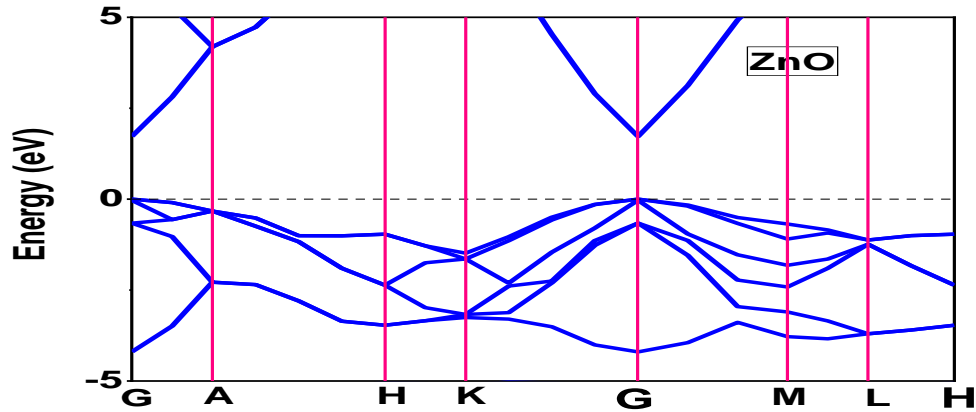
Fig. VII.3: Calculated band structure of ZnX (X = Te, S and O) compounds using PBE-GGA approximation.

Table VII.2. Calculated band-gap value of ZnX (X = Te, S and O) at 0 GPa.

Compound	*This work*	*Other theoretical calculations*	*Experiments*
ZnTe	2.436[n]	1.711[d] 1.804[f]	*2.39[f]*
ZnS	2.698[n]	2.07[e] 2.11[g] 1.317[h] 2.17[j]	*3.68[h]*
ZnO	1.721[n]	0.8[a] 3.38[c] 0.73[k] 3.37[l]	

[a] Ref [21], [c] Ref [18], [d] Ref [22], [e] Ref [23], [j] Ref [24], [k] Ref [25], [g] Ref [26], [h] Ref [27], [l] Ref [28], [n] Present calculations.

To gain a deeper understanding of the band and optical characteristics of ZnX (where X can be Te, S, or O), it is crucial to explore the electronic density of states (DOS) (T. Kato *et al.*, 2019) [29] and its correlation with the band structure. In this investigation, we

determined the DOS and examined its connection with the band structure. We used the partial DOS (PDOS) to illustrate the chemical bonding of ZnX, considering individual atoms, and the total DOS (TDOS) for all atoms. The electronic DOS plays a pivotal role in providing insights into the band structure. Fig. VII.4 displays the TDOS and PDOS obtained through the GGA-PBE approximation, with the Fermi level serving as the reference energy point. The electron configurations for Zn, Te, S, and O were $3d^2 4s^2$, $3s^2 3p^6$, $4s^2 4p^6 5s^2$ and $2s^2 2p^4$, respectively. Around the Fermi level, there are two distinct regions denoted as BV and BC. In all three compounds, the BV region, which spans from -5 eV to 0 eV, is predominantly characterized by Te-p, S-p, and O-p states. On the other hand, the BC region, situated between 0 eV and 5 eV, is mainly influenced by Zn-s-p, Te-s-p, and S-s-p states. These findings are in alignment with previously reported results.
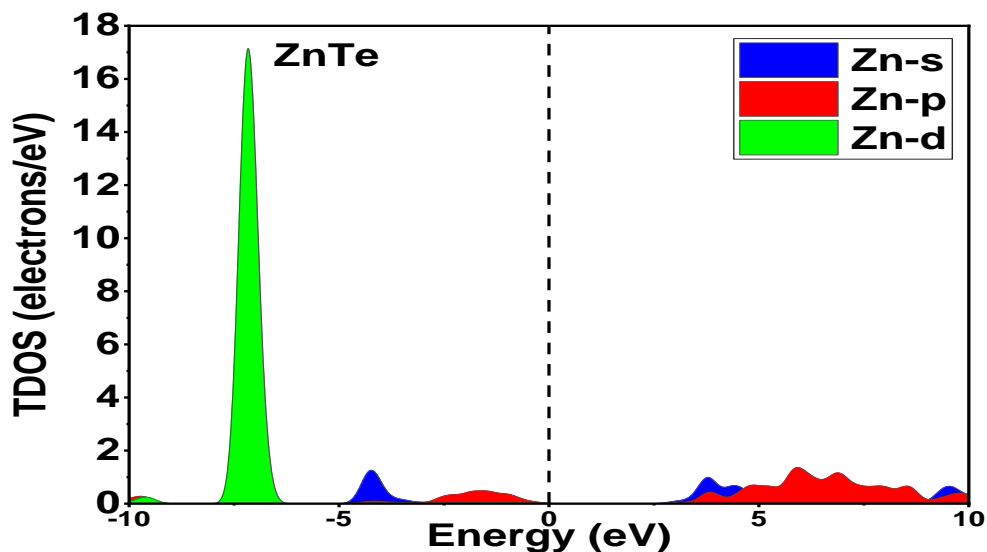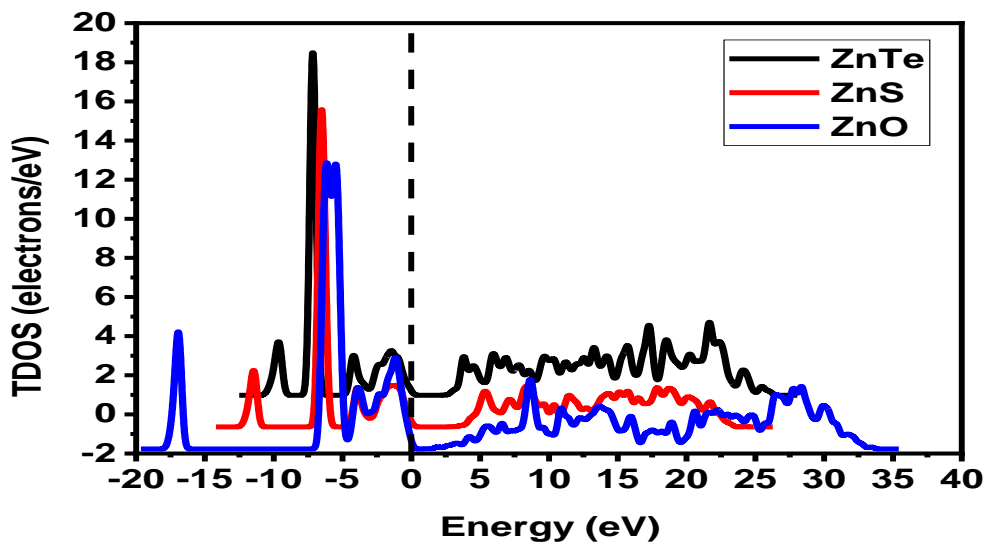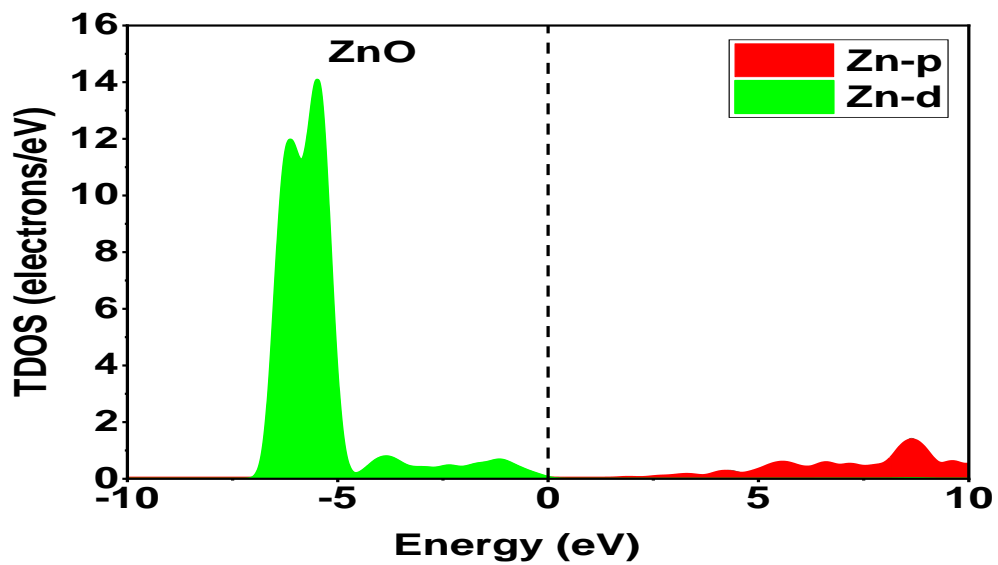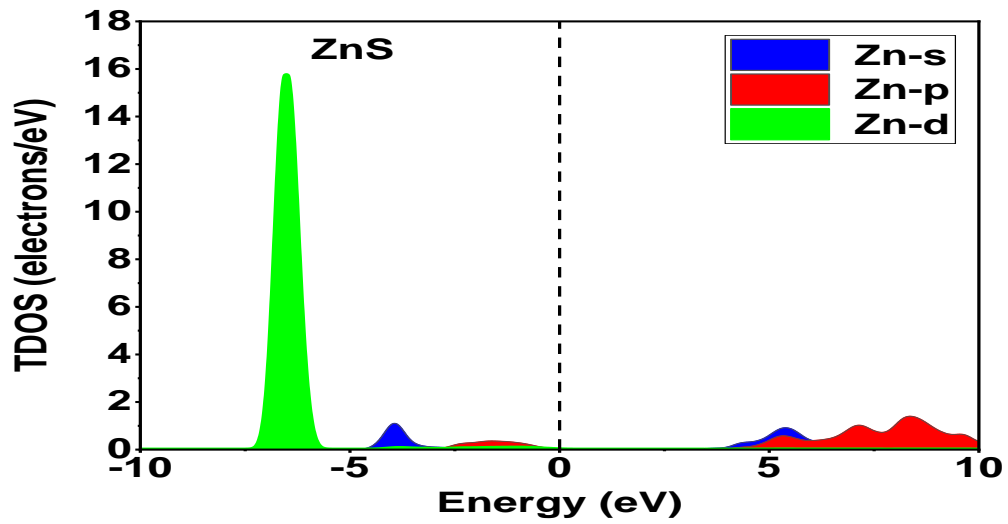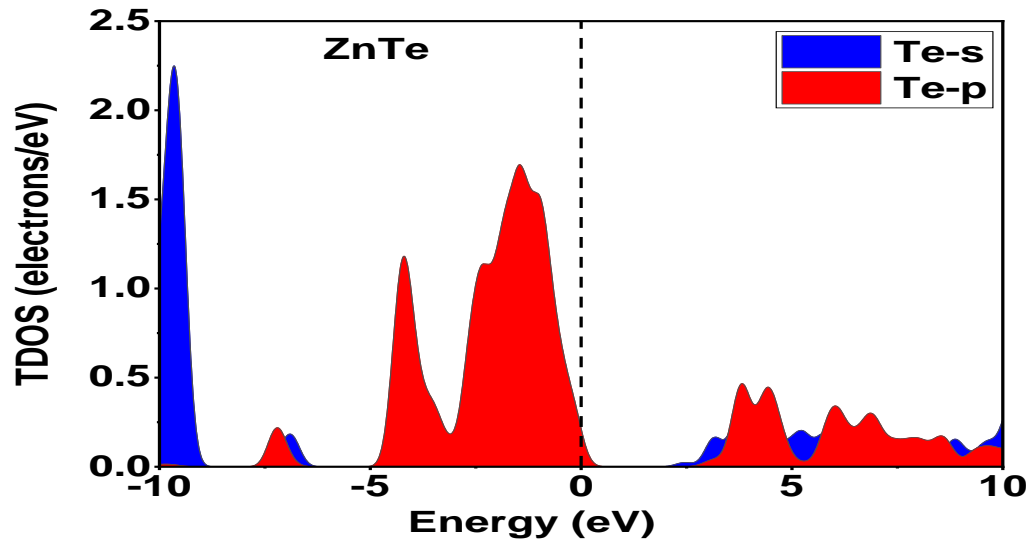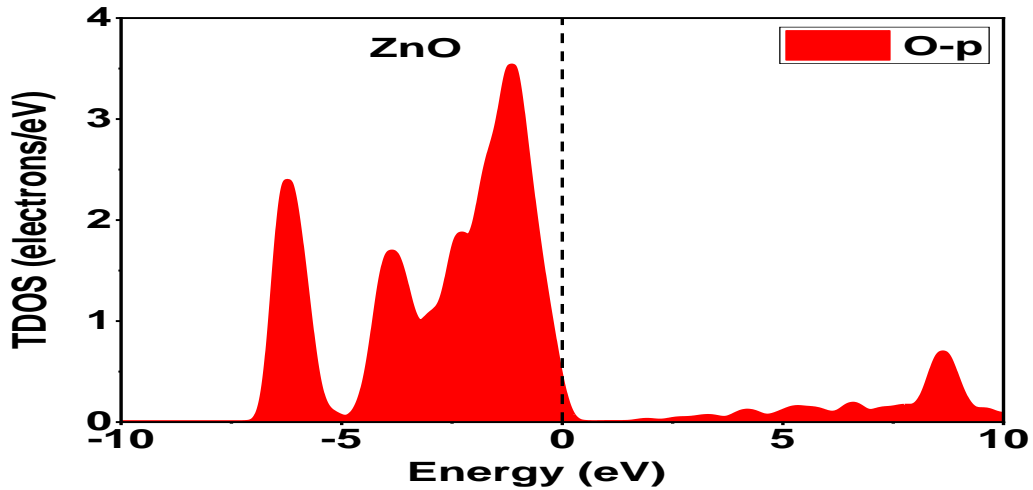
Fig. VII.4. TDOS and PDOS spectra calculated using GGA-PBE approximation of ZnX
(X = Te, S and O) compounds.

VII.3.3 Optical Properties

Examining the photonic characteristics of these compounds is of paramount importance, given their potential utility in photovoltaic technologies and the semiconductor sector. To elucidate the optical attributes of these substances, we employ the transverse dielectric function $\varepsilon(\omega)$ (A. Bouzidi *et al.*, 2017) [30], which enables us to compute the frequency-dependent dielectric constants using the following formula:

$$\varepsilon(\omega) = \varepsilon_1(\omega) + i.\varepsilon_2(\omega) \tag{VII.3}$$

The dielectric function comprises two parts: the real part denoted as $\varepsilon_1(\omega)$ and the imaginary part referred to as $\varepsilon_2(\omega)$ (S.K. Gupta *et al.*, 2009) [31]. $\varepsilon_1(\omega)$ represents the dispersion of incident photons by the material, while $\varepsilon_2(\omega)$ indicates the energy absorbed by the material. The complex dielectric function, $\varepsilon(\omega)$, is composed of two components: intraband and interband transitions [31]. Intraband transitions are significant primarily for metals, whereas interband transitions can be further categorized into direct and indirect transitions. In our study, we disregarded the indirect interband transitions, which involve phonon scattering and have a minimal impact on $\varepsilon(\omega)$. We used the components of the complex dielectric function to derive various optical parameters, including reflectivity (R), refractive index (n), optical conductivity (σ), and absorption (α) (R. Tala-Ighil Zaïr *et al.*, 2021) [32]. Fig. VII.5 to VII.9 illustrate a range of optical characteristics for ZnX (where X can be Te, S, or O), encompassing reflection spectra, absorption spectra, the real and imaginary components of the dielectric function, and photoconductivity.

VII.3.3.1 Reflectivity R

The utilization of computational tools like the CASTEP program enables the precise prediction of the reflectivity (R) for ZnX compounds, where X represents Te, S, or O. For instance, CASTEP simulations have demonstrated that ZnTe exhibits remarkable reflectivity, reaching around 96% in the infrared region, rendering it a promising candidate for applications in infrared detectors and solar cells. Similarly, ZnS and ZnO have displayed elevated reflectivity values in the visible and ultraviolet regions, respectively, with percentages climbing to 87% and 96%. Researchers can tailor the reflectivity of ZnX compounds to match specific requirements by adjusting their composition and morphology. For example, by growing ZnO thin films with a particular orientation, researchers can achieve high reflectivity in the visible light spectrum while preserving transparency. Our analysis, as depicted in Fig. VII.5, demonstrates that the reflectivity peaks of ZnTe, ZnS, and ZnO compounds increase at lower energies (up to 7 eV) and decrease notably at higher energies (below 20 eV), concurrent with the reduction in the forbidden bandwidth.
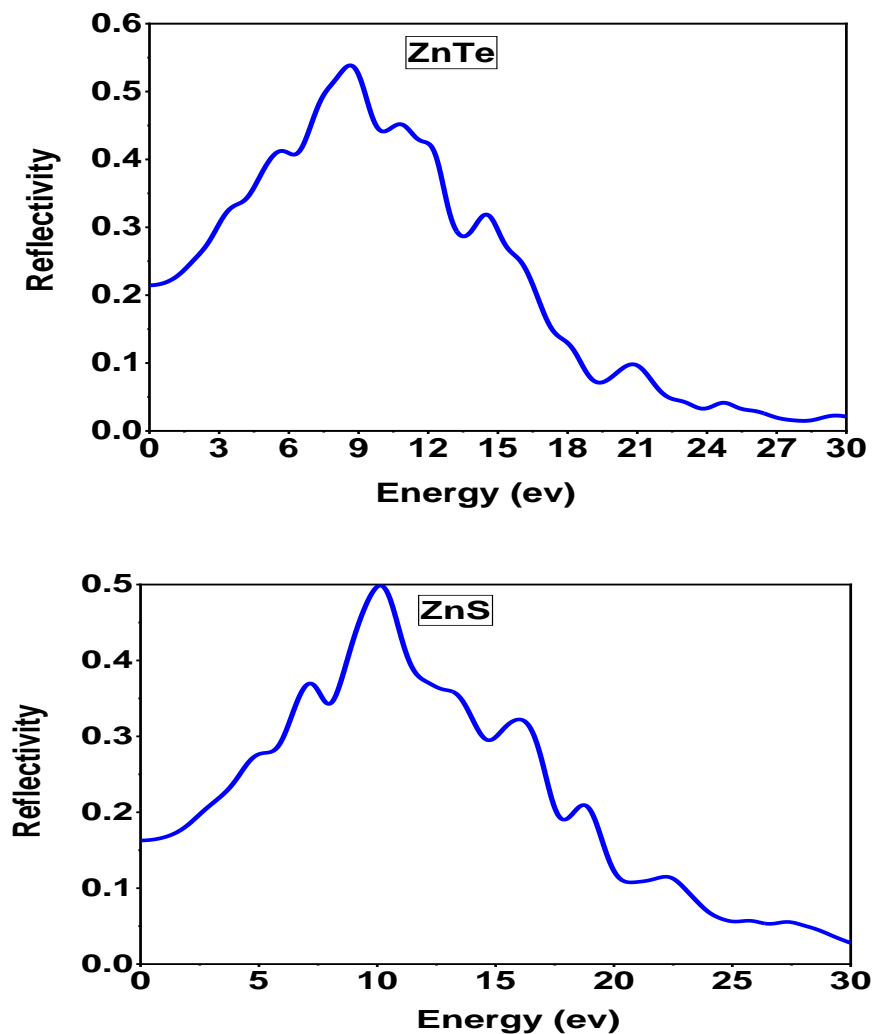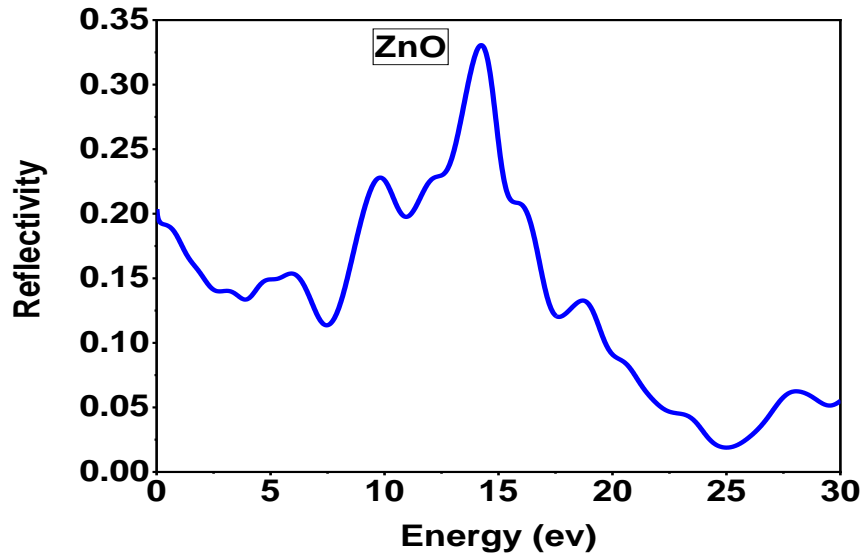
Fig. VII.5: Reflectivity R as a function of energy of ZnTe, ZnS and ZnO compounds calculated using GGA-PBE approximation.

VII.3.3.2 Absorption A

Absorption, represented as A, stands as a significant optical attribute of materials, characterizing the quantity of light absorbed by the substance. The absorption properties of ZnX compounds, where X can represent Te, S, or O, can be precisely anticipated through computational tools like the CASTEP program. The outcomes have revealed that ZnTe exhibits a substantial absorption coefficient, approximately 25×10^4 cm^{-1}, within the mid-infrared spectrum, positioning it as a promising material for mid-infrared detectors and emitters. Similarly, ZnS and ZnO have demonstrated notable absorption characteristics in the ultraviolet and visible spectra, respectively, with values reaching up to 3×10^5 cm^{-1}. By comprehending the absorption attributes of ZnX compounds, researchers can craft materials with specific absorption properties tailored for various optoelectronic applications. Our research suggests that when it becomes easier to excite additional electrons from the valence band to the conduction band, less energy is necessary, leading to a redshift at the absorption edge. In such circumstances, the likelihood of valence band electrons transitioning to the excited state increases, resulting in a noticeable augmentation in the number of absorption peaks. Our findings, as presented in Fig. VII.6, indicate that the highest transmittance for ZnX (where X = Te, S, and O) is situated within the energy range of 0 eV to 5 eV, predominantly falling within the infrared spectrum.

Fig. VII.6: Absorption A as a function of energy of ZnTe, ZnS and ZnO compounds calculated using GGA-PBE approximation.

VII.3.3.3 Refractive index

The refractive index, symbolized as n, is a crucial optical characteristic that defines the manner in which light travels through a substance. Computational tools like the CASTEP program enable the precise prediction of the refractive index for ZnX compounds, where X can denote Te, S, or O. We have demonstrated that ZnTe boasts an approximate refractive index of 2.5 within the mid-infrared range, positioning it as a promising material for applications such as infrared lenses and waveguides. Similarly, ZnS and ZnO have displayed substantial refractive indices in the ultraviolet and visible regions, respectively, with values

reaching up to 2 and 1.9. By gaining insights into the refractive index of ZnX compounds, researchers can engineer materials with tailored optical properties to suit diverse optoelectronic applications (See Fig. VII.7).

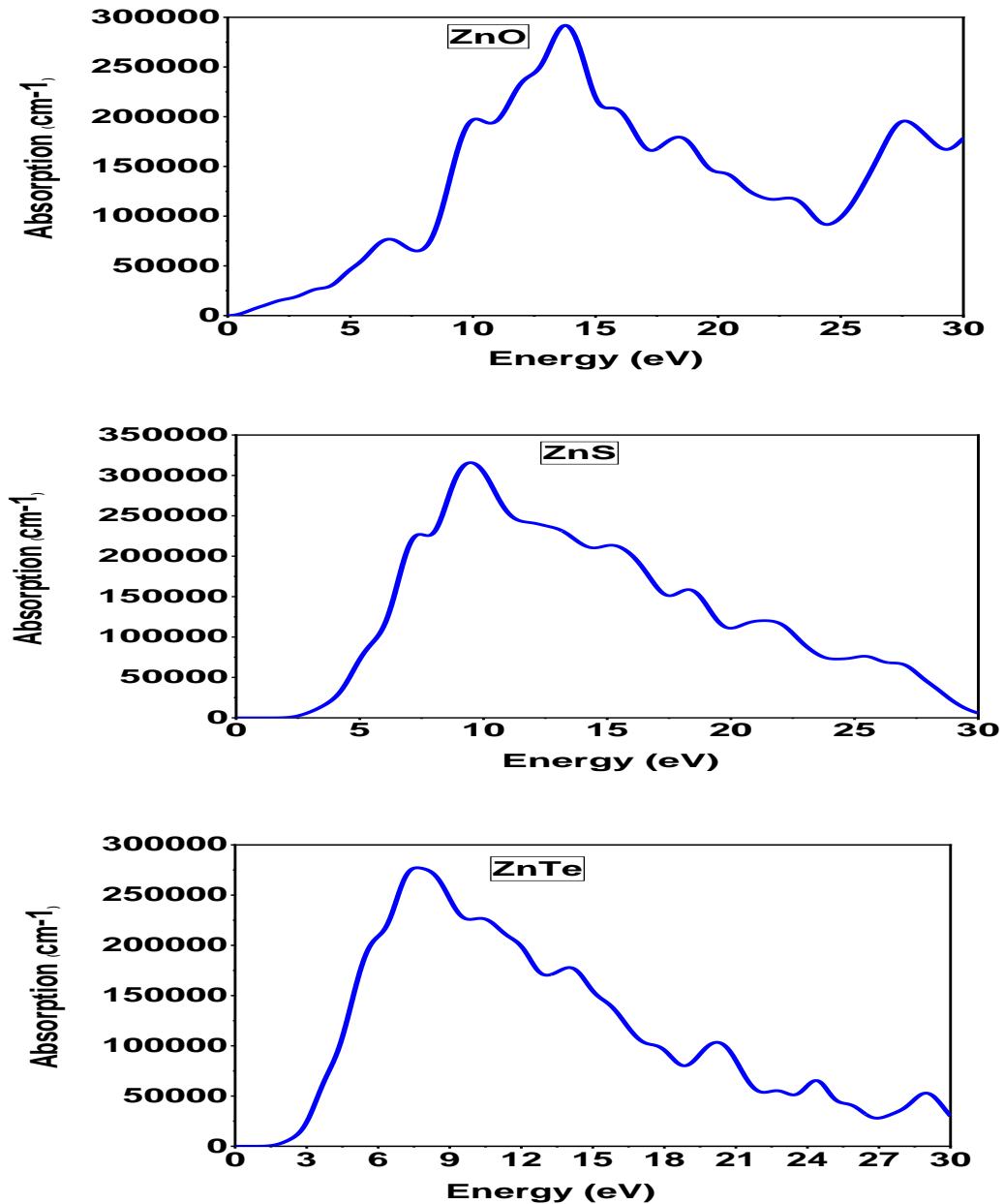**Fig. VII.7:** Refractive index as a function of energy of ZnTe, ZnS and ZnO compounds calculated using GGA-PBE approximation.

VII.3.3.4 Dielectric function

The dielectric function, symbolized as ε, serves as a significant optical characteristic that defines how a material responds to an external electric field. Through simulations employing CASTEP, it has been observed that ZnTe possesses an approximate dielectric function of 12 within the mid-infrared spectrum, positioning it as a promising material for applications like infrared detectors and emitters. In a similar vein, ZnS and ZnO have demonstrated elevated dielectric functions in the ultraviolet and visible ranges, respectively, with values reaching up to 9 and 5. By comprehending the dielectric function of ZnX compounds, researchers can devise materials with tailored optical properties to cater to a variety of optoelectronic applications (Fig. VII.8).
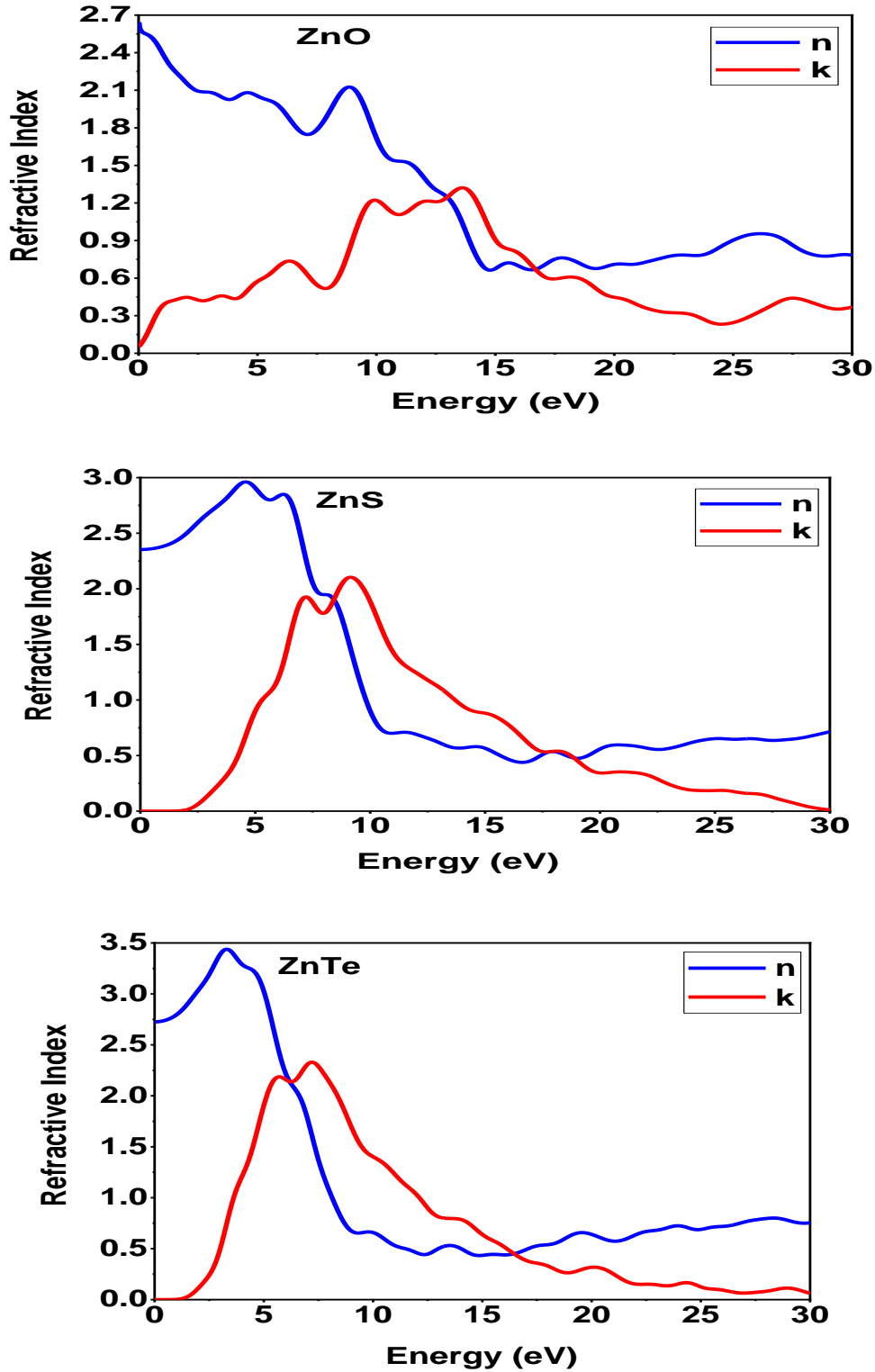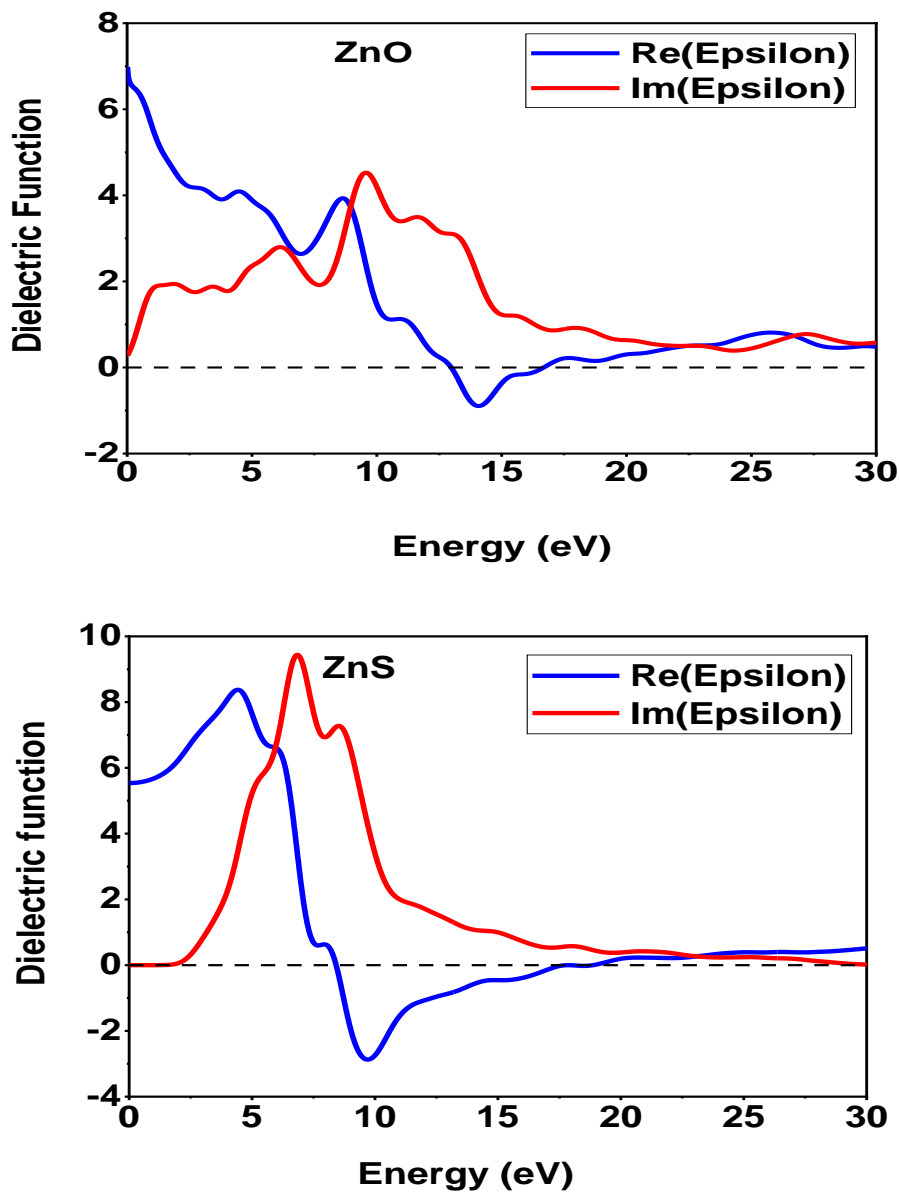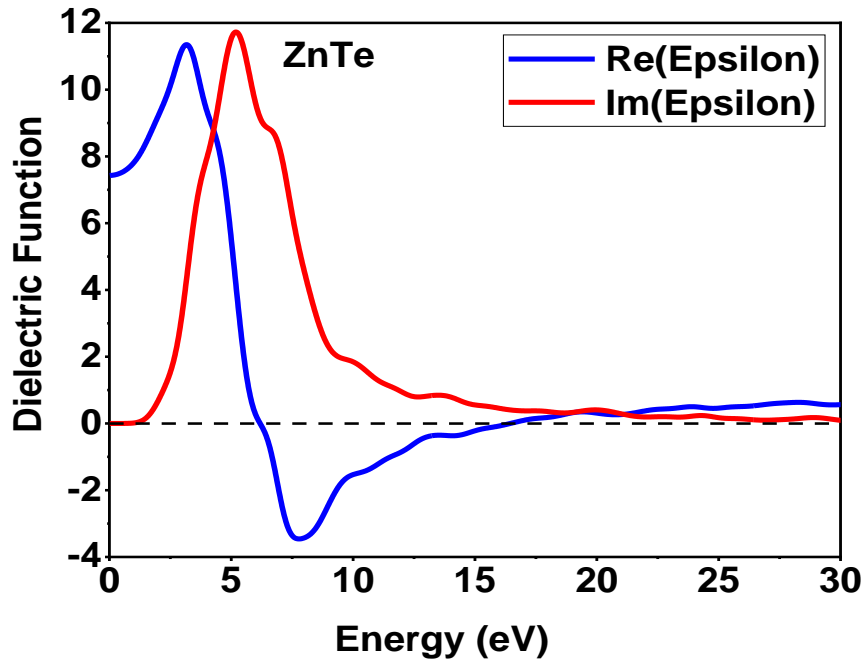
Fig. VII.8: Dielectric function as a function of energy of ZnTe, ZnS and ZnO compounds calculated using GGA-PBE approximation.

VII.4 Application to the substrate Cu(In,Ga)Se$_2$ solar cells

The conventional method of fabricating Cu(In,Ga)Se$_2$ (CIGS) thin-film solar cells involves the use of a substrate configuration that incorporates a CdS buffer layer and a doped ZnO or ITO window layer. This configuration has demonstrated conversion efficiencies exceeding 22% (T. Kato *et al.*, 2019) [29]. The exceptional optoelectronic properties of ZnX (X = Te, Se, S …etc) buffer layers have led to increased attention as a potential alternative to CdS buffer layers in recent years (H.I. Abdalmageed *et al.*, 2021) [33]. It is widely believed that the buffer layers play a critical role in preventing shunting through the TCO/CIGS interface, and they should possess suitable properties that help to minimize carrier recombination at the buffer/CIGS interface (C. Platzer-Björkman *et al.*, 2003) [34]. For example, the efficiency of CIGS solar cells decreases significantly due to severe shunting when a conventional ZnO/TCO is directly deposited onto the CIGS layer (Y.-K. Liao et al., 2013) [35]. According to some studies, the buffer layer demonstrated a higher level of electrical resistance compared to the top contact layer, which is highly conductive (A. Bouzidi *et al.*, 2017) [30]. In this study, the use of ZnTe and ZnS as buffer layers in the substrate CIGS solar cell, along with the incorporation of the ZnO layer as a window layer, were investigated.

VII.4.1 Device settings and simulation process

Fig. VII.9 shows schematic of the substrate n++-ZnO/n-ZnS/p-Cu(In,Ga)Se$_2$ and n++-ZnO/n-ZnTe/p-Cu(In,Ga)Se$_2$ solar cell hetero-structures. To study the transport physics of these structures, the SCAPS-1D software solution solves the dipolar issues of the device using the Poisson equation and continuity equations for both electrons and holes. The SCAPS-1D simulator provides a software environment that can accurately replicate the behavior of a real solar cell [32,36]. Typically, the simulation process for a solar cell would require following the steps outlined in Fig. VII.10 through a series of screen-shots. The initial screenshot, labeled (a), displays the standard information input panel of the SCAPS-1D graphical user interface. This panel provides access to input buttons that enable the user to specify the simulation model and view the device's operating conditions, structure, and material parameters. particular layer's structure and material parameters, along with optical properties and defects, are displayed in screenshot (b). The results of light J-V characteristics in the form of a curve and axes are shown in screenshot (c). The simulation uses AM1.5 illumination spectrum with an incident power of 100 mW/cm^2. Table VII.3 summarizes the input parameters of each layer, including thickness, permittivity constant, band gap, electron affinity, electron/hole mobility, effective density of states in conduction/valence band, donor/acceptor concentration, defect concentration, and absorption coefficient within a range of 320 - 1100 nm wavelength. The thermal velocity recombination for holes/electrons at front and back contacts is 1.0×10^7 cm/s. All data that have been previously calculated using CASTEP are being considered in the simulation.
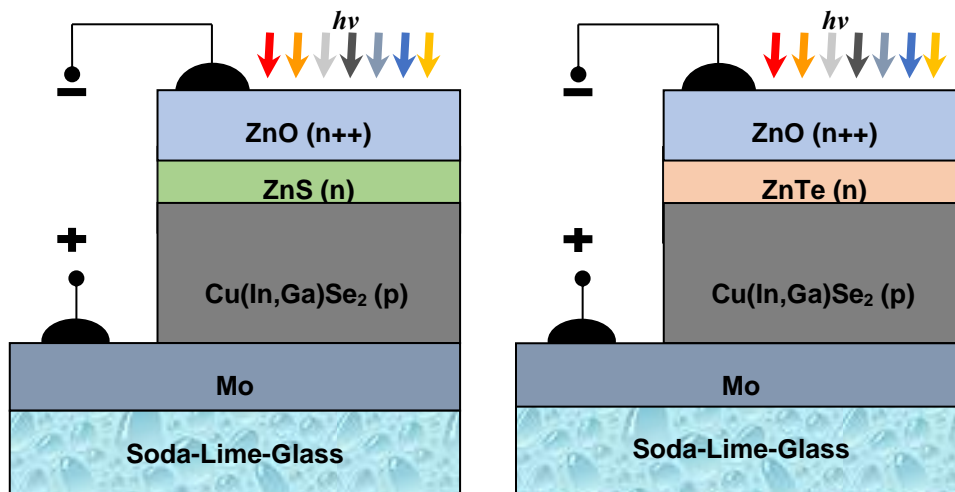
Fig. VII.9: Schematic of the n++-ZnO/n-ZnS/Cu(In,Ga)Se$_2$ and n++-ZnO/n-ZnS/Cu(In,Ga)Se$_2$ solar cell structures.
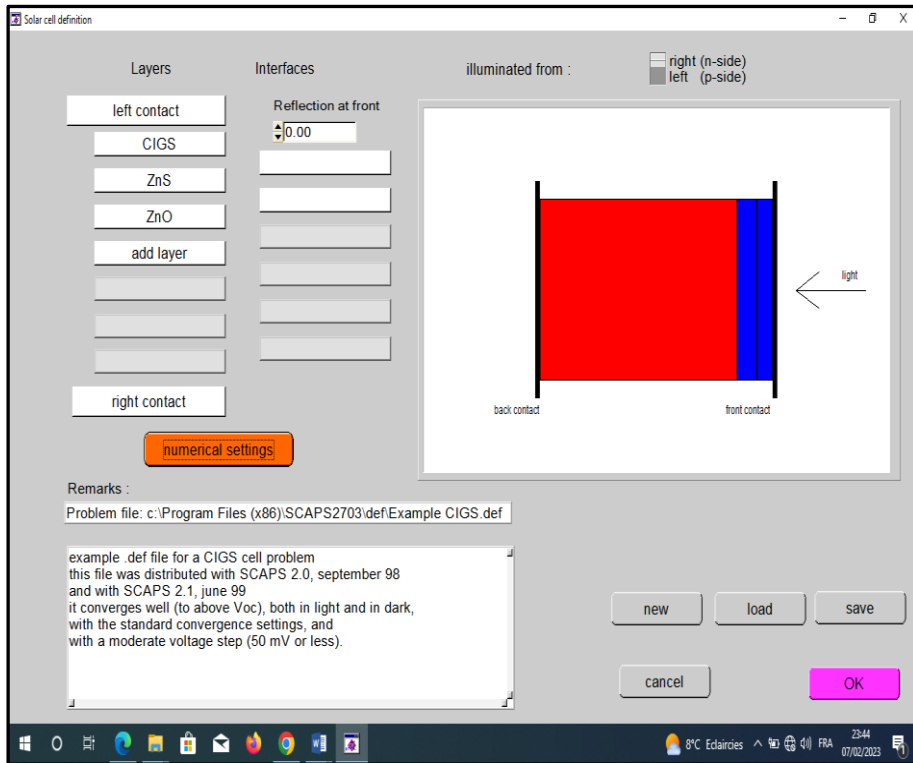
(a)
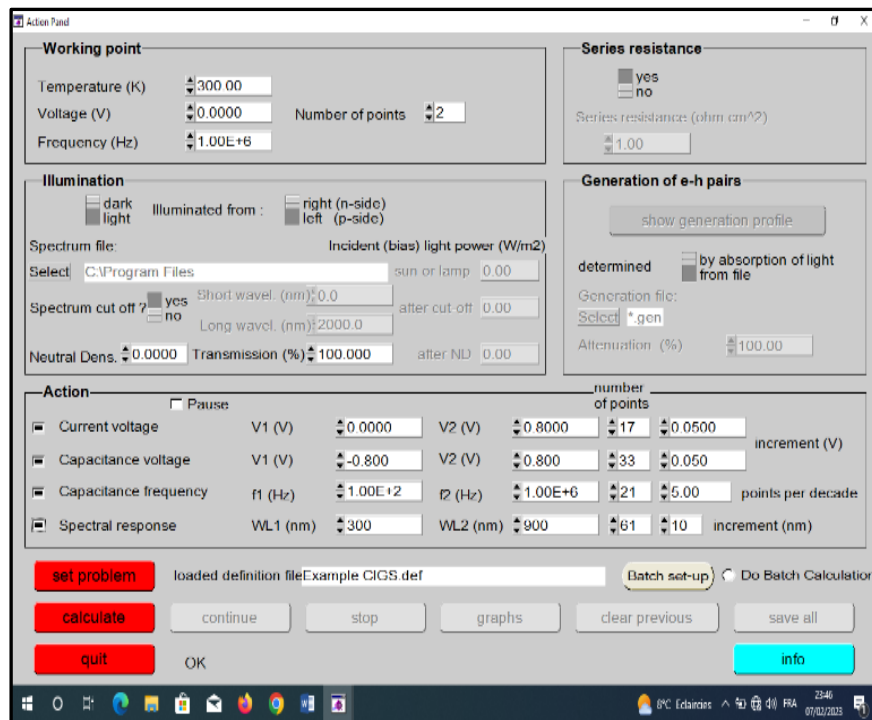
(b)
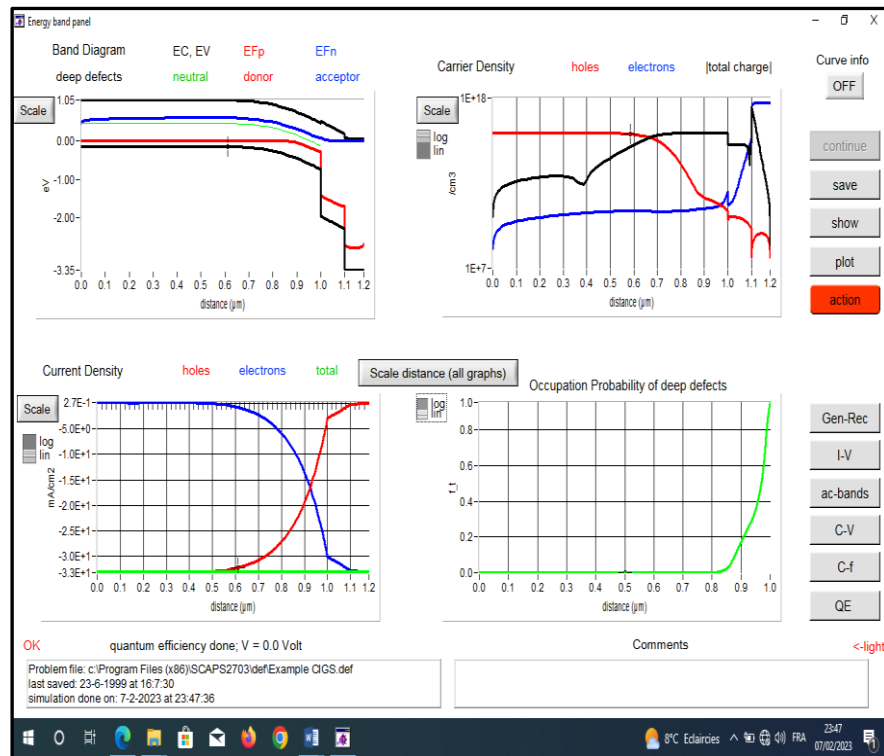
(c)

Fig. VII.10: Typical data input panels of the SCAPS-1D graphical user interface, allowing to configure the solar cell device and its corresponding settings.

Table VII.3: Settings for ZnO, ZnTe, ZnS and Cu(In,Ga)Se$_2$ layers used in the simulation.

Parameters	Cu(In,Ga)Se$_2$ Absorber	ZnTe buffer	ZnS buffer	ZnO window
Thickness (nm)	3000	100	100	*200*
Band gap E$_g$ (eV)	1.12	2.43	2.69	*3.3*
Electron affinity χ$_e$ (eV)	4.1	4.07	4.09	*4.09*
Relative permittivity ε$_r$ (-)	13.6	10	10	*9*
Electron mobility μ$_n$ (cm²/V s)	100	100	100	*100*
Electron mobility μ$_p$ (cm²/V s)	25	25	25	*25*

Conduction band effective density of states N_C (cm^{-3})	2.0×10^{18o}	2.0×10^{17o}	2.0×10^{17o}	*4.0×10^{19o}*
Conduction band effective density of states N_V (cm^{-3})	2.0×10^{19o}	1.5×10^{1p}	1.5×10^{1p}	*9.0×10^{1o}*
shallow donor density (1/cm^3)	0	1.0×10^{17q}	1.0×10^{17q}	*1.0×10^{18p}*
shallow acceptor density (1/cm^3)	5.5×10^{16r}	0	0	0

[o] Ref [37], [p] Ref [31], [q] Ref [38], [r] Ref [39].

VII.4.2 Effect of CIGS absorber thickness on solar cell performance

In an attempt to determine the most favorable thickness for a high-performance substrate CIGS solar cell that employs ZnTe and ZnS buffer layers, the thickness of the CIGS absorber was modified.

VII.4.2.1 Case of ZnO/n-ZnS/p-CIGS/Mo solar cell structure

It is desirable to reduce the thickness of the absorber layer, *d*(CIGS), in order to lower costs while still maintaining high performance. ZnTe and ZnS buffer layers can help achieve this goal due to the abundance of these materials. In the calculations, the thickness of the buffer layers is fixed at 100 nm. As shown in Fig. VII.12, the short-circuit current density (*J*sc), open circuit voltage (*V*oc), Fill Factor (*FF*), and power conversion efficiency (η) are all affected by the thickness of the CIGS absorber layer. For absorber thicknesses up to 4 µm, *J*sc remains around 32.1 mA/cm^2 and *V*oc is above 0.61 Volt. However, for the thinnest CIGS absorber layer, there is a slight reduction in *V*oc which may be due to an increased influence of recombination at the Mo back contact layer, resulting in a smaller effective minority carrier lifetime. The fill factor slightly increases but remains above 79% for all absorber thicknesses greater than 4 µm. The short-circuit current density and open circuit voltage show a strong dependence on the absorber thickness, *J*sc increases from 29.12 mA/cm^2 to 32.08 mA/cm^2 as the CIGS absorber thickness varies from 1 to 4 µm. For devices thinner than 1 µm, current loss may be due to optical and/or electrical losses. The losses in *J*sc and *V*oc mainly contribute to the conversion efficiency losses. The optimum thickness for the CIGS absorber layer is greater than 4 µm, which results in a maximum conversion efficiency of 15.6% with *FF* = 78.5%, *V*oc = 0.61 Volt and *J*sc = 32.1 mA/cm^2.

Fig. VII.11: Solar cell performance using ZnS buffer layer as a function of the p-CIGS thickness.

VII.4.2.2 Case of ZnO/n-ZnTe/p-CIGS/Mo solar cell structure

Fig. VII.13 presents the performance of ZnO/ZnTe/CIGS/Mo solar cell as a function of CIGS absorber thickness. It shows that the recorded efficiency is 14.66% and 16.58% at the CIGS thickness of 1 µm and 4 µm, respectively.

Fig. VII.12: Solar cell performance using ZnTe buffer layer as a function of p-CIGS thickness.

A comparison of these results with the 16.12% efficiency at 2 µm reveals that decreasing the absorber thickness by 1 µm leads to an 11.58% drop in efficiency, whereas increasing it by 1 µm results in only a 3.8% increase in efficiency. This trend continues to hold for absorber thicknesses more than 2 µm. These findings support the theoretical assumption that a thickness of around 2 µm is sufficient to absorb most of the incident light.

168

However, reducing the absorber layer thickness below this value would bring the back contact too close to the depletion region, which would facilitate electron capture by the back contact during the recombination process. The open circuit voltage (Voc) and short circuit current density (Jsc) increase with the thickness of the absorber layer, primarily due to the longer wavelengths' absorption, which contributes to electron-hole pair generation. When d(CIGS) is greater than 4 µm, the maximum Fill Factor of 79.5% is obtained. The highest efficiency of approximately 16.58%, with FF = 79.5%, Voc = 0.61 Volt, and Jsc = 34.05 mA/cm^2 can be achieved when d(CIGS) is approximately 4 µm.

VII.5 Conclusions

Utilizing computational tools such as CASTEP offers a robust means for designing and enhancing these materials, facilitating the development of advanced optoelectronic devices. In this study, we delved into the electronic structure and optical characteristics of ZnX systems, employing first principles through the pseudopotential approach of density functional theory and the generalized gradient approximation method implemented with CASTEP. Our investigation yielded the following findings: The lattice parameters exhibited varying values, making it feasible to deposit these materials on different substrates. The binary alloy holds particular interest due to its wide bandgap (2.436 eV, 2.698 eV, 1.721 eV) for ZnTe, ZnS, and ZnO, respectively. The results obtained for the structural, physical, and optical properties closely align with existing theoretical and experimental data, affirming the accuracy of our calculation methodology. The properties of pure ZnX materials, where X can be Te, S, or O, suggest significant potential for use in solar cells. Our calculations further indicate that while efficiency increased with absorber thickness, denoted as d(CIGS), the rate of this increase diminished significantly beyond 2 µm. Consequently, it is likely that the ideal thickness for the CIGS absorber layer exceeds 4 µm.

References

[1] B.G. Svensson, "Electronic structure and optical properties of Zn X (X =O, S, Se, Te)," pp. 1–14, 2018.

[2] M. Lee, Y. Peng, and H. Wu, "Effects of intrinsic defects on electronic structure and optical properties of Ga-doped ZnO," J. Alloys Compd. 616, 122-127 (2014 https://doi.org/10.1016/j.jallcom.2014.07.098.

[3] R. Khenata, "Elastic, electronic and optical properties of ZnS, ZnSe and ZnTe under pressure," Computational Materials Science, 38, 29-38 (2006). https://doi.org/10.1016/j.commatsci.2006.01.013.

[4]   Y. Yu, J. Zhou, H. Han, and C. Zhang, "Ab initio study of structural, dielectric, and dynamical properties of zinc-blende ZnX (X = O, S, Se, Te)," Journal of Alloys and Compounds, 471, 492-497 (2009). https://doi.org/10.1016/j.jallcom.2008.04.039

[5]   S. Jeetendra, H. Nagabhushana, K. Mrudula, C.S. Naveen, P. Raghu, and H.M. Mahesh, "Concentration Dependent Optical and Structural Properties of Mo doped ZnTe Thin Films Prepared by e-beam Evaporation Method," Int. J. Electrochem. Sci. 9, 2944-2954 (2014). http://www.electrochemsci.org/papers/vol9/90602944.pdf

[6]   S.M. Ali, A.A.A. Shehab, and S.A. Maki, "Study of the Influence of Annealing Temperature on the Structural and Optical Properties of ZnTe Prepared by Vacuum Thermal Evaporation Technique," Ibn Al-Haitham Journal for Pure and Applied sciences, 31(1), 50-57 (2018). https://doi.org/10.30526/31.1.1851

[7]   Zheng, J. H., Song, J. L., Jiang, Q., & Lian, J. S. (2012). Optical properties of Cu-doped ZnO nanoparticles experimental and first-principles theory research. Journal of Materials Science: Materials in Electronics, 23(8), 1521–1526. doi:10.1007/s10854-012-0622-z.

[8]   D. Bahri and L. Amirouche, "Ab initio study of the structural, electronic and optical properties of ZnTe compound," AIP Conference Proceedings, 1653(1), (2015). https://doi.org/10.1063/1.4914210

[9]   J. Serrano, Y. Tech, A. H. Romero, and R. Lauck, "Pressure dependence of the lattice dynamics of ZnO: An ab initio approach," Physical Review B, 69, 094306 (2004). https://doi.org/10.1103/PhysRevB.69.094306.

[10]   V.O.I. Ume, P. Walter, L. Cohen, and Y. Petroff, "Calculated and Measured Reflectivity of ZnTe and ZnSef," Phys. Rev. B, 1, 2661 (1970). https://doi.org/10.1103/PhysRevB.1.2661

[11]   M. Caid et al., "Electronic structure of short-period ZnSe/ZnTe superlattices based on DFT calculations," Condensed Matter Physics, 25(1), 1-10 (2022). https://doi.org/10.5488/CMP.25.13701

[12]   F. Parandin, J. Jalilian, and J. Jalilian, "Tuning of electronic and optical properties in ZnX (X = O, S, Se and Te) monolayer: Hybrid functional calculations," Chemical Review & Letters, 2(2), 76-83 (2019). https://doi.org/10.22034/crl.2019.195774.1019

[13]   Z. Nourbakhsh, "Structural, electronic and optical properties of ZnX and CdX compounds (X = Se, Te and S) under hydrostatic pressure," J. Alloys Compd. 505(2), 698-711 (2010). https://doi.org/10.1016/j.jallcom.2010.06.120.

[14]   F.D. Murnaghan, "The Compressibility of Media under Extreme Pressures," Proceedings of the National Academy of Sciences of the United States of America, 30(9), 244-247 (1944). https://www.jstor.org/stable/87468

[15]   M. Safari, Z. Izadi, J. Jalilian, and I. Ahmad, "Metal mono-chalcogenides ZnX and CdX (X = S, Se and Te) monolayers: Chemical bond and optical interband transitions by first principles calculations," Phys. Lett. A, 381(6), 663-670 (2017). https://doi.org/10.1016/j.physleta.2016.11.040.

[16]   S. K. Gupta, S. Kumar, and S. Auluck, "Structural, electronic and optical properties of highpressure stable phases of ZnTe," Physica B: Condensed Matter, 404, 3789-3794 (2009). https://doi.org/10.1016/j.physb.2009.06.149

[17] A.A. Audu, W.A. Yahya, and A.A. Abdulkareem, Physics Memoir: Journal of Theoretical & Applied Physics, "Ab initio Studies of the Structural, Electronic and Mechanical Properties of Zn1−xCrx e," 3, 38-47 (2021).

[18] M. Achehboune, M. Khenfouch, I. Boukhoubza, I. Derkaoui, B.M. Mothudi, I. Zorkani, A. Jorio, "Effect of Yb Concentration on the Structural, Magnetic and Optoelectronic Properties of Yb Doped ZnO: First Principles Calculation". http://dx.doi.org/10.21203/rs.3.rs-877060/v1

[19] R. John, and S. Padmavathi, "Ab Initio Calculations on Structural, Electronic and Optical Properties of ZnO in Wurtzite Phase," Cryst. Struct. Theory Appl. 5(2), 24-41 (2016). https://doi.org/10.4236/csta.2016.52003

[20] R. Chowdhury, S. Adhikari, and P. Rees, "Optical properties of silicon doped ZnO," Phys. B Condens. Matter, 405(23), 4763 4767 (2010). https://doi.org/10.1016/j.physb.2010.08.072

[21] C. Feng et al., "First-principle calculation of the electronic structures and optical properties of the metallic and nonmetallic elements-doped ZnO on the basis of photocatalysis," Phys. B Condens. Matter, 555, 53-60 (2019). https://doi.org/10.1016/j.physb.2018.11.043.

[22] L. Chen, X. Zhou, and J. Yu, "First-principles study on the electronic and optical properties of the ZnTe/InP heterojunction," J. Comput. Electron. 18(3), 749-757 (2019). https://doi.org/10.1007/s10825-019-01358-8

[23] A.M. Ghaleb, and A.Q. Ahmed, "Structural, electronic, and optical properties of sphalerite ZnS compounds calculated using density functional theory (DFT)," Chalcogenide Lett. 19(5), 309-318 (2022). https://doi.org/10.15251/CL.2022.195.309

[24] Q. Hou, and S. Sha, "Effect of biaxial strain on the p-type of conductive properties of (S, Se, Te) and 2 N co-doped ZnO," Mater. Today Commun. 24, 101063 (2020). https://doi.org/10.1016/j.mtcomm.2020.101063

[25] Md.A. Momin, Md.A. Islam, A. Majumdar, "Influence on structural, electronic and optical properties of Fe doped ZnS quantum dot: A density functional theory based study," Quantum Chemistry, 121(1), 1-13 (2020). https://doi.org/10.1002/qua.26786.

[26] M. Dong, P. Zhou, C. Jiang, B. Cheng, and J. Yu, "First-principles investigation of Cu-doped ZnS with enhanced photocatalytic hydrogen production activity State Key Laboratory of Advanced Technology for Materials Synthesis and," Chem. Phys. Lett. 668, 1-6 (2016). https://doi.org/10.1016/j.cplett.2016.12.008.

[27] A. Pattnaik, M. Tomar, P.K. Jha, A.K. Bhoi, V. Gupta, and B. Prasad, "Theoretical Analysis of the Electrical and Optical Properties of ZnS," In: A. Konkani, R. Bera, and S. Paul, editors, Advances in Systems, Control and Automation. Lecture Notes in Electrical Engineering, vol. 442. (Springer, Singapore, 2018). https://doi.org/10.1007/978-981-10-4762-6_2.

[28] Y.L. Su, Q.Y. Zhang, N. Zhou, C.Y. Ma, X.Z. Liu, and J.J. Zhao, "Study on Co-doped ZnO comparatively by fi rst-principles calculations and relevant experiments," 250, 123-128 (2017). https://doi.org/10.1016/j.ssc.2016.12.002.

[29] T. Kato, J. L. Wu, Y. Hirai, H. Sugimoto, and V. Bermudez, "Record Efficiency for Thin-Film Polycrystalline Solar Cells Up to 22.9% Achieved by Cs-Treated Cu(In,Ga)(Se,S)2," IEEE J. Photovoltaics, 9(1), 325-330 (2019). https://doi.org/10.1109/JPHOTOV.2018.2882206.

[30] A. Bouzidi, and I. Bouchama, "Numerical study of the buffer influence on the Cu(In,Ga)Se2 solar cells performances by SCAPS-ID," in: International Conference on Electronics and New Technologies (ICENT), 2017.

[31] S.K. Gupta, S. Kumar, and S. Auluck, "Structural, electronic and optical properties of high pressure stable phases of ZnTe," Phys. B Condens. Matter, 404(20), 3789-3794 (2009). https://doi.org/10.1016/j.physb.2009.06.149.

[32] R. Tala-Ighil Zaïr, C. Oudjehani, and K. Tighilt, "SCAPS Simulation for Perovskite Solar Cell," J. Sol. Energy Res. Updat. 8, 21-26 (2021). https://doi.org/10.31875/2410-2199.2021.08.3.

[33] H.I. Abdalmageed, M. Fedawy, and M.H. Aly, "Effect of absorber layer bandgap of CIGS-based solar cell with (CdS/ZnS) buffer layer," J. Phys. Conf. Ser. 2128(1), (2021). https://doi.org/10.1088/1742-6596/2128/1/012009.

[34] C. Platzer-Björkman, J. Kessler, and L. Stolt, "Analysis of Zn(O,S) films for Cu(In,Ga)Se2 solar cells," Proc. Estonian Acad. Sci. Phys. Math. 52(3), 299-307 (2003). https://doi.org/10.3176/phys.math.2003.3.06.

[35] Y.-K. Liao et al., "A look into the origin of shunt leakage current of Cu(In, Ga)Se2 solar cells via experimental and simulation methods," Sol. Energy Mater. Sol. Cells, 117, 145-151 (2013). https://doi.org/10.1016/j.solmat.2013.05.031.

[36] P. Srivastava et al., "Theoretical study of perovskite solar cell for enhancement of device performance using SCAPS-1D," Phys. Scr. 97(2), 12 (2022). https://doi.org/10.1088/1402-4896/ac9dc5.

[37] M. Safari, Z. Izadi, J. Jalilian, I. Ahmad, and S. Jalali-Asadabadi, "Metal mono-chalcogenides ZnX and CdX (X = S, Se and Te) monolayers: Chemical bond and optical interband transitions by first principles calculations," Phys. Lett. Sect. A Gen. At. Solid State Phys. 381(6), 663-670 (2017). https://doi.org/10.1016/j.physleta.2016.11.040.

[38] H. T. Ganem, and A. N. Saleh, "The effect of band offsets of absorption layer on CNTS/ZnS/ZnO solar cell by SCAPS-1D," Tikrit Journal of Pure Science, 25 (6), 79-87 (2020). http://dx.doi.org/10.25130/tjps.25.2020.114.

[39] N. Adim, M. Caid, D. Rached, and O. Cheref, "Computational study of structural, electronic, magnetic and optical properties of (ZnTe)m/(MnTe) n superlattices," Journal of Magnetism and Magnetic Materials, 499, 166314 (2020). https://doi.org/10.1016/j.jmmm.2019.166314 jstor.

GENERAL CONCLUSIONS AND

FUTURE WORK

General Conclusions and future works

This comprehensive study conducted by CASTEP program has made significant strides in elucidating the impact of doping on semiconducting compounds. By employing computational simulations utilizing the GGA-PBE-DFT methodology, the investigation delved into the effects of various proportions of zinc, aluminum and tellurium doping on the structural, mechanical, electronic, electrical, and optical attributes of $SrTiO_3$, $CuInS_2$ and ZnO. The findings underscored the profound influence of doping on compound properties, spotlighting changes in bandgap, electronic structure, and optical absorption.

This study has yielded invaluable insights into the intricate interplay between doping and the properties of semiconductor composites, a pivotal aspect in advancing the design and fabrication of high-performance photovoltaic materials. The outcomes hold promise for guiding experimental synthesis processes towards the creation of novel, improved materials tailored for photovoltaic applications. Specifically, the following key findings emerge from this research:

➤ **Zinc doping in $SrTiO_3$ material:**

- Zinc doping increases lattice constant, volume, and volume modulus.
- Zinc doping decreases elastic constants, B/G ratio, and energy gap.
- $SrZn_xTi_{1-x}O_3$ is a semiconductor with improved optical properties.
- Zinc doping influence's dielectric function and refractive indices.

➤ **Aluminum doping in $CuInS_2$ material:**

- Aluminum doping decreases lattice parameters, mass modulus, volume, and band gap.
- Aluminum doping increases anisotropy, elastic constants, hardness, stiffness, and dielectric constant.
- Aluminum doping enhances absorption and transparency at specific wavelengths.
- Aluminum doping reduces reflectivity and refractive index.

➤ **Tellurium doping in ZnO:**
The effects of zinc oxide doping with tellurium in very small proportions:

- Lattice constant decreases.
- Volume decreases.
- Bulk modulus increases.

- o Band gap decreases.

- o State density increases.

- o Absorption coefficient increases in the ultraviolet region.

- o Reflectivity decreases in the ultraviolet region.

- o Refractive index increases in the ultraviolet region.

- o Dielectric function becomes negative in the ultraviolet region.

Implications for potential applications:

- o Improved performance of optoelectronic devices

- o Increased efficiency of solar cells

- o Enhanced photocatalytic activity

➢ **Application to photovoltaic solar cells:**

- ✓ ZnX systems exhibit varying lattice parameters, making them suitable for different solar cells structures.

- ✓ Binary ZnX alloys have wide bandgaps (2.436 eV, 2.698 eV, 1.721 eV for ZnTe, ZnS, and ZnO, respectively).

- ✓ The calculated structural, physical, and optical properties are consistent with existing theoretical and experimental data.

- ✓ Pure ZnX materials have potential for solar cell applications.

- ✓ The efficiency of solar cells increases with absorber thickness, but the rate of increase diminishes significantly beyond 2 µm.

- ✓ The ideal thickness for the CIGS absorber layer is likely to exceed 4 µm.

In conclusion, the findings of this comprehensive study underscore the remarkable potential of doping with Zn, Al, and Te in enhancing the structural, mechanical, electronic, and optical attributes of $SrTiO_3$, $CuInS_2$, and ZnO compounds, respectively. These remarkable improvements position these compounds as highly promising candidates for diverse applications in the realms of photo-electricity and optical sensors.

As we look toward the future, it becomes evident that a wealth of opportunities awaits further exploration. To harness the full potential of these doped compounds, we suggest several future works, including:

- ♦ Development of Novel Applications: The improved properties exhibited by these compounds strongly advocate for the development of novel photoelectric applications and optical sensors. These innovations could

174

include the creation of highly efficient solar cells and ultra-sensitive optical sensors, contributing to sustainable energy solutions and advanced sensing technologies.

+ Delving deeper into the intricacies of property enhancement induced by doping holds immense promise. Investigating the underlying mechanisms responsible for these changes at a fundamental level could pave the way for more effective doping strategies. This deeper understanding is crucial for tailoring the properties of these compounds to meet specific application requirements.

+ While doping has evident macroscopic effects, its influence on the nanoscale properties of these compounds remains a fascinating frontier. Exploring these nanoscale effects is essential to comprehend their implications on the overall performance of the materials.

SECTION III

List of scientific productions

List of scientific productions

a) International scientific publications:

1- F. Benlakhdar, M. A. Ghebouli, Z. Zerrougui, K. Bouferrache, Y. Slimani, B. Ghebouli, I. Bouchama, T. Chihi, M. Fatmi, Saif A. Mouhammad, Norah Algethami and Sultan Alomairy, "Structural, elastic, mechanical and optoelectronic properties of zinc-doped SrTiO3 perovskite compounds,", Modern Physics Letters B 2350200 (2023) 1-14.

DOI: 10.1142/S0217984923502007

2- Faiza Benlakhdar, Idris Bouchama, Tayeb Chihi, Ibrahim Ghebouli, Mohamed Amine Ghebouli, Zohra Zerrougui, Khettab Khatir, Mohamed Alam Saeed, "AB-INITIO STUDY OF STRUCTURAL, ELECTRONIC AND OPTICAL PROPERTIES OF ZnX (X = Te, S and O): APPLICATION TO PHOTOVOLTAIC SOLAR CELLS", East European Journal of Physics, 3 (2023) 413-423.

DOI:10.26565/2312-4334-2023-3-45

b) International communications:

1- Faiza Benlakhdar1, Tayeb Chihi, Ibrahim Ghebouli, Idris Bouchama, M. A. Ghebouli, M. Fatmi, Z. Zerrougui, "Advancing the Properties of CuInX-1GaXS2 Compounds using the CASTEP Program: A Computational Exploration of Structural, Electronic, and Optical Characteristics," 5th International Conference on Applied Engineering and Natural Sciences, July 10-12, 2023, Konya, Turkey.

2- Faiza Benlakhdar1, Tayeb Chihi, Ibrahim Ghebouli, Idris Bouchama, Z. Zerrougui, M. Fatmi, M. A. Ghebouli, "The Effects of Fluorine Doping on the Structure and Electronic Properties of Hexachloro-tungsten (WCl6) for Photocatalysis," 3rd International Conference on Innovative Academic Studies, September 26-28, 2023: Konya, Turkey.

3- Faiza Benlakhdar1, Tayeb Chihi, Ibrahim Ghebouli, Idris Bouchama, M. Fatmi, M. A. Ghebouli, Z. Zerrougui, "Comprehensive Investigation of Structural and Electronic Properties of Sulfur-Doped Zinc Oxide using CASTEP Program,", 3rd International Conference on Innovative Academic Studies, September 26-28, 2023: Konya, Turkey.

World Scientific
www.worldscientific.com

Structural, elastic, mechanical and optoelectronic properties of zinc-doped SrTiO$_3$ perovskite compounds

F. Benlakhdar*, M. A. Ghebouli*, Z. Zerrougui†, K. Bouferrache‡,
Y. Slimani§, B. Ghebouli¶, I. Bouchama*,‖, T. Chihi*, M. Fatmi*,††,
Saif A. Mouhammad**, Norah Algethami** and Sultan Alomairy**

*Research Unit on Emerging Materials (RUEM), University Ferhat Abbas of Setif 1,
Setif 19000, Algeria

†Laboratory of Studies Surfaces and Interfaces of Solids Materials,
Faculty of Technology, University Ferhat Abbas of Setif 1,
Setif 19000, Algeria

‡Department of Physics, Faculty of Sciences,
University of Mohamed Boudiaf, M'sila 28000, Algeria

§Laboratory of Intelligent System (LSI), Faculty of Technology,
University Ferhat Abbas of Setif 1, Setif 19000, Algeria

¶Laboratory for the Study of Surfaces and Interfaces of Solid Materials (LESIMS),
University Ferhat Abbas of Setif 1, Setif 19000, Algeria

‖Department of Electronic, Faculty of Technology, University of Mohamed Boudiaf,
M'sila 28000, Algeria

**Department of Physics, College of Science, Taif University,
P. O. Box 11099, Taif 21944, Saudi Arabia
††fatmimessaoud@yahoo.fr

Structural, elastic, mechanical and electronic properties of pure and zinc-doped SrTiO$_3$ at the concentration in the range (1–10%) are studied by first-principles calculations. The structural parameters of synthesized compounds agree well with the standard data depicting the growth of stable compounds. A slight obvious increase in the lattice constant of 3.9245 Å is observed in Zn-doped SrTiO$_3$ due to the deviation of the atomic radii of Zn and Ti. Elastic constants and mechanical parameters of SrTiO$_3$ are closer to their available theoretical and experimental data. The investigated compounds exhibit brittle behavior for all Zn ratios. The doping zinc concentration reduces the indirect band gap value. The doping concentration 2%, gives a band gap value closer to the experimental one. The band gap of pure SrTiO$_3$ is 1.827 eV and after doping with Zn for concentration from 1% to 10%, the optimized values are 1.970, 1.886, 1.802, 1.718, 1.635, 1.552, 1.470, 1.389, 1.310, 1.231 and 1.154 eV.

Keywords: SrTiO$_3$; CASTEP; DFT; doping; elastic properties; electronic properties.

††Corresponding author.

1. Introduction

The improvement of the conductivity and the photocatalytic capacity is obtained by introducing certain metallic elements such as Zn into the pure $SrTiO_3$. The disadvantage of the photocatalytic system lies in their low use of visible light, the rapid recombination of charges and the low migration capacity of photo-generated electrons and holes. Therefore, noble and transition metals, nonmetals and metalloids are doped into the photocatalyst as co-catalyst to improve photodegradation performance.[1] Strontium perovskite titanate ($SrTiO_3$ or STO) shows high chemical stability, and abundance of constituent elements.[2] Eglitis and Kotomin give the results of Nb impurities substituting for Ti ions in $SrTiO_3$ using super cells containing up to 135 atoms.[3] $SrTiO_3$ with a simple crystal structure is one of the most popular semiconductor used in photovoltaic applications and its mechanical properties are more sensitive to Sr-site cation.[4] The determining factors in the ferroelectricity of $SrTiO_3$ are the decent ring, the geometric size and the electronic configuration of the Sr atoms. From the literature, we distinguish the transition from the parent cubic structure to the tetragonal one or from the rhombohedra phase to the orthorhombic or monoclinic structure.[5] The calculated optical band gap of the cubic phase of $SrTiO_3$ is 3.57 eV and in very good agreement with experimental data.[6] $SrTiO_3$ perovskite material exists in three phases depending on temperature; the orthorhombic phase exists below 100 K, the tetragonal structure in the range 100–300 K and the cubic one above 300 K, which is the most stable. Concerning the work carried out by other researchers, Ghebouli *et al.* studied some properties of $SrMO_3$ (M = Ti and Sn) in their standard forms.[7] The elastic constants of $SrTiO_3$ obtained from a polynomial fit to the energy–strain relation were calculated by both LDA and GGA approaches.[8] $SrTiO_3$ has simple cubic perovskite structure at high temperature and goes through an anti-ferrodistortive AFD transition at 105 K to a tetragonal phase.[9] The elastic characteristics of materials give the valuable data about the bonding property between adjacent atomic planes, bonding anisotropic, stiffness and structural stability of the material.[10] The crystal anisotropy is related to the modulus of elasticity, has significance in the fields of engineering and material sciences and occurs when the relationship between stress and strain depends on its orientation.[11] Benrekia Ahmed Redha *et al.* presented a study on structural, electronic, vibrational and optical properties of para-electric $SrTiO_3$.[12] Gulden Selik and Suleyman Cabuk reported electronic and optical properties of Sr(Ti, Zr)O_3 crystals in the cubic (Pm-3m) and tetragonal (I4/mcm) phase using the local density approximation.[13] The current work emphasizes investigating the structural, mechanical and electronic properties of Zn-doped $SrTiO_3$. The Zn concentration is varied to optimize the appropriate content in $SrTiO_3$ matrix for potential applications. The doping of $SrTiO_3$ by zinc atoms allows this new material to have a suitable band gap and absorption factor in order to use it as an absorber in photovoltaic cells. Zinc impurities favor replacing Ti ion instead of Sr and O-ion in $SrTiO_3$. In the doped sample, Zn atoms in proportions that vary in the range 1–10% replace the Ti atoms.

Density functional theory with generalized gradient approximation (GGA-PBE) was employed to achieve the stability of Zn-doped $SrTiO_3$ through elastic constant and tolerance factor. We attempted to synthesize $SrZn_xTi_{(1-x)}O_3$ nanopowder experimentally. The doping of $SrTiO_3$ by Zn induces variations in the studied properties and opens up new prospects for potential applications of this material in the optoelectronic field. The structural, elastic, mechanical, electronic and optical properties were investigated.

2. Computation Details

First-principles calculations were performed in the DFT framework with GGA-PBE approximations using the CASTEP code.[14] The ultra-soft-pseudopotential method and the GGA-PBE approximation functional[15] describe the exchange-correlation effect. The best convergence of the computed structures and energies requires the use of Monkhorst–Pack points of $6 \times 6 \times 6$ grid and cut-off energy of $800\,\text{eV}$.[16] The calculation of the optical quantities requires the use of dense mesh of uniformly distributed $20 \times 20 \times 20$ k-points. The minimization technique of Broyden–Fletcher–Goldfarb–Shanno[17] determines the structural parameters, which provides a fast way to find the lowest energy structure. The tolerance for geometry optimization was performed with affinity resolution of the set as the difference of total energy $10^{-5}\,\text{eV/}$ atom, maximum ionic Hellmann–Feynman force $3 \times 10^{-2}\,\text{eV/Å}$ and maximum stress $2 \times 10^{-2}\,\text{eV/Å}^3$. The approach adopted in this study facilitates the calculation of the forces and stresses involved, controls the convergence of every computational parameter and neglects the effect of nucleus electrons.

3. Results and Discussions

3.1. *Structural parameters*

The structure of pure and Zn-doped $SrTiO_3$ material was optimized using CASTEP and GGA-PBE core assembly. The electronic configuration of Sr, Ti, Zn and O is $4s^2 4p^6 5s^2$, $3s^2 3p^6 3d^2 4s^2$, $3d^{10} 4s^2$ and $2s^2 2p^4$. Figure 1 shows the crystal structure of standard $SrTiO_3$. The optimized lattice constant, bulk modulus and its pressure derivative of pure and Zn-doped $SrTiO_3$ are reported in Table 1. The reliability of the mentioned results is evident from the correlation between theoretical[18–20] and experimental[21] data. It is observed that the optimized lattice constant, which corresponds to a Zn content of 1%, is 3.924 Å. This result is consistent with the experimental value of 3.905 Å cited in the literature.[21] However, our calculations report a lattice constant of 3.9849 Å for Zn content of 9%.

It is noted that $SrTiO_3$ doped by Nb with a percentage of 1%, 2%, 3%, 5% and 8% shows a lattice constant of 3.9078, 3.9088, 3.9066, 3.905 and 3.9063 Å.[22,23] The value of the lattice constant of $SrTiO_3$ doped by Nb with a percentage of 25% and 50% is about 3.969 and 4 Å,[24] which is closer to the experimental value of 3.980 and 4.002 Å.[25] A slight obvious increase in the lattice constant of 3.9245 Å is observed in
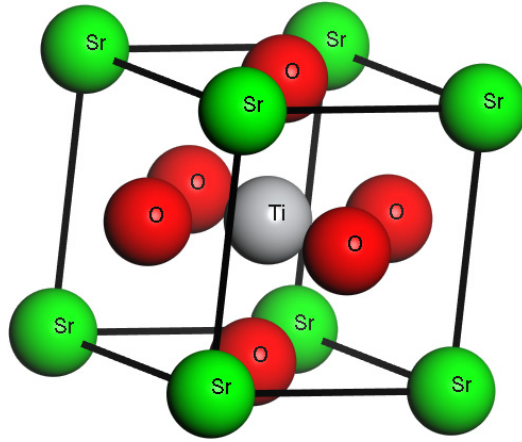
Fig. 1.   (Color online) Crystal structures of $SrTiO_3$ compound.

Table 1.   Lattice constant, volume, bulk modulus and its pressure derivative for standard and Zn-doped $SrTiO_3$ with available theoretical and experimental published data.

Compound	a_0 (Å)	V (Å^3)	B_0 (GPa)	B_0'
$SrTiO_3$	3.917	60.13	173.02	4.33
	3.919[18]			4.712[19]
	3.904[19]		190.67[19]	
	3.940[20]			
	3.905[21] exp.			
$SrZn_{0.02}Ti_{0.98}O_3$	3.9315	60.7701	168.61	4.36
$SrZn_{0.03}Ti_{0.97}O_3$	3.9387	61.1039	166.69	4.37
$SrZn_{0.04}Ti_{0.96}O_3$	3.9459	61.4390	164.45	4.38
$SrZn_{0.05}Ti_{0.95}O_3$	3.9534	61.7890	162.32	4.40
$SrZn_{0.06}Ti_{0.94}O_3$	3.9610	62.1492	159.38	4.42
$SrZn_{0.07}Ti_{0.93}O_3$	3.9688	62.5164	157.07	4.44
$SrZn_{0.08}Ti_{0.92}O_3$	3.9768	62.8942	154.37	4.46
$SrZn_{0.09}Ti_{0.91}O_3$	3.9849	63.28	151.41	4.48
$SrZn_{0.1}Ti_{0.90}O_3$	3.9931	63.67	149.55	4.50

Zn-doped $SrTiO_3$ due to the deviation of the atomic radii of Zn and Ti. The total energy versus volume was plotted for $SrTiO_3$ in the standard state and by doping it with Zn (Zn = 2%, 5% and 10%), as shown in Fig. 2. Optimization of $SrTiO_3$ and $SrTi_{(1-x)}Zn_xO_3$ structures for various Zn contents was achieved by fitting Murnaghan's equation of state.[26] It is noted that the introduction of a percentage of Zn makes the structure less stable.

The lattice constant, volume and bulk modulus as a function of zinc content x for $SrZn_xTi_{1-x}O_3$ alloys are shown in Fig. 3. The volume was observed to decrease as Zn content increases in $SrTiO_3$. The lattice constant (bulk modulus) increases (decreases) with increasing Zn content. The fit of our data regarding the lattice
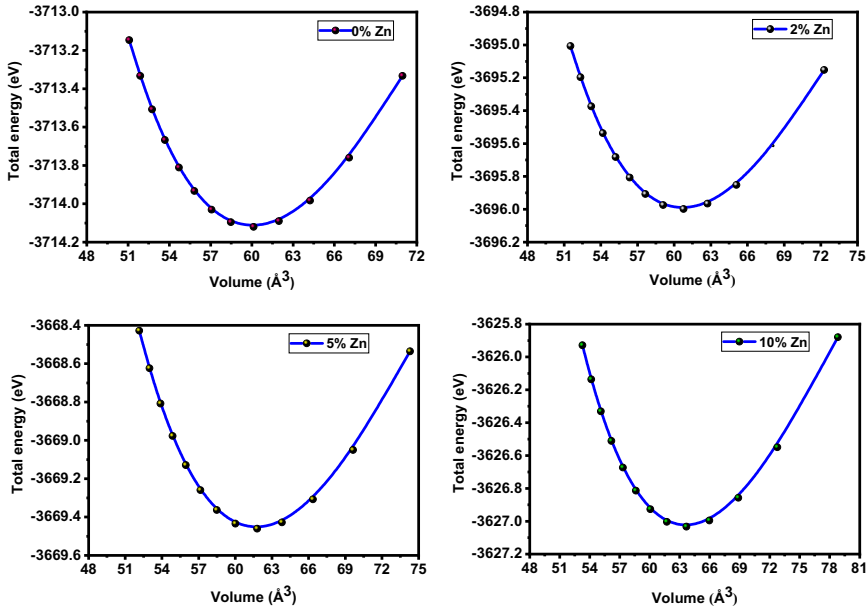
Fig. 2.   (Color online) Total energy versus volume for standard and Zn-doped SrTiO₃ (Zn = 2%, 5% and 10%).

constant, the volume and bulk modulus obeys these polynomial expressions:

$$a_0(x) = 3.9176 + 0.0067x + 7.9 \times 10^{-5} x^2, \tag{1}$$

$$V(x) = 60.1287 + 0.3105x + 0.0043x^2, \tag{2}$$

$$B_0(x) = 172.87 - 1.99x - 0.03x^2. \tag{3}$$

The dynamic stability of SrTiO₃ is studied by visualizing the phonon dispersion curves and their total densities of state, as shown in Fig. 4. SrTiO₃ is dynamically stable due to the non-presence of imaginary phonon frequencies. We will not be able to visualize the spectrum of phonons for a concentration of Nb, because it requires a sophisticated calculation tool that we lack.

3.2. *Elastic constants and mechanical characteristics*

The elastic constants describe the response to applied macroscopic stress and relate the mechanical parameters to the elasticity, stability and stiffness.[27] Understanding the mechanical properties of a material due to the response of external forces requires the use of elastic constants. Mechanical properties include Young's modulus (E), elastic hardness coefficients (C_{ij}), bulk modulus (B), shears modulus (G), Poisson's ratio and anisotropy (A). The stability of the structure and the heterogeneous bond between neighboring atoms are described by the elastic constants of the material. Shear and Young moduli describe the stiffness of the bond and the resistance to deformation and fracture. Elastic constants are related to basic phenomena such as
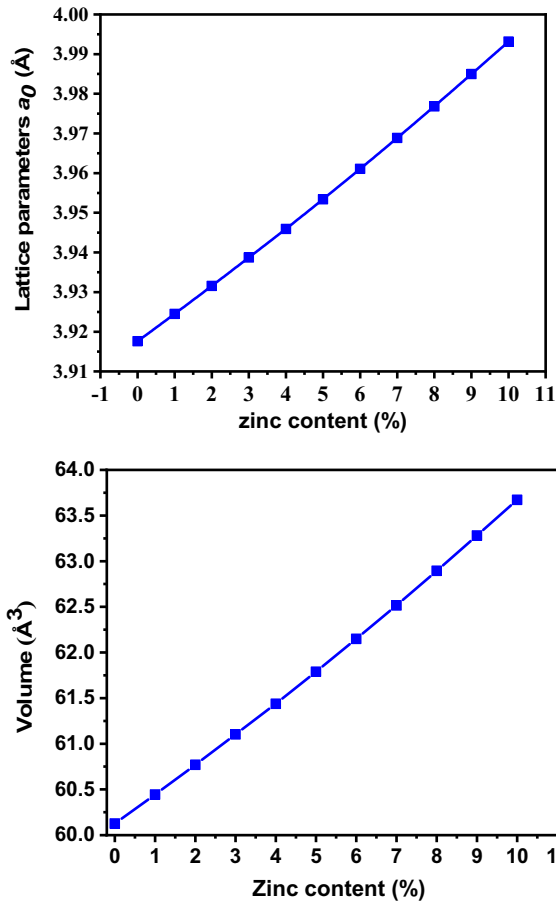
Fig. 3.   (Color online) Volume and lattice constant versus zinc content x in $SrZn_xTi_{1-x}O_3$.

brittleness, ductility, hardness and mechanical stability of the material. Elastic constants provide information about the structure stability, bond behavior, anisotropy and cohesion of a material. C_{11}, C_{12} and C_{44} of $SrTiO_3$ cubic structure at zero pressure are enlisted in Table 2, which are consistent with their theoretical 350.46, 101.16 and 111.02 GPa[19] and experimental[4,28] values. Computed elastic moduli for pure and Zn-doped $SrTiO_3$ are positive and satisfy the following generalized conditions to ensure their elastic stability[29,30]:

$$C_{11} + 2C_{12} \rangle 0, \quad C_{44} \rangle 0, \quad C_{11} - C_{12} \rangle 0, \quad C_{12} \langle B \langle C_{11}. \tag{4}$$

Note that C_{11} is larger and stiffer than C_{12} and C_{44}.

The bulk modulus represents the compressive strength of the material; therefore, $SrTiO_3$ shows perfect volume compressive strength. The bulk modulus, anisotropy factor, shear and Young's moduli, B/G and Poisson's ratios and Vickers hardness of undoped and Zn-doped $SrTiO_3$ are reported in Table 2. The Vickers hardness of
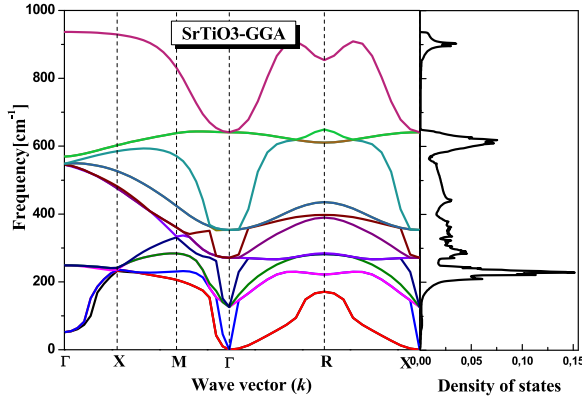
Fig. 4.   (Color online) Phonon dispersion curves and density of states of SrTiO$_3$.

Table 2.   Elastic constants, Shear and Young's moduli, B/G ratio, anisotropy factor, hardness and Poisson's ratio of SrZn$_x$Ti$_{(1-x)}$O$_3$.

	C$_{11}$ (GPa)	C$_{12}$ (GPa)	C$_{44}$ (GPa)	G (GPa)	Y (GPa)	B/G	A	H(GPa)	σ
SrTiO$_3$	317.62	99.71	113.32	111.5	275	1.55	0.98	16.7	0.23
Exp. [24.4.25]	317	102.5	112	95.7	236.3	1.54	1.02		
SrZn$_{0.02}$Ti$_{0.98}$O$_3$	318.20	100.15	113.17	111.47	275.24	1.5525	1.03	16.70	0.23
SrZn$_{0.03}$Ti$_{0.97}$O$_3$	318.17	100.14	113.14	111.45	275.20	1.5526	1.03	16.70	0.23
SrZn$_{0.04}$Ti$_{0.96}$O$_3$	318.13	100.12	113.12	111.43	275.16	1.5527	1.03	16.70	0.23
SrZn$_{0.05}$Ti$_{0.95}$O$_3$	318.10	100.11	113.09	111.41	275.11	1.5528	1.03	16.69	0.23
SrZn$_{0.06}$Ti$_{0.94}$O$_3$	318.07	100.09	113.07	111.40	275.07	1.5629	1.03	16.69	0.23
SrZn$_{0.07}$Ti$_{0.93}$O$_3$	318.04	100.08	113.04	111.38	275.02	1.5530	1.03	16.69	0.23
SrZn$_{0.08}$Ti$_{0.92}$O$_3$	318.01	100.07	113.02	111.36	274.98	1.5530	1.03	16.69	0.23
SrZn$_{0.09}$Ti$_{0.91}$O$_3$	317.98	100.05	112.99	111.34	274.94	1.5531	1.03	16.68	0.23
SrZn$_{0.1}$Ti$_{0.90}$O$_3$	317.95	100.04	112.97	111.32	274.90	1.5532	1.03	16.68	0.23

SrZn$_x$Ti$_{(1-x)}$O$_3$ was estimated using the semi-empirical model $H = 0.0607 \times Y$.[31] The mechanical characteristics of the SrZn$_x$Ti$_{(1-x)}$O$_3$ materials behavior were described under Zn content effect.[32,33] Figure 5 shows the dependence of elastic constants on zinc content for SrZn$_x$Ti$_{1-x}$O$_3$ alloys according to GGA-PBE approximation. It is noted that all these parameters decrease almost monotonously with the addition of zinc content. The bulk and shear moduli of Voigt and Reus limit for a cubic crystal are given as

$$B = (B_R + B_v)/2, \tag{5}$$

$$G = (G_v + G_R)/2. \tag{6}$$

Young's modulus, Poisson's ratio and anisotropic factor can be obtained by

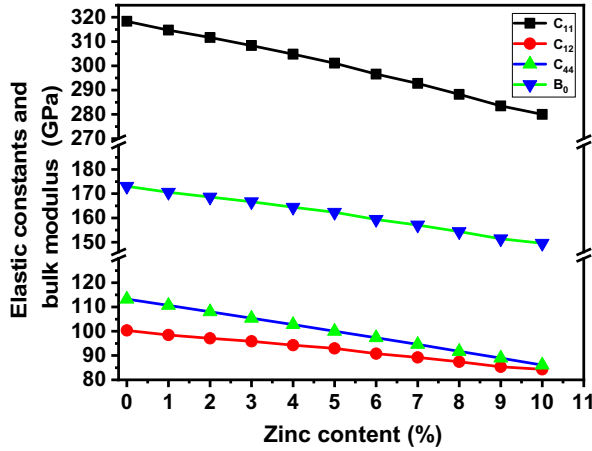$$E = 9GB/(3B + G), \tag{7}$$

$$\sigma = (3B - 2G)/2(3B + G), \tag{8}$$

Fig. 5.   (Color online) Elastic constants and bulk modulus versus zinc content x for $SrZn_xTi_{1-x}O_3$ alloys.

$$A = 2C_{44}/(C_{11} - C_{12}). \tag{9}$$

B/G ratio describes the ductility and brittleness of material, if this ratio is greater than 1.75, the material is ductile, otherwise it exhibits fragile nature. The B/G ratio for pure and Zn-doped $SrTiO_3$ is less than 1.75 indicating its brittleness.

Figure 6 depicts the nonlinear behavior of B/G ratio as a function of Zn concentration. Young's modulus and Shear modulus exhibit a decreasing trend for the strain with increasing concentration of zinc as shown in Fig. 7.

The quoted values are in good agreement with those reported in the literature[19] and experiments.[34] The Poisson ratio determines the stability of the material and the nature of bonding forces. The poisson ratio is 0.23, indicating the significant ionic contribution
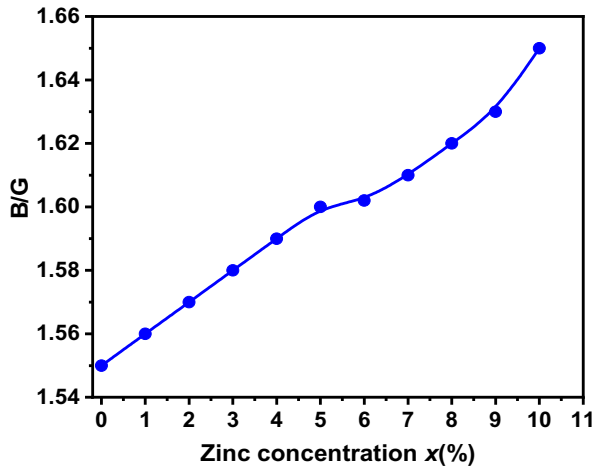

Fig. 6.   (Color online) B/G as a function of zinc content x for $SrZn_xTi_{1-x}O_3$ alloys.
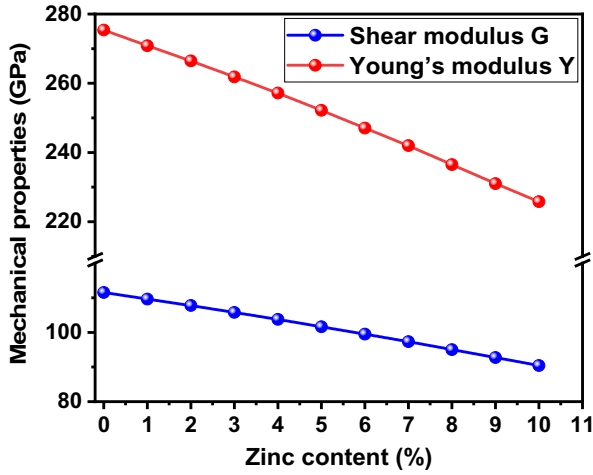
Fig. 7. (Color online) Shear and Young's Modulus as a function of zinc content x for SrZn$_x$Ti$_{1-x}$O$_3$ alloys.

towards intra-atomic bonding. SrTiO$_3$ is isotropic because the elastic anisotropy value is close to unity. The resistivity of this material to the deformation was studied using mechanical parameters.[35] Cauchy pressure $(Cp = C_{12} - C_{44} < 0)$ shows that SrZn$_x$Ti$_{(1-x)}$O$_3$ is covalent in nature.[36] The values of Young's modulus compared to the large bulk modulus indicate that this material is more difficult to crush.

3.3. *Electronic properties*

Electronic properties, in particular the energy gap, help in understanding the nature of bonds, electronic conductivity, optical behavior and stability. It is noted that the energy gap influences the optical characteristics responsible for the photocatalytic properties of the material. The determination of the band structure provides information on the nature of the compound, whether it is conductor, semi-conductor or insulator. The band structures as a function of zinc content x for SrZn$_x$Ti$_{1-x}$O$_3$ ($x = 0\%$, 2%, 5% and 10%) alloys are shown in Fig. 8. The energy band structure for standard SrTiO$_3$ demonstrated a valence band in the range from -5 eV to 0 eV and a conduction band in the range from 2.20 eV to 5 eV. It is noticed that the observed energy gap is 1.97 eV, as shown in Fig. 8(a). This value is comparable to those reported by experiment, which are 1.92 eV[37] and 1.90 eV[38] and other theoretical values.[6,39]

The maximum valence band is located at the Fermi level, so all the studied compounds are semiconducting in nature, with indirect $R \rightarrow \Gamma$ band gap. The separation between conduction and valence bands is due to the large number of electrons in their corresponding bands and thus in the occupancy states close to the Fermi level.[39] All calculated band gap values of Zn-doped SrTiO$_3$ at 0 GPa are shown in Table 3.

F. Benlakhdar et al.
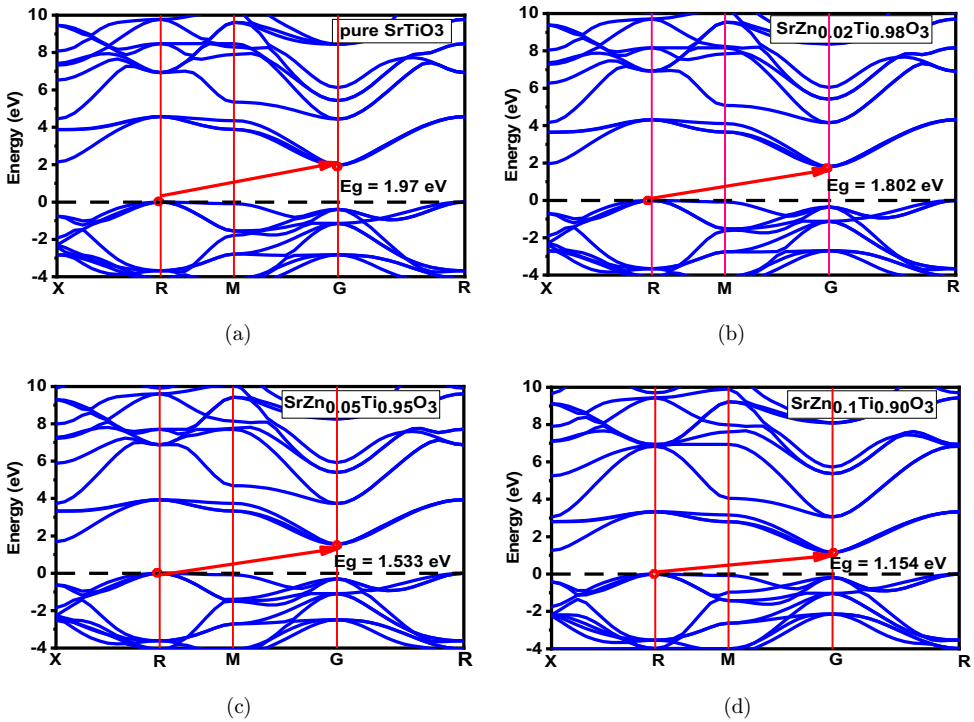
Fig. 8.   (Color online) Calculated band structure as a function of zinc content for $SrZn_xTi_{1-x}O_3$ alloys.

Table 3.   Calculated band gap value of Zn-doped $SrTiO_3$ at 0 GPa.

x (%) Zn content	E_g (eV) This work	E_g (eV) Other	E_g (eV) Experiment
0	1.97	1.84[39]	1.92[37]
	55	1.99[6]	1.90[38]
2	1.802	—	—
5	1.533	—	—
10	1.54	—	—

Figure 9 shows the variation in band gap energy as a function of Zn concentration. Note that there is a linear decrease in the band gap when Zn content is enhanced. The reduced band gap energy of the Zn-doped $SrTiO_3$ compounds leads to an argument that studied compounds can offer upgraded optical properties. The reduction of the energy gap with the increase of the doping by Zn content allows the studied compound to improve the optical properties. By doping $SrTiO_3$ with Zn content varying in the range 1–10%, the energy gap is located in the interval 1.802–1.154 eV. The fit of our data regarding the variation of E_g as a function of Zn content
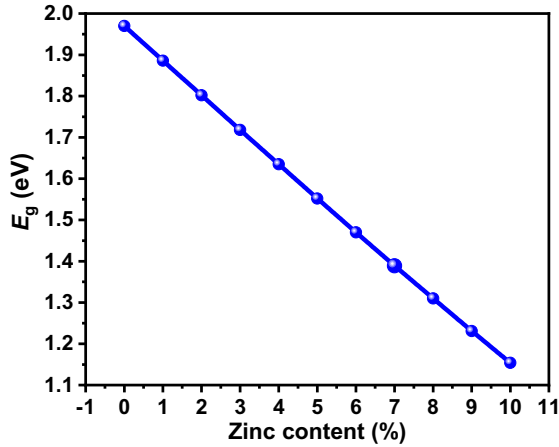
Fig. 9. (Color online) Band gap as a function of zinc content for SrZn$_x$Ti$_{1-x}$O$_3$ alloys.

x obeys the second-order polynomial expressions:

$$E_g(x) = 1.97113 - 0.08581x + 3.99767 \times 10^{-4}x^2. \tag{10}$$

The character of the band structure and the trend of the energy gap versus Zn content are reasonable and reliable. The calculation of the band structure intuitively describes the effect of doping on the energy gap. For the 5%, 10% and 20% S-doped SrTiO$_3$ the band gap energy is 2.87, 2.73 and 3 eV.[40] The value of the energy gap of SrTi$_{0.875}$Nb$_{0.125}$O$_3$ is about 1.85 eV, which is small with respect to the experimental value of about 3.2 eV.[24] The growth of Al concentrations of 10% and 20%-doped SrTiO$_3$ films on Si(100) substrate indicates that the band gap is increased by 0.3 eV over undoped SrTiO$_3$.[41] The Ag-doping on SrTiO$_3$ reduces the band gap by 0.15 eV.[42] The transition metal dopant has no effect on STO band gap, except for Pd and Pt that are able to reduce the STO band gap, while doping S and Se significantly reduces STO's band gap.[43] The resulting band gap values 3.09, 3.12 and 3.17 eV are related to the Nb-doped SrTiO$_3$ with 20%, 30% and 10%.[44] The total and partial densities of states analyze the physical properties of the material and give the detailed electronic contribution of the states of the elements Sr, Ti, Zn and O, which constitute the studied element. The TDOS and PDOS for standard and Zn (10%)-doped SrTiO$_3$ computed using GGA-PBE approximation are illustrated in Fig. 10. Note that the lower valence bands for SrTiO$_3$ and SrZn$_{(0.1)}$Ti$_{(0.9)}$ are located in the range -20 eV to -10 eV energy levels. These bands consist of Sr-p and Sr-s states for SrTiO$_3$ and Sr-p, O-p, Zn-s and Zn-p for SrZn$_{(0.1)}$Ti$_{(0.9)}$. The high valence bands lie from about -5 eV to the Fermi level and consist mainly of Sr-p, Sr-d and O-p states for SrTiO$_3$, and Ti-p, Ti-d, O-p and Zn-d and Zn-p for SrZn$_{(0.1)}$Ti$_{(0.9)}$. However, near the Fermi level, the contributions of Sr-p, Sr-d and O-p states for SrTiO$_3$ and Ti-p, Ti-d and O-p states for SrZn$_{(0.1)}$Ti$_{(0.9)}$ predominate. The increase in Zn content leads to the mixing of Zn-p and Zn-d with O-p, and therefore the band gap is reduced.
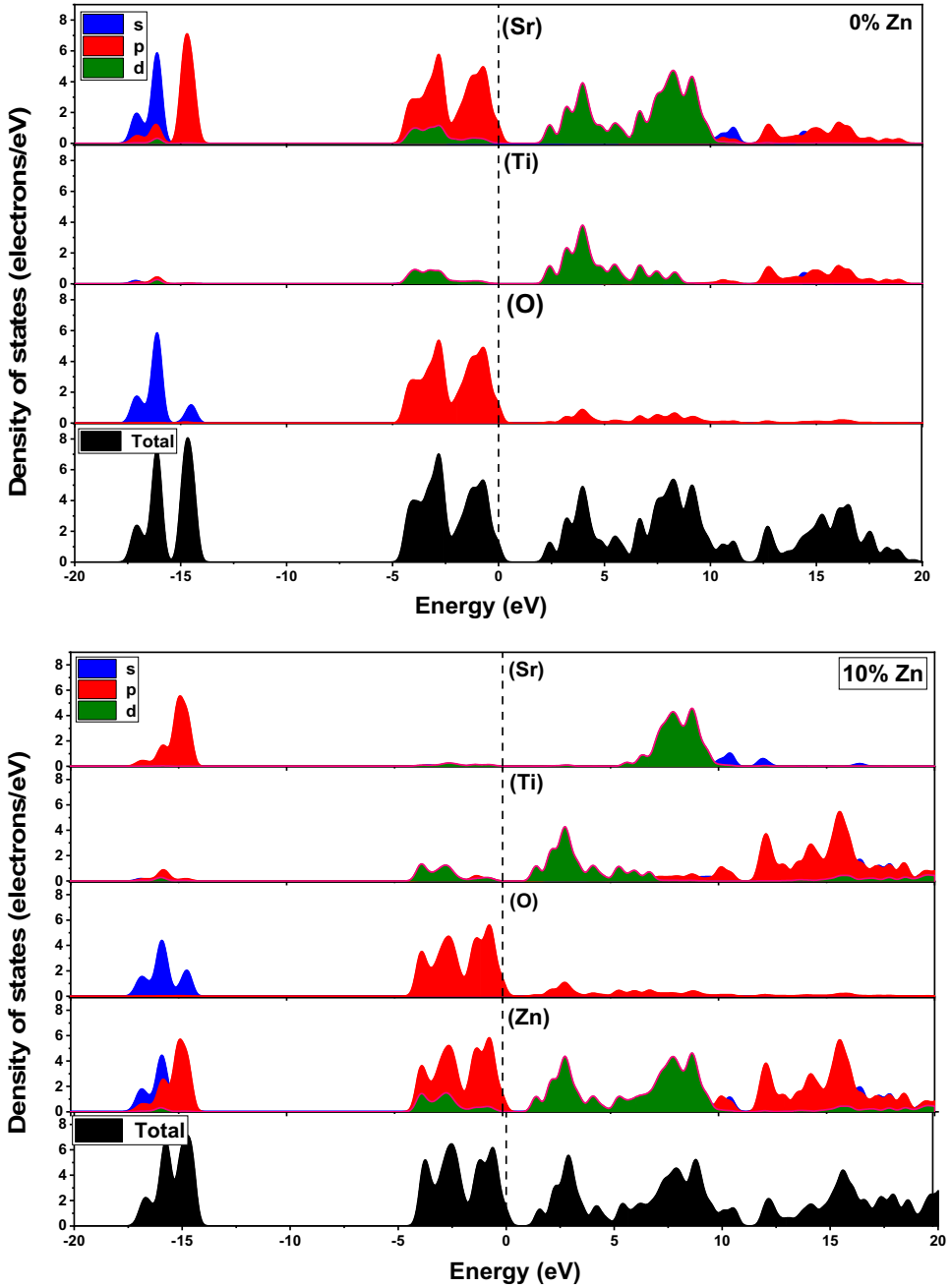
Fig. 10.   (Color online) TDOS and PDOS for standard and Zn (10%)-doped SrTiO$_3$ using GGA-PBE approximation.

4. Conclusion

Structural, elastic, mechanical and electronic properties of pure and Zn-doped SrTiO$_3$ compounds have been investigated using first-principles calculation via the CASTEP code. The investigated compounds exhibit an isotropic cubic structure with brittle nature. The Zn-doped SrTiO$_3$ (10%) is observed to be the most stable compound with narrow band gap energy. The substitution of Ti atoms by those of Zn improves the photocatalytic activity of SrTiO$_3$ compound. The band structure of SrZn$_x$Ti$_{1-x}$O$_3$ alloys exhibits an indirect $R \rightarrow \Gamma$ band gap. The partial and total DOS analysis shows that the conduction band is mainly composed of Zn and Ti-d with a mixture of Sr-s and Sr-d states of SrTiO$_3$, while O-p is mainly dominated by the valence band states. The increase in Zn content leads to the mixing of Zn-p and Zn-d with O-p, and therefore the band gap is reduced. The characterizations of pure and Zn-doped SrTiO$_3$ materials suggest that these materials have a significant potential to be used in photocatalytic devices. The doping of SrTiO$_3$ compound by Zn atoms shifts the top of the valence band towards the Fermi level.

Acknowledgments

References

1. W. S. Koe, J. W. Lee, W. Ch. Chong, Y. L. Pang and L. Ch. Sim, *Environ. Sci. Pollut. Res.* **27** (2020) 2522, doi: 10.1007/s11356-019-07193-5.
2. P. Reunchan, S. Ouyang, N. Umezawa, H. Xu, Y. Zhang and J. Ye, *J. Mater. Chem. A* **1** (2013) 4121, doi: 10.1039/C2TA00450J.
3. R. I. Eglitis and E. A. Kotomin, *Phys. B: Condens. Matter* **405** (2010) 3164, doi: 10.1016/j.physb.2010.04.033.
4. N. Pandech, K. Sarasamak and S. Limpijumnong, *J. Appl. Phys.* **117** (2015) 174108, doi: 10.1063/1.4919837.
5. M. A. Carpenter, *Am. Mineral* **92**(2–3) (2007) 309, doi: 10.2138/am.2007.2295.
6. S. Piskunov, E. Heifets, R. I. Eglitis and G. Borstel, *Comput. Mater. Sci.* **29** (2004) 165, doi: 10.1016/j.commatsci.2003.08.036.
7. B. Ghebouli, M. A. Ghebouli, T. Chihi, M. Fatmi, S. Boucetta and M. Reffas, *Solid State Commun.* **149**(47–48) (2009) 2244, doi: 10.1016/j.ssc.2009.09.001.
8. N. Pandech, K. Sarasamak and S. Limpijumnong, *J. Chin. Chem. Soc.* **63** (2016) 521, doi: 10.1002/jccs.201500377.
9. M. E. Lines and A. M. Glass, *Principles and Applications of Ferroelectrics and Related Materials* (Clarendon Press, Oxford, 1977).
10. J. S. Edrees, M. M. Shuker and M. M. Obeid, *Comput. Condens. Matter* **14** (2018) 20.
11. C. M. Kube, *AIP Adv.* **6** (2016) 095209, doi: 10.1063/1.4962996.
12. A. R. Benrekia, N. Benkhettou, A. Nassour, M. Dris, M. Sahnoun and S. Lebègue, *Phys. B Condens. Matter* **407**(13) (2012) 2632, doi: 10.1016/j.physb.2012.04.013.
13. G. Celik and S. Cabuk, *Cent. Eur. J. Phys.* **11**(3) (2013) 387. https://DOI: 10.2478/s11534-013-0176-6.

14. M. A. Ghebouli, B. Ghebouli, L. Krache, S. Alomairy, M. Fatmi, T. Chihi and M. Reffas, *Bull. Mater. Sci.* **45**(3) (2022) 124.

15. J. P. Perdew, K. Burke and M. Ernzerhof, *Phys. Rev. Lett.* **77** (1996) 3865, doi: 10.1103/PhysRevLett.77.3865.

16. H. J. Monkhorst and J. D. Pack, *Phys. Rev. B* **13** (1976) 5188, doi: 10.1103/PhysRevB.13.5188.

17. T. H. Fischer and J. Almlof, *J. Phys. Chem.* **96** (1992) 9768, doi: 10.1021/j100203a036.

18. Y. Naceur, H. Bourbaba, M. A. Ghebouli, L. Krache, B. Ghebouli, T. Chihi and S. Alomairy, *Sci. Rep.* **12**(1) (2022) 1.

19. K. Bouferrache, M. A. Ghebouli, B. Ghebouli, M. Fatmi, S. Alomairy and T. Chihi, *Chin. J. Phys.* **81** (2023) 303.

20. S. A. Saoucha, I. Bouchama, S. Alomairy, M. A. Ghebouli, B. Ghebouli and M. Fatmi, *Solid State Commun.* **354** (2022) 114897.

21. K. van Benthem, C. Elsasser and R. H. French, *J. Appl. Phys.* **90**(12) (2001) 6156.

22. J. Karczewski, B. Riegel, M. Gazda, P. Jasinski and B. Kusz, *J. Electroceram.* **24** (2010) 326, doi: 10.1007/s10832-009-9578-7.

23. T. Zhao, H. Lu, F. Chen, S. Dai, G. Yang and Z. Chen, *J. Cryst. Growth* **212**(3–4) (2000) 451.

24. X. G. Guo, X. S. Chen, Y. L. Sun, L. Z. Sun, X. H. Zhou and W. Lu, *Phys. Lett. A* **317** (2003) 501.

25. T. Tomio, H. Miki, H. Tabata, T. Kawai and S. Kawai, *J. Appl. Phys.* **76** (1994) 5886.

26. F. D. Murnaghan, *Proc. Natl. Acad. Sci. USA* **30** (1944) 5390.

27. M. Zafar, M. Shakil, S. Ahmed, M. Hashmi, M. A. Choudhary and Naeem-ur-Rehman, *Sol. Energy* **158** (2017) 63.

28. D. Berlincourt and H. Jaffe, *Phys. Rev.* **111** (1958) 143.

29. H. B. Huntington, *Solid State Phys.* (1958) 213, doi: 10.1016/s0081-1947(08)60553-6.

30. M. Shakil, H. Arshad, M. Zafar, M. Rizwan, S. S. A. Gillani and S. Ahmed, *Mol. Phys.* (2020) 1789770, doi: 10.1080/00268976.2020.1789770.

31. X. Jiang, J. Zhao and X. Jiang, *Comput. Mater. Sci.* **50** (2011) 2287.

32. M. Shakil, A. Akram, I. Zeba, R. Ahmad, S. Gillani and M. Gadhi, *Mater. Res. Express* **7**(2) (2020) 025513, doi: 10.1088/2053-1591/ab727d.

33. M. Zafar, M. Kashif, M. Rizwan, A. Zia, S. Ahmad, A. Akram, C. C. Bao and M. Shakil, *Optik* **182** (2019) 1176.

34. R. O. Bell and G. Ruprecht, *Phys. Rev.* **129** (1963) 90.

35. R. S. Sunmonu, O. Y. Fadimu and O. I. Sonde, *Int. J. Mod. Phys. B* (2023).

36. A. Afaq, A. Bakar, S. Anwar, W. Anwar and Fazal-e-Aleem, *Int. J. Mod. Phys. B* **32** (2018) 1850362, doi: 10.1142/S0217979218503629.

37. J. Robertson, K. Xiong and S. J. Clark, *Thin Solid Films* **496** (2006) 1.

38. E. Mete, R. Shaltraf and S. Ellialtioglu, *Phys. Rev. B* **68** (2003) 035119.

39. J. Yun, T. Yin and Z. Zhang, *Adv. Mater. Res.* **750**–**752** (2013) 1199, doi: 10.4028/www.scientific.net/AMR.750-752.1199.

40. H. K. Le, K. O. Pham, T. T. Tran and M. V. Le, *Sci. Technol. Dev.* **19**(K6) (2016) 176.

41. A. B. Posadas, C. Lin, A. A. Demkov and S. Zollner, *Appl. Phys. Lett.* **103** (2013) 142906, doi: 10.1063/1.4824023.

42. S. A. Azevedo, J. A. S. Laranjeira, J. L. P. Ururi and E. Longo, *Comput. Mater. Sci.* **214**(4) (2022) 111693, doi: 10.1016/j.commatsci.2022.111693.

43. Y. S. Hou, S. Ardo and R. Q. Wu, *Phys. Rev. Mater.* **5** (2021) 065801.

44. M. A. K. Yousaf Shah, S. Rauf, B. Zhu, N. Mushtaq, M. Yousaf, P. D. Lund, C. Xia and M. I. Asghar, *ACS Appl. Energy Mater.* **4**(1) (2021) 365.

AB-INITIO STUDY OF STRUCTURAL, ELECTRONIC AND OPTICAL PROPERTIES OF ZnX (X = Te, S and O): APPLICATION TO PHOTOVOLTAIC SOLAR CELLS†

Faiza Benlakhdar[a,*], Idris Bouchama[b,c], Tayeb Chihi[c,d], Ibrahim Ghebouli[c,d],
Mohamed Amine Ghebouli[c], Zohra Zerrougui[e], Khettab Khatir[f], Mohamed Alam Saeed[g]

[a]*Electronics Department, Faculty of Technology, University of Setif 1, 19000, Algeria*
[b]*Electronics Department, Faculty of Technology, University of Msila, Msila, 28000, Algeria*
[c]*Research Unit on Emerging Materials (RUEM), University Ferhat Abbas of Setif 1, Setif, 19000, Algeria*
[d]*Laboratory for Elaboration of New Materials and Characterization (LENMC), University of Ferhat Abbas, Setif 19000, Algeria*
[e]*Laboratory of Surfaces and Interfaces Studies Solid Materials (LESIMS), Department of Technology,*
Ferhat ABBAS Setif1 University, Setif, Algeria
[f]*Department of Electrical Department, Faculty of Technology, University of Msila, Msila, 28000, Algeria*
[g]*Department of Physics, Division of Science & Technology, University of Education, Lahore, Pakistan*
*Corresponding author e-mail: benlakhdar228@gmail.com

The purpose of this research is to investigate the structural, electronic, and optical properties of ZnX compounds, particularly those with X = Te, S, and O, which have direct bandgaps that make them optically active. To gain a better understanding of these compounds and their related properties, we conducted detailed calculations using density functional theory (DFT) and the CASTEP program, which uses the generalized gradient approximation (GGA) to estimate the cross-correlation function. Our results for lattice modulus, energy bandgap, and optical parameters are consistent with both experimental data and theoretical predictions. The energy bandgap for all compounds is relatively large due to an increase in s-states in the valence band. Our findings suggest that the optical transition between (O - S - Te) - p states in the highest valence band and (Zn - S - O) - s states in the lowest conduction band is shifted to the lower energy band. Therefore, ZnX compounds (X = Te, S and O) are a promising option for optoelectronic device applications, such as solar cell materials.
Keywords: *ZnTe; ZnS; ZnO; CASTEP; DFT; Density of state; Optical properties*
PACS: 36.40.Cg, 87.15.Pc, 87.19.rf, 91.60.Pn, 14.60.Cd, 84.60.Jt, 82.47.Jk

I. INTRODUCTION

Zinc monochalcogenides (ZnX: X = O, S, Se and Te) are considered the prototype of II-VI semiconductors and can crystallize in either the zinc-blende (z) or wurtzite (w) type structures. The ZnX-z phases are optically isotropic, while the ZnX-w phases are anisotropic, with c serving as the polar axis [1]. Due to their optical properties, ZnX phases are considered prime candidates for use in optical devices, such as visual displays, high-density optical memories, transparent conductors, solid-state laser devices, photodetectors, and solar cells [1]. Thus, understanding the optical properties of these materials is crucial in designing and analyzing ZnX-based optoelectronic devices [1]. ZnO, with a wide direct band-gap of approximately 3.37 eV at room temperature, is a typical semiconductor used for optoelectronic applications. It also possesses transparent properties in visible light and is non-toxic since zinc is abundant in the earth [2].

ZnS, ZnSe, and ZnTe are part of a family of IIB-VIA compounds that crystallize in the cubic zinc-blende structure at ambient pressure and have direct energy band-gaps [3]. These wide band-gap semiconductors are of significant interest since they are capable of emitting light even at room temperature [4]. Zinc Telluride (ZnTe) is of particular interest due to its low cost, high optical absorption coefficient, and suitability for use in PV applications [5]. It has also made extensive contributions to the field of microelectronics and optoelectronics applications [6]. Researchers have conducted various studies to investigate the electronic, structural, and dynamic properties of zinc-based semiconductors, such as Agrawal et *al.*, who used ab-initio to calculate these properties [7]. D. Bahri et *al.* investigated the structural, electronic, and optical properties of ZnTe cubic zinc-blende phase with the space group F-43m [8]. J. Serrano et *al.* used ab-initio to study the network dynamics of ZnO [9]. P. Walter et *al.* calculated the electronic energy band structures of ZnTe and ZnSe using the experimental pseudo-voltage method, which included spin-orbit coupling [10].

The focus of current research is on investigating the structural, electronic, and optical properties of ZnX (X = Te, S, and O) for potential photovoltaic applications, using the Density Functional Theory and GGA/PBE gradient approximation.

II. COMPUTATIONAL DETAILS

In this research, we utilized the CASTEP software [11] to analyze the structural, electronic, and optical characteristics of ZnX compounds, where X denotes Te, S, and O. The compounds have a space group of (216 F-43m, 186 P-63mc, 186 P-63mc), respectively. Through our assessments, we determined that (8×8×8) BZ k-point cell densities and planar wave discontinuities of 750 eV for ZnTe, 850 eV for ZnS, and 800 eV for ZnO were adequate. In general, the

GGA approach is preferred over LDA because LDA tends to underestimate the lattice parameters and cell volume, whereas GGA overestimates them. To approximate the GGA method, we used the Perdew-Burke-Ernzerhof [12] approach to estimate the band gap. We conducted geometric optimization with a precision of 1×10^{-5} eV/atom and we used the Broyden–Fletcher–Goldfarb–Shanno (BFGS) algorithm to relax at the lowest energy levels, with force, pressure, and displacement values set at 0.001 eV/A, 0.05 GPa, and 5.0×10^{-4} Å, respectively. We examined the electronic structures and other optical properties using total and partial densities of states, such as TDOS and PDOS, to achieve a more refined geometry.

III. RESULTS AND DISCUSSIONS
a. Structural Properties

In the first stage of our study, we performed calculations to determine the equilibrium structural parameters of ZnX (X = Te, S, and O), including the lattice constant a0, size modulus B0, and its first derivative B0'. The crystal structure of ZnX (X = Te, S, and O) is shown in Fig. 1. We focused on investigating the structural properties of ZnX and optimizing the lattice constants, and the results are presented in Table 1. The accuracy and validity of our research are confirmed by comparing our findings with existing theoretical and experimental data (as shown in Table 1). Our calculations show that the lattice constant a0 is 6.28 Å for ZnTe, 5.62 Å for ZnS, and 3.25 Å for ZnO. These values are slightly larger than the experimentally recorded values of 6.1 Å [13], 5.41 Å [13], and a = 3.249 Å, c = 5.204 Å [9], respectively. However, this discrepancy can be attributed to the difference in the atomic radii of ZnTe, ZnS, and ZnO, as well as the larger total energies, lattice relaxation constants, volume coefficients, and ground state energy of each material.
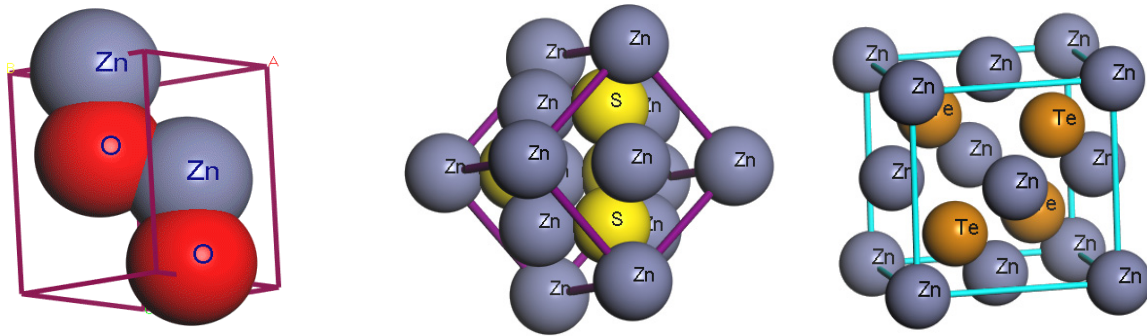
Figure 1. Crystal structures of: (a) ZnTe, (b) ZnS and (c) ZnO compounds.

We have optimized the structures of ZnTe, ZnS and ZnO at different pressure by fitting the Murnaghan equation of state [14], which gives the variation of the total energy as a function of the volume and given by:

$$E(V) = E_0 + \left[\frac{B_0 V}{B'(B'-1)}\right] \cdot \left[B'\left(1 - \frac{V_0}{V}\right) + \left(\frac{V_0}{V}\right)^{B'} - 1\right] \tag{1}$$

where V_0, B and B' are the volume at equilibrium, the bulk modulus and its derivative. The modulus of compressibility and its pressure derivative B_0' written as follows:

$$B0' = \frac{\partial B}{\partial P} \tag{2}$$

The fits of our data regarding the relative lattice constant a_0 (Å), bulk modulus B_0 (GPa) and the volume are given in Table 1.

Table 1. Calculated lattice constant a_0 (Å), bulk modulus $B`_0$ (GPa) for ZnX (X = Te, S and O) compound compared with already published data.

Compound	a_0(Å)	V(Å^3)	B_0(GPa)	B'_0
	6.28[n]	61.986[n]	41.30[n]	4.266[n]
	6.187[d]	52.66[b]	49.70[b]	4.45[b]
	6.103[i]	52.96[c]	51.40[c]	4.50[c]
ZnTe	6.16[e]	56.73[j]	55.21[h]	4.60[h]
	6.00[h]	58.73[b]	45.20[j]	4.63[j]
	6.17[b]	56.82[b] Exp.	45.25[b]	4.26[b]
	6.1[e] Exp		50.9[h] Exp.	5.04[h] Exp.
	5.62[n]	44.60[n]	62.043[n]	4.094[n]
	5.451[d]		75.6[e]	4.44[h]
ZnS	5.44[e]		89.67[h]	4.00[h] Exp.
	5.342[h]		75[h] Exp.	
	5.41[e] Exp			

Compound	$a_0(Å)$	$V(Å^3)$	$B_0(GPa)$	B'_0
	3.250^n	55.126^n	115.923^n	4.486^n
	$a = 3.244^d$	45.82^d	159.5^g	4.5^g
	$c = 5.027^d$	47.719^f	128.72^i	4.38^i
	$a = 3.249^f$	49.461^k	183^g Exp.	4^g Exp.
ZnO	$c = 5.216^f$	48.335^k Exp.		
	$a = 3.198^g$			
	$c = 5.167^g$			
	$a = 3.2496^g$ Exp.			
	$c = 5.2042^g$ Exp.			

[a]Ref [15], [b]Ref [16], [c]Ref [17], [d]Ref [1], [e] Ref [13], [f]Ref [18], [g]Ref [9], [h]Ref [3], [i]Ref [19], [j]Ref [17], [k] Ref [20], [l] Ref [2]
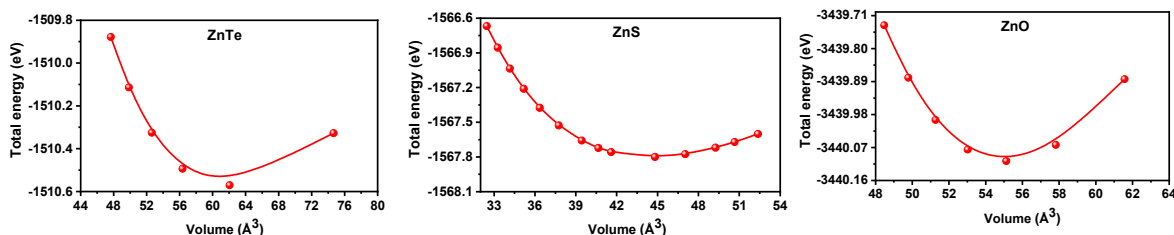[n] Present calculations.

Figure 2. Total energy versus volume for ZnX (X = Te, S and O) compounds.

b.   Electronic properties

The band structure and the total density of states (TDOS) and partial density of states (PDOS) calculated with optimized values were utilized to examine the electronic properties of ZnX (X = Te, S and O). The band-gap energy, particularly, provided insights into the bonding nature. The PBE-GGA approximation was used in the calculations. The computed band-gap of the three compounds revealed that all were semiconducting in nature, as illustrated in Fig. 3. In addition, the direct band-gap values for ZnX (X = Te, S and O) were 2.436, 2.698, and 1.721 eV, respectively. The conduction and valence bands were situated above and below the Fermi level. Both the bottom of the conduction band and the top of the valence band were located at the same point k (G - G), confirming that ZnX (X = Te, S and O) is a direct band-gap. All the calculated band-gap values for ZnX (X = Te, S and O) at 0 GPa are presented in Table 2. All values shown in Table 2 are consistent with theoretical and experimental data reported in other references that employ the PBE-GGA approximation. It is worth noting that the calculated band-gaps were lower than experimental values, which is attributed to the known Kohn-Sham DFT calculation error. The relatively higher band-gap energy of ZnTe, ZnS and ZnO compounds suggests that these compounds could potentially exhibit enhanced optical properties.
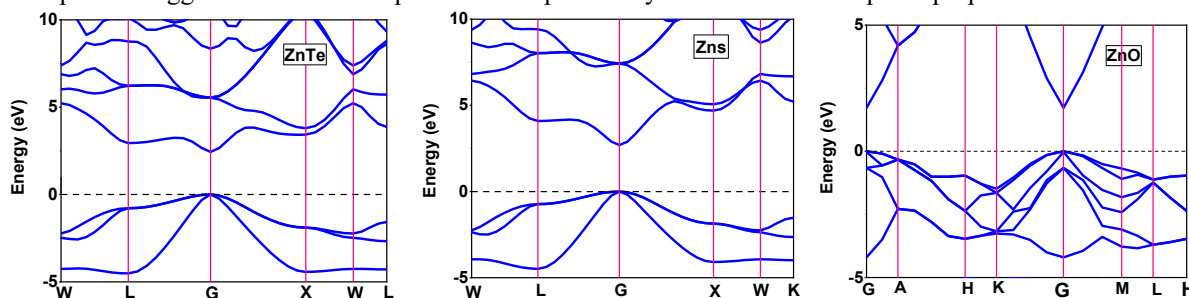
Figure 3. Calculated band structure of ZnX (X = Te, S and O) compounds using PBE-GGA approximation.

Table 2. Calculated band-gap value of ZnX at 0 GPa.

Compound	This work	Other theoretical calculations	Experiments
	2.436^n	1.711^d	2.39^f
ZnTe		1.804^f	
	2.698^n	2.07^e	3.68^h
ZnS		2.11^g	
		1.317^h	
		2.17^j	
	1.721^n	0.8^a	
ZnO		3.38^c	
		0.73^k	
		3.37^l	

[a] Ref [21], [c] Ref [18], [d] Ref [22], [e] Ref [23], [j] Ref [24], [k] Ref [25], [g] Ref [26], [h] Ref [27], [l] Ref [28], [n] Present calculations.

c. Density of States

To better understand the band and optical properties of ZnX (X = Te, S and O), it is important to investigate the electronic density of states (DOS) [29] and its relationship with the band structure. In this study, the DOS was determined and its connection with the band structure was examined. The chemical bonding of ZnX was illustrated by counting single atoms using partial DOS (PDOS) and all atoms using total DOS (TDOS). The electronic DOS is a crucial electronic property as it provides a deeper understanding of the band structure. Fig. 4 shows the TDOS and PDOS obtained using the GGA-PBE approximation, with the Fermi level taken as the energy origin. The electron configuration of Zn, Te, S, and O were 3d24s2, 3s23p6, 4s24p65s2, and 2s22p4, respectively. There are two regions, BV and BC, on both sides of the Fermi level: the BV region, dominated by Te-p, S-p, and O-p states, is centered between -5 eV and 0 eV for all three compounds. The second region, BC, centered between 0 eV and 5 eV, is dominated by Zn-s-p, Te-s-p, and S-s-p states. These results are consistent with previous reports.
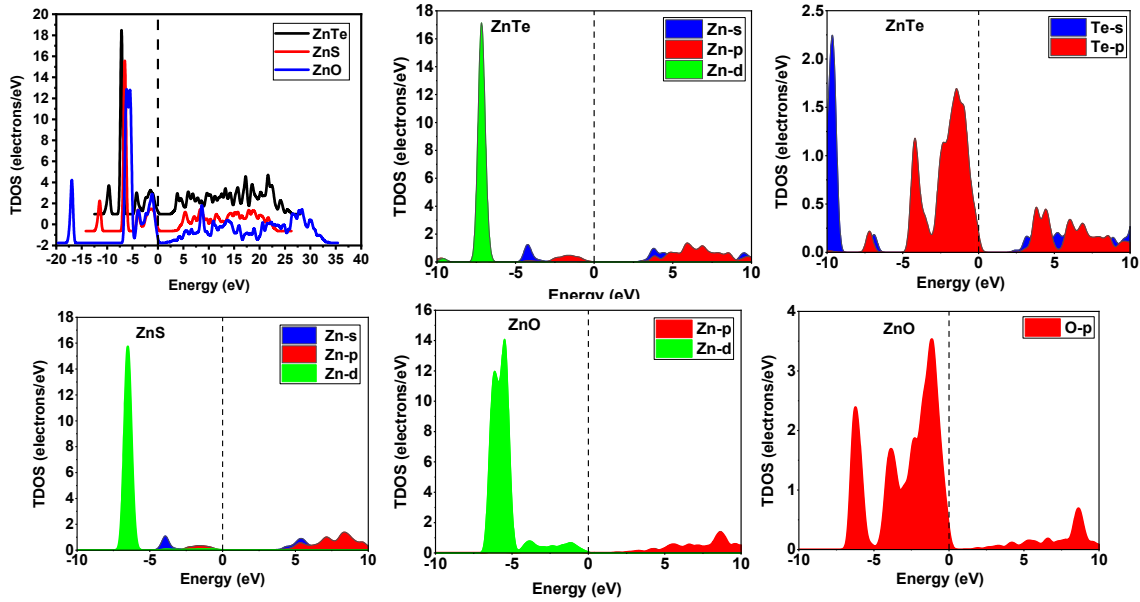

Figure 4. TDOS and PDOS spectra calculated using GGA-PBE approximation of ZnX (X = Te, S and O) compounds.

d. Optical Properties

The investigation of photonic properties is crucial for the studied compounds, as they have potential applications in photovoltaic devices and the semiconductor industry. To describe the optical properties of these materials, the transverse dielectric function ε(ω) [30] is used. The frequency-dependent dielectric constants have been calculated using the following formula:

$$\varepsilon(\omega) = \varepsilon_1(\omega) + i.\varepsilon_2(\omega) \tag{3}$$

The dielectric function is characterized by the real and imaginary parts, $\varepsilon_1(\omega)$ and $\varepsilon_2(\omega)$, respectively [31]. The real part of $\varepsilon_1(\omega)$ corresponds to the dispersion of incident photons by the material, while the imaginary part of $\varepsilon_2(\omega)$ represents the energy absorbed by the material. The complex dielectric function ε(ω) is made up of two contributions: intraband and interband transitions [31]. The contribution from intraband transitions is significant only for metals. The interband transitions can be further divided into direct and indirect transitions. In this study, the indirect interband transitions, which involve phonon scattering and contribute minimally to ε(ω), were neglected.

The complex dielectric function components were utilized to determine other optical parameters, including reflectivity R, refractive index n, optical conductivity σ, and absorption α [32]. The equations used to calculate these parameters are as follows:

$$R(w) = \frac{(n-1)^2 + k^2}{(n+1)^2 + k^2} \tag{4}$$

$$n(w) = \frac{\sqrt{\varepsilon_1^2(w) + \varepsilon_2^2(w)} + \varepsilon_1^{\frac{1}{2}}}{\sqrt{2}} \tag{5}$$

$$Re[\sigma(w)] = \frac{w}{4\pi}\varepsilon_2(w) \tag{6}$$

$$\alpha(w) = \sqrt{2}(w)\left[\sqrt{\varepsilon_1^2(w) + \varepsilon_2^2(w)} - \varepsilon_1(w)\right]^{\frac{1}{2}} \tag{7}$$

Fig. 5 through 9 depict various optical properties of ZnX (X = Te, S and O), including reflection spectra, absorption spectra, imaginary and real parts of the dielectric function, and photoconductivity.

1. Reflectivity R

The reflectivity R of a compound ZnX (where X = Te, S, or O) can be accurately predicted using computational tools such as the CASTEP program. For example, CASTEP simulations have shown that ZnTe exhibits a high reflectivity of approximately 96% in the infrared region, which makes it a promising material for infrared detectors and solar cells. Similarly, ZnS and ZnO have been found to exhibit high reflectivity in the visible and ultraviolet regions, respectively, with values reaching up to 87% and 96%. By tuning the composition and morphology of ZnX compounds, researchers can manipulate their reflectivity to suit specific applications. For instance, by growing ZnO thin films with a specific orientation, researchers can achieve high reflectivity of visible light while maintaining transparency.

Our analysis, as presented in Fig. 5, reveals that the reflectivity peaks of ZnTe, ZnS, and ZnO compounds increase at low energy (up to 7 eV), and decrease significantly at high energy (below 20 eV), as the forbidden bandwidth reduces.
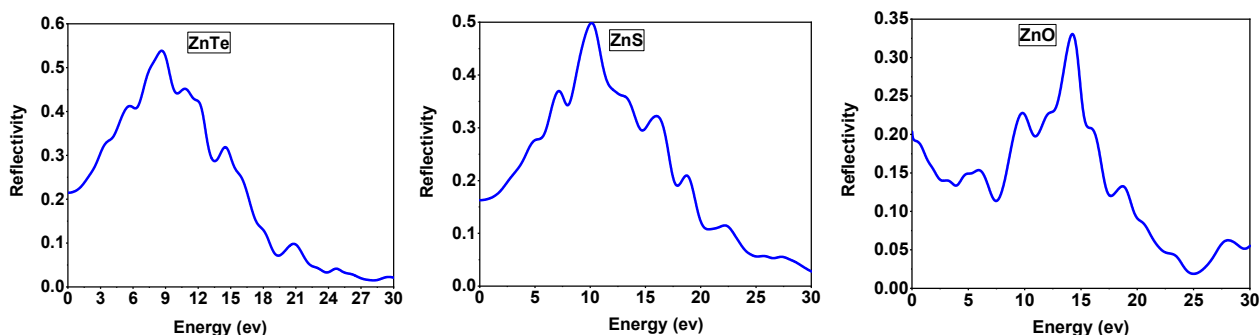

Figure 5. Reflectivity R as a function of energy of ZnTe, ZnS and ZnO compounds calculated using GGA-PBE approximation.

2. Absorption A

The absorption, denoted by A, is an important optical property of materials that describes the amount of light absorbed by the material. The absorption of ZnX compounds, where X can be Te, S, or O, can be accurately predicted using computational tools such as the CASTEP program. The results have shown that ZnTe has a high absorption coefficient of approximately 25×10^4 cm^{-1} in the mid-infrared region, making it a promising material for mid-infrared detectors and emitters. Similarly, ZnS and ZnO have been found to exhibit high absorption in the ultraviolet and visible regions, respectively, with values reaching up to 3×10^5 cm^{-1}. By understanding the absorption properties of ZnX compounds, researchers can design materials with specific absorption properties for various optoelectronic applications.

According to our study, when more electrons can be easily excited from the valence band to the conduction band, less energy is required, resulting in a redshift at the absorption edge. In this scenario, the probability of valence band electron guide transitioning to the excited state increases, leading to an obvious increase in the number of absorption peaks. Our findings, presented in Fig. 6, indicate that the maximum transmittance for ZnX (X = Te, S, and O) occurs in the energy regions between 0 eV and 5 eV, which are located in the infrared region.
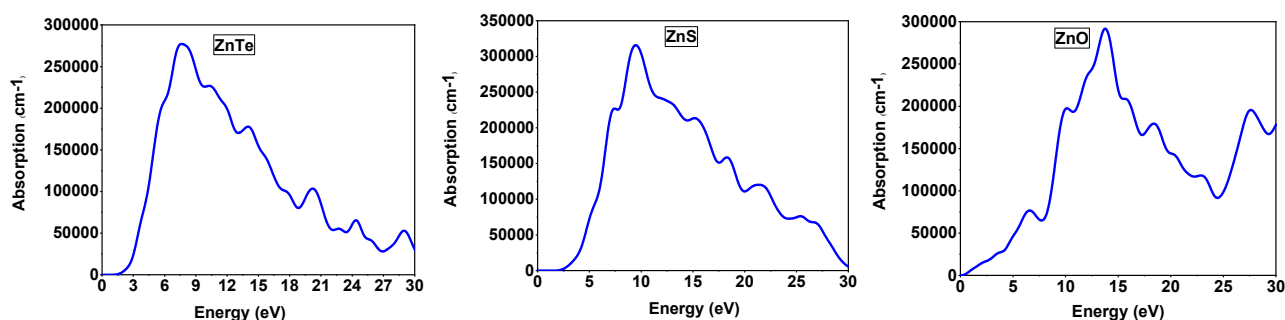

Figure 6. Absorption A as a function of energy of ZnTe, ZnS and ZnO compounds calculated using GGA-PBE approximation

3. Refractive index

The refractive index, denoted by n, is an important optical property that characterizes how light propagates through a material. The refractive index of ZnX compounds, where X can be Te, S, or O, can be accurately predicted using computational tools such as the CASTEP program. We have shown that the refractive index of ZnTe is approximately 2.5 in the mid-infrared region, making it a promising material for applications such as infrared lenses and waveguides. Similarly, ZnS and ZnO have been found to exhibit high refractive indices in the ultraviolet and visible regions, respectively, with values reaching up to 2 and 1.9. By understanding the refractive index of ZnX compounds, researchers can design materials with specific optical properties for various optoelectronic applications.
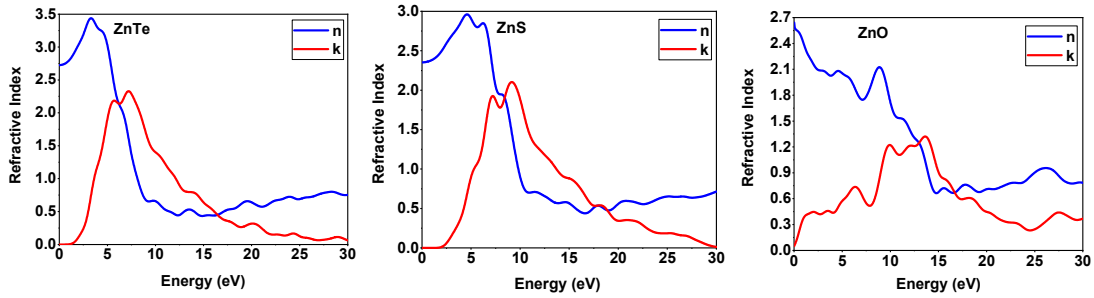
Figure 7. Refractive index as a function of energy of ZnTe, ZnS and ZnO compounds calculated using GGA-PBE approximation.

4. Dielectric function

The dielectric function, denoted by ε, is an important optical property that characterizes the response of a material to an external electric field. The simulation results using CASTEP have shown that the dielectric function of ZnTe is approximately 12 in the mid-infrared region, making it a promising material for applications such as infrared detectors and emitters. Similarly, ZnS and ZnO have been found to exhibit high dielectric functions in the ultraviolet and visible regions, respectively, with values reaching up to 9 and 5. By understanding the dielectric function of ZnX compounds, researchers can design materials with specific optical properties for various optoelectronic applications.
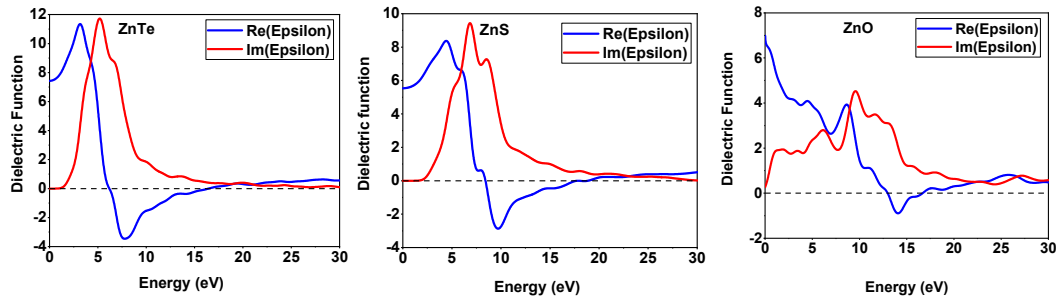

Figure 8. Dielectric function as a function of energy of ZnTe, ZnS and ZnO compounds calculated using GGA-PBE approximation.

5. Conductivity

The conductivity, denoted by σ, is an important electronic property that characterizes the ability of a material to conduct electric current. The conductivity of ZnX can be accurately predicted using computational tools such as the CASTEP program. The simulation results have shown that ZnTe has a high electrical conductivity of approximately 7 S/m at room temperature, making it a promising material for applications such as solar cells and thermoelectric devices. ZnS and ZnO materials exhibit moderate to high electrical conductivity, respectively, with values reaching up to 9 and 5 S/m.

Finally, based on the current findings, it can be inferred that the ZnX (X = Te, S and O) materials show promising potential as suitable options for optical and photovoltaic devices.
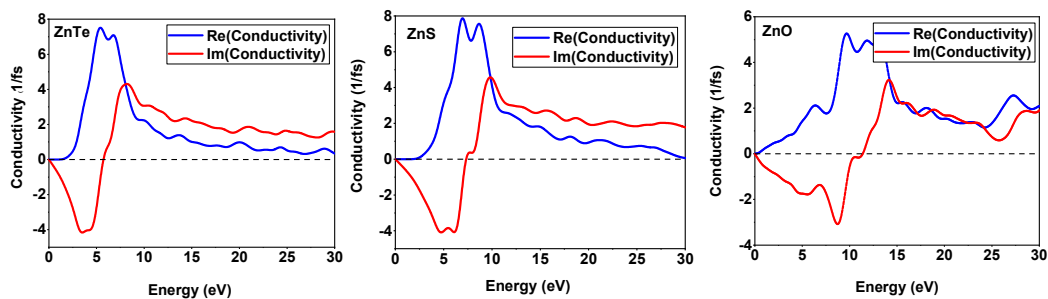
Figure 9. Conductivity as a function of energy of ZnTe, ZnS and ZnO compounds calculated using GGA-PBE approximation.

IV. Application to the substrate Cu(In,Ga)Se₂ solar cells

The conventional method of fabricating $Cu(In,Ga)Se_2$ (CIGS) thin-film solar cells involves the use of a substrate configuration that incorporates a CdS buffer layer and a doped ZnO or ITO window layer. This configuration has demonstrated conversion efficiencies exceeding 22% [29]. The exceptional optoelectronic properties of ZnX (X = Te, Se, S …etc) buffer layers have led to increased attention as a potential alternative to CdS buffer layers in recent years [33]. It is widely believed that the buffer layers play a critical role in preventing shunting through the TCO/CIGS interface, and they should possess suitable properties that help to minimize carrier recombination at the buffer/CIGS interface [34]. For

example, the efficiency of CIGS solar cells decreases significantly due to severe shunting when a conventional ZnO/TCO is directly deposited onto the CIGS layer [35]. According to some studies, the buffer layer demonstrated a higher level of electrical resistance compared to the top contact layer, which is highly conductive [30]. In this study, the use of ZnTe and ZnS as buffer layers in the substrate CIGS solar cell, along with the incorporation of the ZnO layer as a window layer, were investigated.

IV.1. Device settings and simulation process

Fig. 10 shows schematic of the substrate $n++$-ZnO/n-ZnS/p-Cu(In,Ga)Se$_2$ and $n++$-ZnO/n-ZnTe/p-Cu(In,Ga)Se$_2$ solar cell hetero-structures. To study the transport physics of these structures, the SCAPS-1D software solution solves the dipolar issues of the device using the Poisson equation and continuity equations for both electrons and holes. The SCAPS-1D simulator provides a software environment that can accurately replicate the behavior of a real solar cell [32,36]. Typically, the simulation process for a solar cell would require following the steps outlined in Fig. 11 through a series of screen-shots. The initial screenshot, labeled (a), displays the standard information input panel of the SCAPS-1D graphical user interface. This panel provides access to input buttons that enable the user to specify the simulation model and view the device's operating conditions, structure, and material parameters. The device simulation utilizes DOS mode. One particular layer's structure and material parameters, along with optical properties and defects, are displayed in screenshot (b). The results of light J-V characteristics in the form of a curve and axes are shown in screenshot (c). The simulation uses AM1.5 illumination spectrum with an incident power of 100 mW/cm^2. Table 3 summarizes the input parameters of each layer, including thickness, permittivity constant, band gap, electron affinity, electron/hole mobility, effective density of states in conduction/valence band, donor/acceptor concentration, defect concentration, and absorption coefficient within a range of 320 - 1100 nm wavelength. The thermal velocity recombination for holes/electrons at front and back contacts is 1.0×10^7 cm/s.

All data that have been previously calculated using CASTEP are being considered in the simulation.
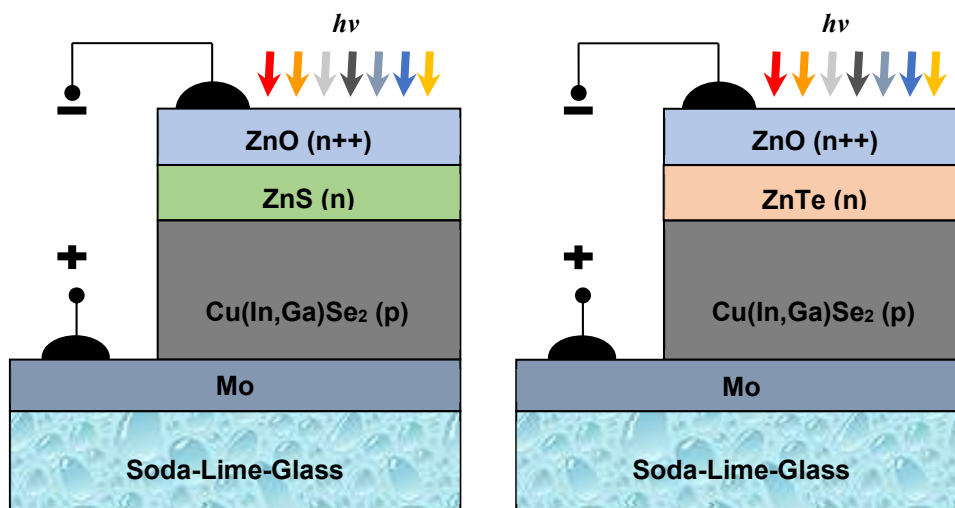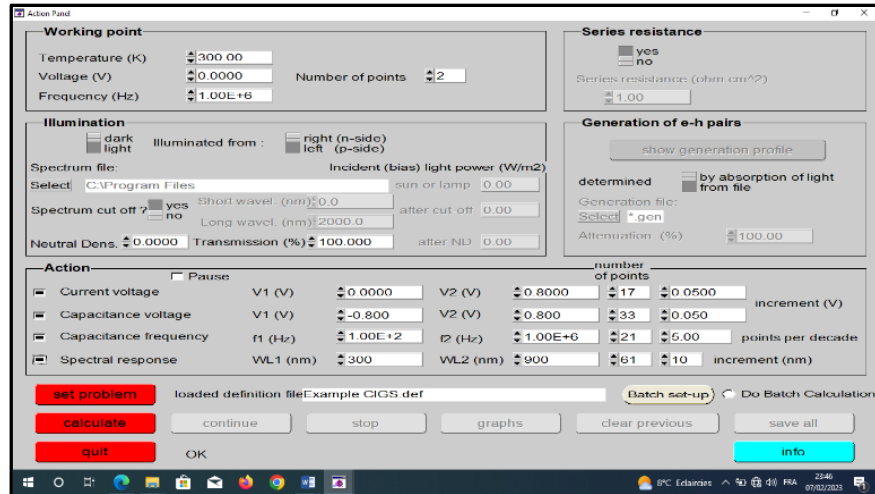

Figure 10. Schematic of the $n++$-ZnO/n-ZnS/Cu(In,Ga)Se$_2$ and $n++$-ZnO/n-ZnS/Cu(In,Ga)Se$_2$ solar cell structures
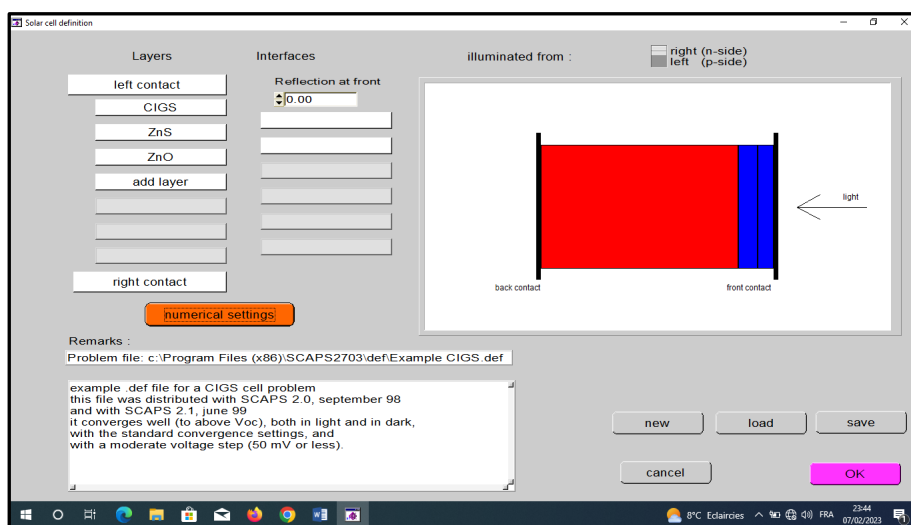
(a)

Figure 11. Typical data input panels of the SCAPS-1D graphical user interface, allowing to configure the solar cell device and its corresponding settings (*continued on the next page*)
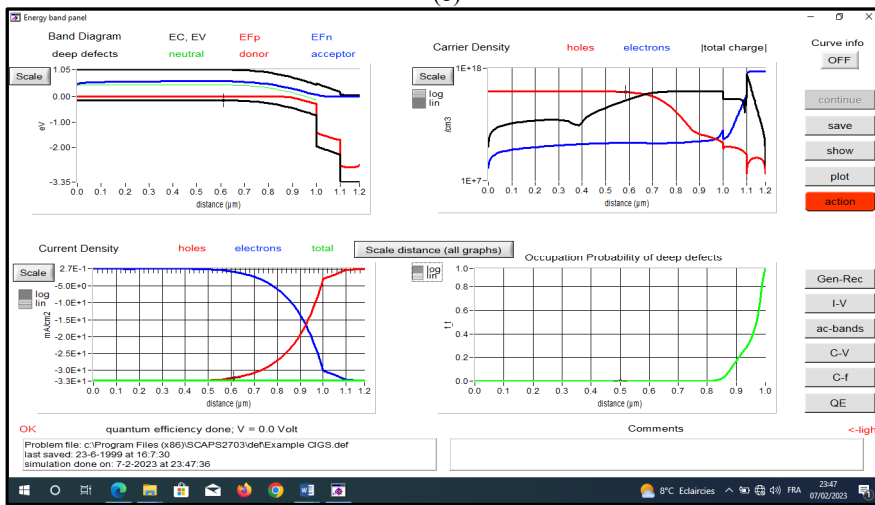
(b)

(c)

Figure 11. Typical data input panels of the SCAPS-1D graphical user interface, allowing to configure the solar cell device and its corresponding settings (*continued*)

Table 3. Settings for ZnO, ZnTe, ZnS and Cu(In,Ga)Se$_2$ layers used in the simulation.

Parameters	Cu(In,Ga)Se$_2$ Absorber	ZnTe buffer	ZnS buffer	ZnO window
Thickness (nm)	*3000*	*100*	*100*	*200*
Band gap E_g (eV)	*1.12*	*2.43*	*2.69*	*3.3*
Electron affinity χ_e (eV)	*4.1*	*4.07*	*4.09*	*4.09*
Relative permittivity ε_r (-)	*13.6*	*10*	*10*	*9*
Electron mobility μ_n (cm^2/V s)	*100*	*100*	*100*	*100*
Electron mobility μ_p (cm^2/V s)	*25*	*25*	*25*	*25*
Conduction band effective density of states N_C (cm^{-3})	*2.0×10°*	*2.0×10°*	*2.0×10°*	*4.0×10°*
Conduction band effective density of states N_V (cm^{-3})	*2.0×10°*	*1.5×10^p*	*1.5×10^p*	*9.0×10°*
shallow donor density (1/cm^3)	*0*	*1.0×10^q*	*1.0×10^q*	*1.0×10^p*
shallow acceptor density (1/cm^3)	*5.5×10^r*	*0*	*0*	*0*

^{o} Ref [37], ^{p} Ref [31], ^{q} Ref [38], ^{r} Ref [39].

IV.2. Effect of CIGS absorber thickness on solar cell performance

In an attempt to determine the most favorable thickness for a high-performance substrate CIGS solar cell that employs ZnTe and ZnS buffer layers, the thickness of the CIGS absorber was modified.

1. Case of ZnO/n-ZnS/p-CIGS/Mo solar cell structure

It is desirable to reduce the thickness of the absorber layer, *d*(CIGS), in order to lower costs while still maintaining high performance. ZnTe and ZnS buffer layers can help achieve this goal due to the abundance of these materials. In the

calculations, the thickness of the buffer layers is fixed at 100 nm. As shown in Fig. 12, the short-circuit current density (Jsc), open circuit voltage (Voc), Fill Factor (FF), and power conversion efficiency (η) are all affected by the thickness of the CIGS absorber layer. For absorber thicknesses up to 4 μm, Jsc remains around 32.1 mA/cm² and Voc is above 0.61 Volt. However, for the thinnest CIGS absorber layer, there is a slight reduction in Voc which may be due to an increased influence of recombination at the Mo back contact layer, resulting in a smaller effective minority carrier lifetime. The fill factor slightly increases but remains above 79% for all absorber thicknesses greater than 4 μm. The short-circuit current density and open circuit voltage show a strong dependence on the absorber thickness, Jsc increases from 29.12 mA/cm² to 32.08 mA/cm² as the CIGS absorber thickness varies from 1 to 4 μm. For devices thinner than 1 μm, current loss may be due to optical and/or electrical losses. The losses in Jsc and Voc mainly contribute to the conversion efficiency losses. The optimum thickness for the CIGS absorber layer is greater than 4 μm, which results in a maximum conversion efficiency of 15.6% with FF = 78.5%, Voc = 0.61 Volt and Jsc = 32.1 mA/cm².
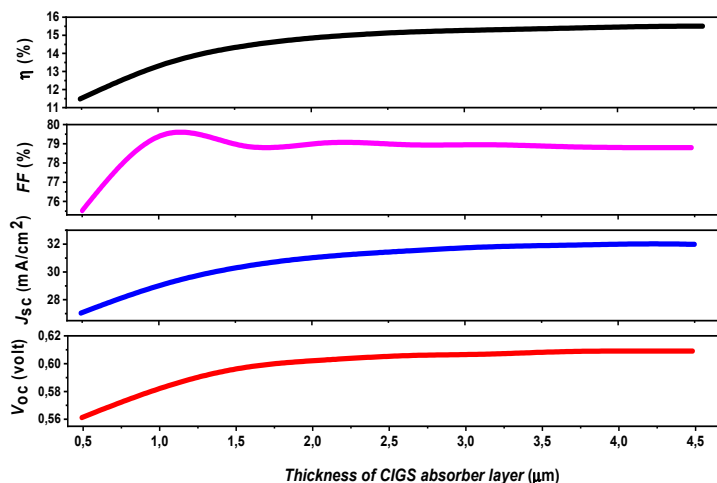

Figure 12. Solar cell performance using ZnS buffer layer as a function of the p-CIGS thickness.

2. Case of ZnO/n-ZnTe/p-CIGS/Mo solar cell structure

Fig. 13 presents the performance of ZnO/ZnTe/CIGS/Mo solar cell as a function of CIGS absorber thickness. It shows that the recorded efficiency is 14.66% and 16.58% at the CIGS thickness of 1 μm and 4 μm, respectively.
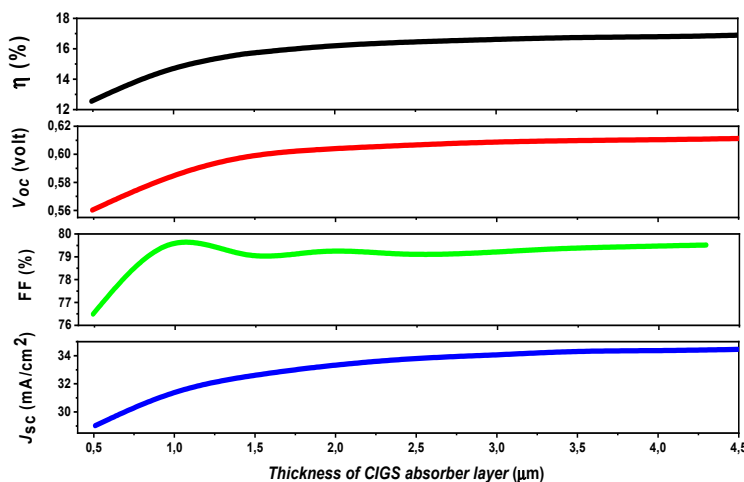

Figure 13. Solar cell performance using ZnTe buffer layer as a function of p-CIGS thickness.

A comparison of these results with the 16.12% efficiency at 2 μm reveals that decreasing the absorber thickness by 1 μm leads to an 11.58% drop in efficiency, whereas increasing it by 1 μm results in only a 3.8% increase in efficiency. This trend continues to hold for absorber thicknesses more than 2 μm. These findings support the theoretical assumption that a thickness of around 2 μm is sufficient to absorb most of the incident light. However, reducing the absorber layer thickness below this value would bring the back contact too close to the depletion region, which would facilitate electron capture by the back contact during the recombination process. The open circuit voltage (Voc) and short circuit current density (Jsc) increase with the thickness of the absorber layer, primarily due to the longer wavelengths' absorption, which contributes to electron-hole pair generation. When d(CIGS) is greater than 4 μm, the maximum Fill Factor of 79.5% is obtained. The highest efficiency of approximately 16.58%, with FF = 79.5%, Voc = 0.61 Volt, and Jsc = 34.05 mA/cm² can be achieved when d(CIGS) is approximately 4 μm.

III. CONCLUSIONS

The use of computational tools like CASTEP provides a powerful tool for the design and optimization of such materials, enabling the development of advanced optoelectronic devices. In this paper, the electronic structure and optical properties of ZnX systems were studied using the first principles of the ultra-smooth pseudovoltage method of density functional theory and the generalized gradient approximation method using the CASTEP tool. The search showed the following results: The network parameters took different values; Therefore, it is possible to deposit them on different substrates. The binary alloy is interesting, because it has a wide bandgap (2.436 eV, 2.698 eV, 1.721 eV) for ZnTe, ZnS and Zn0, respectively. From the results obtained, the structural, physical and optical properties are in close agreement with the available theoretical and experimental data which indicate the accuracy of the proposed calculation scheme. The properties of pure ZnX (X = Te, S, O) materials indicate that these materials have great potential for use in solar cells. The outcomes of the calculation reveal that although the efficiency grew alongside the absorber thickness, d(CIGS), the pace of this increase was much less beyond 2 μm. The result concludes that the CIGS absorber layer's ideal thickness is likely to exceed 4 μm.

ORCID

 Faiza Benlakhdar, https://orcid.org/0009-0003-1131-6289

REFERENCES

[1] B.G. Svensson, "Electronic structure and optical properties of Zn X (X =O, S, Se, Te)," pp. 1–14, 2018.
[2] M. Lee, Y. Peng, and H. Wu, "Effects of intrinsic defects on electronic structure and optical properties of Ga-doped ZnO," J. Alloys Compd. **616**, 122-127 (2014)ю https://doi.org/10.1016/j.jallcom.2014.07.098
[3] R. Khenata, "Elastic, electronic and optical properties of ZnS, ZnSe and ZnTe under pressure," Computational Materials Science, **38**, 29-38 (2006). https://doi.org/10.1016/j.commatsci.2006.01.013
[4] Y. Yu, J. Zhou, H. Han, and C. Zhang, "Ab initio study of structural , dielectric , and dynamical properties of zinc-blende ZnX (X = O, S, Se, Te)," Journal of Alloys and Compounds, **471**, 492-497 (2009). https://doi.org/10.1016/j.jallcom.2008.04.039
[5] S. Jeetendra, H. Nagabhushana, K. Mrudula, C.S. Naveen, P. Raghu, and H.M. Mahesh, "Concentration Dependent Optical and Structural Properties of Mo doped ZnTe Thin Films Prepared by e-beam Evaporation Method," Int. J. Electrochem. Sci. **9**, 2944-2954 (2014). http://www.electrochemsci.org/papers/vol9/90602944.pdf
[6] S.M. Ali, A.A.A. Shehab, and S.A. Maki, "Study of the Influence of Annealing Temperature on the Structural and Optical Properties of ZnTe Prepared by Vacuum Thermal Evaporation Technique," Ibn Al-Haitham Journal for Pure and Applied sciences, **31**(1), 50-57 (2018). https://doi.org/10.30526/31.1.1851
[7] Y. Yu et al., "Ab initio study of structural, dielectric, and dynamical properties of zinc-blende ZnX (X= O, S, Se, Te)," Journal of alloys and compounds, 471(1-2), 492-497 (2009). https://doi.org/10.1016/j.jallcom.2008.04.039
[8] D. Bahri and L. Amirouche, "Ab initio study of the structural , electronic and optical properties of ZnTe compound," AIP Conference Proceedings, **1653**(1), (2015). https://doi.org/10.1063/1.4914210
[9] J. Serrano, Y. Tech, A. H. Romero, and R. Lauck, "Pressure dependence of the lattice dynamics of ZnO : An ab initio approach," Physical Review B, **69**, 094306 (2004). https://doi.org/10.1103/PhysRevB.69.094306.
[10] V.O.I. Ume, P. Walter, L. Cohen, and Y. Petroff, "Calculated and Measured Reflectivity of ZnTe and ZnSef," Phys. Rev. B, **1**, 2661 (1970). https://doi.org/10.1103/PhysRevB.1.2661
[11] M. Caid *et al.*, "Electronic structure of short-period ZnSe/ZnTe superlattices based on DFT calculations," Condensed Matter Physics, **25**(1), 1-10 (2022). https://doi.org/10.5488/CMP.25.13701
[12] F. Parandin, J. Jalilian, and J. Jalilian, "Tuning of electronic and optical properties in ZnX (X = O, S, Se and Te) monolayer : Hybrid functional calculations," Chemical Review & Letters, **2**(2), 76-83 (2019). https://doi.org/10.22034/crl.2019.195774.1019
[13] Z. Nourbakhsh, "Structural , electronic and optical properties of ZnX and CdX compounds (X = Se , Te and S) under hydrostatic pressure," J. Alloys Compd. **505**(2), 698-711 (2010). https://doi.org/10.1016/j.jallcom.2010.06.120.
[14] F.D. Murnaghan, "The Compressibility of Media under Extreme Pressures," Proceedings of the National Academy of Sciences of the United States of America, **30**(9), 244-247 (1944). https://www.jstor.org/stable/87468
[15] M. Safari, Z. Izadi, J. Jalilian, and I. Ahmad, "Metal mono-chalcogenides ZnX and CdX (X = S , Se and Te) monolayers : Chemical bond and optical interband transitions by first principles calculations," Phys. Lett. A, **381**(6), 663-670 (2017). https://doi.org/10.1016/j.physleta.2016.11.040.
[16] S. K. Gupta, S. Kumar, and S. Auluck, "Structural, electronic and optical properties of high pressure stable phases of ZnTe," Physica B: Condensed Matter, **404**, 3789-3794 (2009). https://doi.org/10.1016/j.physb.2009.06.149
[17] A.A. Audu, W.A. Yahya, and A.A. Abdulkareem, Physics Memoir: Journal of Theoretical & Applied Physics, "Ab initio Studies of the Structural, Electronic and Mechanical Properties of $Zn_{1−x}Cr_x$ e," **3**, 38-47 (2021).
[18] M. Achehboune, M. Khenfouch, I. Boukhoubza, I. Derkaoui, B.M. Mothudi, I. Zorkani, A. Jorio, "Effect of Yb Concentration on the Structural, Magnetic and Optoelectronic Properties of Yb Doped ZnO : First Principles Calculation". http://dx.doi.org/10.21203/rs.3.rs-877060/v1
[19] R. John, and S. Padmavathi, "Ab Initio Calculations on Structural, Electronic and Optical Properties of ZnO in Wurtzite Phase," Cryst. Struct. Theory Appl. **5**(2), 24-41 (2016). https://doi.org/10.4236/csta.2016.52003
[20] R. Chowdhury, S. Adhikari, and P. Rees, "Optical properties of silicon doped ZnO," Phys. B Condens. Matter, **405**(23), 4763-4767 (2010). https://doi.org/10.1016/j.physb.2010.08.072

[21] C. Feng *et al.*, "First-principle calculation of the electronic structures and optical properties of the metallic and nonmetallic elements-doped ZnO on the basis of photocatalysis," Phys. B Condens. Matter, **555**, 53-60 (2019). https://doi.org/10.1016/j.physb.2018.11.043.

[22] L. Chen, X. Zhou, and J. Yu, "First-principles study on the electronic and optical properties of the ZnTe/InP heterojunction," *J.* Comput. Electron. **18**(3), 749-757 (2019). https://doi.org/10.1007/s10825-019-01358-8

[23] A.M. Ghaleb, and A.Q. Ahmed, "Structural, electronic, and optical properties of sphalerite ZnS compounds calculated using density functional theory (DFT)," Chalcogenide Lett. **19**(5), 309-318 (2022). https://doi.org/10.15251/CL.2022.195.309

[24] Q. Hou, and S. Sha, "Effect of biaxial strain on the p-type of conductive properties of (S, Se, Te) and 2 N co-doped ZnO," Mater. Today Commun. **24**, 101063 (2020). https://doi.org/10.1016/j.mtcomm.2020.101063

[25] Md.A. Momin, Md.A. Islam, A. Majumdar, "Influence on structural , electronic and optical properties of Fe doped ZnS quantum dot : A density functional theory based study," Quantum Chemistry, **121**(1), 1-13 (2020). https://doi.org/10.1002/qua.26786

[26] M. Dong, P. Zhou, C. Jiang, B. Cheng, and J. Yu, "First-principles investigation of Cu-doped ZnS with enhanced photocatalytic hydrogen production activity State Key Laboratory of Advanced Technology for Materials Synthesis and," Chem. Phys. Lett. **668**, 1-6 (2016). https://doi.org/10.1016/j.cplett.2016.12.008

[27] A. Pattnaik, M. Tomar, P.K. Jha, A.K. Bhoi, V. Gupta, and B. Prasad, "Theoretical Analysis of the Electrical and Optical Properties of ZnS," In: A. Konkani, R. Bera, and S. Paul, editors, *Advances in Systems, Control and Automation. Lecture Notes in Electrical Engineering*, vol. 442. (Springer, Singapore, 2018). https://doi.org/10.1007/978-981-10-4762-6_2

[28] Y.L. Su, Q.Y. Zhang, N. Zhou, C.Y. Ma, X.Z. Liu, and J.J. Zhao, "Study on Co-doped ZnO comparatively by fi rst-principles calculations and relevant experiments," **250**, 123-128 (2017). https://doi.org/10.1016/j.ssc.2016.12.002

[29] T. Kato, J. L. Wu, Y. Hirai, H. Sugimoto, and V. Bermudez, "Record Efficiency for Thin-Film Polycrystalline Solar Cells Up to 22.9% Achieved by Cs-Treated Cu(In,Ga)(Se,S)$_2$," IEEE J. Photovoltaics, **9**(1), 325-330 (2019). https://doi.org/10.1109/JPHOTOV.2018.2882206

[30] A. Bouzidi, and I. Bouchama, "Numerical study of the buffer influence on the Cu(In,Ga)Se$_2$ solar cells performances by SCAPS-ID," in: International Conference on Electronics and New Technologies (ICENT), 2017.

[31] S.K. Gupta, S. Kumar, and S. Auluck, "Structural, electronic and optical properties of high pressure stable phases of ZnTe," Phys. B Condens. Matter, **404**(20), 3789-3794 (2009). https://doi.org/10.1016/j.physb.2009.06.149

[32] R. Tala-Ighil Zaïr, C. Oudjehani, and K. Tighilt, "SCAPS Simulation for Perovskite Solar Cell," J. Sol. Energy Res. Updat. **8**, 21-26 (2021). https://doi.org/10.31875/2410-2199.2021.08.3

[33] H.I. Abdalmageed, M. Fedawy, and M.H. Aly, "Effect of absorber layer bandgap of CIGS-based solar cell with (CdS/ZnS) buffer layer," J. Phys. Conf. Ser. **2128**(1), (2021). https://doi.org/10.1088/1742-6596/2128/1/012009

[34] C. Platzer-Björkman, J. Kessler, and L. Stolt, "Analysis of Zn(O,S) films for Cu(In,Ga)Se$_2$ solar cells," Proc. Estonian Acad. Sci. Phys. Math. **52**(3), 299-307 (2003). https://doi.org/10.3176/phys.math.2003.3.06

[35] Y.-K. Liao et al., "A look into the origin of shunt leakage current of Cu(In, Ga)Se$_2$ solar cells via experimental and simulation methods," Sol. Energy Mater. Sol. Cells, **117**, 145-151 (2013). https://doi.org/10.1016/j.solmat.2013.05.031

[36] P. Srivastava *et al.*, "Theoretical study of perovskite solar cell for enhancement of device performance using SCAPS-1D," Phys. Scr. 97(2), 12 (2022). https://doi.org/10.1088/1402-4896/ac9dc5

[37] M. Safari, Z. Izadi, J. Jalilian, I. Ahmad, and S. Jalali-Asadabadi, "Metal mono-chalcogenides ZnX and CdX (X = S, Se and Te) monolayers: Chemical bond and optical interband transitions by first principles calculations," Phys. Lett. Sect. A Gen. At. Solid State Phys. **381**(6), 663-670 (2017). https://doi.org/10.1016/j.physleta.2016.11.040

[38] H. T. Ganem, and A. N. Saleh, "The effect of band offsets of absorption layer on CNTS/ZnS/ZnO solar cell by SCAPS-1D," Tikrit Journal of Pure Science, **25** (6), 79-87 (2020). http://dx.doi.org/10.25130/tjps.25.2020.114

[39] N. Adim, M. Caid, D. Rached, and O. Cheref, "Computational study of structural, electronic, magnetic and optical properties of (ZnTe)m/(MnTe) n superlattices," Journal of Magnetism and Magnetic Materials, **499**, 166314 (2020). https://doi.org/10.1016/j.jmmm.2019.166314 jstor

АВ-INITIO ДОСЛІДЖЕННЯ СТРУКТУРНИХ, ЕЛЕКТРОННИХ ТА ОПТИЧНИХ ВЛАСТИВОСТЕЙ ZnX (X = Te, S i O): ЗАСТОСУВАННЯ ДО СОНЯЧНИХ БАТАРЕЙ

Файза Бенлахдар[a], Ідріс Бушама[b,c], Тайєб Чіхі[c,d], Ібрагім Гебулі[c,d],
Мохамед Амін Гебулі[c], Зохра Зерругуі[e], Кеттаб Хатір[f], Мохамед Алам Сайєд[g]
[a]Кафедра електроніки, технологічний факультет, Університет Сетіфа 1, 19000, Алжир
[b]Кафедра електроніки, технологічний факультет, Університет Мсіла, Мсіла, 28000, Алжир
[c]Дослідницький відділ нових матеріалів (RUEM), Університет Ферхат Аббас із Сетіфа 1, Сетіф, 19000, Алжир
[d]Лабораторія розробки нових матеріалів і характеристик (LENMC), Університет Ферхата Аббаса, Сетіф 19000, Алжир
[e]Лабораторія досліджень поверхонь і розділу твердих матеріалів (LESIMS), Департамент технологій,
Ферхат АББАС Сетіфський університет, Сетіф, Алжир
[f]Кафедра електротехніки, технологічний факультет, Університет Мсіла, Мсіла, 28000, Алжир
[g]Департамент фізики, Відділ науки та технологій, Педагогічний університет, Лахор, Пакистан

Метою роботи є дослідження структурних, електронних і оптичних властивостей сполук ZnX, зокрема тих, у яких X = Te, S i O, які мають пряму заборонену зону, що робить їх оптично активними. Щоб краще зрозуміти ці сполуки та їхні пов'язані властивості, ми провели детальні розрахунки за допомогою теорії функціоналу щільності (DFT) і програми CASTEP, яка використовує узагальнене градієнтне наближення (GGA) для оцінки функції крос-кореляції. Наші результати щодо модуля гратки, ширини забороненої зони та оптичних параметрів узгоджуються як з експериментальними даними, так і з теоретичними прогнозами. Енергетична заборонена зона для всіх сполук є відносно великою через збільшення s-станів у валентній зоні. Наші результати показують, що оптичний перехід між (O - S - Te) - p-станами у найвищій валентній зоні та (Zn - S - O) - s-станами в нижчій зоні провідності зміщується до нижчої енергетичної зони. Таким чином, сполуки ZnX (X = Te, S i O) є перспективним варіантом для оптоелектронних пристроїв, таких як матеріали для сонячних елементів.
Ключові слова: *ZnTe; ZnS; ZnO; CASTEP; DFT; щільність стану; оптичні властивості*

CERTIFICATE *Of* PARTICIPATION

Faiza Benlakhdar

has participated in 5th International Conference on Applied Engineering and Natural Sciences on 10-12 July in 2023 at Konya/Turkey.

PAPER TITLE

Advancing the Properties of CuInX-1GaXS2 Compounds using the CASTEP Program: A Computational Exploration of Structural, Electronic, and Optical Characteristics

PRESENTATION TYPE

Oral

ICAENS 2023 CONFERENCE CHAIRMAN
Asst. Prof. Dr. Umut ÖZKAYA

CERTIFICATE *Of* PARTICIPATION

Faiza Benlakhdar

has participated in 3rd International Conference on Innovative Academic Studies September 26 – 28 in 2023 at Konya/Turkey.

PAPER TITLE

The Effects of Fluorine Doping on the Structure and Electronic Properties of Hexachloro-tungsten (WCl6) for Photocatalysis

PRESENTATION TYPE

Oral

ICIAS

All Sciences Academy

CERTIFICATE *Of* PARTICIPATION

Faiza Benlakhdar

has participated in 3rd International Conference on Innovative Academic Studies September 26 – 28 in 2023 at Konya/Turkey.

PAPER TITLE

Comprehensive Investigation of Structural and Electronic Properties of Sulfur-Doped Zinc Oxide using CASTEP Program

PRESENTATION TYPE

Oral

ICIAS

All Sciences Academy

مـلـخص

تبحث هذه الدراسة عن تأثير تطعيم ثلاث مواد متميزة من أشباه الموصلات - SrTiO₃ مع الزنك (Zn)، وCuInS2 مع الألومنيوم (Al)، وأكسيد الزنك مع التيلوريوم (Te) - على خصائصها الهيكلية والميكانيكية والإلكترونية والبصرية. الهدف هو تقييم الملاءمة المحتملة لهذه المواد المخدرة للدمج في التطبيقات الكهروضوئية، مع التركيز بشكل خاص على مدى صلتها بالخلايا الشمسية Cu(In,Ga)Se₂ (CIGS). تكشف التحليلات الحسابية الشاملة باستخدام برنامج CASTEP عن رؤى مثيرة للاهتمام حول تأثيرات المنشطات على هذه المواد. تشير النتائج إلى التشوهات الهيكلية الدقيقة، وتغييرات الخصائص الميكانيكية، والتحولات في الخواص الإلكترونية، والتغيرات في أطياف الامتصاص البصري الناتجة عن كل عملية منشط. في حين أن هذه النتائج تقدم رؤى قيمة، فإن الاستخدام الناجح لهذه المواد المخدرة في الخلايا الشمسية CIGS.

الكلمات الرئيسية: *المنشطات، SrTiO₃، CuInS₂، خواص المواد، المرونة، الخواص الإلكترونية، الخواص البصرية، بنية النطاق، خواص العزل الكهربائي.*

Abstract

This study investigates the impact of doping three distinct semiconductor materials—SrTiO₃ with zinc (Zn), CuInS₂ with aluminum (Al), and ZnO with tellurium (Te)—on their structural, mechanical, electronic, and optical properties. The objective is to assess the potential suitability of these doped materials for integration into photovoltaic applications, with a particular focus on their relevance to Cu(In,Ga)Se₂ (CIGS) solar cells. Comprehensive computational analyses utilizing the CASTEP program reveal intriguing insights into the effects of doping on these materials. The findings indicate subtle structural distortions, mechanical property alterations, shifts in electronic properties, and changes in optical absorption spectra resulting from each doping process. While these results offer valuable insights, the successful utilization of these doped materials in CIGS solar cells.

Keywords: *Doping, SrTiO₃, CuInS₂, Material properties, Elasticity, Electronic properties, Optical properties, Band Structure, Dielectric Properties.*

Résumé

Cette étude examine l'impact du dopage de trois matériaux semi-conducteurs distincts : SrTiO₃ avec du zinc (Zn), CuInS₂ avec de l'aluminium (Al) et ZnO avec du tellure (Te) – sur leurs propriétés structurelles, mécaniques, électroniques et optiques. L'objectif est d'évaluer l'adéquation potentielle de ces matériaux dopés pour une intégration dans des applications photovoltaïques, avec un accent particulier sur leur pertinence pour les cellules solaires Cu(In,Ga)Se₂ (CIGS). Des analyses informatiques complètes utilisant le programme CASTEP révèlent des informations fascinantes sur les effets du dopage sur ces matériaux. Les résultats indiquent des distorsions structurelles subtiles, des altérations des propriétés mécaniques, des changements dans les propriétés électroniques et des changements dans les spectres d'absorption optique résultant de chaque processus de dopage. Bien que ces résultats offrent des informations précieuses, l'utilisation réussie de ces matériaux dopés dans les cellules solaires CIGS.

Mots-clés : *Dopage, SrTiO₃, CuInS₂, Propriétés des matériaux, Élasticité, Propriétés électroniques, Propriétés optiques, Structure de bande, Propriétés diélectriques.*